Improved understanding of polar ozone chemistry and the future of the Antarctic ozone hole

Dissertation
zur Erlangung des akademischen
Grades des Doktors der Naturwissenschaften

eingereicht im
Fachbereich Geowissenschaften
der Freien Universität Berlin

von

Stefanie Kremser
Berlin 28. Februar 2011

Gutachter der Dissertation
Erstgutachterin: Prof Dr Ulrike Langematz, Freie Universität Berlin, Germany
Zweitgutachter: Adjunct Prof Dr Greg Bodeker, Victoria University Wellington, New Zealand
Tag der Disputation: 15. Juni 2011

Abstract

The severe ozone depletion observed in cold winters in the polar stratosphere results from the release of man-made ozone depleting substances such as chlorofluorocarbons (CFCs), halons and other halogenated gases such as HCFCs. The destruction of the stratospheric ozone layer is one example of how human activities can affect the composition of the atmosphere with a significant impact on the Earth's environment and the surface climate. Numerous laboratory, field, and model studies have been performed to improve our understanding of the underlying chemical processes responsible for ozone destruction. This knowledge is required to reliably project the future development of stratospheric ozone in a changing climate. In particular, the future evolution of the Antarctic ozone hole has been the focus of a number of model studies as it is very likely that increasing stratospheric ozone abundances will have a significant impact on the Antarctic surface climate through changes in the radiative balance. Today, there remain open scientific questions regarding stratospheric chemistry and projecting the future of the Antarctic ozone hole remains challenging. This thesis investigates a number of sources of uncertainty when projecting the future of the Antarctic ozone hole. These include uncertainties in the reaction rates of the important ozone depleting catalytic chain reactions, uncertainties resulting from different future greenhouse gas (GHG) emissions, and uncertainties resulting from internal model parameterizations, e.g. different chemistry schemes that are incorporated in coupled chemistry-climate models (CCMs).

Despite the fact that the destruction of stratospheric ozone, and in particular the formation of the Antarctic ozone hole due to halogen induced chemical reactions, is well understood, uncertainties in the key kinetic reactions rates driving polar ozone depletion remain. Numerical models rely on accurate kinetic reaction rates to reliably simulate the timing and extent of ozone depletion, which in turn is crucial to confidently assess future ozone abundances. Atmospheric measurements of ClO and/or ClOOCl provide a means to quantitatively test the key kinetic parameters determined in the laboratory. This thesis presents two methods, both using ground-based ClO measurements, to investigate the key kinetic parameters (J/k_f) that control the day-time partitioning of ClO and ClOOCl and there-

fore ozone loss. It was found that the derived kinetic parameters are in general agreement with earlier studies. The results confirm that rather a higher value of J/k_f than currently recommended and used in model simulations is necessary to explain the atmospheric measurements. These findings highlight the need for long-term atmospheric measurements of day and night-time ClO and ClOOCl and the need to investigate model performance under stratospheric conditions. Because the scope of this thesis included the making of ClO measurements in Antarctica by the candidate (including annual visits to Antarctica to refurbish and calibrate the ClO microwave radiometer) and because of the need to quantify the uncertainties in the ClO measurements used to derive kinetic parameters, this thesis includes a description of how of ClO microwave radiometer measurements are made in Antarctica and the retrieval of ClO profiles from measured spectra.

Enhanced GHG emissions are expected to affect global ozone abundances through the production of species that are part of catalytic ozone chain reactions and through GHG-induced temperature changes in the stratosphere. Uncertainties in future emissions of GHGs exist and contribute to the uncertainty in future projections of stratospheric ozone. CCMs are used to simulate stratospheric ozone changes and to project future ozone over the 21^{st} century. However, due to their high computational expense, CCMs cannot explore the full range of uncertainty that arises from the uncertainty in future GHG emissions in the future evolution of stratospheric ozone. This thesis presents a semi-empirical model approach which is used to investigate the evolution of stratospheric activated chlorine concentrations and related changes in Antarctic ozone depletion in a changing climate. The sensitivity of the return dates of Antarctic ozone to historic levels (e.g. 1960 or 1980) to GHG emissions scenarios is examined. It was found that the return date is largely insensitive to GHG concentrations. More importantly, this study shows that the tight coupling between ozone and temperature plays an important role in determining the return date of Antarctic ozone and therefore it is imperative that the ozone-temperature coupling is included in numerical models used to project future ozone abundances.

To have confidence in CCM simulations of spring-time polar ozone loss and projections of the future evolution of stratospheric ozone it is necessary to validate CCMs using a process-oriented approach rather than only comparing the model end-products with atmospheric observations. This thesis presents a semi-empirical model that provides a tool to assess and evaluate the key processes driving polar ozone depletion in CCMs. The semi-empirical model, SWIFT, describes the time rate of change of key trace gases governing chlorine activation and deactivation. SWIFT is trained on atmospheric observations of trace gases, providing a set of empirical fit-coefficients. When applying SWIFT to CCM output, and comparing the derived fit-coefficients with those obtained in reality, the ability of the

CCM to faithfully simulate key chemical processes can be assessed. Because a number of issues where revealed when applying SWIFT to CCMs, this thesis presents only preliminary results from the application of SWIFT to a selected CCM, EMAC-FUB. It was found that known model deficiencies in CCMs complicate the direct use of SWIFT as a diagnostic tool. Nevertheless, SWIFT reproduces the key processes for chlorine activation and deactivation very well and therefore, if accounting for known model deficiencies, SWIFT can provide a powerful tool not only to evaluate key processes but also to estimate the importance of the model deficiencies on the key processes driving polar ozone depletion.

Zusammenfassung

Der gravierende Ozonabbau in der winterlichen polaren Stratosphäre wird durch die Freisetzung von anthropogenen Ozon zerstörenden Substanzen wie Fluorchlorkohlenwasserstoffe (FCKW), Halogene und andere Halogenkohlenwasserstoffverbindungen verursacht. Dieser starke Ozonabbau ist ein Beispiel dafür, wie menschliche Aktivitäten erhebliche Auswirkungen auf die Umwelt und das Klima haben können. Um unser Verständnis von den ursächlich mit dem Ozonabbau im Zusammenhang stehenden chemischen Prozessen zu verbessern, wurden zahlreiche Labor- und Modellstudien sowie Messkampagnen durchgeführt. Aufbauend auf diese wissenschaftlichen Studien können sowohl die zukünftige Entwicklung des stratosphärischen Ozons als auch die Auswirkungen auf das Klima zuverlässig abgeschätzt werden. Insbesondere auf das Antarktische 'Ozonloch' konzentrieren sich verschiedene Modellstudien, die zeigen, dass das ansteigende stratosphärische Ozon und die damit verbundene veränderte Strahlungsbilanz mit grosser Wahrscheinlichkeit erhebliche Auswirkungen auf das antarktische Klima haben werden. Es gibt auch gegenwärtig noch ungeklärte wissenschaftliche Fragen zum Ablauf der ozonabbauenden Prozesse, so dass die Prognose zur zukünftigen Entwicklung des Antarktischen Ozonlochs weiterhin eine Herausforderung bleibt. Die vorliegende Arbeit untersucht eine Reihe von Unsicherheitsfaktoren in den Prognosen zur weiteren Entwicklung des Antarktisches Ozonlochs. Dazu zählen die Unsicherheiten in den Reaktionsgeschwindigkeiten der katalytischen, ozonzerstörenden Zyklen, die Unsicherheiten in den zukünftigen Treibhausgasemissionen (engl. greenhouse gas, GHG) sowie die Unsicherheiten, die sich aus der internen Modell-Parametrisierung ergeben, z.B. unterschiedliche Chemiemodule, die in gekoppelten Klima-Chemie Modellen eingebaut werden (engl. chemistry-climate-models, CCMs).

Die katalytischen Reaktionszyklen und ihre Auswirkungen auf das stratosphärische Ozon sind heute bekannt und gut verstanden. Dennoch verbleiben Unsicherheiten zu den kinetischen Reaktionsgeschwindigkeiten der katalytischen Reaktionszyklen, die für den Abbau des polaren Ozons verantwortlich sind. Numerische Modelle sind auf genaue Angaben zu kinetischen Reaktionsgeschwindigkeiten angewiesen, um den zeitlichen Verlauf und die Intensität der Ozonzerstörung verlässlich simulieren zu können, was eine wichtige Voraus-

setzung ist um eine realistische Beschreibung zukünftiger Ozonkonzentrationen ableiten zu können. Mit Hilfe von atmosphärischen Messungen von ClO und/oder ClOOCl wurden die Labormessungen der kinetischen Reaktionsgeschwindigkeiten quantitativ getestet.

Die vorliegende Arbeit stellt zwei Methoden für die Ermittlung der kinetischen Reaktionsgeschwindigkeiten vor, welche die Aufteilung zwischen ClO und ClOOCl während des Tages kontrollieren (J/k_f). Bei beiden Methoden werden bodengebundende ClO Messungen verwendet. Die Ergebnisse dieser Arbeit stimmen im Allgemeinen gut mit den Ergebnissen von früheren Studien überein. Ebenso bestätigen die gewonnen Ergebnisse, dass im Vergleich zu den derzeit empfohlenen und verwendeten kinetischen Parametern ein eher größerer Wert für J/k_f benötigt wird, um die atmosphärischen Messungen von ClO erklären zu können. Die Resultate dieser Arbeit untersteichen die Notwendigkeit von langfristigen atmosphärischen Tag- und Nachtmessungen von ClO und ClOOCl sowie die Notwendigkeit, die kinetischen Parameter unter stratosphärischen Bedingungen zu untersuchen. Eingeschlossen in die vorliegende Arbeit waren regelmäßige atmosphärische Messungen einschließlich jährlicher Arbeitsaufenthalte in der Antarktis zur Instandhaltung und Kalibrierung des ClO Mikrowellenradiometers. Um die Unsicherheiten der ermittelten kinetischen Parameter, die von der Genauigkeit der verwendeten ClO Messungen abhängen, besser beurteilen zu können, beinhaltet diese Arbeit eine ausführliche Beschreibung des Mikrowellenradiometers und des Messprinzips sowie eine Beschreibung der Retrieval-Methode, welche zur Ermittlung atmosphärischer ClO Profile von den gemessenen Spektren verwendet wird.

Es wird erwartet, dass die zukünftig zunehmenden Emissionen der GHGs die globalen stratosphärischen Ozonkonzentrationen beeinflussen werden, denn mit ansteigenden GHGs werden zusätzliche chemische Substanzen freigesetzt, die an den katalytischen Reaktionszyklen beteiligt sind. Des Weiteren verursachen ansteigende GHGs eine Temperaturabnahme in der Stratosphäre und tragen damit zu verstärktem Ozonabbau bei. Aus diesen Gründen bleiben die Unsicherheiten über zukünftige GHG-Emissionen bestehen, die wiederum zu den Unsicherheiten in den Prognosen zur zukünftigen Entwicklung des Ozons führen. Komplexe CCMs werden heutzutage verwendet, um die Veränderungen im stratosphärischen Ozon zu simulieren und um Prognosen zur zukünftigen Entwicklung des Ozons im 21. Jahrhundert zu erstellen. Diese Simulationen erfordern jedoch einen sehr hohen Rechenaufwand und können jeweils nur ein bis zwei GHG-Emissions-Szenarien zur Erstellung von Prognosen auswerten. Somit kann unter der Verwendung von CCMs nicht die komplette Bandbreite aller genannten Unsicherheiten abgeschätzt werden. Diese Arbeit stellt einen semi-empirischen Modellansatz vor, um die Entwicklung stratosphärischer Chlor-Konzentrationen und die damit verbundene Veränderung im antarktischen Ozon un-

ter den Aspekten des Klimawandels zu prognostizieren. Dabei wurde das Problem der Ozonerholung auf historische Werte (z.B. von 1960 oder 1980) in Abhängigkeit verschiedener GHG-Emissions-Szenarien berücksichtigt. Die Untersuchungen machten den Einfluss des Temperatur-Ozon-Feedbacks deutlich: wird dieser nicht berücksichtigt, dann ist der Zeitpunkt der Ozonerholung größtenteils unabhängig von der Treibhausgasentwicklung. Die Ergebnisse dieser Arbeit verdeutlichen die Bedeutung der engen Kopplung zwischen Temperatur und Ozon und ihre entscheidende Rolle bei der Erstellung von Prognosen zur Entwicklung der Ozonkonzentration in der Antarktis.

Um den CCM-Simulationen des polaren Ozonverlusts und den Prognosen zur zukünftigen Entwicklung des stratosphärischen Ozons vertrauen zu können, ist es erforderlich, neben dem Vergleich der Modell-Ergebnisse mit den Beobachtungen durch eine Überprüfung der CCMs mit Hilfe von Prozess-orientierten Methoden anzuschließen. Das in dieser Arbeit vorgestellte semi-empirische Modell kann zur Evaluierung der wichtigsten CCM Prozesse verwendet werden, die die Ozonzerstörung antreiben. Dieses semi-empirische Modell, SWIFT, beschreibt die zeitliche Veränderung von Spurengasen, die die Aktivierung und Deaktivierung von Chlor regulieren. SWIFT wird an atmosphärischen Messungen verschiedener Spurengase trainiert, woraus empirische Fitkoeffizienten hervorgehen. Wenn SWIFT dann auf CCM Daten angewendet wird, können die berechneten Fitkoeffizienten mit den Koeffizienten die aus den Beobachtungen gewonnen werden, verglichen werden. Dieser Vergleich ermöglicht es abzuschätzen, wie genau die CCMs die chemischen Prozesse simulieren können. Bei der Anwendung von SWIFT auf Ergebnisse von CCM Läufen wurden einige potentielle Probleme aufgedeckt. Aus diesem Grund können hier nur vorläufige Ergebnisse vorgestellt werden, die die SWIFT-Anwendung auf ein ausgewähltes CCM, nämlich EMAC-FUB, betreffen. Es wurde gezeigt, dass die vorhandenen Modelldefizite in CCMs die direkte Anwendung von SWIFT auf CCM Daten erschweren. Jedoch lässt diese Arbeit die deutliche Schlussfolgerung zu, dass SWIFT die für den polaren Ozonabbau wichtigen chemischen Prozesse sehr gut reproduzieren kann. Aus diesem Grunde wird mit SWIFT ein Tool zur Verfügung gestellt, das unter Berücksichtigung der Modelldefizite nicht nur zur Evaluierung von Schlüsselreaktionen in CCMs verwendet werden kann sondern auch für die Abschätzung des Einflusses der Modelldefizite auf diese Schlüsselreaktionen.

Acknowledgements

The work presented in this thesis was carried out at the National Institute of Water and Atmospheric Research (NIWA) in Lauder, New Zealand and this thesis was submitted to the Freie Universität Berlin in Germany. I would like to take this opportunity to acknowledge the help and support from various people during my studies.

First, I wish to thank Prof Dr Ulrike Langematz for supporting me in undertaking my PhD in New Zealand, for her interest in this work and for her supervision.

I am very thankful to my second supervisor, Dr Greg Bodeker, for his encouragement, guidance, excellent support and invaluable advice from the initial to the final stages of my PhD. Thank you for the great effort to explain things clearly and for always taking time to discuss my work.

I also would like to thank the German Academic Exchange Service (DAAD) for their support throughout the Doktorandenstipendium, which allowed this work to be conducted.

I am very grateful for all of the support and contributions I received during my PhD which made it possible to conduct the work presented in this thesis. In particular I would like to mention the following friends and colleagues and I would like to acknowledge their contributions to this thesis:

The ClO measurements were provided by the Stony Brook University and NIWA, who jointly operate a ground-based ClO millimeter-wave radiometer and Scott Base, Antarctica. The first year of my PhD studies was focused on the millimeter wave radiometry. My host institute, NIWA, is responsible for operating and maintaining the ClO microwave radiometer (ChlOe) at Scott Base, while the Stony Brook University is responsible for the data processing which includes the retrieval of ClO profiles from the raw radiometer measurements. During my first year I had the opportunity to meet Dr Alan Parish at the University of Massachusetts, in Amherst, who designed and built the instrument. I would like

to thank Alan for taking the time to explain the entire hardware of ChlOe, i.e. how ChlOe is constructed, and how ChlOe works. During the visit to the United States, I also took the opportunity to visit James Barret and Dr Tom Mooney at Stony Brook University. James and Tom are responsible for the data processing of the ClO measurements made at Scott Base. They introduced me to the complexity of the ClO retrieval. I also visited the microwave group, led by Dr Gerald Nedoluha, at the Naval Research Laboratory in Washington D.C., who are developing an improved microwave instrument to measure water vapour and ozone. In New Zealand I worked closely with Mike Kotkamp and Dr Brian Connor who provided training on the microwave radiometer based in Lauder. Mike is responsible for maintaining and calibrating the ozone and water vapour instruments at Lauder and ChlOe at Scott Base. My working visits to the United States and the training provided at Lauder were the first key steps of my PhD studies that allowed me to take over some responsibilities of maintaining the ClO instrument at Scott Base during my three working visits to Scott Base, Antarctica. I am very grateful that I had the opportunity to meet these people who are part of the international microwave community, and to get involved in the ClO microwave project. A big thank you goes to all of these people, as they were very helpful during the entire time of my PhD. Thanks for answering all my questions and thanks very much for your patience. I also acknowledge Antarctica New Zealand, in particular Paul Woodgate, for supporting my visits to Scott Base. I would like to thank Stony Brook University and NIWA for their financial support of my working visits.

I would like to acknowledge Dr Ross Salawitch and Dr Tim Canty for providing the photochemical box model and ClO-dimer photolysis rates which were used in Chapter 3 of this thesis. In this regard, I would like to thank Dr Katja Frieler and Dr Robyn Schofield for providing the optimal estimation model-code which was extended and adapted to the Antarctic ClO measurements in this thesis. This support is very much appreciated. Special thanks go to Dr Robyn Schofield for collaboration and the invaluable support. Thank you for being there and answering all my questions.

Chapters 4 and 5 of this thesis present semi-empirical models which were trained on satellite-based measurements to derive empirical fit-coefficients. These measurements were provided by Dr Michelle Santee of JPL, Pasadena. A first version of the semi-empirical models presented in Chapter 4 was developed by Dr Petra Huck who then provided these models for the further studies described in this chapter. The semi-empirical model, SWIFT, was developed by Dr Markus Rex, and was provided to test its applicability to observations and to EMAC-FUB output. I would like to acknowledge Markus Kunze for providing the EMAC-FUB data and for patiently answering all of my questions. I would like to thank Dr Petra Huck for her support during my PhD and for the collaboration on this work. Thank

you very much for all of the discussions and for your valuable help. I would also like to thank Dr Markus Rex for his valuable discussions and his ‘hundreds of new ideas’ which definitely improved the work presented here.

During my PhD I had the opportunity to attend three international conferences where I presented some of the results of this work. I would like to thank NIWA and SPARC for providing funding to attend these conferences.

Special thanks go to Dr Karin Kreher for her encouragement and invaluable support. Thanks very much for taking care of me and for making my time in NZ so enjoyable. Many thanks to all NIWA staff at Lauder for making my time in the middle of nowhere so pleasant. In particular, I would like to thank Graeme Strang for asking how things are going and for his support during the time of my PhD. Thank you to Paul Johnston for his interest in my work and for his support. Special thanks go to Dr Hella Garny and Dr Birgit Hassler with whom I had a great time in Lauder and around the world. Thanks to you two for all your invaluable help and support and for being there even if you were not around the corner. I would also like to thank Margaret Auger for her support and kindness, in particular during the final stages of my PhD. Many thanks to Mike Gomez who was ‘microwaving’ to me from time to time and who also was very supportive during my PhD.

Last but not least I would like to thank my friends and family I left behind at home. Thanks for all your support across the sea, the surprises, the pictures and all the hours of very important phone calls in the last three years. It meant very much to me that you were always there even if about 18366.40 km lay between us. Thanks so much!

Contents

1 Introduction **1**

1.1 Overview of stratospheric ozone 1

1.2 Dynamical control of ozone 3

1.3 Chemical control of ozone 5

1.3.1 Pure oxygen chemistry - Chapman chemistry 5

1.3.2 Gas-phase chemistry 7

1.3.3 Chemistry in the cold polar stratosphere 11

1.4 Uncertainties in projecting the future evolution of stratospheric ozone . . . 18

2 Remote Sensing Measurements and Retrieval Algorithm **23**

2.1 Microwave Spectroscopy 24

2.1.1 Blackbody Radiation 25

2.1.2 The Equation of Radiative Transfer 26

2.2 Ground-based ClO microwave radiometer - ChlOe 27

2.2.1 Microwave Radiometer 28

2.2.2 Observing method 31

2.2.3 Calibration procedure - determining the unperturbed signal 31

2.2.4 Day minus night analysis of measured ClO spectra 35

2.3 Satellite observations 38

2.3.1 UARS Microwave Limb Sounder 39

2.3.2 Aura Microwave Limb Sounder 40

2.3.3 ACE-FTS 42
2.4 The Optimal Estimation Retrieval Method 43
2.4.1 Optimal Estimation 43

3 Retrievals of key chlorine chemistry kinetic parameters 49
3.1 Introduction and Motivation 49
3.2 Observations 56
3.3 Model data - SLIMCAT 3D CTM 58
3.4 The optimal estimation method 58
3.4.1 Forward model - Photochemical box model 59
3.4.2 A priori 61
3.4.3 A priori covariance - $\mathbf{S_a}$ 62
3.4.4 SLIMCAT ClO_x profiles 63
3.4.5 Retrieval model 66
3.4.6 Retrieval output parameter 68
3.5 Exploring the full parameter space 70
3.6 Kinetic parameters retrieved from optimal estimation 71
3.7 Kinetic parameters derived from exploring the parameter space 75
3.8 Discussion and Conclusions 78

4 Projections of the evolution of Antarctic ozone 83
4.1 Introduction 83
4.2 GHG emissions scenarios and AOGCM description 87
4.2.1 GHG emissions scenarios 88
4.2.2 Atmosphere-ozone general circulation model - HadCM3 89
4.3 Semi-empirical model for chlorine activation 90
4.3.1 Calculation of FAP 92
4.3.2 Calculation of FAS 92

4.3.3 Determination of ClO_x model fit-coefficients 93
4.4 Semi-empirical model for the change in ozone 95
4.4.1 Calculation of 1960 ozone baseline 98
4.4.2 Determining the fit-coefficients for the semi-empirical model describing the change in ozone 108
4.5 Evolution of Antarctic chlorine and ozone anomalies 110
4.5.1 Evolution of Antarctic chlorine 110
4.5.2 Generating future temperature time series 112
4.5.3 Future evolution of Antarctic ozone depletion 116
4.6 Discussion 121
4.7 Conclusions 124

5 A semi-empirical diagnosis of polar chemistry 127

5.1 Introduction 127
5.2 The semi-empirical model - SWIFT 129
5.2.1 The ozone tendency equation 130
5.2.2 Chlorine activation 131
5.2.3 Chlorine deactivation 133
5.3 Empirical determination of the fit-coefficients 136
5.3.1 Fitting the HNO_3 equation 138
5.3.2 Simulating chlorine activation and deactivation 140
5.4 Application of SWIFT to EMAC-FUB 146
5.4.1 Model description - EMAC-FUB 146
5.4.2 Preparation of EMAC-FUB input 147
5.4.3 Fitting the HNO_3 equation 148
5.5 Conclusion and Outlook 155

6 Conclusion and Outlook 159

A **165**

A.1 Potential temperature 165

A.2 Potential vorticity and calculation of equivalent latitude 165

A.3 Equivalent latitude 166

A.4 Using equivalent latitude to define the vortex edge 168

Chapter 1

Introduction

1.1 Overview of stratospheric ozone

The word ozone is derived from the Greek word *όζειν* meaning 'to smell' and ozone was first produced in the laboratory in 1839 and discovered in the atmosphere in 1867 by Christian F. Schönbein. Atmospheric measurements were required to determine the total amount of atmospheric ozone and its vertical distribution. The first spectroscopic measurements of the total column amount of ozone (i.e., the vertically integrated ozone concentration) were made by Fabry and Buisson (1921). Later, in the mid-1920s, G.M.B. Dobson designed a Féry photographic spectrometer which provided regular ground-based measurements of total column ozone. The spectrophotometer developed further also by Dobson (Dobson, 1931), now called the Dobson Ozone Spectrophotometer, is still used to provide the most accurate total column ozone measurements. Dobson made the first global scale measurements of atmospheric column ozone, from which limited information on the latitudinal distribution of ozone could be derived. In honor of Dobson, the unit in which total column ozone is measured is named the Dobson unit (DU). A column amount of ozone of e.g. 300 DU corresponds to a layer 3 mm thick when compressed to standard temperature (0°C) and pressure (1013 hPa). Today, atmospheric concentrations of ozone are measured by various ground-, balloon-, airplane-, and satellite-based instruments. In addition to column amounts many of these measurements provide information on the vertical distribution of ozone. These long-term measurements of atmospheric ozone revealed that ozone is not distributed uniformly around the globe but varies with altitude, latitude, longitude, and season. About 90% of ozone in the atmosphere resides in the stratosphere, the atmospheric layer extending from the tropopause[1] to about 50 km. Maximum concentrations of ozone are found

[1]The tropopause is the boundary that separates the troposphere from the stratosphere. The tropopause is characterized by the minimum temperature observed between 7 and 16 km, depending on latitude.

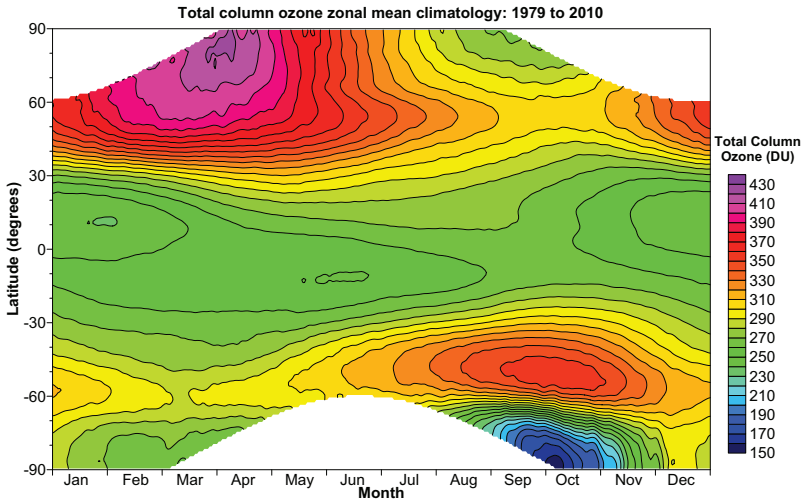

Figure 1.1: Total column ozone climatology as a function of latitude and month. The data were taken from the NIWA combined total column ozone database (Bodeker et al., 2005) for the period 1979 to 2010.

in the lower stratosphere, forming the commonly known 'ozone layer' at altitudes between 20 and 25 km. The stratospheric ozone is important in shielding the Earth from harmful incoming solar ultraviolet (UV) radiation as it absorbs the incoming solar radiation at wavelengths smaller than 320 nm. The absorption of UV radiation by ozone is responsible for the increase in temperature with altitude above the tropopause maintaining a dynamically stable layer where vertical motions are inhibited. This temperature inversion characterizes the stratosphere. The troposphere, that is the lowest part of Earth's atmosphere, contains the remaining 10% of atmospheric ozone which is primarily formed in reactions caused by human-made pollutant gases. High surface levels of ozone are harmful to humans, animals, and plants.

The long-term measurements of atmospheric ozone since the mid 1920s provide a picture of the meridional distribution of ozone as illustrated in Figure 1.1. The main features of the global ozone distribution shown in Figure 1.1 are:

(i) The strong latitudinal gradient, with lower values in the tropics (between 250 and 270 DU) and higher values over the mid and high latitudes (up to 430 DU).
(ii) Seasonality: ozone builds up in the extra-tropics during winter and decreases during summer.
(iii) Severe ozone loss in the Antarctic, resulting in ozone abundances around 150 DU.

These features of the ozone distribution are caused by an interplay of dynamics, i.e. transport processes on a variety of timescales, and atmospheric chemistry, involving ozone production and ozone destruction. These processes are described in detail in the following Sections 1.2 and 1.3.

1.2 Dynamical control of ozone

The polar vortex that develops in the stratosphere during the winter in both hemispheres, plays an important role in explaining the low ozone abundances observed in cold Arctic and Antarctic winters (Figure 1.1). With the onset of polar darkness, the sunlight incident on the polar stratosphere decreases and the emission of thermal radiation leads to radiative cooling of the upper stratosphere. As a result, the polar air masses sink, leading to a low pressure system in the upper stratosphere. At mid and low latitudes, where the sun is shining, the stratospheric air is warmer and the pressure is higher. Therefore, a meridional pressure gradient develops and the air flows away from the high pressure system to the low pressure system. The air is deflected to the right as it moves north and to the left as it moves south due to the coriolis force, that results from the rotation of the Earth. This deflection of the air flow leads to a circumpolar belt of westerly winds (from west to east), called the polar night jet or polar vortex. The strong westerly winds act as a dynamical barrier against meridional transport and hence the air within the polar vortex remains isolated from air masses at lower latitudes. The potential vorticity (Appendix A) is a convenient quantity to describe the polar vortex edge, as it is the analog to atmospheric angular momentum and as such a conserved quantity following the motion. Potential vorticity increases with latitude and reaches its maximum in the center of the polar vortex. In the Southern Hemisphere potential vorticity is generally negative, while it is positive in the Northern Hemisphere. Potential vorticity together with the equivalent latitude coordinate system (that is derived from the potential vorticity) can be used to define the vortex structure and to determine the vortex edge and its meridional impermeability as described in detail in Appendix A.

Meridional mixing across the polar vortex edge is usually induced by planetary wave activity. During winter the westerly mean flow in the stratosphere enables planetary waves, excited in the troposphere due to topography and land-sea thermal differences, to propagate vertically into the middle atmosphere. The dissipation of planetary waves in the stratosphere leads to momentum exchange with the mean zonal flow, decelerating the westerly winds. The deceleration, in turn, results in a meridional poleward motion, driving stratospheric circulation. This wave-driven large scale stratospheric circulation is known as the Brewer-Dobson Circulation (BDC). The BDC transports air upward in the tropics (tropical

upwelling), poleward from low to high latitudes and downwards at high latitudes. Where air is transported upwards (tropical stratosphere) adiabatic expansion results in adiabatic cooling which in turn drives the temperatures below radiative equilibrium. Therefore, solar radiation is absorbed, leading to a diabatic ascent of the tropical air masses (radiative heating). At high latitudes, where air masses descend due to the supply of mass, adiabatic compression results in adiabatic warming which in turn drives the stratospheric temperatures above radiative equilibrium. Therefore, the air masses release radiation, leading to a diabatic decent of the polar air masses (radiative cooling).

The upward transport in the tropics is the main pathway for natural and anthropogenic chemical species to enter the stratosphere, while the downward transport of stratospheric air masses contributes to tropospheric ozone levels at high latitudes. The global distribution of stratospheric ozone with the strong latitudinal gradient (Figure 1.1) is strongly linked to the BDC, as ozone is transported from its main source region (tropics) to the extra-tropics. Dobson suggested such a meridional circulation in order to explain the meridional distribution of ozone, based on the early atmospheric ozone measurements made in 1929. The existence of such a circulation was later confirmed by Brewer (1949) based on stratospheric water vapour concentrations.

During summer, the easterly mean flow in the stratosphere inhibits the propagation of planetary waves into the stratosphere and the BDC is therefore weaker in summer. This seasonality of the BDC explains the variation in ozone abundances with season in the extra-tropics (Figure 1.1). Furthermore, due to the differences in land-sea distribution between the Northern and Southern Hemisphere, planetary wave activity is greater in the Northern Hemisphere than in the Southern Hemisphere. This results in a stronger BDC during the northern winter than during the southern winter and explains the higher extra tropical ozone abundances during boreal winter relative to austral winter (Figure 1.1). In addition, the larger wave activity in the Northern Hemisphere disturbs the Arctic vortex more frequently than its southern counterpart. Therefore, the Antarctic polar vortex is far stronger and more stable than the Arctic vortex. This implies at the same time that the Antarctic air is generally more isolated from the heat and momentum flux supplied from middle and low latitudes than Arctic air. As a result, the Antarctic stratospheric temperatures in the interior of the vortex are lower than in the Arctic (Figure 1.6 in Section 1.3.3), which is a prerequisite for the formation of the Antarctic ozone hole (details below).

1.3 Chemical control of ozone

The stratospheric ozone abundances and its meridional distribution is not only affected by dynamical processes (see above) but also by chemical processes, involving photochemical ozone production and ozone destruction by catalytic cycles. The theory of ozone production and destruction is described by the Chapman cycles (Section 1.3.1). However, this cycle is insufficient to describe the observed distribution of stratospheric ozone. First, Bates and Nicolet (1950) pointed out the role of hydrogen in the catalytic destruction of ozone. In the early 1970s, Crutzen (1970, 1971) proposed that besides loss cycles involving hydrogen, ozone loss cycles including nitrogen species also have to be considered. In 1974, Stolarski and Cicerone showed that additional ozone destruction takes place with chlorine acting as a catalyst. First, Molina and Rowland (1974) and Cicerone et al. (1974) reported the importance of man-made chlorofluorocarbons (CFCs) as a major source for the ozone-depleting chlorine. They proposed that the photolysis of CFCs in the upper stratosphere releases chlorine atoms which destroy ozone in a chlorine-catalytic chain reaction, resulting in ozone loss rates exceeding the natural sinks of ozone. This suggestion by Cicerone et al. (1974) was later validated when a dramatic reduction in ozone abundances was reported by Farman et al. (1985). Total column ozone measurements at the British Antarctic Survey station Halley Bay, showed a decrease by more than half of the total amount of ozone during the Antarctic spring-time. The severe depletion of the Antarctic ozone layer, forming the Antarctic 'ozone hole', was confirmed by satellite measurements which showed spatially that the ozone depletion encompasses a large region over Antarctica.

Since then, great effort has been focused on understanding the chemical and photochemical processes underlying polar ozone depletion. Numerous laboratory, field, and modelling studies, have been carried out in the past three decades. Today, the processes leading to stratospheric ozone depletion are well understood and the primary chemistry controlling stratospheric ozone abundances is described in the following sections.

1.3.1 Pure oxygen chemistry - Chapman chemistry

The theory of formation and destruction of stratospheric ozone involving only oxygen reactions was originally proposed by Sir Sydney Chapman (1930). These reactions, known today as the Chapman reactions, are driven by the photochemical processes illustrated in Figure 1.2. In a first step, highly energetic solar UV radiation breaks an oxygen molecule (O_2) apart, resulting in two oxygen atoms ($2\,O$). The two resulting oxygen atoms combine with oxygen molecules in a second step to form two ozone molecules ($2\,O_3$). The third body M is a collision partner needed for conservation of momentum. As solar UV radiation

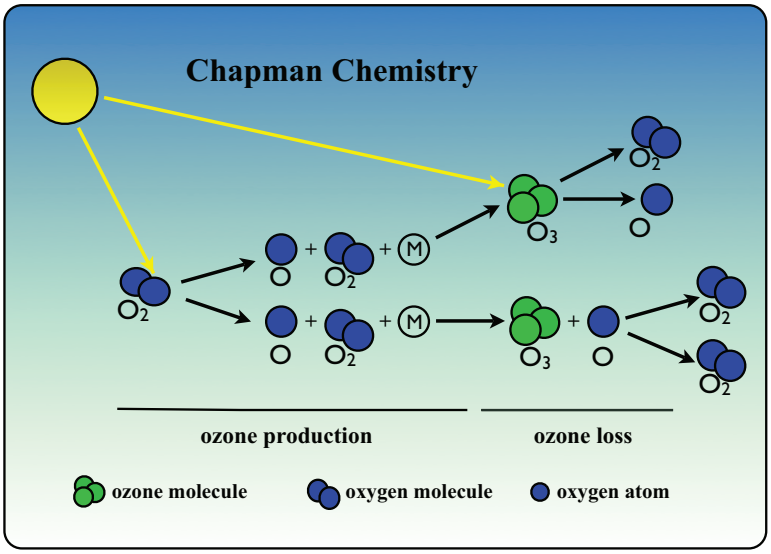

Figure 1.2: Stratospheric ozone production and destruction by the Chapman cycle.

is a prerequisite in forming ozone, most of the ozone is produced in the tropical stratosphere. The fast photolysis of O_3 leads to the formation of molecular and atomic oxygen. Through the formation and photolysis of ozone, a photochemical equilibrium between O and O_3 is established, and a steady-state ozone concentration is achieved. The recombination of ozone with atomic oxygen, forming two oxygen molecules, provides a loss of an O atom and an O_3 molecule (odd-oxygen). The reaction rates of the Chapman cycle depend strongly on temperature (Brasseur and Solomon, 2005). The reaction rate of the ozone production (k_{prod}, $O + O_2 \overset{k_{prod}}{\rightarrow} O_3$) increases with decreasing temperature, while the reaction rate of the loss term (k_{loss}, $O_3 + O \overset{k_{loss}}{\rightarrow} O_2 + O_2$) decreases with decreasing temperature. As a result, a decrease in temperature leads to higher ozone concentrations in the stratosphere, considering the Chapman chemistry only.

The ozone produced and depleted via the Chapman chemistry differs from what is observed. The Chapman theory alone overestimates the ozone abundances in the lower stratosphere. Today, it is well known that additional ozone loss processes exist as discussed in Sections 1.3.2 and 1.3.3 below. Numerous laboratory, field and model studies have lead to an improved understanding of the chemical processes in the stratosphere and today the catalytic ozone depleting cycles involving hydrogen, nitrogen, chlorine, and bromine radicals are well understood. A radical can be recycled many times without being consumed by the chemical reactions of the catalytic cycle. Therefore, catalytic cycles can be very efficient in destroying ozone, even if the concentration of the catalyst is much smaller than that of ozone. The most relevant ozone depleting catalytic cycles are described in more detail below.

1.3.2 Gas-phase chemistry

The catalytic cycles presented below are driven by atomic oxygen densities as oxygen is required to keep the catalyst active. The atomic oxygen density decreases rapidly with decreasing altitude and therefore these cycles are less important in the lower stratosphere. Other cycles, that are not limited by the availability of atomic oxygen, become more important in the lower stratosphere. These cycles are described in Section 1.3.3.

Hydrogen and nitrogen catalytic cycles

The catalytic cycles involving reactive hydrogen species ($HO_x = H + OH + HO_2$; collectively called odd hydrogen) and reactive nitrogen species ($NO_x = NO + NO_2$; called odd nitrogen) are illustrated in Figure 1.3 and are described below.

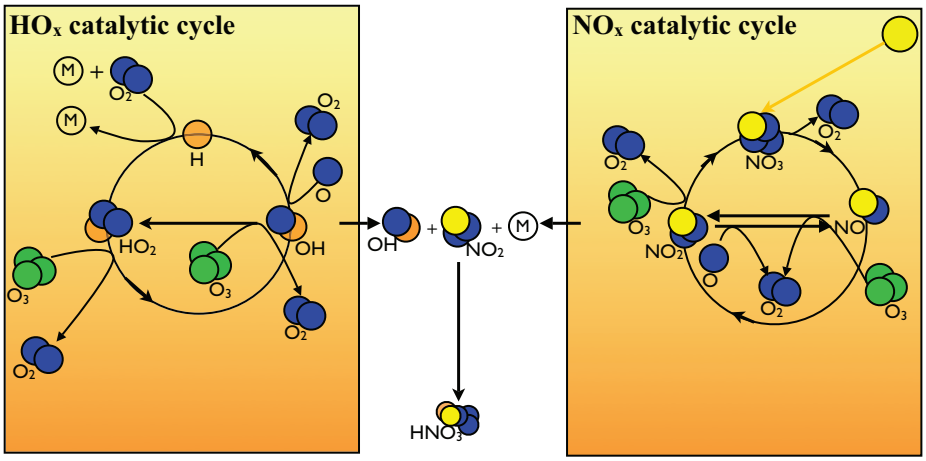

Figure 1.3: A schematic of the main catalytic cycles involving hydrogen (HO_x) and nitrogen (NO_x) species.

Stratospheric odd hydrogen (HO_x) is formed from the stratospheric break down of methane (CH_4), water vapour (H_2O), and molecular hydrogen (H_2) transported from the troposphere. In the stratosphere water vapour reacts with electronically excited oxygen atoms, producing hydroxyl radicals: $H_2O + O(^1D) \rightarrow 2\,OH$. Another source of hydroxyl radicals is molecular hydrogen (H_2) because it also reacts rapidly with an electronically excited oxygen atom: $H_2 + O(^1D) \rightarrow H + OH$. The importance of the hydroxyl radical is twofold, as it reacts with atomic oxygen (important at altitudes above 40 km) and as it reacts with ozone. In both cases the reactions produce hydroperoxyl (HO_2) which in turn also destroys ozone as illustrated in Figure 1.3. These three reactions are part of the hydrogen catalytic cycle (so-called HO_x-cycle). This cycle is one of the most effective photochemical loss

processes for odd oxygen in the upper stratosphere at altitudes between 40 and 50 km (Osterman et al., 1997).

The kinetic reaction rates of the ozone production and destruction of the Chapman chemistry together with the reaction rates of the HO_x-cycle are still too small to explain the observed ozone loss at altitudes between 30 and 35 km. Crutzen (1970) reported that the missing link in determining stratospheric ozone abundances are the reactions with oxides of nitrogen as shown in Figure 1.3. The presence of nitrogen oxides (NO_x) in the middle stratosphere results primarily from the dissociation of nitrous oxide (N_2O) by reaction with an excited oxygen atom (Brasseur and Solomon, 2005): $N_2O + O(^1D) \rightarrow 2\,NO$. N_2O, produced by biological processes, originates in the troposphere and is transported to the stratosphere by troposphere-stratosphere exchange. Nitrogen dioxide (NO_2) can also be injected into the lower stratosphere by aircraft engines. Under normal conditions, catalytic cycles involving nitrogen monoxide (NO) and NO_2 (Figure 1.3) provide a major loss process for odd oxygen at altitudes between ∼25 and 38 km (Lary, 1997; Osterman et al., 1997).

The hydrogen and nitrogen oxides cycles interact forming nitrogen containing species, such as nitric acid (HNO_3) which represent a nitrogen 'reservoir'. The HNO_3 molecule is formed by a three body process, involving OH, NO_2 and any other molecule M, as illustrated in Figure 1.3. The chemical reaction forming HNO_3 provides a sink for the NO and OH catalysts. The primary loss process for HNO_3 is photolysis which releases NO_x so that it can return to participate in the catalytic cycle. However, the photolysis of HNO_3 is very slow which suggests that HNO_3 is an effective reservoir for NO_x. Hence, NO_x is removed from the ozone destruction cycle through the formation of HNO_3 which will eventually be transported from the stratosphere to the troposphere followed by rainout and washout (denitrification).

Catalytic cycles involving halogen compounds

Additional ozone destruction takes place through reactions involving reactive halogen gases such as fluorine, chlorine, bromine, and iodine, that act as catalysts. The main source gases of stratospheric halogens are ozone depleting substances[2] (ODSs) emitted at the surface.

Iodine-containing source gases, iodocarbons such as methyl iodine, $ClCH_2I$ and CH_2IBr, are emitted into the troposphere by primarily biological processes in the oceans. The

[2]Ozone depleting substances are chlorofluorocarbons (CFCs), hydrochlorofluorocarbons (HCFCs), halons, carbon tetrachloride, 1,1,1-trichloroethane (methyl chloroform), and methyl bromide (WMO, 2007).

carbon-halogen bond is very week and photochemically active (Finlayson-Pitts and Pitts, 1999; Solomon et al., 1994). As a result, active iodine is released rapidly from source gases in the troposphere and therefore, the atmospheric chemical and photochemical lifetime of iodine compounds is very short and the amount of iodine reaching the stratosphere is very limited. Solomon et al. (1994) suggested that iodine compounds could be transported by deep convective events from the lower troposphere to the upper troposphere and lower stratosphere. If iodine atoms are released above the tropopause they react with ozone, releasing the iodine monoxide radical. Iodine monoxide interacts with other halogen gases such as chlorine monoxide (ClO) and bromine monoxide (BrO), forming chlorine, bromine and iodine atoms and therefore, these reactions could make a major contribution to ozone destruction in the lowermost stratosphere (Brasseur and Solomon, 2005; Finlayson-Pitts and Pitts, 1999). However, total stratospheric iodine abundances as large as 1 part per trillion (ppt) are required to significantly influence the stratospheric ozone depletion (Solomon et al., 1994). Field studies by Wennberg et al. (1997), Pundt et al. (1998), and Butz et al. (2009) suggest that undetectable low amounts of iodine species reside in the stratosphere. Therefore, it seems to be unlikely that sufficient iodine abundances reach the stratosphere to make a significant contribution to the overall ozone destruction.

The fluorine atoms released in the stratosphere from fluorocarbon source gases are removed by reacting with CH_4 and H_2O rapidly, forming hydrofluoric acid, HF. The bond strength between the hydrogen atom (H) and the fluorine atom (F), forming HF, is very strong so that essentially all fluorine in the stratosphere is irreversible and rapidly 'neutralized' as HF (Brasseur and Solomon, 2005). Therefore, the effects of fluorine chemistry on ozone destruction is negligible.

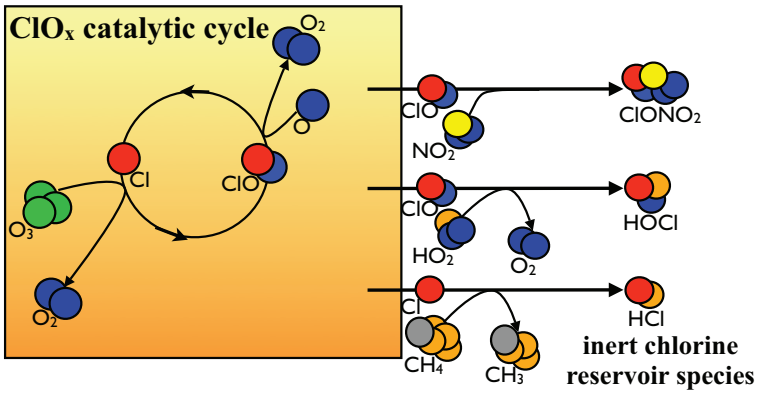

Figure 1.4: A schematic of the main catalytic ozone loss cycles involving chlorine (ClO_x) species.

The release of chlorine atoms from the photolysis of CFCs is currently the main source of anthropogenic stratospheric chlorine. In the upper stratosphere, the high energy UV ra-

diation above the ozone layer can break the CFC bonds, releasing chlorine atoms that are converted into ClO mainly by destroying ozone via the catalytic cycle illustrated in Figure 1.4. ClO undergoes reactions with atomic oxygen to reform atomic chlorine that in turn destroys ozone. As the effectiveness of these catalytic cycles depend on the availability of atomic oxygen, these reactions constitute an important cycle that destroys odd-oxygen primarily in the upper stratosphere at altitudes between 40 and 50 km (Lary, 1997). In the lower stratosphere, ClO reacts with NO to reform chlorine atoms (not shown). This reaction represents an important coupling between the chlorine and nitrogen cycles. There are several reactions that transform reactive chlorine into inert reservoir species, reducing the rate of the chlorine catalytic reactions. The methane molecule and hydrogen and nitrogen oxides interfere with chlorine monoxide, deactivating the reactive chlorine species into nonreactive reservoir species hydrogen chloride (HCl), hypochlorous acid ($HOCl$), and chlorine nitrate ($ClONO_2$) as shown in Figure 1.4. The loss processes for HCl are the reactions with OH, $O(^1D)$, $O(^3P)$, and photolysis. $HOCl$ and $ClONO_2$ are mostly destroyed by photolysis, producing atomic chlorine which can return to participate in the chlorine catalytic cycle. The reservoir gases therefore can be reconverted into chlorine atoms by gas-phase stratospheric chemistry. Therefore, the amount of Cl and ClO available to participate in ozone destructing catalytic chemistry depends on the partitioning of chlorine between these active chlorine radicals and the non-ozone-destroying 'reservoirs'.

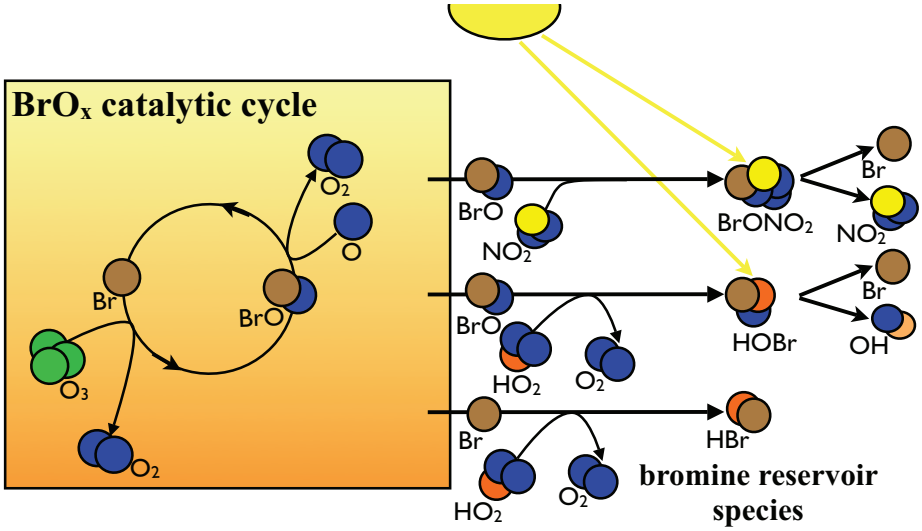

Figure 1.5: A schematic of the ozone depleting catalytic cycle involving bromine (BrO_x) species.

The major sources of stratospheric inorganic bromine compounds (Br_y = $BrCl$ + $HOBr$ + Br + BrO etc.) are anthropogenic Halon-1211 ($CBrClF_2$), Halon-1301 ($CBrF_3$), and methyl bromine (CH_3Br) which has both natural and anthropogenic sources. Once the bromine-containing organics reach the stratosphere they are dissociated by UV photolysis

at wavelengths shorter than 280 nm, releasing bromine atoms. In the case of methyl bromine, reactions with water, the hydroxyl radical, and chlorine ions also generate bromine-containing organic radicals. The production of bromine atoms via photolysis of halons is followed by reaction with ozone to produce bromine monoxide (BrO) (Figure 1.5). Despite its short chemical lifetime, BrO is the most abundant inorganic bromine compound in the stratosphere below 40 km (Lary, 1996). In the upper stratosphere, where ground-state oxygen atom concentrations are higher, the main loss of BrO is through its reaction with atomic oxygen as shown in Figure 1.5. In the sunlit lower stratosphere the main destruction of BrO is by photolysis, and reaction with NO_2. Similar to ClO, BrO can react with NO_2 and HO_2 to form reservoir species such as $BrONO_2$ and $HOBr$, respectively (Figure 1.5). Contrary to the reservoir species of chlorine compounds, the species $BrONO_2$ and $HOBr$ are rapidly photolyzed and hence have very short lifetimes (Lary, 1996). HBr is the longest lived reservoir since the photolysis of HBr in the stratosphere is slow because it involves shortwave ultraviolet light. The lifetime of HBr in the sunlit lower stratosphere is about one day, decreasing to one hour in the upper stratosphere.

Bromine is about 50 times more efficient, per atom, in destroying ozone than chlorine since catalytic cycles involving reaction of reactive bromine (BrO and Br) with ClO, NO_2 and HO_2 do not require free oxygen atoms to destroy ozone. Therefore, these reactions can occur in the lower stratosphere where only a few oxygen atoms are available. Furthermore, $BrONO_2$ and $HOBr$ are very easily photolyzed, so that bromine is present more in its catalytically active forms rather than in its nonreactive forms. However, the abundances of total man-made stratospheric bromine are about 300 times smaller than those of chlorine (SPARC, 2009).

1.3.3 Chemistry in the cold polar stratosphere

The severe ozone loss observed over the Antarctic in late winter/early spring and the large ozone depletion observed in cold Arctic winters, cannot be explained purely with gas phase chemistry (homogeneous processes), as described above. In polar regions, where temperatures are very low (Figure 1.6), additional processes take place leading to accelerated ozone loss. The formation of polar stratospheric clouds (PSCs) at very low temperatures is key to explaining the severe ozone loss in the polar stratosphere. As already suggested in 1986 by Solomon et al., inactive chlorine reservoir species can react on the surface of PSCs (heterogeneous chemistry) leading to an increase in ClO abundances so that additional catalytic cycles involving ClO and BrO must be considered in the chemical destruction of ozone. Before these additional cycles and the heterogeneous processes are described, the formation of the key ingredients, the PSCs, is discussed in the following section.

Polar stratospheric Clouds

PSCs as observed in the cold winter polar stratosphere form at altitudes between 12 and 26 km and are a condensation product of water vapor, sulfate aerosols and nitric acid. Depending on the composition of PSCs, two classes of PSCs can be differentiated: Type I and Type II PSCs.

First, Toon et al. (1986) and Crutzen and Arnold (1986) suggested that PSC particles might consist of nitric acid trihydrate (NAT). The important ingredients for NAT particles to form are the stratospheric sulfate aerosols (SSA) that occur between the tropopause and $\sim$30 km, forming the so called Junge layer (Finlayson-Pitts and Pitts, 1999). The importance of stratospheric aerosols is threefold:

(i) The uptake of water and nitric acid onto SSA, forming PSC particles, i.e. SSA serve as nuclei for PSC formation.
(ii) Several heterogenous chemical reactions occur on the surface of SSA.
(iii) SSA grow as they cool and take up water and nitric acid. These particles can grow big enough so that they sediment, removing water and nitric acid from the polar stratosphere, thereby causing dehydration and denitrification, resulting in an enhancement of ozone destruction.

The SSA consist mainly of sulfuric acid (H_2SO_4) and exists mostly in the liquid state. These particles take up water and nitric acid (HNO_3) as the temperature falls, and at temperatures between 195 and 215 K sulfuric acid tetrahydrate ($SAT = H_2SO_4 \cdot 4\,H_2O$) freezes out. As temperatures decrease more water is taken up and frozen aerosol becomes primarily a HNO_3-H_2O mixture. When the temperature drops below 195 K, NAT freezes out of the solution. As a result, PSCs composed of NAT particles can form well above the ice frost point. However, this process of the formation of solid NAT particles is not satisfactorily understood as laboratory studies indicate that particles containing H_2SO_4, H_2O, and HNO_3 remain liquid even at very low temperatures (e.g. Beyer et al., 1994). Particles that consist of a liquid solution of $HNO_3/H_2SO_4/H_2O$ are termed supercooled ternary solution (STS). These PSC particles that can be both liquid and solid are known as type I PSCs. Type I PSCs are subdivided into type Ia PSCs (solid-phase of NAT) and type Ib PSCs (liquid STS).

PSCs that are composed mainly of water ice particles form when the temperature falls below the ice frost point temperature (T$<$189 K). These PSCs are known as type II PSCs. Due to the relatively large sizes of type II particles (diameter of typically 1-30 μm), they sediment rapidly, leading to a dehydration of the polar stratosphere. Type II PSCs are quite

often observed in the Antarctic as the temperature often drops below the threshold temperature in each winter (Figure 1.6). In the Arctic, on the other hand, where the stratosphere is more often disturbed by dynamical variability, ice PSCs are only occasionally observed. Therefore, dehydration occurs more frequently in the Antarctic stratosphere than in the Arctic.

The minimum temperatures for the Antarctic and Arctic averaged over the period 1978 to 2004 together with the temperature thresholds for forming type II PSCs (T_{ice}) and for forming type I PSCs (T_{NAT}) are shown in Figure 1.6. In the polar vortex the Antarctic air masses are $\sim$10 K cooler than air masses in the Arctic vortex. Furthermore, in the Antarctic, minimum temperatures fall below both T_{NAT} and T_{ice}, and remain below these temperatures for quite some time (June to September), so that PSCs are frequently formed. In the warmer Arctic vortex, on the other hand, temperatures below the T_{ice} threshold are a very rare occurrence and even temperatures below T_{NAT} do not occur in every winter. Even when T_{NAT} temperatures are encountered, the PSC period is much shorter compared to the Antarctic (Figure 1.6). Therefore, the heterogeneous processes as described below, are much more effective in the Antarctic than in the Arctic winter.

A more recent study by Drdla and Müller (2010) indicate that chlorine activation via heterogeneous processes is dominated by reactions on cold SSA particles, without the requirement of PSCs. While the formation temperature for type I PSCs depends on stratospheric H_2O and HNO_3 concentrations, the chlorine activation temperature on cold SSA particles depends on H_2O and sulfate aerosol loading. If correct, this study suggests that enhanced stratospheric aerosol concentrations, e.g. due to large volcanic eruptions, resulting in an enhancement of chlorine activation and ozone loss well above the temperature threshold for forming type I PSCs. Therefore, SSA would play a more significant role in chlorine activation and thereby in polar ozone depletion than currently thought.

Heterogeneous chemistry

The most important heterogeneous reactions on the surface of PSCs and aerosol particles (solid or liquid) are shown in Figure 1.7. The chemical reactions illustrated in Figure 1.7 are very slow in the gas phase but occur rapidly in liquid phase and on solid particle surfaces. Therefore, the inert chlorine reservoir species ($ClONO_2$, HCl) become highly reactive on the surface of cloud and aerosol particles. The reservoir species are converted into less stable, more active forms such as Cl_2 (chlorine activation). The product Cl_2 is released as a gas and is photolyzed rapidly in sunlit air, freeing up two chlorine atoms that efficiently destroy ozone, releasing ClO. Furthermore, heterogeneous reactions suppress the stratos-

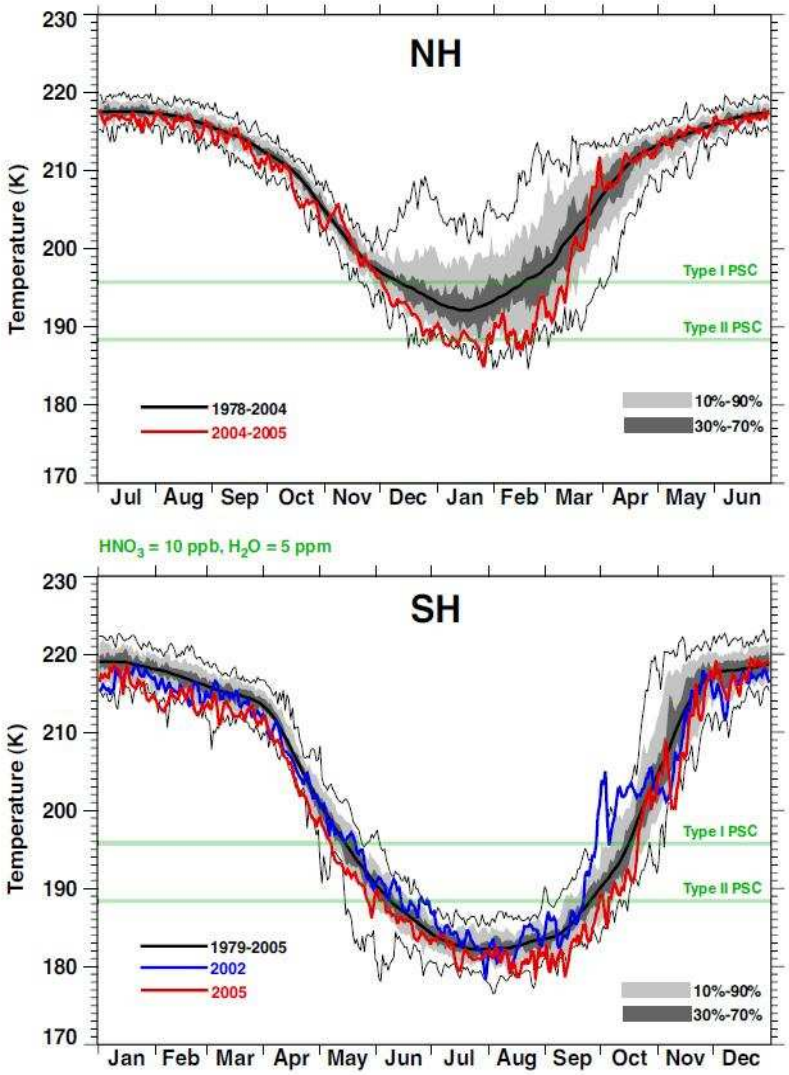

Figure 1.6: 50 hPa daily minimum polar temperature between 50°N and 90°N (top) and between 50°S and 90°S (bottom) from the National Centers for Environmental Prediction/National Center for Atmospheric Research (NCEP/NCAR) re-analysis. The mean annual cycle for the period 1978 to 2004 (Northern Hemisphere (NH)) and 1979 to 2005 (Southern Hemisphere (SH)) (black line) is included. The red line shows the NH winter 2004-2005 and SH winter 2005. For the SH the anomalous winter 2002 is also shown (blue line). The maximum (minimum) values of the 27 years observation period are indicated with thin black lines. The dark gray shading shows the 30 to 70% probability of observations, the light gray areas show the 10 to 90% probability. The threshold temperatures for the formation of PSCs are indicated by the horizontal green lines (Figure from WMO (2007)).

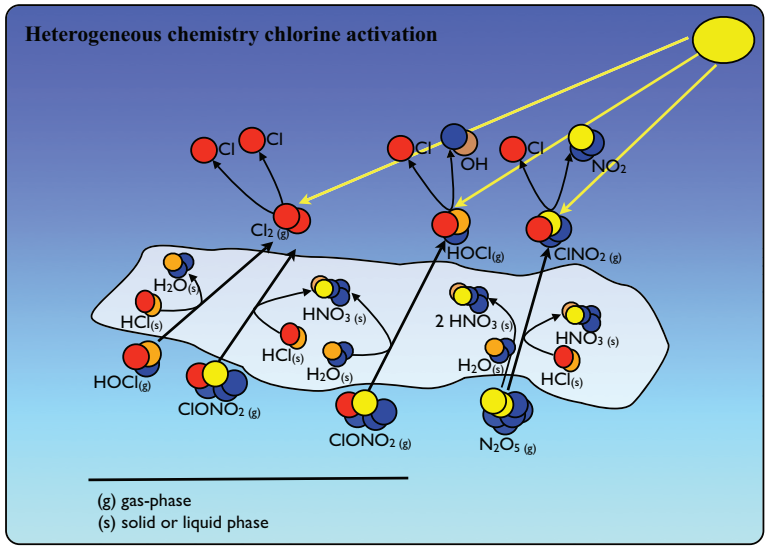

Figure 1.7: A schematic of the main heterogeneous reactions occurring on the surface of polar stratospheric clouds (PSCs) and on aerosols.

pheric NO_x concentrations by converting N_2O_5 into HNO_3 which remains in the solid or liquid phase (Figure 1.7). The removal of NO_x from the stratosphere is known as denoxification and this conversion keeps chlorine active since less ClO is tied up in the $ClONO_2$ reservoir. Under normal conditions, the reaction of $ClONO_2$ with HCl (Figure 1.7) is the most effective reaction for the activation of chlorine via heterogeneous processes. As the stratospheric temperatures decrease the solubility of HCl in a liquid aerosol increases and the two reservoir species react on the PSC surface producing Cl_2 and HNO_3. Heterogeneous reactions such as the hydrolysis of chlorine nitrate ($ClONO_2 + H_2O$), the reaction of HCl with N_2O_5 and the reaction of $HOCl$ with HCl (Figure 1.7) also contribute to chlorine activation. As the products Cl_2, $HOCl$ and $ClNO_2$ are photolyzed rapidly, releasing reactive chlorine atoms, the catalytic ozone depleting cycles become active.

When the sunlight returns after polar darkness, the temperature increases, PSCs no longer from and, as a result, the chlorine activation on the surface of PSCs ceases. Chlorine species are then gradually deactivated by being transformed back to the reservoir species HCl and $ClONO_2$.

However, due to the extensive PSC formation in the Antarctic stratosphere, HNO_3 is removed by sedimentation (denitrification). Therefore, less HNO_3 is available to deactivate chlorine since the production of NO_2 via HNO_3 photolysis is suppressed. Furthermore, ozone can be destroyed almost completely during the Antarctic spring suppressing ClO formation, since the reaction $Cl + O_3 \rightarrow ClO + O_2$ cannot occur in the absence of ozone

and thereby increasing stratospheric chlorine concentrations. As a result, the reservoir species HCl is formed via the reaction with methane (Figure 1.4). Both effects explain why HCl is primarily responsible for deactivating chlorine in the Antarctic stratosphere.

In the more dynamically disturbed Arctic vortex, on the other hand, denitrification occurs less frequently and less intensively such that more HNO_3 remains in the gas-phase. However, as the photolysis of HNO_3 is slow, the formation of the reservoir species is delayed due to denoxification. The reservoir species $ClONO_2$ cannot be formed until HNO_3 is photolyzed and NO_x is freed up to react with ClO. As soon as enough sunlight is available to produce enough NO_x so that Cl atoms can be produced (via $ClO + NO \rightarrow Cl + NO_2$), the HCl reservoir species can be produced.

ClO-Dimer Cycle

Heterogenous processes releasing chlorine in the form of Cl_2 that photolyzes rapidly releasing two chlorine atoms. Chlorine in its atomic form has a very short lifetime (Brasseur and Solomon, 2005) as it destroys ozone immediately, forming chlorine monoxide (ClO). ClO recombines with itself, forming the ClO-dimer, chlorine peroxide ($ClOOCl$). The photolysis of $ClOOCl$ releases two Cl atoms that then react again with ozone.

Numerous Antarctic ground-based measurements of ClO and other trace gases (De Zafra et al., 1987; Solomon et al., 1987; Farmer et al., 1987) suggested that elevated ClO abundances are associated with the strong ozone loss observed in Antarctica. In 1989, Anderson et al. showed that a strong anticorrelation between ozone and ClO within the polar vortex exists and they concluded that ClO is the dominant contributor to stratospheric ozone depletion via catalytic cycles. First, Molina and Molina (1987) proposed a catalytic cycle involving ClO and its dimer, chlorine peroxide ($ClOOCl$), which is independent of atomic oxygen concentrations and today is known as the ClO-dimer cycle. The interaction between ClO and BrO within a catalytic ozone loss cycle (ClO-BrO cycle) was presented by McElroy et al. (1986). These cycles become extremely efficient when high ClO concentrations are present in the lower stratosphere (which is the case after heterogeneous reactions re-activate reservoir species as described in Section 1.3.3). The ClO-dimer cycle and the reaction between ClO and BrO are illustrated in Figure 1.8. Since the chlorine abundances are much higher than bromine abundances in the polar stratosphere, the ClO-dimer cycle is the most destructive ozone loss process. This cycle is typically responsible for 55% to 70% of the spring-time ozone depletion in the Antarctic stratosphere (SPARC, 2009). Nevertheless, as bromine is much more efficient than chlorine, the ClO-BrO cycle is not negligible and from trace gas measurements it was estimated that about 20-30% of the total ozone loss

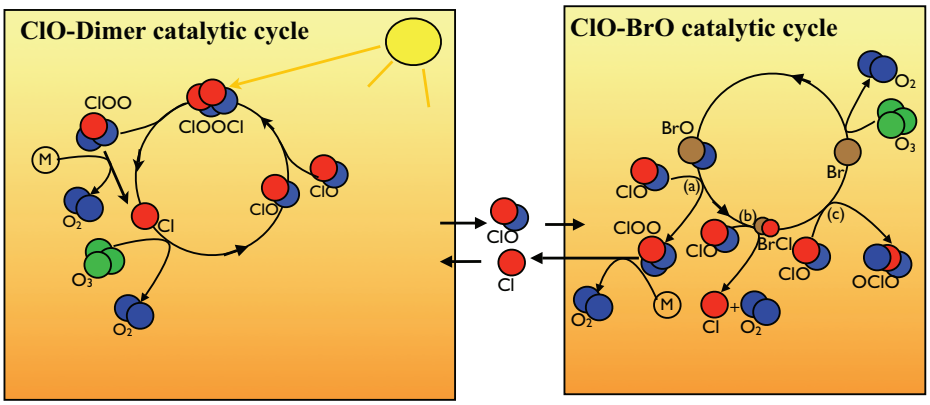

Figure 1.8: ClO-dimer cycle and the interaction of ClO and BrO.

observed at McMurdo during September 1987 and 1992 was due to the ClO-BrO cycle (Finlayson-Pitts and Pitts, 1999, and references herein). Both catalytic cycles require sunlight to be active and to maintain the large ClO abundances via the photolysis of the dimer. Therefore, the greatest ozone depletion can only occur when the polar air masses within the vortex are both, cold and exposed to sunlight. These conditions are limited to the period of late winter/early spring, coinciding with the period of observed ozone loss.

The rate of photodissociation of a molecule such as the dimer ClOOCl is described by the photolysis rate J. As the photolysis rate of the $\mathrm{ClO-dimer}$ (J_{ClOOCl}) is subject this thesis (Chapter 3), a brief description of how to calculate the photolysis rate is given here.

The photolysis rate J for a molecule takes into account the actinic flux $F(\lambda)$, the absorption cross-section $\sigma(\lambda)$ of the molecule and the quantum yield $\phi(\lambda)$ for photodissociation, integrated over all wavelengths (λ) for which the molecule photodissociates, i.e.:

$$J = \int_{\lambda} \phi(\lambda)\sigma(\lambda)F(\lambda)d\lambda \tag{1.1}$$

The actinic flux represents the intensity of available light for absorption and photodissociation and depends on many factors, such as geographical location, the total amount of ozone and the total amount of particles which scatter light traveling through the atmosphere. A radiative transfer model is usually employed to determine actinic fluxes. The absorption cross-sections of the molecule and quantum yields are usually taken from the Jet Propulsion Laboratory (JPL) recommendations.

Today, it is well established that surface emissions of ozone depleting substances are the primary cause of the severe ozone depletion. In response, an international agreement to

protect the ozone layer was signed in 1987 (the Montreal Protocol), and came into force in 1989. The Montreal Protocol and its amendments and adjustments have strongly limited the production and emission of halogen source gases that contribute to the destruction of stratospheric ozone. Consequently, the global production of these chemicals dropped by about 90% in the late 1990s (Solomon, 2004) and stratospheric halogen levels are now decreasing (WMO, 2007). However, due to the long lifetimes of the most important halogen source gases (such as CFC-12 with a lifetime of about 100 years) the removal of the ozone depleting substances from the atmosphere will take many decades. In the absence of changes in other factors affecting ozone, ozone would return to unperturbed levels (e.g. 1960 levels) on a similar time scale (WMO, 2007; Austin et al., 2010a).

1.4 Uncertainties in projecting the future evolution of stratospheric ozone

The future evolution of stratospheric ozone depends not only on future abundances of ozone depleting substances, but also on climate change, brought about in part, by enhanced greenhouse gas (GHG) concentrations (WMO, 2007). Elevated GHGs are expected to affect ozone through GHG-induced stratospheric cooling, resultant changes in the stratospheric circulation, and changes in the abundances of reactive chemical species (Oman et al., 2010). Changes in stratospheric temperatures affect ozone concentrations because the chemical reaction rates and the formation of PSCs are temperature dependent. Furthermore, the BDC is expected to strengthen in a changing climate (SPARC-CCMVal, 2010) thereby affecting transport of chemically reactive trace species. On the other hand, changes in chemical composition affect climate through radiative processes and thereby changing temperatures and consequentially influence atmospheric dynamics. Therefore, to attribute the full elevated impact of GHG concentrations on surface climate, it is becoming more evident that interactions between changes in stratospheric ozone and changes in climate must be considered (WMO, 2007; Eyring et al., 2010a; Austin et al., 2010b). This requires the coupling of chemistry, radiation and dynamical atmospheric processes, including their feedbacks, in models.

Coupled atmosphere-ocean general circulation models (AOGCMs, sometimes referred to as coupled general circulation models, CGCMs), that simulate both atmospheric and ocean processes, are currently used to attribute and quantify the response of the global climate system to increasing GHG concentrations (IPCC, 2007). However, AOGCMs are most often not designed to simulate stratospheric changes, and ozone concentrations are usually prescribed in 21st century simulations. Calculating ozone off-line instead of interactively

in the simulations means that internal feedbacks, e.g. the interaction between changes in temperature and changes in ozone, are missing. Therefore, AOGCMs cannot be used to reliably project the future evolution of the ozone layer.

Coupled chemistry-climate models (CCMs) are currently the most appropriate tools for projecting the evolution of the ozone layer through the 21st century and its impact on climate. CCMs are atmospheric general circulation models (AGCMs or AOGCMs) that are coupled interactively to a detailed chemistry scheme. The AGCM describes radiative and dynamical (transport) processes in the atmosphere including their feedbacks. The AGCM provides input to the chemistry scheme e.g. temperature fields and some trace gas concentrations, which are then processed by the chemistry scheme, generating chemical constituent fields. The output from the chemistry scheme is then returned to the AGCM to be used to calculate radiative forcings. The radiative forcing is defined as the change in the balance between incoming solar and outgoing terrestrial radiation (WMO, 2007). Radiative forcings induce temperature changes while changes in temperature affect dynamics and therefore the transport of trace gases.

To have confidence in the performance of a CCM it is necessary to assess and evaluate the CCM output through model-model and model-observation comparisons. The chemistry-climate model validation (CCMVal) activity (Eyring et al., 2005, 2008), established in 2005, aims to improve our understanding of CCMs through process-oriented evaluation of CCMs so that reliable projections of stratospheric ozone and its impact on climate can be conducted. The assessment and evaluation of CCM output within the CCMVal activity, and additional model studies, revealed numerous sources of uncertainties in projections of the stratospheric ozone layer through the 21st century (SPARC-CCMVal, 2010; Charlton-Perez et al., 2010; Oman et al., 2010). Three sources of uncertainty, contributing to the overall uncertainty in ozone projections, can be identified (Charlton-Perez et al., 2010): (i) model uncertainty due to differences in the formulation of CCMs and an inaccurate representation of dynamical and/or chemical processes, (ii) internal variability and (iii) uncertainty in future emissions of GHGs and ozone depleting substances. Charlton-Perez et al. (2010) indicate that the model uncertainty and uncertainties arising from future emissions scenarios, are the dominant contributors to the overall uncertainty in the projections of future ozone abundances. They suggest that continued development and improvement of CCMs would contribute to refined future ozone projections. In addition, to quantify the uncertainties in future GHG emissions in a more robust way, a larger ensemble of models running at least three different GHG emissions scenarios is required.

CCMs are computationally very demanding and so are expensive to run. Due to the complexity of dynamical, chemical and radiation processes in the atmosphere and their interactions, several external forcings such as sea surface temperatures (SSTs), aerosols, GHG emissions and emissions of ozone depleting substances have to be prescribed in CCM simulations. It is known that uncertainties in CCM simulations are in part a result of these external forcings and their uncertainties (Morgenstern et al., 2010). For example, the future stratospheric sulfate aerosol loading is uncertain due to unpredictable natural variability (volcanic eruptions) and due to human-introduced changes in aerosol levels, e.g sulfur geoengieneering[3]. Stratospheric sulfate aerosols act as condensation nuclei, so that enhanced aerosol loading favours resulting in an enhancement of heterogeneous chemistry and therefore accelerates stratospheric ozone depletion. CCM simulations cannot account for these aerosol-driven changes in ozone destruction as aerosols concentrations are prescribed. Uncertainties in future GHG emissions contribute to the overall uncertainty in CCM projections as enhanced GHGs affect stratospheric ozone via: (i) additional HO_x and NO_x production due to the expected increase in CH_4 and N_2O, (ii) GHG-induced stratospheric cooling as GHGs emit more long-wave radiation than they absorb in the stratosphere. Furthermore, the induced changes in temperatures affect wave driving which influences the strength of the BDC and therefore the transport of ozone and ozone depleting substances. It was shown that the main forcing responsible for changes in the BDC is an increase in sea surface temperatures (SSTs) (Oman et al., 2009) resulting from enhanced GHGs. In addition, changes in atmospheric lifetimes induced by changes in atmospheric dynamics or chemistry can affect the projection of future concentrations of ozone depleting substances.

From this wide array of sources of uncertainty in projections of future ozone levels, three have been selected as foci for in-depth investigation in this thesis.

First, Antarctic ground-based ClO measurements are used to test current values of the kinetic reaction rates driving the effectiveness of the ClO-dimer cycle during the day. Obtaining reliable reaction rates, used in CCM chemistry scheme to simulate ozone, is the first step in correctly projecting future polar ozone abundances.

Second, this thesis aims to test the applicability of using AOGCM temperature fields that include the climate change response of temperature to enhanced GHGs, as input to a semi-empirical model to project the future evolution of ozone through the 21^{st} century. The semi-empirical model accounts for the effect of temperature on ozone that is currently missing in AOGCMs. The sensitivity of the dates of return of ozone

[3]Manipulating Earth's energy balance to off-set the human-driven climate change, e.g. due to injecting light-scattering aerosols into the upper atmosphere (Keith et al., 2010).

to historic values (e.g. 1960 and 1980 values) to enhanced GHG concentrations is examined in this thesis.

Third, this thesis aims to test the applicability of a semi-empirical model, SWIFT, as a diagnostic tool in assessing the representation of key chemical processes in CCMs. SWIFT is first trained on satellite-based measurements to demonstrate that SWIFT can reproduce the chemical processes driving polar ozone depletions and to provide a set of fit-coefficients that can form the basis for using SWIFT as a diagnosing tool to validate CCMs.

Chapter 2

Remote Sensing Measurements and Retrieval Algorithm

Electromagnetic radiation emitted, scattered or transmitted by the atmosphere, is used in remote sensing to observe atmospheric compositions using instruments on satellites, aircrafts, balloons or ground-based instruments on the Earth's surface. In this thesis, measurements from a ground-based microwave radiometer installed at Scott Base, Antarctica, are used to investigate the current understanding of key kinetic parameters that play a central role in polar stratospheric ozone destruction (Chapter 3). Furthermore, atmospheric measurements from the Microwave Limb Sounder (MLS) onboard the UARS and Aura satellite as well as from the Atmospheric Chemistry Experiment Fourier Transform Spectrometer (ACE-FTS) onboard the Canadian satellite SCISAT-1 are used in this thesis to train semi-empirical models that describe the rate of change of polar ozone loss (Chapter 4 and 5). All instruments employ a passive remote sensing technique to measure atmospheric chemical species. Both, the ground-based radiometer and the MLS instrument observe millimeter and sub-millimeter-wavelength thermal radiation emitted by the atmosphere, while the ACE-FTS instrument measures atmospheric infrared absorption spectra to derive vertical profiles of atmospheric constituents, temperature, and pressure.

Spectroscopy studies the propagation of electromagnetic radiation through molecular gases by observing and analyzing absorption and emission spectra. Section 2.1 describes the basics of spectroscopy in the microwave region, followed by an introduction of the radiative transfer theory used to describe the interactions of electromagnetic radiation and the atmosphere. The passive ground-based instrument measuring the thermal emission of chlorine monoxide (ClO) is described in detail in Section 2.2. The observation of the Earth's limb using the passive UARS-MLS, Aura-MLS, and ACE-FTS instruments is presented in Section 2.3. Retrieval algorithms, such as the optimal estimation approach, are used to estimate

the atmospheric state, i.e. the distribution of the observed atmospheric substances, from the measured absorption and emission spectra. An alternative application of optimal estimation is presented in this thesis (Chapter 3) where the retrieval algorithm is employed to retrieve key kinetic reactions rates that govern polar ozone depletion using ground-based ClO measurements. Therefore, a general description of the optimal estimation method is given in this chapter (Section 2.4).

2.1 Microwave Spectroscopy

Spectroscopy in the millimeter and sub-millimeter wavelength range is the study of propagating electromagnetic radiation through molecular gases associated with transitions from one energy state to another within the molecule. There are three different types of transitions between two excited states: transitions between electronic states, which typically occur in the ultraviolet, vibrational transitions, which occur in the infrared, and rotational transitions. Rotational energy changes are relatively small, and therefore the wavelengths associated with transitions between pure rotational states lie within the microwave region at wavelengths of 1 to $100\,\mathrm{mm}$ or at frequencies between 3 GHz and 300 GHz. Wavelength is inversely proportional to frequency so that short wavelengths correspond to high frequencies and vice versa. When describing microwave radiation it is most common to use frequency rather than wavelength. Radiation, resulting from transitions, is emitted only when an electron makes a transition from one state with energy E_i to a state with lower energy E_{i-1}. The emitted photon has an energy given by the difference between these two states:

$$\Delta E = E_i - E_{i-1} = h\nu \tag{2.1}$$

where h is Planck's constant ($h = 6.626 \times 10^{-34}$ J s) and ν is the frequency. The transition from E_{i-1} to E_i, requires an absorption of a photon with the energy $h\nu$. Each jump/transition between fixed energy levels results in the emission or absorption of a characteristic frequency or wavelength.

In the atmosphere, at altitudes below 60 km, where the pressure is high enough for molecular collision to occur sufficiently rapid, vibrational and rotational energy transitions of all radiatively active molecules are dominated by molecular collisions, inducing excitation and de-excitation, and the gas is said to be in local thermodynamic equilibrium (LTE). In LTE, the relative populations of the states with energies E_i and E_j is described by the Boltzmann distribution:

$$\frac{N_i}{N_j} = e^{\frac{-(E_i - E_j)}{k_b T}} = e^{\frac{-h\nu}{k_b T}} \tag{2.2}$$

where N_i (N_j) is the number of molecules in the state of energy E_i (E_j), k_b is Boltzmann's constant ($k_b = 1.38 \times 10^{-23}\mathrm{J\,K^{-1}}$) and T is the local absolute temperature in K. Therefore, in LTE Planck's function (see Section 2.1.1) can be used to represent the spectral radiance.

The equation of radiative transfer describes how the intensity of radiation is affected when propagating through a medium which absorbs, emits and scatters the radiation. The following section describes some aspects of electromagnetic radiative transfer in the atmosphere, focussing on microwave radiation. Microwave and millimeter wave radiation is not affected by atmospheric aerosols and the intensity is only slightly reduced by clouds. Therefore, scattering is negligible and only emission and absorption need to be considered. The law of blackbody radiation is a component for understanding absorption and emission processes in the atmosphere. Hence, blackbody radiation is introduced (Section 2.1.1) before the radiative transfer equation is described (Section 2.1.2).

2.1.1 Blackbody Radiation

The term blackbody is used for a material/substance that completely absorbs all incident radiation at all wavelengths. A blackbody is also a perfect radiator, and the radiation from it is a function of temperature and wavelength alone. The radiation emitted by a blackbody at temperature T and frequency ν is given by Planck's function:

$$B_\nu(T) = \frac{2h\nu^3}{c^2} \frac{1}{e^{\frac{h\nu}{k_b T}} - 1} \tag{2.3}$$

where k_b is Boltzmann's constant and c is the speed of light. The Planck function described the spectrum of intensity B_ν at frequency ν emitted from molecules at temperature T. The wavelength λ_m of the Planck or blackbody radiance intensity at its maximum decreases with increasing temperature.

For frequencies in the microwave region, where $h\nu \ll k_b T$ is valid, the Rayleigh-Jeans law gives an approximation of Planck's law and equation 2.3 can be written as:

$$B_\nu(T) \simeq \frac{2\nu^2 k_b T}{c^2} \tag{2.4}$$

By using the relation between frequency and wavelength ($\nu = \frac{c}{\lambda}$) equation 2.4 can also be expressed as:

$$B_\lambda(T) \simeq \frac{2k_b T}{\lambda^2} \tag{2.5}$$

Therefore, the blackbody radiance intensity is directly proportional to the physical temperature and the brightness temperature T_B can be defined:

$$T_B = \frac{c^2 B_\nu}{2\nu^2 k_b} = \frac{\lambda^2 B_\nu}{2k_b} \tag{2.6}$$

The brightness temperature, T_B, of a blackbody is equal to its temperature, T, in the millimeter wave region, i.e. where the Rayleigh-Jeans approximation to Planck's law is valid.

2.1.2 The Equation of Radiative Transfer

The radiative transfer equation describes the interactions of radiation propagating through a medium. Considering absorption and emission only, the change in the intensity (I_ν) inside a pencil of radiation at a point s along the path in the direction of propagation is given by the differential radiative transfer equation:

$$dI_\nu = \underbrace{-\alpha_\nu I_\nu ds}_{loss} + \underbrace{\varepsilon_\nu ds}_{gain} \tag{2.7}$$

where α_ν and ϵ_ν are the absorption and emission coefficients, respectively.

Introducing the source function $S_\nu = \frac{\varepsilon_\nu}{\alpha_\nu}$, which describes the loss and gain of energy into a given direction, equation 2.7 can be written as:

$$\frac{dI_\nu}{\alpha_\nu ds} = -I_\nu + S_\nu \tag{2.8}$$

This is the general radiative transfer equation, considering absorption and emission only.

In LTE, Kirchhoff's law is valid which states that at a given temperature and frequency the ratio of radiation emittance to absorption is constant and equal to the radiation of a blackbody at that temperature and the emission ε_ν can be written as:

$$\varepsilon_\nu = \alpha_\nu B_\nu(T) \tag{2.9}$$

where $B_\nu(T)$ is the Planck function (equation 2.3). Therefore, the source function S_ν is given by Planck's function ($S_\nu = B_\nu(T)$) leading to the equation of radiative transfer in the form:

$$\frac{1}{\alpha_\nu}\frac{dI_\nu}{ds} = -I_\nu + B_\nu(T) \tag{2.10}$$

This equation is also known as Schwarzschild's equation and is the most fundamental des-

cription of radiative transfer in a nonscattering medium. The first term on the right hand side of equation 2.10 indicates the reduction in intensity due to absorption. The second term denotes the increase in the intensity arising from blackbody emission of the medium.

Equation 2.10 is integrated over the thickness ds from s_0 to s by multiplying both sides by the integrating factor $e^{-\tau_\nu}$ which leads to the solution of the radiative transfer equation:

$$I_\nu(s) = I_\nu(s_0)e^{-\tau_\nu} + \int_{s_0}^{s} B_\nu(T(s))e^{-\tau_\nu}\alpha_\nu ds \tag{2.11}$$

$I_\nu(s)$ is the intensity of radiation at frequency ν seen at the receiver. The first term on the right hand side of equation 2.11 describes an exponential decrease with optical depth of the incident intensity $I_\nu(s_0)$, where $I_\nu(s_0)$ is the intensity of radiation at frequency ν entering the atmosphere at position s_0 along the line-of-sight. The second term describes the intensity attenuated due to absorption by the medium and the contribution to the intensity increase due to emission by the medium along the line-of-sight from s_0 to s. The optical depth τ of the medium between two points s_0 and s on the line-of-sight is defined as:

$$\tau_\nu(s, s_0) = \int_{s_0}^{s} \alpha(s')ds' \tag{2.12}$$

For microwave wavelengths, the Rayleigh-Jeans approximation implies that the intensity I_ν is direct proportional to the so-called brightness temperature T_B. Therefore, the radiative transfer equation can be written in brightness temperature units:

$$T_B(\nu) = T_{B0}(\nu)e^{-\tau_\nu(s)} + \int_{s_0}^{s} T(s)e^{-\tau_\nu(s)}\alpha_\nu(s)ds \tag{2.13}$$

where T_{B0} is the background brightness temperature and T(s) is the local temperature. This form of the radiative transfer equation is commonly used in microwave remote sensing and as described below, where $T_B(\nu)$ is the quantity seen by the receiver of the microwave radiometer.

2.2 Ground-based ClO microwave radiometer - ChlOe

The ground-based millimeter-wave instrument for measuring stratospheric chlorine monoxide (ClO) is described in this section. The instrument detects the thermally-excited emission resulting from transitions between rotational energy levels in the ClO molecule. Stony Brook University and the National Institute of Water and Atmospheric research

(NIWA) jointly operate a ground-based ClO microwave radiometer as part of the Network for the Detection of Atmospheric Composition Change (NDACC) at Scott Base ($77.85°$S, $166.75°$E), Antarctica. A millimeter-wave instrument was installed at the New Zealand research station Scott Base to provide long-term ClO measurements over the Antarctic and has produced useful measurements since February 1996. The main periods where the instrument was not operating were from mid-November 1996 to early February 1997, when components of the instrument failed and were returned to the United States for repair, late April to late June 1998, when the cryogenic system which cools the detector failed, and late January to February 2007 when there were problems with the detector. Except for those periods of downtime and excluding occasional days lost due to bad weather conditions and minor equipment failures, the instrument has been in continuous operation (24 hours a day and year around). A schematic of the ClO millimeter-wave radiometer system is illustrated in Figure 2.2 and the assembly/configuration of the instrument is described in Section 2.2.1, followed by a detailed description of the observing method (Section 2.2.2). Ground-based instruments for stratospheric measurements suffer from the disadvantage that tropospheric water vapour attenuates the stratospheric signal. Therefore, a measurement of the tropospheric attenuation must be made to calibrate the observed emission of ClO. Relating the output of the spectrometer to the intensity of the line that is independent of observing conditions such as atmospheric opacity, results in the observed intensity without any tropospheric attenuation (Section 2.2.3). The high spectral resolution of the instrument allows the measurement of pressure-broadened line shapes, permitting the altitude profile of ClO to be obtained from the shape of the observed spectrum using the retrieval algorithm described in Section 2.4.

2.2.1 Microwave Radiometer

The ground-based ClO millimeter-wave instrument consists of a quasi-optical beam-forming subassembly, a cryogenically cooled heterodyne receiver, operating at 278.6 GHz, and multichannel spectrometer (Figure 2.2). The purpose of the quasi-optical subassembly is to focus the millimeter wave signal coming from the sky and to prepare the incoming signal to be accepted by the heterodyne receiver. The optical devices combine the incoming millimeter wave signal with a signal coming from a local oscillator (LO). A polarization interferometer and a wire polarization grid are used to rotate the polarization of the input signal and the LO signal to that which is accepted by the mixer. The wire grid transmits the incoming radiation if its polarization is orthogonal to the direction of the wires. If the polarization of the incoming radiation is parallel to the direction of the wires, the grid reflects the incoming radiation. Both signals, the incoming millimeter wave signal and the LO signal, are directed through a parabolic mirror into the mixer feedhorn (Figure 2.2) with the same polarization.

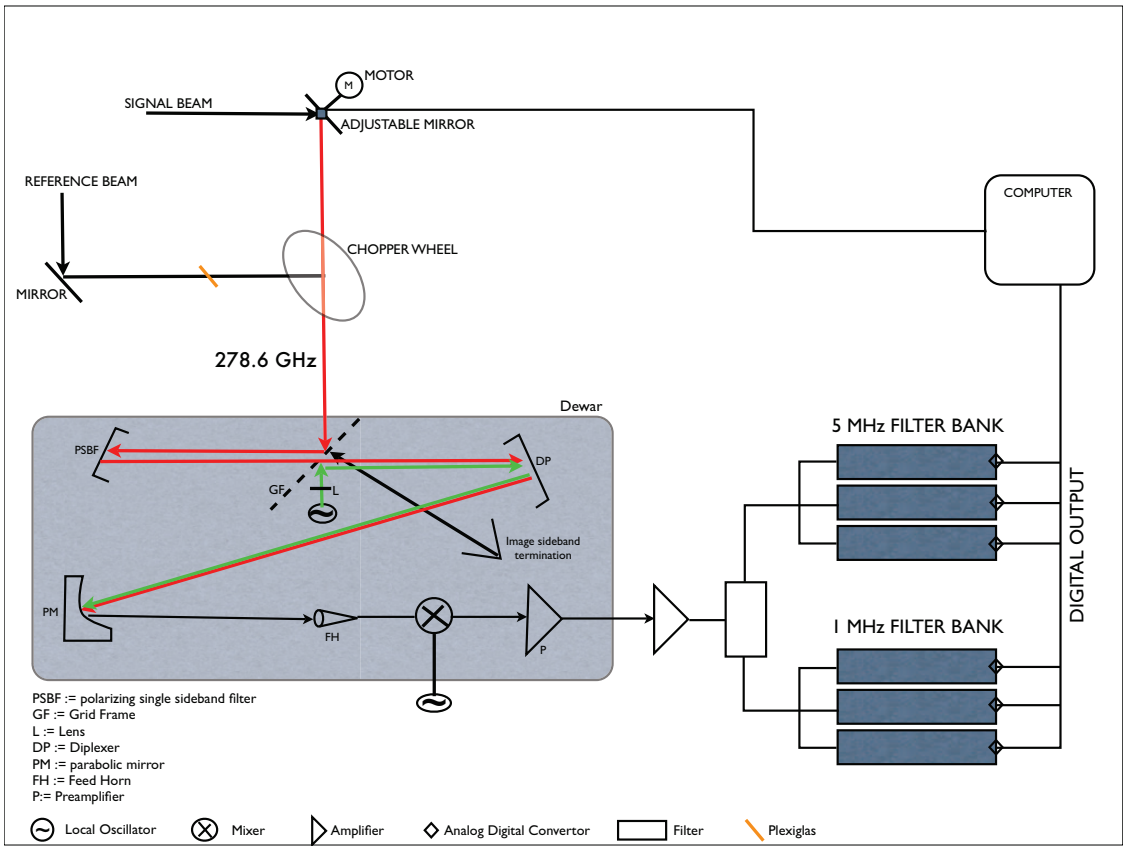

Figure 2.1: A schematic of the ClO millimeter-wave instrument. The instrumental set-up (switching technique), the optical layout within the cooled dewar and the conceptual design of the filter-banks are shown.

A combination of any two signals results in an addition and a subtraction. The addition is called the upper sideband and the subtraction is called the lower sideband. When receiving a signal, it is desirable to use only one sideband and therefore, the unwanted image sideband is reflected into a V-shaped termination at 20 K (Figure 2.2). The optical layout described above and shown in Figure 2.2 is essentially the same as presented in Parrish (1994).

After the incoming signal has passed the quasi-optics and was deflected into the feedhorn, the signal is delivered to the heterodyne receiver. In a heterodyne receiver, the received millimeter wave signal, called the radio frequency signal (RF), is converted to lower 'intermediate' frequency signal (IF), by mixing the RF signal with another, much stronger signal, from a frequency-stabilized local oscillator (LO) before it is detected. The process of 'mixing' the RF signal with the LO signal is termed as the first stage IF mix. The output product is a signal whose frequency is the difference between the RF and LO frequencies. The power in this output signal is proportional to the power in the RF signal, such that the spectral information of the incoming signal is preserved. The mixer output is first connected to a preamplifier (hereafter referred to as the preamp) before the output signal goes into an amplifier with approximately 28 dB gain (first IF amplifier). The preceded preamp prepares the signal for further amplification. The quasi-optic subassembly, the heterodyne receiver and the first IF amplifier are cooled to $\sim$20 K by a closed cycle helium refrigerator to minimize receiver noise.

The IF output of the receiver varies within a band of 1.4-1.9 GHz. Further amplification of the IF signal is provided in the two multichannel filter banks, using conventional electronic techniques. The filter banks are shown only conceptually in Figure 2.2 as there are several more conversion stages and amplifiers than shown in Figure 2.2 (which are, for the purpose of this instrument description, too complex to describe here in any detail). The filter banks, taken together, cover a total bandwidth of 506 MHz, with 306 filter channels. The filters have different resolutions and spacing because the information content of the ClO line per unit frequency is much greater at the line center than at the wings. There are 30 filter channels with a bandwidth of 5 MHz on the left side of the line center (low-frequency side), 256 channels of 1 MHz at the center, and 20 channels of 5 MHz on the right side (high-frequency side). The signal output of each filter is detected/measured by a diode-based square-law detector, and produces an output voltage which is very nearly proportional to the input power. The output voltage is digitized by a voltage to frequency converter and integrated by counting the output of the converter over a specific time interval. The counters accumulate the data for all channels and the data are periodically stored in the computer. The processing of the observed ClO spectra is described in Section 2.2.4.

2.2.2 Observing method

The observing method is the beam switching technique as described in Parrish et al. (1988). The beam switching technique is employed to minimize nonlinearities (Parrish, 1994). The thermal emission of ClO is measured in a zenith reference direction (R) and in a signal direction (S) at a low and adjustable elevation angle (ranging between $5°$ and $28°$). Both reference and signal beams pass through microwave windows in the sidewall of the observatory building and set at Brewster's angle with respect to the beams to eliminate reflections. To eliminate reflections over a range of elevation angles, the window in the signal direction is also curved. A flat mirror at a $45°$ angle outside the building is used to deflect the reference beam from the zenith towards the instrument. The adjustable mirror in the signal beam determines its elevation angle and therefore its the path length through the troposphere. Switching between the signal beam and reference beam is accomplished by a rotating semicircular mirror-surfaced chopper wheel. A lossy dielectric sheet (sheet of plexiglas) is placed at Brewster's angle in the reference beam path, acting as a gray-body emitter to equalize the continuum intensity seen in the signal and reference beam. The elevation angle of the signal beam is then continuously and automatically adjusted to keep the continuum emission equal as the tropospheric opacity changes. The computer calculates the difference between the signal and reference continuum and transmits pulses to a stepping motor driving the elevation mirror to minimize the continuum difference. Since the elevation angle is a necessary parameter in the calibration procedure it is recorded periodically. The computer integrates the detected signal intensity (the chopper wheel is not in the signal path) and reference intensity (the chopper wheel is in the signal path) independently for a preselected time period (usually 20 min) and then computes and stores the quantity (S-R)/R.

The intensity of the observed signal in the reference and signal direction is directly proportional to the brightness temperature according to the Rayleigh-Jeans approximation. Therefore, the intensity seen at the receiver is described by the radiative transfer equation written in brightness temperature units (equation 2.13). To account for tropospheric attenuation of the stratospheric signal (S and R) and to account for receiver noise, the observed intensity must be related to a signal independent of any noise and tropospheric attenuation. To accomplish this, calibration measurements, as outlined below, are performed.

2.2.3 Calibration procedure - determining the unperturbed signal

The measured spectra must be calibrated independently of observing conditions, such as atmospheric opacity and elevation angle of the signal beam, by measuring the thermal radiation from blackbody sources at known temperatures. The blackbody calibration sources

are made out of carbon-loaded epoxy. The calibration procedure determines the stratospheric line intensity T^*, which is the intensity that would be observed in the zenith direction in absence of tropospheric attenuation. The relationship between the observed intensity (measurements in the signal and reference directions) and T^* are derived in the following.

Assuming that the observed species is only located in the stratosphere, and attenuated only in the troposphere, the radiated intensity of an optically thin stratospheric emitter is linearly proportional to the stratospheric path length (Parrish et al., 1988). The relationship between the measured intensities in the signal and reference beam and T^* is then given by:

$$T_S(\nu) = T^* A_s e^{-A_{ts}\tau_z} + T_{atm}(1 - e^{-A_s\tau_z}) + T_{RX} \quad (2.14)$$

$$T_R(\nu) = T^* A_r e^{-A_{tr}\tau_z} e^{-\tau_p} + T_p(1 - e^{-\tau_p}) + T_{atm}(1 - e^{-A_r\tau_z})e^{-\tau_p} + T_{RX} \quad (2.15)$$

where

$T_S(\nu)$, $T_R(\nu)$ are the radiation temperatures of the spectral line seen during the signal and reference observations

A_s, A_r represent the stratospheric air mass factors in the signal and reference direction

A_{ts}, A_{tr} are the air mass factors of the tropospheric absorbing layer in the signal and reference direction

τ_z is the tropospheric opacity

T_{atm} is the atmospheric temperature

T_{RX} is the receiver noise temperature

τ_p, T_p are the opacity and temperature of the dielectric absorber (plexiglas)

Knowing that the servomechanism continuously adjusts the elevation angle of the signal beam to keep the continuum power levels equal ($T_S = T_R$) results in the balance equation:

$$T_{atm}(1 - e^{-A_{ts}\tau_z}) = T_{atm}(1 - e^{-A_{tr}\tau_z})e^{-\tau_p} + T_p(1 - e^{-\tau_p}) \quad (2.16)$$

Substituting equation 2.16 into equation 2.15, which describes the intensity in the reference beam, and knowing that the stratospheric signal ($T^* A_r e^{-A_{tr}\tau_z} e^{-\tau_p}$) is negligible compared with ($T_{atm}(1 - e^{-A_{ts}\tau_z}) + T_{RX}$), it follows that the measured signal ($S - R/R$) is related

to the stratospheric line intensity T^* by the equation:

$$\begin{aligned} \frac{S-R}{R} &\simeq \frac{(A_s e^{-A_{ts}\tau_z} - A_r e^{-A_{tr}\tau_z} e^{-\tau_p}) T^*}{T_{RX} + T_{atm}(1 - e^{-A_s\tau_z})} \\ T^* &= \frac{T_{RX} + T_{atm}(1 - e^{-A_s\tau_z})}{A_s e^{-A_{ts}\tau_z} - A_r e^{-A_{tr}\tau_z} e^{-\tau_p}} \cdot \frac{S-R}{R} \end{aligned} \tag{2.17}$$

To obtain the stratospheric spectral intensity T^* by solving equation 2.17, the air mass factors A_s, A_r, A_{ts}, A_{tr}, the receiver noise temperature T_{RX} and the opacity of the atmosphere in the zenith direction (τ_z) have to be determined.

Air Mass Factor

The air mass factor is given by the optical path length through Earth's atmosphere normalized to the optical path length in the zenith and is obtained from spherical trigometry. It follows that the stratospheric air mass factor in the signal and reference direction is given by:

$$A = \frac{R + z_{source}}{\sqrt{(R + z_{source})^2 - ((R + z_{obs})cos(\theta))^2}} \tag{2.18}$$

where is R the radius of the earth ($R = 6378.1$ km), z_{source} is the altitude of the source, i.e. ClO, z_{obs} is the altitude of the instrument, with $z_{obs} = 0$ for Scott Base, and θ is the elevation angle in the reference ($\theta = 90°$) and signal (readout from adjustable mirror) direction with respect to a horizontal plane at the instrument's position.

Assuming a plane parallel atmosphere in which the curvature of the Earth is ignored and the atmosphere is regarded as highly stratified and homogeneous in the horizontal, the air mass factor for small zenith angles (ξ) can be approximated with:

$$A = 1/cos(\xi) \tag{2.19}$$

When the air mass factor is defined with the elevation angle, which is the angle between the horizon and the signal, using $\theta = 90° - \xi$, the air mass factor can be written as:

$$A = 1/sin(\theta) \tag{2.20}$$

The plane parallel approximation is satisfied for the troposphere, therefore it follows that the tropospheric air mass factors in the signal and reference directions are given by:

$$A_{ts} = A_{tr} = 1/sin(\theta) \tag{2.21}$$

The tropospheric air mass factor in the reference direction is by definition ($\theta = 90°$): A_{tr}=1

Receiver noise temperature

The receiver noise temperature (T_{RX}) is obtained from the calibration measurements, which involve substituting of the thermal radiation from two blackbody sources (microwave absorbing materials) for the radiation from the sky. T_{RX} is determined by placing a hot load and a cold load in the antenna beam. The hot load has the ambient temperature, while the cold load is cooled to $\sim$77 K using liquid nitrogen. The relationship between the corresponding measured detector output voltages V_h and V_c and the corresponding temperatures T_h and T_c is given by:

$$\frac{V_h}{V_c} = \frac{T_h + T_{RX}}{T_c + T_{RX}} \tag{2.22}$$

with $V_h = \alpha(T_{RX} + T_h)$ and $V_c = \alpha(T_{RX} + T_c)$, where α is the temperature to voltage conversion factor.
If both voltages and the temperatures are known, then the receiver noise temperature (T_{RX}) is characterized as:

$$T_{RX} = \frac{T_h V_c - T_c V_h}{V_h - V_c} \tag{2.23}$$

Tropospheric opacity

Besides measuring radiation temperature of two blackbody sources, the tropospheric radiation temperature is also measured during the calibration procedure and used to derive the sky temperature (T_{sky}). T_{sky} is obtained by measuring the spectrometer outputs V_h, V_c, and $V(T_{sky})$ with the hot load at T_h, cold load at T_c, and sky at T_{sky} in the signal direction, respectively. Using these measured output voltages the sky radiation temperature is given by:

$$T_{sky} = \frac{V(T_{sky}) - V_c}{V_h - V_c}(T_h - T_c) + T_c \tag{2.24}$$

The tropospheric opacity (τ_z) can be determined from the tropospheric sky radiation temperature, T_{sky}, because, if the temperature structure of the gas is known, the absorption and emission of a gas are related through the equation of radiative transfer (equation 2.13). The lower part of the troposphere, where most of the absorbing water vapour is located, mainly determines the tropospheric opacity. Assuming that this part of the troposphere is a nearly isothermal absorbing layer, because the temperature changes only slightly, the equation of radiative transfer (equation 2.13) reduces to:

$$T_{sky}(\theta) = T_{atm}(1 - e^{-\frac{\tau_z}{sin\theta}}) \tag{2.25}$$

where τ_z is the opacity at elevation angle θ and T_{atm} is the atmospheric temperature. Equation 2.25 represents the relationship between the measured sky temperature and the tropospheric opacity which can be solved for τ_z leading to:

$$\tau_z = -sin(\theta)\ln(1 - \frac{T_{sky}}{T_{atm}}) \tag{2.26}$$

The calibration procedure enables the determination of the receiver noise temperature, T_{RX}, and the tropospheric attenuation, τ_z, which can be used in equation 2.17 to calculate the intensity without any noise and tropospheric attenuation. In this manner the pure stratospheric emission line of ClO is obtained.

2.2.4 Day minus night analysis of measured ClO spectra

Millimeter-wave measurements, performed as described above, provide a stratospheric emission spectrum which represents the stratospheric emission line of ClO, every 20 minutes of the day. The derived information during the calibration procedure (see Section 2.2.3) is used to account for tropospheric attenuation and receiver noise, so that the pure stratospheric ClO spectra are obtained. As the ClO molecule has a very weak line amplitude, it is necessary to integrate the measured signals over some time period. Therefore, to generate the day-time and night-time ClO spectrum, the ClO spectra measured in 20 minutes time intervals, are averaged over the day-time and night-time period, respectively, where all 'bad' spectra are excluded beforehand. If, for example, the tropospheric opacity is greater than a threshold value of 0.12, the spectrum is flagged as 'bad' and is not included in the daily average. Day-time is defined as 3 hours after sunrise until 1 hour before sunset at 20 km altitude while night-time is defined as 4 hours after sunset until 1 hour before sunrise. The sunset and sunrise at 20 km altitude is defined by a solar zenith angle (SZA) of $94.5°$. Dusk and dawn are not included as ClO is not in photochemical equilibrium during that time of the day, and therefore ClO encounters a rapid change in its mixing ratio. In the morning, ClO concentrations rapidly increase due to the photolysis of the ClO dimer, while in the evening a somewhat slower decrease occurs due to the formation of the ClO dimer. As an example, the generated day-time and night-time ClO spectra on 6 September 2005 are shown in Figure 2.2. The spectral line intensity is expressed in degrees Kelvin using the Rayleigh-Jeans approximation (Section 2.1.2) for millimeter wavelengths.

In addition to the ClO line at 278.6 GHz, the bandwidth of the spectrometer (506 MHz) also includes emission lines of ozone and nitrogen dioxide ($\mathrm{NO_2}$). The ozone line at 278.5 GHz is the strongest line in the spectrum (see Figure 2.2). Furthermore, the measured ClO spectrum also contains baseline artefacts of instrumental origin. Both the additional lines and

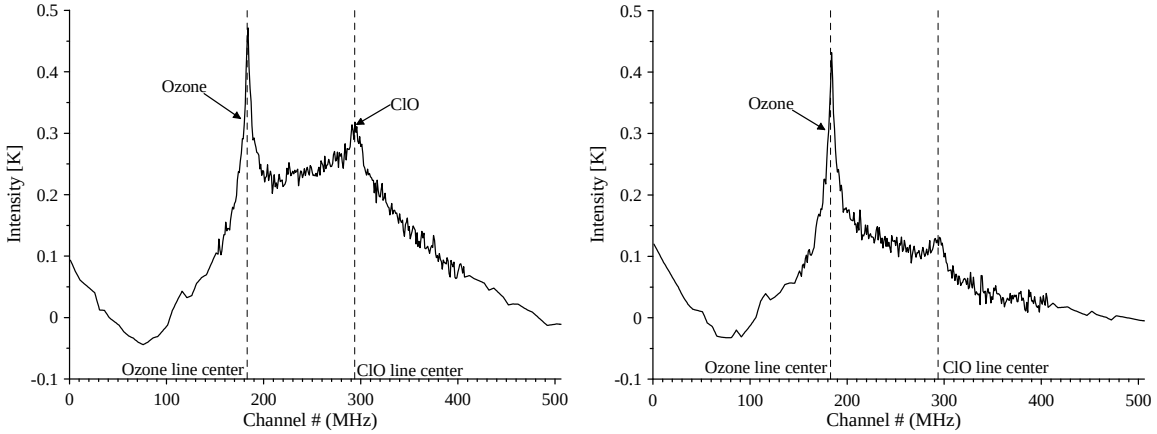

Figure 2.2: ClO day-time spectrum (left panel) and night-time spectrum (right panel) recorded 6 September 2005. The 5 MHz channels (described in Section 2.1.1) are interpolated to 250 1 MHz channels which are then combined with the 256 1 MHz channels. This results in a total number of 506 1 MHz channels.

artefacts, must be removed from the spectrum to obtain the pure ClO line shape. Therefore, the strong diurnal variation of ClO is used and the night-time ClO spectra are subtracted from the day-time spectra to eliminate the interfering lines and artefacts (Solomon et al., 1984; De Zafra et al., 1989). The day minus night ClO spectrum observed on 6 September 2005 is shown in Figure 2.3. During night-time almost all of the ClO is in the form of ClOOCl in the lower stratosphere and as a result, depending on the day of the year, night-time ClO is less than $\sim 20\%$ of day-time ClO. Therefore, the night-time ClO signal is much weaker and narrower. This substraction removes the interference from the additional lines (primarily the ozone line) and removes the artefact almost completely, whereas almost all of the ClO day-time signal is preserved.

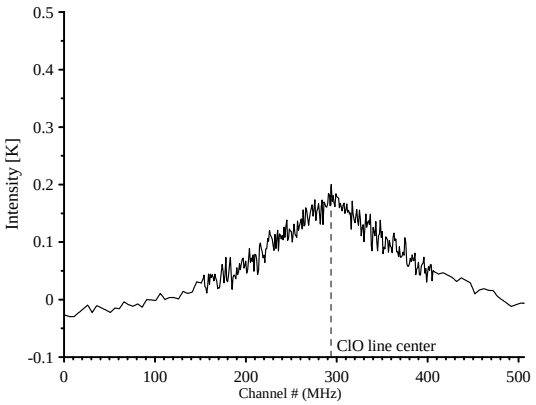

Figure 2.3: ClO day minus night spectrum as derived for the 6 September 2005.

Besides obtaining daily day minus night ClO spectra, the diurnal variation in ClO can also be determined from the ClO measurements. Similar to the day-time ClO spectra, the interfering ozone line and instrumental artefacts need to be eliminated from the measured ClO spectra. Therefore, the ClO spectra for the day-time hours and night-time hours are determined, respectively. As hourly ClO spectra are going to be derived from the measurements, the definition of the day-time and night-time is adjusted, including now dusk and dawn. This adjustment enables to observe the rapid increase in ClO concentrations in the morning as well as the slow decrease in the evenings. To account for dusk and dawn, the day-time hours are defined now from 7 a.m. to 11 p.m. while the period between 12:30 a.m. and 5:30 a.m. is considered as night-time, assuming that most of the ClO is bounded in the ClO dimer. To generate a ClO spectrum for one hour of the day, the 3 ClO spectra measured in 20 minutes intervals are averaged over that hour. As the ClO signal is very weak, this average is not enough to generate an hourly ClO spectrum. Therefore, an average is calculated using the hourly ClO spectra from three consecutive days where ClO measurements are available, i.e. to determine the ClO spectrum at 7 a.m. on the 21 August 2005, the mean of the ClO spectra at 7 a.m. on 20, 21 and 22 August 2005 is calculated. This results in 17 ClO spectra for the day-time and 5 ClO spectra for the night-time. The night-time ClO spectra are averaged over the 5 hours of the night, resulting in one night-time ClO spectrum per 2 hour period. As done with the daily ClO spectra, the night-time ClO spectrum is subtracted from the hourly day-time spectra, respectively, to remove the interference of the ozone line and artefacts. The resulting set of hourly day minus night ClO spectra represent the diurnal variation of ClO. To derive hourly ClO spectra continuously, ClO measurements on three consecutive days are required. Therefore, there are only a limited number of diurnal measurements per season available.

In the lower atmosphere where the pressure is high, intermolecular collisions, which perturb the radiative transitions of the emitting molecules and hence the frequency of the emission, occur very frequently. This so-called pressure broadening affects the absorption/emission lines and the measured ClO spectral emission lines are therefore said to be dominantly pressure-broadened. Pressure broadening arises from the decrease in the lifetime of the excited states of the ClO molecule due to collision. The higher the pressure, the shorter the time between collisions and therefore the shorter the lifetime of the excited states and the greater the bandwidth of the radiated energy. Therefore, the signal in the wings of the spectral line originates from molecules at higher pressure, or lower altitudes, while the molecules responsible for the signal close to the line center originate from lower pressure, or higher altitudes. For more information on broadening of spectral lines see e.g. Liou (2002), McCartney (1983) and Petty (2004). Because the measured ClO spectral line is pressure broadened, its shape contains information on the altitude distribution of the emitting ClO

molecules and a ClO altitude profile can be retrieved between about 15 and 40 km. The vertical resolution of the retrieved ClO profile is 8 to 10 km, however, the location of the peak in the ClO mixing ratio can be determined to an accuracy of 1 to 2 km (Solomon et al., 2000, 2006).

The shape of the measured day minus night ClO spectra, as derived as described above, are used to retrieve daily ClO mixing ratio vertical profiles. The optimal estimation method described by Rodgers (2000) combines the measurements and *a priori* knowledge to make the retrieval as described in Section 2.4. The ground-based measured ClO profiles used in this study (Chapter 3) are based on the derived **day minus night** ClO spectra as described above.

This thesis aims to investigate multiple sources of uncertainties in projecting future polar ozone abundances. To accomplish this, the tools which were used in this thesis require besides ground-based ClO measurements, other atmospheric measurements of chemical species such as ClO, HCl, HNO_3, and $ClONO_2$ with a broad horizontal coverage. Instruments onboard satellites provide these necessary measurements and below, these satellite instruments are described.

2.3 Satellite observations

In addition to ground-based instruments, remote sounding from satellites provides measurements of atmospheric substances. In this thesis, measurements of several atmospheric chemical species from the Microwave Limb Sounder (MLS) and from the Atmospheric Chemistry Experiment Fourier Transform Spectrometer (ACE-FTS) mounted on satellites are used. ClO measurements were obtained from the passive microwave radiometer MLS onboard the Upper Atmosphere Research Satellite (UARS), while HCl and HNO_3 measurements were provided by the MLS on the Aura satellite. As these MLS instruments onboard UARS and Aura do not observe atmospheric $ClONO_2$ concentrations, these measurements were obtained from the ACE-FTS instrument installed on the Canadian satellite SCISAT-1. The UARS-MLS, Aura-MLS, and ACE-FTS instrument are briefly described in this Section. A detailed description of the instruments and their measurements can be found in Livesey et al. (2003), Santee et al. (2003), Waters et al. (2006), Santee et al. (2008a), and Bernath et al. (2005) [and references therein].

2.3.1 UARS Microwave Limb Sounder

The National Aeronautics and Space Administration's (NASA) UARS satellite was launched on 12 September 1991 and designed to operate for three years. UARS exceeded its designed operational lifetime and was finally decommissioned on 14 December 2005, after the launch of Aura (see below). Despite the long life of the host satellite, MLS measurements were only performed until August 1999, after which antenna problems precluded further measurements. The MLS instrument, one of ten instruments onboard UARS, was primarily designed to observe the millimeter- and sub-millimeter-wavelength thermal emission of stratospheric ClO (from $\sim$15-45 km), O_3 (from $\sim$15-80 km), H_2O (from $\sim$15-85 km), temperature (from $\sim$30-60 km), and pressure (from $\sim$30-60 km) as shown in Figure 2.4. At the time, UARS was the first satellite experiment using limb sounding techniques at microwave frequencies (Barath et al., 1993). The UARS-MLS instrument field-of-view is scanned through the limb of Earth's atmosphere, i.e. the instrument views the atmosphere tangentially. The simultaneous UARS-MLS measurements are made globally and continuously during day and night.

The UARS-MLS instrument consists of three assemblies: spectrometer, power supply and sensor. A three-mirror antenna system receives thermal radiation from the atmospheric limb. The antenna system mechanically scans the atmospheric limb in the vertical plane. The received signal is diverted to the three heterodyne radiometers measuring the stratospheric microwave emission spectrum near 63, 205, and 183 GHz, respectively, that belong to the sensor assembly. These radiometers operate at ambient temperature. The signal from the atmospheric limb is combined with a local oscillator signal, employing an ambient temperature Schottky diode, resulting in an intermediate frequency. Six identical filter-banks that are part of the spectrometer assembly spectrally resolve the stratospheric emission lines and produce an output spectrum which gets digitized to pass along to UARS for transmission to the ground.

Measurement coverage

The UARS orbit and MLS viewing geometry are such that MLS measurements were made between 34° N and 80° S for a period of 36 days (referred to as one UARS month), which was followed by a 180° yaw maneuver which changes the observing range to 80° N to 34° S. As a result, MLS alternated between viewing the northern and southern middle and high latitudes ten times a year. The MLS field of view is directed 90° from the UARS orbital vector and a vertical scan of the Earth's limb from 1 km to 90 km altitude is performed. A complete vertical scan takes 65.636 s.

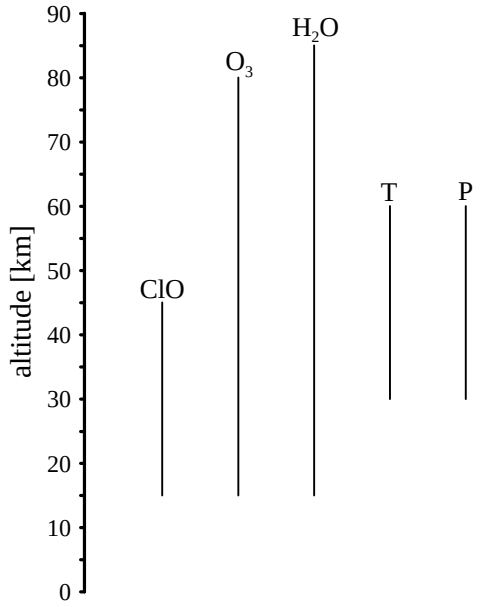

Figure 2.4: The vertical ranges of the observed chemical species and temperature (T) and pressure (P) by UARS-MLS. [Figure adapted from Barath et al. (1993)]

In mid-April 1993, stratospheric H_2O and mesospheric ozone measurements ended due to the failure of the 183 GHz radiometer. As a result of the degradation in the performance of the antenna scanning mechanism and due to problems with the UARS power system, the measurement coverage became more intermittent from late 1993 onwards. The frequency of MLS observations continued to decrease and after the antenna scan problems intensified, the instrument was placed in stand by mode in July 1999. The MLS daily data coverage decreases from 100% from late 1991 through 1993, to 50% in 1994, and only a few tens of measurements per day from 1995 onwards (Livesey et al., 2003).

2.3.2 Aura Microwave Limb Sounder

Most of the UARS measurements of atmospheric composition are being continued with the NASA Aura satellite that was launched on 15 July 2004, with a designed operational period of at least 5 years. The Earth Observing System MLS is one of four instruments onboard Aura. UARS-MLS and Aura-MLS are very similar limb viewing instruments, with AURA-MLS, however, measuring many more atmospheric chemical species such as OH, HO_2, H_2O, O_3, HCl, ClO, $HOCl$, BrO, HNO_3, N_2O, CO, HCN, CH_3CN, and volcanic SO_2 in the region between ~ 8 km and ~ 90 km altitude.

The Aura-MLS instrument consists of three modules. The first module, the GHz radiome-

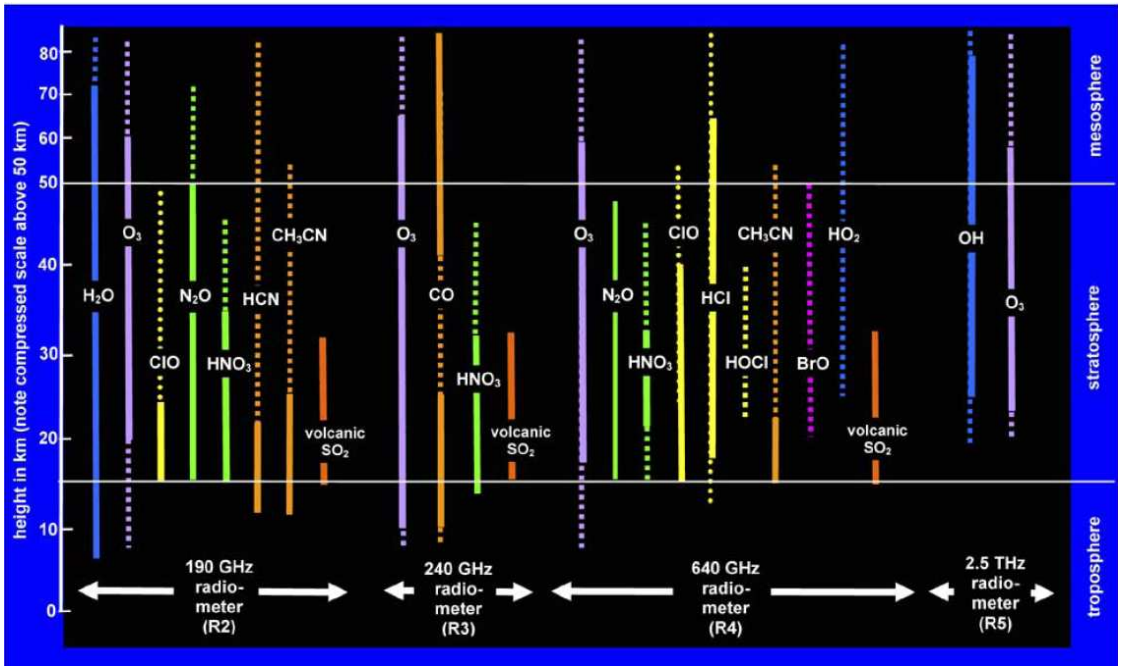

Figure 2.5: Chemical species observed by Aura-MLS. Solid lines indicate that the signal on its own can be used for individual profiles and dotted lines indicate that zonal averages are needed to obtain vertical profiles.[Figure adapted from Waters et al. (2006)]

ter module, consists of five heterodyne radiometers operating at ambient temperature. The radiometers cover the broad spectral regions centered near 118, 190, 240, and 640 GHz. Furthermore, the module includes the GHz antenna system, calibration targets, optical multiplexer and a switching mirror. The second module, the THz radiometer module, contains two heterodyne radiometers centered at 2.5 THz. In addition, a switching mirror, calibration targets, and the THz telescope are parts of the second module. The vertical ranges of all chemical species measured by these radiometers is shown in Figure 2.5. The third module, the spectrometer module, receives signals from the GHz and THz radiometers, detects and digitizes them, and passes the digitized signals to the spacecraft for telemetry to the ground.

Measurement coverage

Aura is in a near-polar, sun-synchronous orbit at 705 km altitude. The Aura satellite travels from the north to the south pole as the Earth rotates to the east underneath the satellite. Therefore, Aura can cover the entire Earth's surface with roughly 13 orbits per day. Sun-synchronous satellites either ascends (north-going) in sunlight or descends (south-going) in darkness or vice versa. In both cases the sunlit orbit occurs over the same part of the Earth at roughly the same local solar time each day. Aura samples the northern high latitudes with ascending measurements near midday local time and the southern high latitudes by

ascending measurements in the late afternoon. The ascending local solar equator crossing time is 1:45 P.M. The Aura-MLS field of view looks in the forward direction of orbital motion and vertically scans the limb in the orbital plane, leading to data coverage from 82° S to 82° N latitude on each orbit. A complete vertical scan takes $\sim$24.7 seconds and every orbit has a fixed number of scans (240 scans per orbit) at essentially fixed latitudes, resulting in roughly 3500 scans over the globe every 24 hours. The number of limb scans in the Northern and Southern Hemisphere are the same. The Aura-MLS vertical resolution is approximately 3 to 4 km, depending on chemical species and altitude range.

2.3.3 ACE-FTS

The Atmospheric Chemistry Experiment (ACE) is a Canadian satellite mission for remote sensing of the Earth's atmosphere. On 12 August 2003 the SCISAT-1 satellite was launched by NASA into a low earth circular orbit with high inclination of 74° at 650 km altitude, providing global coverage from 85° S to 85° N. Several atmospheric species such as H_2O, O_3, NO_2, CO, $ClONO_2$, are measured with the main goal of investigating the chemical and dynamical processes that affect stratospheric ozone depletion. The instruments mounted on the satellite provide vertical profiles of atmospheric constituents from typically 10 to 100 km. The measurements are usually taken during solar occultation, i.e. the spectrum of the sun is measured as sunlight passes through the Earth's atmosphere. Routine science operation began in February 2004.

Instrument design and operation

The ACE high spectral resolution Fourier Transform Spectrometer (ACE-FTS) with a broad spectral coverage, operating from 2.2 to 13.3μm, is the main instrument on SCISAT-1. The FTS measures sequences of infrared absorption spectra during sunrise and sunset where a maximum of 15 sunrises and sunsets per day can be observed. The measurements are carried out in the limb viewing geometry with different slant paths and at a series of tangent heights. In analyzing these measured spectra, the slant columns are combined and inverted into vertical profiles of the atmospheric constituents. The ACE-FTS instrument records measurements every 2 s below altitudes of about 150 km. The vertical resolution of the instrument is 3-4 km. The measured sun spectra are divided by exo-atmospheric measurements (solar measurements with no atmospheric attenuation) and therefore, the instrument is self-calibrating.

When employing solar occultation instruments, the geographical coverage is non-uniform. This results from the fact that the instrument requires sunlight to perform the measurements

and sunlight is not available at all geographical locations and all the time. For example, during the transition between polar day and night, the polar vortex is only partially exposed to sunlight and as a result, the vortex is only partially sampled during the satellite overpass in that period. When using measurements from solar occultation instruments and especially when using vortex average concentrations of solar occultation data, these sampling effects have to be taken into account (Manney et al., 2007). If measurements were taken close to the vortex edge where mixing of mid-latitude air masses into the vortex plays a role (especially in the Arctic vortex), then this might lead to an overestimation of the calculated vortex average.

2.4 The Optimal Estimation Retrieval Method

The use of optimal estimation as the retrieval algorithm, in general, is a standard technique to derive the vertical distribution of atmospheric species inferred from the measured emission or absorption spectra of these species. Besides retrieving atmospheric profiles from measurements, optimal estimation can be also employed to examine the effectiveness of chemical reaction cycles driving polar ozone destruction as shown in Chapter 3. This section describes the basics of the optimal estimation approach in general which then can be individually applied to the purpose of interest, e.g. retrieving trace gas profiles from measured spectra. A more detailed description of the general optimal estimation method can be found in Rodgers (1976, 2000), while the retrieval algorithm specifically applied to the ground-based ClO measurements is described in detail in Solomon et al. (2000) and Parrish et al. (1992). Livesey and Wu (1999) and Livesey et al. (2006) describe thoroughly the retrieval process algorithm for UARS-MLS and Aura-MLS measurements, respectively. The retrieval algorithm employed to derive atmospheric vertical profiles of the spectra measured by the ACE-FTS instrument is described in detail Boone et al. (2005).

2.4.1 Optimal Estimation

Optimal estimation is a algorithm that is used to process measurements together with a description of the measurement uncertainties, the relationship between the measurements and the unknown state, as well as initial condition information (*a priori*). The retrieval process consists of two main parts: the forward model and the retrieval model, also known as the inverse model. To retrieve the vertical distribution of a target molecule from a measured spectrum, the retrieval process requires an accurate understanding of the physics of the measurement process. In practice, there are always uncertainties within the measurement process and the underlying physics of the measurement may not always be fully understood.

Therefore, the detailed physics must be approximated by the **forward model** $\mathbf{F}(\mathbf{x}, \mathbf{b})$. The forward model $\mathbf{F}$ calculates estimates of radiances that would be observed in a given state of the atmosphere. The forward model consists, in general, of modules describing spectroscopy, radiative transfer for a non-scattering atmosphere, and instrumental characteristics.

The second part of the retrieval algorithm, the **retrieval model** 'inverts' the forward model calculations and deduces an atmospheric state using a given set of atmospheric measurements (i.e. measured spectra). Therefore, retrieving vertical profiles from measurements, made from an instrument located on the ground or mounted on a satellite, is generally known as inverse problems.

The atmospheric state which is to be determined, is represented by the unknown state vector $\mathbf{x}$ of length n. In case of the microwave radiometer measurements the state vector $\mathbf{x}$ represents vertical profiles of the atmospheric species of interest (e.g. ClO). The atmospheric measurements (spectra) are described by the measurement vector $\mathbf{y}$ of length m and the measurement error ϵ. The forward model $\mathbf{F}$ relates the atmospheric state $\mathbf{x}$, together with forward model parameters $\mathbf{b}$ that are not intended to be retrieved but important, to the measurements by:

$$\mathbf{y} = \mathbf{F}(\mathbf{x}, \mathbf{b}) + \epsilon \tag{2.27}$$

The forward model then calculates ClO spectra, $\hat{\mathbf{y}}$, which describe the radiances that the instrument would observe if the atmosphere were in the state represented by the state vector, $\mathbf{x}$. The calculated spectra $\hat{\mathbf{y}}$ are compared with the measured spectra $\mathbf{y}$. The difference between the observed and modelled spectra is described by the cost function, χ^2:

$$\chi^2 = (\mathbf{y} - \hat{\mathbf{y}})^T \mathbf{S_e}^{-1} (\mathbf{y} - \hat{\mathbf{y}}) \tag{2.28}$$

$\mathbf{S_e}$ in equation 2.28 is the covariance matrix of the measurement errors and the exponents -1 and T denote the inverse and the transpose, respectively.

There is an infinite set of state vectors $\mathbf{x}$ that would form solutions for equation 2.27, reproducing the measured spectra and therefore the inverse problem is ill-posed. However, as there are more measurements than elements in the state vector (i.e. unknowns), the inverse problem is also said to be over-constrained. Therefore, the retrieved state (the atmospheric profile) cannot be obtained from the measurements alone and *a priori* information of the state ($\mathbf{x_a}$) is required to determine a single solution of equation 2.27. The *a priori* is the best estimate of the atmospheric state before the measurements are made. The *a priori*, and *a priori* covariances, are generally taken from climatological values or, if climatological data are not available, model output can be used as the *a priori*.

The difference between the retrieved state of the atmosphere ($\hat{\mathbf{x}}$) and the *a priori* ($\mathbf{x_a}$) must be considered in the cost function. Thus, the cost function given in equation 2.28 changes to:

$$\chi^2 = (\mathbf{y} - \hat{\mathbf{y}})^T \mathbf{S_e}^{-1} (\mathbf{y} - \hat{\mathbf{y}}) + (\hat{\mathbf{x}} - \mathbf{x_a})^T \mathbf{S_a}^{-1} (\hat{\mathbf{x}} - \mathbf{x_a}) \tag{2.29}$$

where $\mathbf{S_a}$ is the covariance matrix of $\mathbf{x_a}$. The first term in equation 2.29 represents how well the modelled ClO spectrum fits the measurements and the second term weights the difference between the retrieved state and *a priori* state. The greater the measurement uncertainty the more influence the *a priori* has on the retrieved profile. For small measurement errors, the retrieved profile will be mostly determined by the measurements. It follows that the retrieved values will be identical to the *a priori* values at altitudes where the measurement error is too big, i.e. where the information content of the measurements is too low.

To minimize the cost function (equation 2.29), i.e. derive the optimal state of the atmosphere which matches the measured spectra, the standard Gauss-Newton method is applied which iteratively calculates the state vector $\hat{\mathbf{x}}$. The Gauss-Newton iterative equation can be written as:

$$\hat{\mathbf{x}}_{i+1} = \mathbf{x_a} + (\mathbf{S}_a^{-1} + \mathbf{K}_i^T \mathbf{S}_e^{-1} \mathbf{K}_i)^{-1} \mathbf{K}_i^T \mathbf{S}_e^{-1} (\mathbf{y} - \mathbf{F}(\hat{\mathbf{x}}_i) + \mathbf{K}_i (\hat{\mathbf{x}}_i - \mathbf{x}_a)) \tag{2.30}$$

where $\mathbf{K}$ is a $m \times n$ weighting function matrix, also known as the Jacobian, with each element representing the partial derivative of the modelled spectrum with respect to the state vector element:

$$\mathbf{K_{ij}} = \frac{\partial \mathbf{F_i}(\mathbf{x})}{\partial \mathbf{x_j}} \tag{2.31}$$

The weighting function matrix $\mathbf{K}$ is determined by consecutively perturbing each state vector quantity and recalculating the ClO spectrum using the forward model. The weighting functions describe the sensitivity of the modelled spectrum to variations in the state vector.

The iteration of equation 2.30 stops when a prescribed convergence criterion is achieved, i.e. when $\hat{\mathbf{x}}_{\mathbf{i+1}}$ does not significantly differ from $\hat{\mathbf{x}}_{\mathbf{i}}$. The general structure of the described retrieval algorithm is illustrated in Figure 2.6.

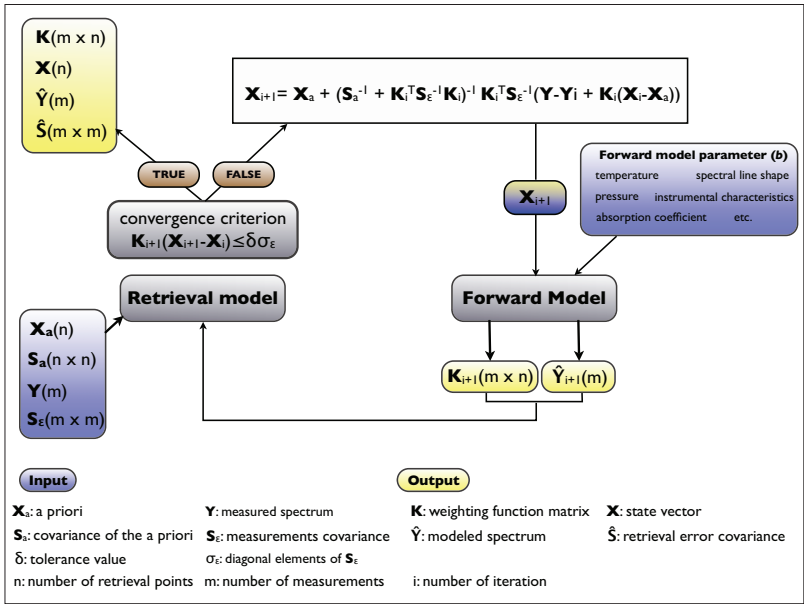

Figure 2.6: A schematic illustrating the basics of the optimal estimation retrieval algorithm.

The described Gauss-Newton method is applied to non-linear problems e.g. the retrieval of vertical profiles of the species obtained from satellite measurements and the retrieval of key kinetic reaction rates (Chapter 3). However, if the retrieval problem is linear because changes in the emission line are linear to changes in the trace gas mixing ratios (which is the case for the described ground-based ClO measurements) the solution of equation 2.30 can be written as:

$$\hat{\mathbf{x}} = \mathbf{x_a} + \mathbf{S}_a\mathbf{K}^T(\mathbf{K}\mathbf{S}_a\mathbf{K}^T + \mathbf{S}_e)^{-1}(\mathbf{y} - \mathbf{K}(\mathbf{x}_a)) \tag{2.32}$$

Retrieval Resolution

The averaging kernel matrix, $\mathbf{A}$, describes the relationship between the retrieved state and the true state, i.e. the response of the retrieved state to changes in the true state and is given by:

$$\mathbf{A} = \frac{\partial\hat{\mathbf{x}}}{\partial\mathbf{x}} = (\mathbf{K}^T\mathbf{S_e}^{-1}\mathbf{K} + \mathbf{S_a}^{-1})^{-1}\mathbf{K}^T\mathbf{S_e}^{-1}\mathbf{K} \tag{2.33}$$

The averaging kernel matrix is a measure of how and where the retrieval $\hat{\mathbf{x}}$ is sensitive to the true state $\mathbf{x}$. For an ideal inverse method, $\mathbf{A}$ would be the identity matrix, and therefore $\hat{\mathbf{x}} = \mathbf{x}$. In practice, the rows of $\mathbf{A}$ are functions with a peak at the altitude where the measurements provide information. At altitudes where the measurements do not provide enough information, no significant peak at the corresponding altitude is present. The rows of $\mathbf{A}$ are called 'averaging kernel's' or smoothing functions, as they represent

where the retrieval is sensitive to changes in the true profile. Each column of $\mathbf{A}$ represents the response of the retrieval at a given altitude to a perturbation of the true state vector at the same altitude. Therefore, the columns of $\mathbf{A}$ are a measure of how the retrieval is sensitive to changes in the true state.
The width of the averaging kernels peak quantitatively describes the vertical resolution of the retrieval. The narrower the width the better the resolution and vice versa. If the kernels are well peaked and centered at the appropriate level then a good way to define the vertical resolution is to determine the full width at half maximum of the averaging kernels (Connor et al., 1995).

Retrieval Error

The total error of the retrieval, i.e. the difference between the retrieved state and the true state, consists of three main components due to (1) uncertainties in the measurements, (2) errors in the forward model and inverse model, and (3) smoothing, which accounts for the influence of the *a priori* (Rodgers, 1990).

The error in the retrieval due to the total uncertainties in the measurements ϵ is described by the retrieval noise $\mathbf{G_y}\epsilon$. The contribution function matrix $\mathbf{G_y}$ described the sensitivity of the retrieval to changes in the measurements and ϵ is the measurement error ($\mathbf{G_y} = \mathbf{S}_a\mathbf{K}^T(\mathbf{K}\mathbf{S}_a\mathbf{K}^T + \mathbf{S}_e)^{-1}$). The covariance of the retrieval noise is given by:

$$\mathbf{S_m} = \mathbf{G_y}\mathbf{S_e}\mathbf{G_y}^T \tag{2.34}$$

The covariance matrix $\mathbf{S_e}$ is diagonal, if the measurements $\mathbf{y}$ are determined independently. The measurements errors ϵ are then uncorrelated.

The ‘smoothing’ of the retrieved profile using the *a priori* where the information content of the measurement is poor introduces an error and the covariance of that error, using the identity matrix $\mathbf{I}$, is given by:

$$\mathbf{S_s} = (\mathbf{A} - \mathbf{I})\mathbf{S_a}(\mathbf{A} - \mathbf{I})^T \tag{2.35}$$

The last contribution to the total retrieval error is the error due to uncertainties in the forward model parameters, represented by $\mathbf{G_y}\delta_y$. δ_y describes the errors in the calibration of the measurements or in the calculations of the modelled spectra using the forward model. The

forward model covariance can be formulated as:

$$\mathbf{S_f} = \mathbf{G_y} \mathbf{K_b} \mathbf{S_b} \mathbf{K_b}^T \mathbf{G_y}^T \tag{2.36}$$

where $\mathbf{S_b}$ is the error covariance matrix of the forward model parameter $\mathbf{b}$ and $\mathbf{K_b}$ is the forward model parameters weighting functions, i.e. the sensitivity of the forward model to the forward model parameters ($\mathbf{K_b} = \partial \mathbf{F} / \partial \mathrm{b}$).

The overall retrieval error combines the described covariances corresponding to (1) errors in the measurements, (2) smoothing error, and (3) errors resulting from the forward model parameters and is described with the covariance of the retrieved atmospheric state ($\hat{\mathbf{S}}$) of the last iteration:

$$\hat{\mathbf{S}} = \mathbf{S_s} + \mathbf{S_m} + \mathbf{S_f} \tag{2.37}$$

Chapter 3

Retrievals of key chlorine chemistry kinetic parameters[1]

3.1 Introduction and Motivation

As stated in Chapter 1, an accurate understanding of polar stratospheric ozone depletion is a prerequisite for reliably projecting the future evolution of polar ozone and its impact on climate. Confidence in the ability to simulate ozone loss processes and projecting future polar ozone abundances in numerical models depends on the understanding polar ozone loss processes. Coupled chemistry-climate models (CCMs) are employed to simulate stratospheric ozone changes and to project the evolution of stratospheric ozone throughout the 21st century. CCM are coupled interactively to an chemistry scheme that calculates an ozone field using kinetic reaction rates that were determined in the laboratory and by means of field measurements. These kinetic reaction rates are provided by the JPL data panel (e.g. Sander et al., 2003, 2006, 2009) or the IUPAC data panel (Atkinson et al., 2007). If these kinetic reactions rates are incorrect the simulated ozone field by CCM will be inaccurate. Even the corresponding uncertainties on the kinetic parameters recommended by these panels determine in part the uncertainty on projections of ozone loss (Kawa et al., 2009). Therefore, it is crucial to reduce these uncertainties for an accurate representation of past and present ozone abundances and for a better predictive capability of the future evolution of ozone levels in stratospheric chemistry models.

[1]Part of this chapter has been published in: Kremser, S., Schofield, R., Bodeker, G. E., Connor, B. J., Rex, M., Barret, J., Mooney, T., Salawitch, R. J., Canty, T., Frieler, K., Chipperfield, M. P., Langematz, U., and Feng, W.: Retrievals of chlorine chemistry kinetic parameters from Antarctic ClO microwave radiometer measurements, Atmospheric Chemistry and Physics, 11, 5183-5193, 2011.

The catalytic ClO-dimer cycle, introduced in Chapter 1, is primarily responsible for the severe ozone depletion occurring in the polar stratosphere. Therefore, the accuracy of modelled ozone loss relies predominantly on the accuracy of the kinetic parameters used in the model that govern the effectiveness of the ClO-dimer cycle in depleting ozone. To reduce the uncertainty on the kinetic parameters of the ClO-dimer cycle, numerous laboratory, field, and model studies have been performed. Many of these studies focused on the kinetic parameters that govern the polar ozone depletion by the ClO-dimer cycle, such as the dimer formation rate (k_f), the absorption cross-section of the dimer which is directly related to the photolysis rate (J), and the equilibrium constant (K_{eq}). After the stratospheric air masses within the polar vortex have been processed by PSCs (Chapter 1) high ClO concentrations are present in the polar stratosphere and the ClO-dimer cycle:

$$\mathrm{ClO} + \mathrm{ClO} + \mathrm{M} \underset{k_r}{\overset{k_f}{\rightleftharpoons}} \mathrm{ClOOCl} + \mathrm{M} \quad \text{(R1)}$$

$$\mathrm{ClOOCl} + h\nu \xrightarrow{J} \mathrm{Cl} + \mathrm{ClOO} \quad \text{(R2)}$$

$$\mathrm{ClOO} + \mathrm{M} \rightarrow \mathrm{Cl} + \mathrm{O_2} + \mathrm{M} \quad \text{(R3)}$$

$$2 \times [\mathrm{Cl} + \mathrm{O_3} \rightarrow \mathrm{ClO} + \mathrm{O_2}] \quad \text{(R4)}$$

$$Net : 2\mathrm{O_3} + h\nu \rightarrow 3\mathrm{O_2}$$

becomes an extremely efficient ozone loss process. k_r in reaction (R1) is the thermal dissociation rate of the ClO-dimer. The formation and the photolysis of the ClO-dimer control the effectiveness of the catalytic ClO-dimer cycle. The key reactions in terms of ozone destruction are the dimer photolysis (reaction (R2)) and the reaction of chlorine dioxide (reaction (R3)) with any molecule, releasing chlorine (Cl) atoms that then react with ozone. The photolysis of the dimer is the rate limiting step in this cycle. If ClOOCl decomposes thermally rather than being photolyzed, or if the photolysis reaction produces ClO, a null cycle results, leading to no change in ozone concentrations.

Considering the self-reaction of ClO (reaction (R1)) three additional pathways for the combination of the dimer are possible, producing $\mathrm{Cl_2} + \mathrm{O_2}$, $\mathrm{OClO} + \mathrm{Cl}$ or $\mathrm{ClOO} + \mathrm{Cl}$, respectively. However, laboratory studies report that the overall rate of these reactions is slow (Molina and Molina, 1987, and references therein). Therefore, the dominant product of the ClO self-reaction is the ClO-dimer.

During day-time, when ClOOCl loss occurs mainly by photolysis, the partitioning between ClO and ClOOCl, and the overall rate of the catalytic cycle, is controlled by the dimer formation rate (k_f) and photolysis rate (J). The equilibrium between ClO and ClOOCl is then given by the expression:

$$\frac{[\mathrm{ClO}]^2}{[\mathrm{ClOOCl}]} = J/k_f \tag{3.1}$$

During night-time, when no photolysis of the dimer takes place, the temperature dependent thermal equilibrium constant K_{eq} governs the partitioning between ClO and ClOOCl:

$$K_{eq} = \frac{k_f}{k_r} = \frac{[\mathrm{ClOOCl}]}{[\mathrm{ClO}]^2} \tag{3.2}$$

Uncertainties in the values of these kinetic parameters (J, k_f and K_{eq}) contribute to differences between measured and modelled polar stratospheric ClO (e.g. Stimpfle et al., 2004), affect our ability to accurately describe polar ozone destruction (e.g. Frieler et al., 2006; von Hobe et al., 2007), and our ability to confidently project the response of polar ozone to future changes in stratospheric chlorine loading (e.g. SPARC, 2009).

To calculate the photolysis rate of the ClO-dimer, J_{ClOOCl} (equation (1.1)), the absorption cross-sections are usually taken from the JPL or IUPAC panels. These recommended absorption cross-sections of ClOOCl typically fall between laboratory measurements by Huder and DeMore (1995) (low range in photolytically active region, i.e. the region between 190 and 450 nm where ClOOCl photolyzes) and Burkholder et al. (1990) (high range). In 2007, Pope et al. published ClOOCl absorption cross-sections that were considerably lower than either the Sander et al. (2006) (hereafter: JPL06) or Atkinson et al. (2007) recommendations. This smaller photolysis rate would make it impossible to quantitatively explain observed polar ozone loss, suggesting that as yet unknown processes were active. More recent laboratory studies by von Hobe et al. (2009), Chen et al. (2009), Papanastasiou et al. (2009), and Wilmouth et al. (2009) concluded that the correction applied by Pope et al. to account for $\mathrm{Cl_2}$ contamination in their ClOOCl sample may have been too large. This in turn would lead to cross-sections which are too small for wavelengths that control the photolysis of the ClO-dimer in the atmosphere ($>$300 nm). That said, these studies published in 2009 do not agree on the absorption cross-sections for the dimer, and so there remains uncertainty on the photolysis rate for the ClO-dimer, especially in the atmospherically most important region. The laboratory measurements of the small ClOOCl cross-sections at wavelengths of interest ($>$300 nm) involve some difficulties such as the interference of other species (e.g. $\mathrm{Cl_2}$ and $\mathrm{Cl_2O_3}$) which are unavoidable and difficult to quantify (SPARC, 2009), and the fact that production of ClOOCl production in the laboratory is very challenging. The correction for interfering species such as $\mathrm{Cl_2}$ is the biggest source of uncertainty

regarding the determination of the ClO-dimer cross-section, resulting in large uncertainties among the laboratory studies at atmospherically important wavelengths (e.g. Burkholder et al., 1990; Huder and DeMore, 1995; Chen et al., 2009).

As the ozone loss during day-time is controlled by the photolysis rate (J) and the formation rate (k_f) of the ClO-dimer, the determination of k_f has also been subject to a number of laboratory studies (Trolier et al., 1990; Bloss et al., 2001; Nickolaisen et al., 1994; Boakes et al., 2005). The ClO-dimer formation rate is known to be pressure- and temperature dependent. A decrease in temperature leads to an increase in k_f but also to a decrease in the J/k_f ratio which controls the partitioning of ClO and $ClOOCl$ during the day. The ClO-dimer formation rates determined by the laboratory studies agree very well for temperatures above 240 K (von Hobe et al., 2007). However, as it is difficult to investigate the reaction rates under stratospheric conditions in the laboratory, a large discrepancy among the derived k_f values at stratospheric temperatures between 180 and 220 K exists (Figure 3.1). At 190 K, for example, the lowest reported value for k_f by Trolier et al. (1990) is smaller by about a factor of 1.8 than the highest reported value (Boakes et al., 2005). The JPL06 and JPL09 recommendations for k_f lie between these two values (Figure 3.1). The difference in the determined k_f values results in part from the extrapolation of the dimer formation rate to the low temperatures occurring in the polar stratosphere.

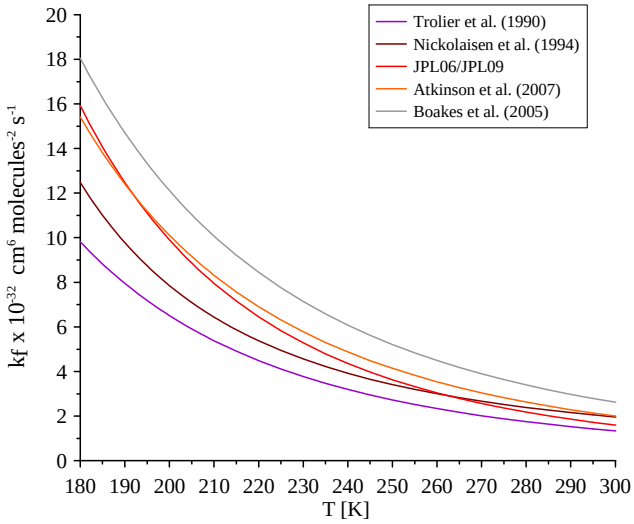

Figure 3.1: The ClO-dimer formation rate (k_f) versus temperature as reported in previous studies. The derived k_f values were calculated for temperatures occurring in the stratosphere.

The equilibrium constant K_{eq} controls the partitioning of ClO and ClOOCl during night-time when photolysis is negligible and sufficient time has passed so that equilibrium has been reached. ClO and ClOOCl are then said to be in thermal equilibrium. Numerous laboratory studies have been carried out to determine K_{eq} and its temperature dependence (e.g. Cox and Hayman, 1988; Nickolaisen et al., 1994; Plenge et al., 2005). However, all laboratory studies were performed at temperatures above those occurring in the winter polar stratosphere and therefore extrapolation of K_{eq} to polar vortex conditions, as done by the JPL panel, introduces uncertainties. The equilibrium constant as reported in previous studies is shown in Figure 3.2, where $\mathrm{K_{eq}}$ was calculated for the temperature range 190 to 210 K. The largest reported value for $\mathrm{K_{eq}}$ at 190 K by Nickolaisen et al. (1994) is about 23% larger than the JPL06 value, while the smallest value proposed by von Hobe et al. (2005) is up to 90% smaller than recommended by JPL06. The discrepancies in the derived equilibrium constants from laboratory studies are accordingly large and field studies at stratospheric temperatures are required to narrow down these discrepancies.

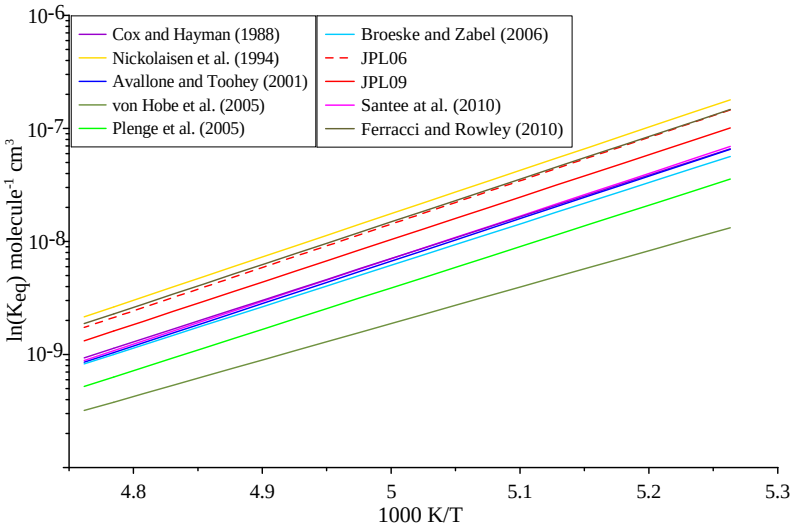

Figure 3.2: The equilibrium constant (K_{eq}) versus temperature as reported in previous studies. The derived K_{eq} values were calculated for temperatures occurring in the stratosphere.

Atmospheric measurements of ClO and its dimer are a useful tool to verify the precision of the kinetics determined in laboratory studies as long as they are sufficiently accurate. Several studies based on atmospheric ground-based, in situ, and satellite day-time and night-time observations of ClO and/or ClOOCl have been performed to investigate the key kinetic parameters of the ClO-dimer cycle. Ground-based day-time measurements of ClO by Shindell and de Zafra (1996) and Solomon et al. (2002) suggested a higher J/k_f ratio than recommended by JPL06 and the more recent JPL09 recommendation, resulting in higher modelled day-time ClO abundances than derived from JPL kinetics. Stimpfle

et al. (2004) presented the first measurements of ClOOCl which were used together with ClO measurements to test understanding of the key kinetic parameters of the ClO-dimer cycle. Stimpfle et al. concluded that their ClO measurements can be reproduced by using the k_f value reported by Trolier et al. (1990) in combination with the photolysis rate J recommended by JPL06. A larger value for k_f as recommended by $k_{f\,JPL06}$ agrees with the observations only if larger ClOOCl absorption cross-sections than recommended by JPL06 are used. Furthermore, night-time measurements of ClO and ClOOCl by von Hobe et al. (2007) and Stimpfle et al. (2004) and satellite measurements of ClO by Santee et al. (2010) indicate discrepancies in the equilibrium constant K_{eq} compared to the JPL06 recommendation, and the more recent JPL09 recommendation. The study by von Hobe et al. (2007) presented an additional a set of parameters which shows overall the best consistency with their observations, namely the equilibrium constant as reported by Plenge et al. (2005), the dimer formation rate as suggested by Nickolaisen et al. (1994) and a photolysis rate using the absorption cross-section that lies between JPL06 and Burkholder et al. (1990). However, the optimal value of K_{eq} by Plenge et al. (2005) does not agree with the finding of the latest and more recent studies by Santee et al. (2010) and Ferracci and Rowley (2010). All these earlier studies suggest that there remain discrepancies in the key kinetic parameters controlling polar ozone depletion. Examining the kinetics at stratospheric temperatures is a prerequisite to reduce these discrepancies, and thereby reducing uncertainties in modelled polar ozone loss.

This study presents two methods, both using day-time ClO microwave radiometer measurements, to constrain the kinetic parameters governing ClO chemistry in the polar stratosphere. This work was motivated by the idea of using daily and hourly measurements of ClO, made in Antarctica, to retrieve the key kinetic parameters (J, K_{eq}, and k_f) governing the partitioning between ClO and its dimer. During the course of this study it became apparent, however, that the available ClO measurements are only weakly sensitive to K_{eq}, since K_{eq} becomes important primarily for the night-time partitioning of ClO and ClOOCl (see equation 3.2). Because the measured ClO night-time spectrum is subtracted from the day-time spectrum to obtain the measured ClO spectrum, almost all information about K_{eq} is removed from the measurements[2]. Therefore, it became apparent that the ground-based measurements are not suitable to derive estimates for K_{eq} and no attempt was made to retrieved K_{eq}. Rather, to test the sensitivity of the results to a choice of K_{eq}, K_{eq} was varied within the uncertainty range recommended by JPL06 (see below).

[2]The data processing and retrieval algorithm of the ClO measurements are described in detail in Chapter 2.

During day-time, the equilibrium between ClO and its dimer is governed by the J/k_f ratio (equation 3.1). The partitioning between ClO and ClOOCl is close to equilibrium a few hours after sunset to sunrise and shortly after sunrise to shortly before sunset. The transition from non-equilibrium to equilibrium provides information on J and k_f individually. However, as the non-equilibrium period is restricted to only a few hours of the day, the application of remote sensing data to determine J or k_f individually is limited. Furthermore, the transition period has been removed from the ground-based measurements because of the day minus night subtraction. As a result, ClO measurements include hardly any information on the individual J and k_f values and therefore no attempt was made to analyze J and k_f individually and the focus of this work is to retrieve optimal J/k_f ratios from the measurements. As the subtraction was also performed to derive hourly ClO profiles, no additional information can be gained from these measurements. Consequently, the decision was made to use only daily ClO measurements to investigate the applicability of ground-based ClO measurements to retrieve key kinetic parameters which govern the partitioning of ClO and its dimer during the day.

This work aims to provide a constraint on the J/k_f ratio based on daily ClO microwave radiometer measurements from Scott Base (78.85° S, 166.75° E), Antarctica, made during the late winter/early spring of 2005 (Section 3.2). First an optimal estimation technique was used to derive J/k_f ratios for a range of prescribed K_{eq} values (Section 3.4). Values of K_{eq} up to 2 times larger than recommended by JPL06 were explored to test the sensitivity of the J/k_f ratio to changes in K_{eq}. The optimal estimation forward model was a photochemical box model that takes J, k_f, and K_{eq} as inputs, together with a priori $\mathrm{ClO_x}$, ozone, temperature and pressure profiles. The photochemical box model was provided by R. Salawitch and T. Canty who also calculated and provided the photolysis rates of the ClO-dimer which were used as *a priori* information in this chapter. The basic model-code for optimal estimation using the box model as a forward model, was provided by K. Frieler and R. Schofield. The SLIMCAT modelled $\mathrm{ClO_x}$ data which were used as *a priori* in optimal estimation were provided by M. Chipperfield. Based on these tools provided, the model-code was extended and adapted to be used with the Antarctic ClO measurements from Scott Base in this chapter.

In optimal estimation the JPL06 kinetics are used as *a priori* for kinetic of the ClO dimer cycle (J,k_f and K_{eq}) and for all other chemistry in the forward model. Using the more recent JPL09 kinetics as *a priori* results in insignificant differences in the retrieved value of J/k_f. The JPL06 kinetics are most commonly used in recently published studies of polar ozone photochemistry and therefore, these kinetic parameters are the point of reference for this study. That said, in some cases, results are also compared with the more recent JPL09

recommendation. The JPL09 K_{eq} value is 70% of the JPL06 value, while J/k_f for JPL09 shows essentially no difference from JPL06. The derived kinetic parameters by employing the optimal estimation method are presented and compared with results from previous studies in Section 3.6.

As a complement to optimal estimation, a second approach was used to derive the optimal kinetic parameters where the full parameter space of J, k_f ,K_{eq} and $\mathrm{ClO_x}$ was explored (Section 3.5), within physically plausible limits, to find the minimum in differences between measured and modelled ClO profiles. The results from exploring the full parameter space are presented and compared to the retrieved values from optimal estimation in Section 3.7. The main findings of this study are summarized in Section 5.5 followed by the conclusion of this study.

3.2 Observations

The Stony Brook University and NIWA jointly operate a ClO millimeter wave radiometer at Scott Base, Antarctica. The instrument provides ClO measurements since 1996. The instrument itself, the observing method and the data processing is described in detail in Chapter 2. The ClO measurements as made between 21 August and 20 September 2005 were used in this study to investigate the kinetic parameters of the ClO-dimer cycle. 2005 offered the most comprehensive data set. Due to bad weather conditions there were no ClO measurements available from 14 to 16 September 2005 (white bar in Figure 3.3) and therefore these days are not considered in the analysis. As a result, 28 days of ClO profiles on 20 altitude levels, from 11 to 30 km, derived from the ClO day minus night spectra were used. The 11 to 30 km altitude range was chosen as this is where ClO concentrations maximize (Figure 3.3). The daily ClO measurements which were used in this study, together with their error estimate are shown in Figure 3.3. The measurement errors on the ClO profiles were determined by applying the formalism of Rodgers (2000) (Chapter 2). The error analysis for the ClO measurements is described thoroughly in Solomon et al. (2000). The seasonal behaviour of ClO is well presented by the measurements shown in Figure 3.3.

At the beginning of the season (late August) the peak ClO mixing ratio occurs at around 22 km. In early September the peak ClO mixing ratio shifts downwards, occurring at 20-21 km. The high ClO concentrations are restricted to altitudes between 17 and 25 km, since this is the region where PSCs occur. PSCs are responsible for activating chlorine through heterogeneous processes (Chapter 1). At the beginning of the analysis period, chlorine is mostly tied up in the chlorine reservoir species such as $\mathrm{ClONO_2}$ and HCl. Therefore,

relatively low ClO concentrations of about 1.2 part per billion (ppb) are observed at the beginning of the analysis period. With an increase in available sunlight during the day more chlorine can be activated through photodissociation of chemical compounds produced by heterogeneous chemistry. Activated chlorine (Cl) destroys ozone via the ClO_x catalytic cycle forming ClO (Chapter 1). Therefore, stratospheric ClO concentrations increase. The maximum ClO concentration during the 2005 season (2.3 ppb) was observed on 7 September 2005. The strong decrease in ClO around day 251 (8 September 2005) is a result of dynamical variability of the polar vortex. During the Antarctic late winter/early spring, the ClO concentrations are high inside the polar vortex due to stratospheric chemical processes as described in Chapter 1. Outside the polar vortex, ClO concentrations are very low. The polar vortex is neither stationary nor centered on the pole but moves due to dynamical activity. Therefore, the observation site can lie within or outside the polar vortex or at the vortex edge, which determines the amount of ClO measured by the instrument. This movement of the polar vortex explains the drop in the ClO measurements at Scott Base where peak values of 0.8 and 0.6 ppb on day 251 (8 September) and 252 (9 September), respectively, are observed. After this period of low ClO abundances, high ClO concentrations of 2.2 ppb were observed again, as the measurement site lies again within the polar vortex. With temperatures increasing towards the end of the analysis period, fewer PSCs are formed, reducing the amount of chlorine that gets activated. Therefore, more and more ClO is deactivated through the formation of reservoir species, which explains the decreasing ClO abundances from ∼13 Sept onwards.

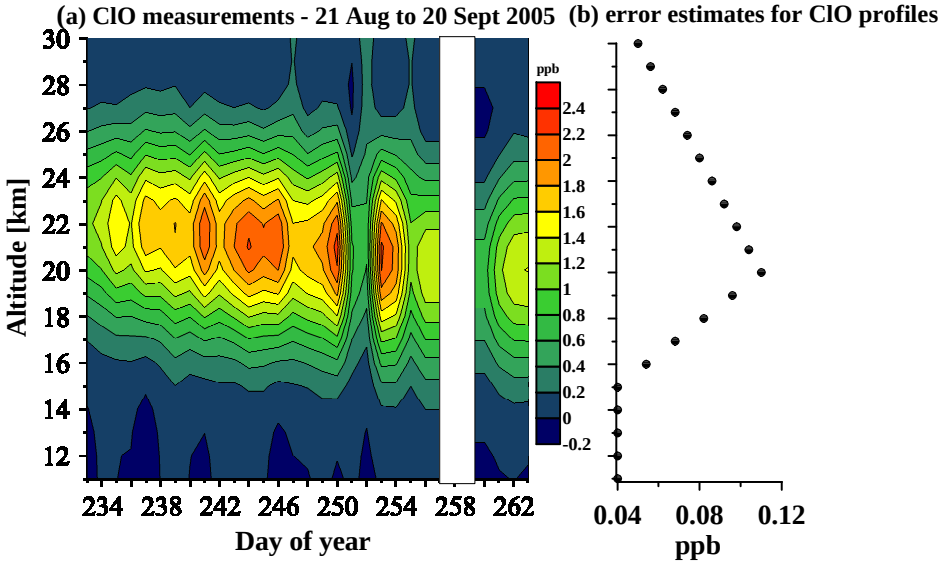

Figure 3.3: Daily ClO concentrations in ppb (panel a) as a function of altitude, observed at Scott Base, Antarctica, during the period of 21 August (day 233 of the year) to 20 September 2005 (day 263 of the year). The corresponding error estimates on the ClO altitude profiles are shown in panel b.

3.3 Model data - SLIMCAT 3D CTM

Output from the SLIMCAT three-dimensional off-line chemical transport model was used to provide estimates of the abundance of $\mathrm{ClO_x}$ ($\mathrm{ClO} + 2 \times \mathrm{ClOOCl}$), $\mathrm{BrO_x}$ ($\mathrm{BrO} + \mathrm{BrCl}$), and ozone over Antarctica. The model is described in detail in Chipperfield (1999, 2006). Therefore, only a brief overview of SLIMCAT is given in this section. The SLIMCAT model contains a detailed stratospheric chemistry scheme, including heterogeneous reactions on liquid and solid PSCs. The chemistry module uses a limited number of chemical families for species which are in rapid photochemical equilibrium. Cl, ClO and ClOOCl form a family and the partitioning between these species is determined assuming instantaneous photochemical equilibrium. All other inorganic chlorine species (e.g. OClO, HOCl etc.) are integrated separately using a simple forward Euler integration scheme. Similarly Br and BrO are treated as a family while all other inorganic bromine species are integrated separately (e.g. BrCl). The run included a source of bromine from very short-lived species, which contributed about 6 parts per trillion (ppt) in 2005 (Feng et al., 2007). Except for the absorbtion cross-section of ClOOCl which was taken from Burkholder et al. (1990), the photochemical data recommended by Sander et al. (2003) are used within the model. A photochemical scheme based on Lary and Pyle (1991) is used to calculated the photolysis rates.

For this study, output was taken from run 509 of the SLIMCAT 3D CTM (509 is the reference number of this particular simulation). This run has a resolution of $5.6^\circ \times 5.6^\circ$ longitude/latitude with 32 levels from the surface to about 60 km, starting on 1 January 1977. The model uses a hybrid σ-θ coordinate system where isentropic surfaces (θ) are used in the stratosphere and terrain-following hybrid surfaces (σ) are used near the surface. Diabatic ascent and decent rates (heating rates) are calculated from a radiation scheme implemented in the model to account for vertical motion across the isentropic surfaces (surfaces of constant potential temperature, Appendix A.2). The run was forced using horizontal winds and temperatures from the European Centre for Medium-Range Weather Forecasts (ECMWF) meteorological analyses (ERA-Interim after 1989), which are described in detail in Uppala et al. (2005). Daily profile output from the model run was stored for the location of Scott Base.

3.4 The optimal estimation method

The optimal estimation approach as described in detail in Rodgers (2000) and introduced in Chapter 2, is employed to retrieve the optimal J/k_f ratio and the optimal daily $\mathrm{ClO_x}$

profiles, that best represent the Antarctic ClO measurements. The forward model, *a priori* information, and the retrieval model used by optimal estimation are introduced and described.

3.4.1 Forward model - Photochemical box model

The forward model describing the physics of the measurements is one of the essential components of optimal estimation, as it relates the state of the atmosphere, together with additional information, including ozone, temperature etc., to the observed quantities. The forward model $\mathbf{F}$ (see equation 2.27) employed in this study, is a photochemical steady state box model, based on polar ozone photochemistry and described in detail in Salawitch et al. (1993). The photochemical box model includes the catalytic cycles involving ClO_x and BrO_x species, while the chemistry of NO_x is neglected in the model. As this study concentrates on catalytic ozone depleting cycles involving chlorine compounds, neglecting NO_x chemistry does not affect the results or conclusions. The model contains chemically active species such as ozone, O, ClO, $ClOOCl$, $OClO$, $HOCl$, BrO, $BrCl$, and $HOBr$. The box model, as employed here uses the JPL06 recommendations (Sander et al., 2006) for all reaction kinetics for the chemical reactions implemented unless overwise noted. The photolysis rates for the different species, such as $ClOOCl$, $BrCl$, $HOBr$ are calculated as described in Chapter 1 (1.1). JPL06 recommendations for the absorption cross-sections and quantum yields are used to derive the photolysis rates. The radiative transfer model that was used to calculate the actinic fluxes, uses a constant value of surface albedo appropriate to an ice or snow covered surface (0.8) and the same temperature, pressure and ozone profiles which were used as required input parameter to the photochemical box model (see below).

The forward model parameter (termed as $\mathbf{b}$ in equation 2.27) including ozone, temperature and BrO_x ($BrO + BrCl$) profiles, are used to constrain the photochemical box model. The daily BrO_x profiles were obtained from the SLIMCAT (Section 3.3). Because vertical ozone profiles from ozonesondes were not available for each day of the analysis period, ozone profiles were extracted from the SLIMCAT simulation. The difference between measured (ozonesonde) and modelled ozone (SLIMCAT) profiles were calculated on days were ozonesonde measurements (taken from Hassler et al., 2008) were available. These differences were linearly interpolated for the analysis period (21 August to 14 September 2005) applying a kriging interpolation technique. The interpolated differences were then added to the SLIMCAT ozone profiles to generate what are hereafter referred to as 'corrected' ozone profiles. Besides BrO_x and ozone profiles the forward model also required temperature and pressure profiles as input variables. These profiles have been extracted from the National Centers for Environmental Prediction, NCEP (Kalnay et al., 1996) reanalysis data using

bilinear interpolation. The same temperature and pressure profiles were used to derive the day-time ClO profiles from the measured ClO spectra as described in Chapter 2.

To calculate the daily ClO abundances, the forward model also requires the total amount of activated chlorine, ClOx, (ClO_x that is estimated here from the abundances of ClO and its dimer; ClO_x=ClO+2×ClOOCl) available in the polar stratosphere above Scott Base. As there are no measurements of Antarctic ClO_x concentrations available, the SLIMCAT modelled ClO_x profiles between 11 and 30 km altitude are used. The ClO_x, BrO_x and ozone mixing ratios specified as inputs to the model are converted into number densities in the forward model at each altitude level (between 11 and 30 km) using:

$$[X] = \chi_x \cdot \frac{p}{1.38 \cdot 10^{-19} \cdot T} \tag{3.3}$$

where [X] refers to the number density of the species in molecule/cm^3 (i.e. ClO_x, BrO_x, ozone), χ_x is the mixing ratio (number of molecules per unit volume) of the species of interest, p is the pressure in hPa and T is the temperature in K. Therefore, as altitude is used as vertical coordinate in this study, the corresponding temperature and pressure values are required to calculate the number density of the species at a given altitude.

The temperature and pressure profiles provided as input to the forward model are the same as the profiles used within the data processing of the ClO measurements, i.e. the retrieval of ClO profiles from measured ClO spectra, and were provided by NCEP (see above). However, the temperature and pressure profiles used within SLIMCAT are different, i.e. the measured ClO mixing ratio at 21 km corresponds to a pressure level of 181 hPa while within SLIMCAT, the mixing ratio given at 21 km corresponds to the 184 hPa pressure level, resulting in a vertical altitude offset as described below. Using the example of ClO measured and modelled on 7 September 2005, the altitude shift within the ClO profiles is illustrated in Figure 3.4.1. Due to the differences between actual and modelled pressure profiles, using altitude as the vertical coordinate, as it is the case in the box model, introduces uncertainties in the modelled SLIMCAT species when converting them into number densities (equation 3.3). To correct for this, the SLIMCAT species such as BrO_x and ClO_x were interpolated to the pressure levels used by the forward model. This correction reduces the differences between the altitude of the peak in ClO mixing ratio between SLIMCAT and observations (shown in Figure 3.4.1). However, this correction does not eliminate the vertical offset completely for all days of the analysis period. Following the correction, the SLIMCAT modelled species correspond to the same pressure levels as used within the forward model. This correction was not applied to the modelled ozone profiles from SLIMCAT since these profiles were corrected with ozonesonde measurements as described above.

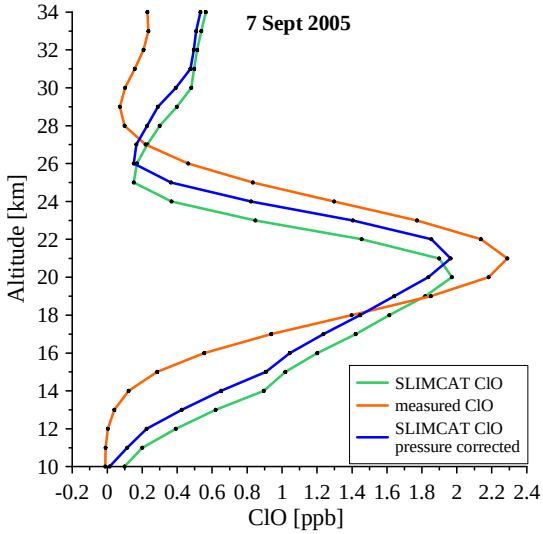

Figure 3.4: Measured ClO profile (orange) as observed on the 7 Sept. 2005 compared to the modelled ClO profile (green) from SLIMCAT for the same day. The altitude shift between the peak measured and modelled ClO mixing ratio is illustrated. The corrected ClO profile from SLIMCAT is indicated by the blue line (for details see text).

Using the input parameters described above, the Salawitch et al. (1993) photochemical box model calculates ClO for altitudes levels between 11 and 30 km at 30 minutes resolution for the 28 day period considered. Daily day minus night ClO profiles, hereafter referred to as modelled ClO ($\hat{\mathbf{y}}$), are calculated from the 30 minute resolution output of the box model, using the same definitions of the day-time (night-time) as for the measured ClO profiles (Chapter 2) to provide compatibility with the measurements.

3.4.2 A priori

Optimal estimation requires *a priori* information about the state of the system to solve the inverse problem. Specifically, a best first guess of the atmospheric state is required to make the inverse problem well-posed. The *a priori* also includes the ensemble covariance of the state. Optimal estimation depends on both the measurements and the *a priori*. The extent to which the retrieved state will be influenced by the *a priori* depends on the information content of the measurements. As described in Chapter 2, at altitudes where the information content of the measurements is insufficient, the retrieved value at this altitude will be dominated by the *a priori*. On the other hand, at altitude levels where the measurements contain enough information, the retrieved values are less affected by any *a priori* and will be almost entirely determined by the measurements. Therefore, the solution provided by optimal estimation (e.g. the retrieved atmospheric state) is optimal with respect to the *a priori*. It is important to note that for a different *a priori* the same solution of the inverse

problem will not be optimal. The *a priori* provides a constraint of the retrieval and has to be independent of the measurements. Using the *a priori* to constrain the retrieval is critical in solving an inverse problem and the set up of the *a priori*, together with the uncertainties, is not straightforward. It is possible that the *a priori* constraint is too loose, too tight or just wrong and care has to be taken when setting up the *a priori*.

The goal of this chapter is to use optimal estimation to retrieve the best set of kinetic parameters which govern the partitioning of ClO and its dimer during the day. The retrieved set of parameters optimize the agreement between the measured ClO profiles and profiles generated by the optimal estimation forward model. The amount of available ClO not only depends on the kinetic parameters but also on the amount of available $\mathrm{ClO_x}$ (by definition $\mathrm{ClO_x} = \mathrm{ClO} + 2\times\mathrm{ClOOCl}$) and therefore, the optimal daily $\mathrm{ClO_x}$ profiles are also quantities to be retrieved. Therefore, the atmospheric state is described by the kinetic parameters J, k_f and K_{eq} and the vertical distribution of $\mathrm{ClO_x}$ using an independent atmospheric *a priori* state vector ($\mathbf{x_a}$). The state vector $\mathbf{x_a}$ describes the overall quantities to be retrieved. Rather than working with J, k_f and K_{eq} explicitly, they are specified as scalings (multiplicative factors) relative to the JPL06 recommendations. The first three entries of $\mathbf{x_a}$, representing the *a priori* values for $k_{f\,scale}$, $K_{eq\,scale}$ and J_{scale}, are all set to unity so that the *a priori* for the kinetics are the JPL06 recommendations. A set of 28 $\mathrm{ClO_x}$ profiles, corresponding to each day of measurement, is represented by the subsequent entries of the *a priori* state vector $\mathbf{x_a}$. As there are no measurements of $\mathrm{ClO_x}$ concentrations available, the SLIMCAT output provides the required $\mathrm{ClO_x}$ profiles.

3.4.3 A priori covariance - $\mathbf{S_a}$

The *a priori* state vector $\mathbf{x_a}$ describing the best estimate of the atmospheric state was constructed by using the JPL06 recommendation for J, k_f, and K_{eq}, as well as 28 $\mathrm{ClO_x}$ profiles modelled by SLIMCAT (see above). The resulting state vector has 563 elements, 3 kinetic parameters plus 28 days $\times$ 20 altitudes of *a priori* $\mathrm{ClO_x}$. The uncertainties on the elements of $\mathbf{x_a}$ are expressed along the diagonal of a covariance matrix $\mathbf{S_a}$. The diagonal elements of $\mathbf{S_a}$ are the variances of $\mathbf{x_a}$ and the assumption is made that the uncertainties of $\mathbf{x_a}$ are uncorrelated. Therefore, the off-diagonal elements of $\mathbf{S_a}$ are set to zero. Selection of the $\mathbf{S_a}$ settings requires some subjective judgement noting that if excessively small values are chosen, the retrieval will be constrained too tightly. In this case the retrieval will make little use of the information provided by the measurements and will differ little from the prescribed *a priori* $\mathbf{x_a}$. On the other hand, if excessively large values for $\mathbf{S_a}$ are chosen, this results in an unrealistic retrieval where the measurement noise is interpreted as information. Furthermore, if the constraint is too loose, the retrieval trusts the measurements completely

and the retrieval tries to fit the measurements exactly. Therefore no convergence will be achieved. Here, $\mathbf{S_a}$ is used as a tuning parameter to retrieve the maximum information and minimal error. The uncertainties for the kinetic parameters and for the *a priori* $\mathrm{ClO_x}$ values were determined separately, following a L-curve method described in Schofield et al. (2004). Using the L-curve method the size of the diagonal elements of $\mathbf{S_a}$ is determined by rerunning the retrieval several times varying the $\mathbf{S_a}$ values from a very low to a very high value. The root mean square (RMS) difference between the retrieved ClO profiles and the measurements is determined for every retrieval run and the $\mathbf{S_a}$ values are chosen where a further increase results in no further improvement in the measurement fit. The optimal $\mathbf{S_a}$ values were selected where the change in the RMS values is small but also where the uncertainties on the retrieved values are small. This method resulted in the variances of J_{scale} and $k_{f_{scale}}$ on the diagonal of $\mathbf{S_a}$ of $\sigma^2_{k_{f_{scale}}} = 0.043$ and $\sigma^2_{J_{scale}} = 0.173$, respectively. The $\mathbf{S_a}$ value corresponding to the equilibrium constant K_{eq} was set close to zero since the equilibrium constant is not retrieved and therefore the retrieval trusts the $K_{eq_{scale}}$ value completely. The L-curve method cannot be applied on its own in determining the uncertainties on the *a priori* $\mathrm{ClO_x}$ concentrations. Additional information on the atmospheric state is required, as the best RMS, i.e. the best fit of the measurements, is obtained using a large uncertainty in the $\mathrm{ClO_x}$ values. However, this large uncertainty also results in unrealistic retrieved $\mathrm{ClO_x}$ mixing ratios which exceed the total amount of inorganic chlorine. In determining the size of $\mathbf{S_a}$ for $\mathrm{ClO_x}$ mixing ratios, the fact that $\mathrm{ClO_x}$ concentrations cannot exceed the total amount of inorganic chlorine in the stratosphere ($\mathrm{Cl_y}$) must be accounted for. Rather than using a single percentage for the uncertainties on the *a priori* $\mathrm{ClO_x}$ concentrations, it was determined that using a higher uncertainty at lower altitudes than at higher altitudes results in a better fit of the measurements. Therefore, the $\mathbf{S_a}$ values for the *a priori*, which were numerically determined as described above, were set to 70% of the daily maximum $\mathrm{ClO_x}$ value at altitudes from 11 to 13 km and to 20% at altitudes above 13 km, individually for each day.

3.4.4 SLIMCAT $\mathrm{ClO_x}$ profiles

The *a priori* $\mathrm{ClO_x}$ profiles consist of daily ClO and ClOOCl profiles as modelled by SLIMCAT. Early in this study it became apparent that using the SLIMCAT modelled $\mathrm{ClO_x}$ concentrations as *a priori* would involve some difficulties as the model overestimates the ClO concentrations at the beginning of the analysis period and underestimates ClO at the end of the analysis period. In particular, SLIMCAT overestimates the peak amount of ClO at the beginning of the period by about 0.5 ppb. The concentration of ClO in the stratosphere above Scott Base depends on the occurrence of PSCs and on the availability of sunlight. Furthermore, the dimer formation rate is temperature dependent and the photolysis rate of

the ClO-dimer depends on the solar zenith angle (SZA). These kinetic parameters control the partitioning of ClO_x during the day. For low temperatures and high SZAs, as the case at the beginning of the season, most of the ClO_x is in the form of $ClOOCl$. Through the course of the season, as more sunlight becomes available and SZA decreases the ClO-dimer can be photolyzed over a longer time period and for lower SZA the ClO-dimer gets photolyzed more quickly. Therefore, later in the season most of the ClO_x is in the form of ClO during the day. Therefore, an incorrect temperature and/or photolysis rate of the ClO-dimer in SLIMCAT could be one explanation for incorrect representation of ClO mixing ratios in SLIMCAT. The SLIMCAT model uses temperatures from the ECMWF meteorological reanalyses which are known to have a cold temperature bias in the Antarctic stratosphere (Parrondo et al., 2007). As reported in Parrondo et al. (2007), this cold bias leads to an overestimation of the PSC area. This could, in part, explain why SLIMCAT overestimates the amount of ClO compared to the observations. However, the NCEP reanalysis data used to retrieve the ClO profiles are known to have a warm temperature bias (1.51 K) in the Southern Hemisphere. So both reanalysis data set do have their uncertainties which have to be accounted for then using them. Nonetheless, using incorrect temperatures in SLIMCAT has a greater effect on the uncertainty of the modelled ClO concentrations than using incorrect temperatures within the retrieval algorithm used for the determination of the ClO profiles from ground-based ClO measurements. This results from the fact that SLIMCAT calculates ClO using a chemistry scheme with temperature dependent kinetic reaction rates and SLIMCAT calculations are not constrained by any observations. The retrieval of the ClO profile, on the other hand, is constrained by the measured spectrum and does not include any chemical processes and reaction rates. Therefore, using incorrect temperatures in SLIMCAT has a greater effect on the uncertainty of the modelled ClO concentrations than using incorrect temperatures within the retrieval algorithm used for the determination of the ClO profiles from ground-based ClO measurements. In this study, however, no quantitative estimate can be made of the sensitivity of modelled ClO to changes in temperature since the output data required to conduct such a test are not available. Therefore, the possible causes of uncertainties in the modelled ClO profiles can be discussed but not verified. In addition, there might be additional sources of uncertainty within SLIMCAT that are responsible for an overestimation or underestimation of ClO concentrations compared to the observations. However, it is not the purpose of this study to investigate the SLIMCAT uncertainties and to validate SLIMCAT.

From the comparison of the available SLIMCAT ClO data to the ClO observations, two assumptions can be made. Either the modelled ClO_x abundances are correct but the partitioning of ClO and its dimer, and therefore, the J/k_f ratio is incorrect, or the J/k_f ratio within the model is correct but the amount of ClO_x simulated by SLIMCAT is overestima-

ted due to the cold temperature bias, leading to an overestimation of the PSC area. Based on several previous studies (e.g. Parrondo et al., 2007), it seems more likely that the latter assumption is valid. Furthermore, the fact that most of the peak day-time ClO mixing ratios are also overestimated by SLIMCAT towards the end of the analysis period confirms the latter assumption, since most of the day-time $\mathrm{ClO_x}$ is in the form of ClO towards the end of the period. This result suggests that more chlorine is activated within the model than expected from the observations. The study by Santee et al. (2010) confirms that SLIMCAT overestimates the $\mathrm{ClO_x}$ concentration by about 25% in the Antarctic.

Using SLIMCAT modelled $\mathrm{ClO_x}$ profiles as *a priori* within the optimal estimation to retrieve the optimal set of kinetic parameters would not be an issue if only the J/k_f ratio within SLIMCAT is incorrect, as the method used in this study, requires an independent $\mathrm{ClO_x}$ profile (independent of the J/k_f ratio). The retrieved optimal parameters then describe the partitioning of $\mathrm{ClO_x}$, corresponding to the measurements, and the parameters can be different from the set of parameters which were used in producing the $\mathrm{ClO_x}$ profiles. However, because the parameters depend on the amount of available $\mathrm{ClO_x}$, using an incorrect $\mathrm{ClO_x}$ profile can result in higher uncertainties on the retrieved parameters, i.e. the same J/k_f ratio results in different $\mathrm{ClO}/\mathrm{ClOOCl}$ concentrations using different $\mathrm{ClO_x}$ profiles.

Early in this study it became apparent that using the SLIMCAT $\mathrm{ClO_x}$ as *a priori* within the optimal estimation resulted in unrealistic high concentrations of the retrieved $\mathrm{ClO_x}$ on some days of the analysis period. The retrieved $\mathrm{ClO_x}$ concentrations exceeded the amount of available $\mathrm{Cl_y}$ at some altitudes. Consequently, a different approach to generate the required $\mathrm{ClO_x}$ profiles was investigated. As mentioned above, there are reasons to assume that SLIMCAT modelled $\mathrm{ClO_x}$ concentrations might be incorrect. However, there is a higher confidence in the SLIMCAT $\mathrm{ClO_x}/\mathrm{ClO}$ ratio (see above). Therefore, this ratio was used to generate *a priori* $\mathrm{ClO_x}$ profiles by using:

$$\mathrm{ClO_x} = \frac{\mathrm{SLIMCAT\,ClO_x}}{\mathrm{SLIMCAT\,ClO}} \times \mathrm{measured\,ClO} \tag{3.4}$$

The ClO measurements were scaled with the SLIMCAT $\mathrm{ClO_x}/\mathrm{ClO}$ ratio to generate a more realistic $\mathrm{ClO_x}$ profile. During the course of this study, however, it became apparent that the generated $\mathrm{ClO_x}$ profiles (equation 3.4) are not independent of the kinetic parameters used within SLIMCAT. During the day, the J/k_f ratio determines the partitioning between ClO and ClOOCl, depending on the total amount of available $\mathrm{ClO_x}$. The $\mathrm{ClO_x}/\mathrm{ClO}$ ratio from SLIMCAT depends on the J/k_f ratio used within SLIMCAT and therefore the partitioning of ClO and its dimer is prescribed, i.e. by using this ratio it is known how much of the given $\mathrm{ClO_x}$ is represented in the form of ClO. This portion of ClO depends mainly on the pho-

tolysis rate J used in SLIMCAT, i.e. the higher the photolysis rate the bigger is the portion of ClO in $\mathrm{ClO_x}$. As the goal of this study is to retrieve the J/k_f ratio, the retrieval would become circular and the retrieved ratio would be similar to the ratio used in SLIMCAT. This precludes the use of the generated $\mathrm{ClO_x}$ (equation 3.4) profiles as the *a priori* in the optimal estimation to retrieve the kinetic parameters. For the purpose of this study it is very important to use *a priori* $\mathrm{ClO_x}$ profiles that are independent of the kinetic parameters such as the J/k_f ratio. The only independent $\mathrm{ClO_x}$ profiles available for this study are the modelled $\mathrm{ClO_x}$ mixing ratios from SLIMCAT. Therefore, in the end, SLIMCAT modelled $\mathrm{ClO_x}$ profiles were used as the *a priori* in the optimal estimation, acknowledging the possible uncertainties of the modelled profiles (see above). The *a priori* $\mathrm{ClO_x}$ mixing ratios for the altitudes between 11 and 30 km and the 28 day analysis period, are shown in Figure 3.4.4. The $\mathrm{ClO_x}$ mixing ratios maximize ($\geq$2.2 ppb) between 15 and 25 km as it is within that altitude range that PSCs are formed. The fast chlorine activation within SLIMCAT leads to the maximum $\mathrm{ClO_x}$ mixing ratio of about 3.4 ppb at the beginning of the analysis period. As a result of chlorine deactivation, the amount of $\mathrm{ClO_x}$ decreases towards the end of the season.

As the SLIMCAT $\mathrm{ClO_x}$ profiles were used as *a priori* within the optimal estimation the issue remains that the unrealistically high $\mathrm{ClO_x}$ concentrations were retrieved on two days of the analysis period. However, these elevated $\mathrm{ClO_x}$ abundances can be explained and are of dynamical origin. As detailed above the polar vortex shifted during the observation period and as a result, Scott Base was situated outside the vortex or close to the vortex edge during the analysis period. SLIMCAT shows some reduction in $\mathrm{ClO_x}$ over this period (Figure 3.4.4) but the reduction is not commensurate with the observed reduction in ClO apparent in the disagreement between measured and modelled ClO profiles on these days. With the given resolution of the SLIMCAT run (Section 3.3), the model cannot capture the observed strong gradients at the edge of the vortex. As such, the *a priori* $\mathrm{ClO_x}$ profiles provided by SLIMCAT are too high on those two.

3.4.5 Retrieval model

The retrieval model, the second essential part of optimal estimation in addition to the forward model (see above), determines the atmospheric state using the atmospheric measurements, i.e. the ClO observations. The quantities to be retrieved from the ClO measurements, which are described by the measurement vector ($\mathbf{y}$), are J/k_f and $\mathrm{ClO_x}$. The state vector $\mathbf{x}$ represents these quantities, together with K_{eq} as multiplicative scale factors relative to the JPL06 recommendations. K_{eq} is not intended to be retrieved. Hereafter, all quantities subscripted with scale refer to scaling with respect to JPL06. The relationship between the ClO measurements ($\mathbf{y}$) and the state vector is described by a forward model ($\mathbf{F}$) that calcu-

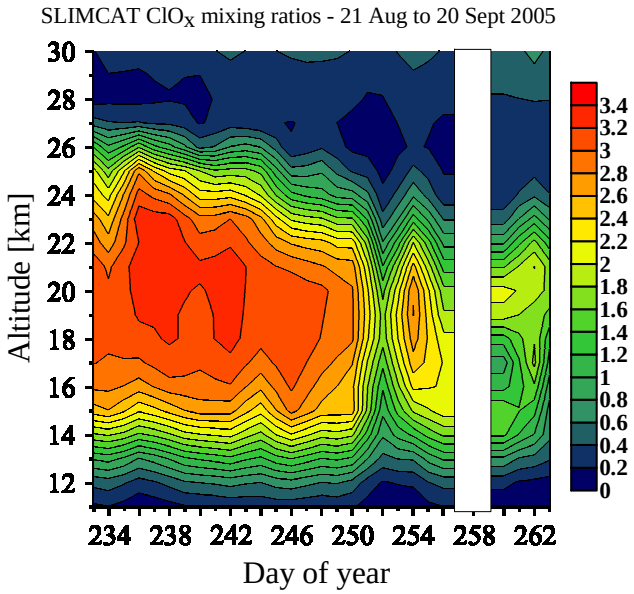

Figure 3.5: SLIMCAT modelled ClO_x mixing ratios from 21 August to 20 September 2005 between 11 and 30 km altitude. As there were no ClO measurements available from day 257 to 259 of 2005, SLIMCAT ClO_x mixing ratios were not considered on these days (white bar).

lates ClO as a function of the state vector $\mathbf{x}$ and other parameters $\mathbf{b}$ (see equation 2.27). The forward model calculates day minus night ClO profiles ($\hat{\mathbf{y}}$) compatible with the ClO measurements. Furthermore, the weighting function matrix $\mathbf{K}$ which describes the sensitivity of the modelled ClO values to changes in the state vector, are derived by the forward model. The ClO profiles computed with the forward model are then compared to the measured profiles ($\mathbf{y}$) and the difference between them is minimized by applying the standard Gauss-Newton method which iteratively calculates the state vector $\hat{\mathbf{x}}$ (equation 2.30). In order to calculate the optimal state vector $\hat{\mathbf{x}}$ which minimizes the difference between measured and modelled ClO, the covariance matrix of the measurement error ($\mathbf{S_e}$) is a required parameter besides the *a priori* ($\mathbf{x_a}$), its covariance ($\mathbf{S_a}$), the weighting functions ($\mathbf{K}$) and the measurements ($\mathbf{y}$). $\mathbf{S_e}$ is constructed by placing the ClO measurement errors as given in Solomon et al. (2000) along the diagonal, and set to zero everywhere else, i.e. the measurement errors are uncorrelated. As the measurement uncertainties do not include the smoothing error (Solomon et al., 2000) a comparison of the ClO measurements to modelled and/or high-resolution measurements cannot be made without accounting for the 'smoothing' of the measured profile. However, the smoothing error can be eliminated from such a comparison by using the averaging kernels (Connor et al., 1995). Before comparing the model calculation and the measurements, the quantity $\mathbf{x}_{a_{meas}} + \mathbf{A}_{meas}(\mathbf{x}_m - \mathbf{x}_{a_{meas}})$ is computed, where $\mathbf{x}_m$ is the ClO profile produced by the forward model, $\mathbf{A}_{meas}$ and $\mathbf{x}_{a_{meas}}$ are the averaging kernels and the *a priori* from the measurements, respectively. The calculated quantity is

then compared to the measured ClO profile. Without applying this convolution procedure one would introduce an error because the measured ClO concentration at e.g. 20 km was derived by using information from the measurements at 19, 20, and 21 km. It would be inappropriate to compare the measured ClO at 20 km with the high-resolution modelled value at 20 km, because the measured ClO at 20 km results from a weighted average of values at 20 km and above and below that level. Therefore, the ClO profile calculated by the forward model is convolved with $\mathbf{A}_{meas}$ and $\mathbf{x}_{a_{meas}}$ before comparing it to the measurements.

3.4.6 Retrieval output parameter

The retrieval model combined with the forward model determines the optimal atmospheric parameters, i.e. the kinetic parameters and the $\mathrm{ClO_x}$ profiles which minimize the difference between the modelled and measured ClO mixing ratios. This optimal state is represented by the retrieved state vector, $\hat{\mathbf{x}}$, containing the optimal set of kinetic parameters and the required optimal $\mathrm{ClO_x}$ concentrations. The uncertainties on the retrieved state vector are described by its covariance $\hat{\mathbf{S}}$. The off-diagonal elements of $\hat{\mathbf{S}}$ provide information on whether the uncertainties of the elements in $\hat{\mathbf{x}}$ are correlated or uncorrelated. Correlation describes the relationship between quantities, i.e. here the uncertainties of the $\hat{\mathbf{x}}$ elements. If the correlation between the errors is greater zero (i.e. off-diagonal elements are greater zero), then they are positive correlated, meaning that as one increases, the other increases as well. The errors are negative correlated, i.e. if one increases, the other decreases, if the correlation is smaller than zero. The errors are uncorrelated if the off-diagonal elements are zero. If the latter is the case, then the elements on the diagonal of $\hat{\mathbf{S}}$ represent the uncertainties of the retrieved state. If the errors are correlated it is important not to ignore the off-diagonal elements and to take them into account when determining the total error on the retrieved state. The off-diagonal elements of the calculated covariances of the 19 optimal estimation runs, show that the errors on the retrieved kinetic parameters are positive correlated and that the retrieved errors on the $\mathrm{ClO_x}$ profiles are uncorrelated. Therefore, to derive the total error on the retrieved $J_{scale}/k_{f_{scale}}$ ratio described by $\sigma_{\frac{J_{scale}}{k_{f_{scale}}}}$, the following equation for combining correlated errors was applied:

$$\sigma_{\frac{J_{scale}}{k_{f_{scale}}}} = \sqrt{\frac{\sigma^2_{J_{scale}}}{k^2_{f_{scale}}} + \frac{J^2_{scale}}{k^4_{f_{scale}}}\sigma^2_{k_{f_{scale}}} - 2\frac{J_{scale}}{k^3_{f_{scale}}} R_{J_{scale}\,k_{f_{scale}}} \sigma_{J_{scale}} \sigma_{k_{f_{scale}}}} \tag{3.5}$$

where

$\sigma^2_{J_{scale}}$ is the variance of J_{scale}

$\sigma^2_{k_{f_{scale}}}$ is the variance of $k_{f_{scale}}$

$\sigma_{J_{scale}}$ is the uncertainty on J_{scale}

$\sigma_{k_{f_{scale}}}$ is the uncertainty on $k_{f\,scale}$

R is the correlation coefficient of J_{scale} and $k_{f_{scale}}$

The optimal retrieved state vector $\hat{\mathbf{x}}$ is then used to calculate the final ClO concentrations ($\hat{\mathbf{y}}$) employing the forward model one more time. The retrieved state vector together with its uncertainties from all 19 optimal estimation runs is presented and discussed in Section 3.6.

Summary

In summary, optimal estimation is used as a method to solve an inverse problem and consists of two main parts, the forward model and the retrieval model. A photochemical box model is employed as the forward model that calculates daily day minus night ClO concentrations between 11 and 30 km, compatible with the ClO measurements, as a function of the state vector $\mathbf{x}$ and other parameters $\mathbf{b}$, which include $\mathrm{BrO_x}$, ozone, temperature, and pressure profiles. The required input parameters represented by $\mathbf{b}$, such as the daily BrOx and ozone profiles were obtained from the SLIMCAT (Section 3.3). However, the ozone profiles provided by SLIMCAT were first scaled to match coincident ozonesonde profiles. The temperature and pressure profiles were provided from NCEP. Besides the ClO profiles, the forward model also computes the weighting function matrix $\mathbf{K}$ which is a necessary input parameter for the retrieval model. The retrieval model calculates the optimal state vector $\hat{\mathbf{x}}$ that minimizes the differences between the measured and the modelled ClO profiles using the iterative Gauss-Newton method (equation 2.30). The other input parameters, besides $\mathbf{K}$, are the *a priori* state vector $\mathbf{x_a}$, its covariance $\mathbf{S_a}$ and the covariance matrix of the measurement errors $\mathbf{S_e}$. $\mathbf{x_a}$ was constructed by inserting multiplicative scale factors for $k_{f_{scale}}$, $K_{eq_{scale}}$ and J_{scale}, all set to 1.0 so that the *a priori* for the kinetics are the JPL06 recommendations. Furthermore, a set of 28 *a priori* $\mathrm{ClO_x}$ profiles, corresponding to each day of measurement, obtained from SLIMCAT is included in the *a priori* state vector. Using the optimal estimation approach, the optimal $J_{scale}/k_{f_{scale}}$ ratio and the optimal $\mathrm{ClO_x}$ concentrations are retrieved, but no attempt is made to retrieve K_{eq}. Rather, to test the sensitivity of the results to the choice of $K_{eq_{scale}}$, the optimal estimation is done 19 times varying $K_{eq_{scale}}$ from 0.2 to 2.0$\times K_{eq_{JPL06}}$ in steps of 0.1.

3.5 Exploring the full parameter space

Optimal estimation is a numerically highly efficient approach for solving an inverse problem and to determine the absolute minimum of the cost function, i.e the absolute minimum in the sum of the squares of the differences between measured and calculated/modelled ClO concentrations by the forward model. In addition, optimal estimation provides quantitative estimates of the uncertainties on the derived parameters given by the covariance matrix, which accounts for the uncertainties on the measurements, the *a priori* and the retrieval noise. Optimal estimation depends on the *a priori* information so that for a given *a priori* it can compute the best optimal solution. However, for a different *a priori* the solution might look different. Furthermore, if the problem to be solved has more than one absolute minimum or if more than one solution exists which gives the best answer where the RMS values are of a similar magnitude, then, defining the N dimensional field (where N is the number of variable parameters) rather than determining the absolute minimum of the cost-function, would provide the full 'picture' of the possible solutions. In such a case optimal estimation might not be the best numerical approach for solving the problem. One way to determine the morphology of the N dimensional space is to explore the whole parameter space (hereafter referred to as 'the sampling method') for all variables of interest. This method, however, is computationally very demanding.

In this chapter, it was computationally possible to sample the 4D space by varying J, k_f, K_{eq} and $\mathrm{ClO_x}$ scale factors within physically plausible limits. J_{scale} was varied between 0.1 and 2.5 while $k_{f_{scale}}$ was varied between 0.4 and 1.6. The chosen ranges for J and k_f are based on the values reported in previous studies, such that the computational burden was not too high. An upper bound of $K_{eq_{scale}}$=1.6 was used since JPL09 and most other studies (with the notable exception of Nickolaisen et al. (1994) and Ferracci and Rowley (2010)) suggest a K_{eq} value smaller than JPL06. Furthermore, to estimate the dependence of the kinetic parameters to changes in the prescribed $\mathrm{ClO_x}$ profile, the $\mathrm{ClO_x}$ profile was scaled between 0.5 and 1.0 times the *a priori* $\mathrm{ClO_x}$ profile used in the optimal estimation approach, in steps of 0.1. Because scalings above 1.0 resulted in $\mathrm{ClO_x}$ concentrations occasionally exceeding the $\mathrm{Cl_y}$ concentrations, only scalings smaller than 1.0 were used in this study. Furthermore, the $\mathrm{ClO_x}$ values were scaled on all days and at all altitude levels equally because scaling the $\mathrm{ClO_x}$ individually for every day would make it even more computationally expensive.

The photochemical model described in Section 3.4.1, using the same input variables such as $\mathrm{BrO_x}$, ozone, temperature and pressure, calculates daily day minus night ClO profiles compatible with the observations for every possible combination of those four parameters,

resulting in 31500 ClO profiles. Using these calculated ClO profiles, the RMS values of the differences between modelled and measured ClO were determined. The results are compared with the kinetic parameters retrieved from the 19 optimal estimation runs and with previous publications in the following section.

3.6 Kinetic parameters retrieved from optimal estimation

The ClO profiles calculated using the forward model, initialized with the optimal retrieved kinetic parameters and with the optimal retrieved $\mathrm{ClO_x}$ profiles, match the measured ClO profiles quite well. The derived root mean square (RMS) differences between measured and modelled ClO ranges from 0.063 to 0.066 ppb, which is smaller than the maximum error of the ClO measurements.

The results from the retrievals performed as described in Section 3.4, expressed as scale factors relative to the kinetic parameters recommended by JPL06, are shown together with 1σ uncertainties in Figure 3.6. A $J_{scale}/k_{f\,scale}$ value of 1.0 refers to the JPL06 recommendations (red symbol in Figure 3.6), where the photolysis rate of the dimer (J) is calculated using the absorption cross-sections recommended by JPL06. The values of J/k_f and K_{eq}, relative to JPL06, obtained in previous studies are indicated with vertical bars along the Y-axis (J/k_f) and with blue dots along the X-axis (K_{eq}) in Figure 3.6. Furthermore, the JPL06 recommendation with the given uncertainty range and the more recent JPL09 recommendation including the uncertainties are displayed in Figure 3.6. The JPL09 values and their uncertainty ranges, as shown in Figure 3.6, are scaled to the recommended JPL06 values, to be better comparable with the results obtained in this study. As detailed above, the JPL06 recommendations are the primary focus reference values. Tests were JPL09 kinetics were used as the *a priori* in optimal estimation showed that the retrieved J/k_f ratios were only slightly different ($\pm$2%) from the results presented in Figure 3.6.
The derived RMS values for the 19 optimal estimation runs vary only by $\sim$5%, but the change in the retrieved $J_{scale}/k_{f_{scale}}$ ratios over the prescribed $K_{eq_{scale}}$ range (0.2 to 2.0) is significant. The ratio retrieved by prescribing $K_{eq_{scale}}$ of 2.0 is about 1.6 times smaller than the $J_{scale}/k_{f_{scale}}$ ratio retrieved for the smallest $K_{eq_{scale}}$ (0.2) used in this study. Furthermore, the RMS values obtained from the optimal estimation runs are elevated as a result of the inclusion of two days of measurements between 7 and 8 September 2005 where the peak ClO concentration dropped from $\sim$2.3 ppb to $\sim$0.8 ppb before increasing back to $\sim$2 ppb on 10 September 2005 (Figure 3.3). As detailed above, the suppressed values of ClO over this two day period are caused by dynamical variability of the polar vortex.

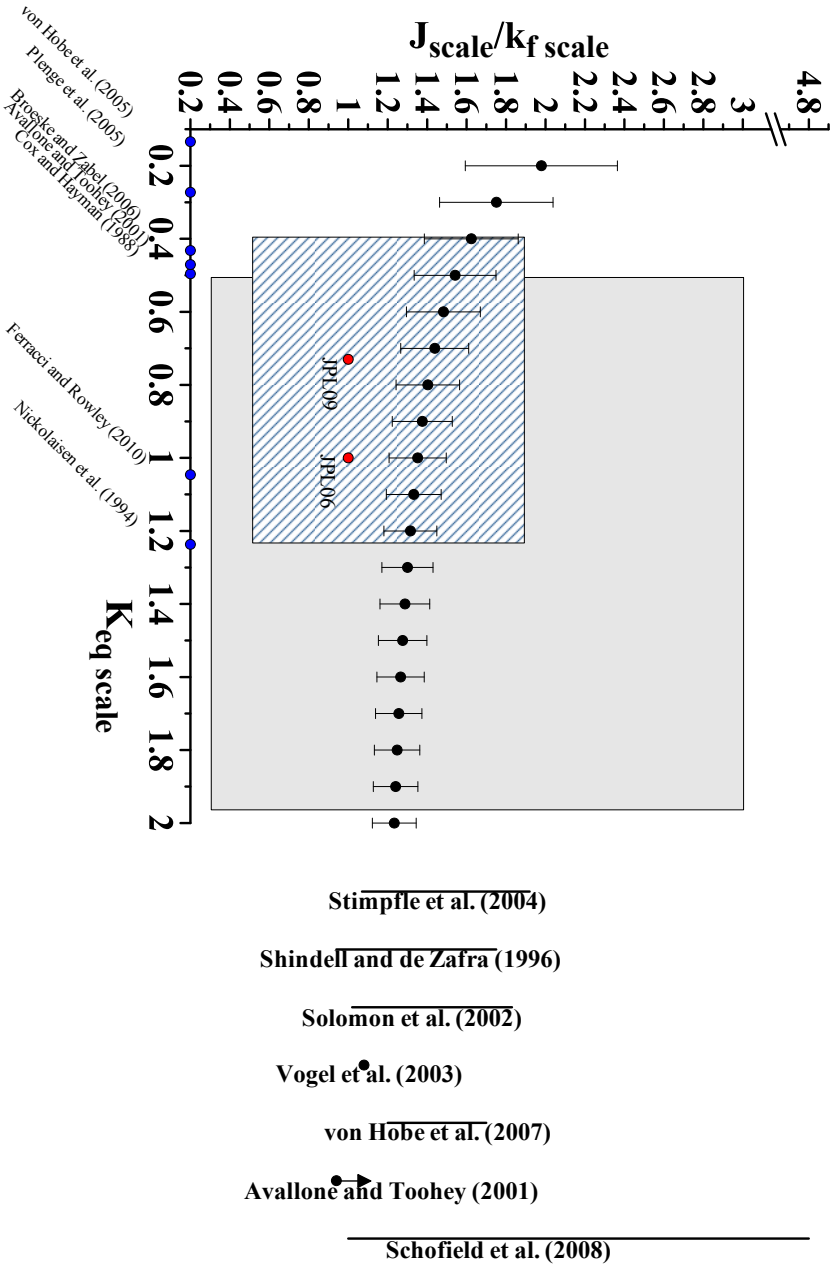

Figure 3.6: Black dots with error bars: the retrieved $J_{scale}/k_{f_{scale}}$ ratios and corresponding 1σ uncertainties resulting from the 19 optimal estimation runs where $K_{eq_{scale}}$ was varied within the uncertainty range given by JPL06. Vertical lines on the right hand side: Results from earlier studies for $J_{scale}/k_{f_{scale}}$ at 190 K. Blue symbols along the X-axis: $K_{eq_{scale}}$ relative to JPL06 determined from earlier studies. Note that the derived $K_{eq_{scale}}$ values from previous studies were calculated for stratospheric temperatures between 190 K and 210 K). The red symbols indicate the scalings for JPL06 and JPL09, respectively. Light grey area: JPL06 uncertainty range on K_{eq} and J/k_f. Hatched area: JPL09 uncertainty range on K_{eq} and J/k_f (for more details see text).

The value of $J_{scale}/k_{f_{scale}}$ is determined by the partitioning of ClO and ClOOCl on all days and is not determined separately for each day. The amount of $\mathrm{ClO_x}$, on the other hand, can vary independently for each day within the given uncertainty range which is determined by the prescribed *a priori* uncertainty. The selection of the elements of $\mathbf{S_a}$ determines the freedom of the optimal estimation, i.e. how well constrained optimal estimation is. The selected uncertainties on the *a priori* $\mathrm{ClO_x}$ profile are likely to be too small for these two days and therefore the optimal estimation is constrained too tightly. The retrieval does not have enough freedom to modulate $\mathrm{ClO_x}$, for the given $J_{scale}/k_{f_{scale}}$, to reproduce the measurements. The combination of $J_{scale}/k_{f_{scale}}$ with higher amount of $\mathrm{ClO_x}$ leads to more ClO than observed and thereby contributes to the higher RMS values. While excluding these two days from the analysis reduces the RMS such that it is smaller than the measurement uncertainty at every altitude level, the retrieved $J_{scale}/k_{f_{scale}}$ increases slightly, from $1.35\pm0.14\times J/k_{f_{JPL06}}$ (all data points) to $1.44\pm0.18\times J/k_{f_{JPL06}}$ (8 and 9 September excluded), if $K_{eq} = K_{eq_{JPL06}}$. The difference between the two calculations is not statistically significant. Since there is no valid scientific reason for excluding these two days, and because they have only a small effect on the retrieved value of $J_{scale}/k_{f_{scale}}$, these two days were retained in the following analyses.

The optimal daily $\mathrm{ClO_x}$ profiles retrieved from the 19 optimal estimation runs exceeded the amount of $\mathrm{Cl_y}$ on two days of the analysis period (7 and 10 September 2005). The amount of $\mathrm{ClO_x}$ required to reproduce the measured ClO concentrations lies above 4.5 ppb. There are two causes for these unrealistically high values. First, since 7 September 2005 is the day where the ClO concentration maximizes the real $\mathrm{ClO_x}$ value needed to explain the ClO measurements is probably very close to $\mathrm{Cl_y}$. Adding the retrieval 'noise' leads to values exceeding $\mathrm{Cl_y}$. On the other hand, the SLIMCAT *a priori* $\mathrm{ClO_x}$ concentrations are maximize at the beginning of the analysis period. From 3 September 2005 onwards $\mathrm{ClO_x}$ concentrations decrease (Figure 3.4.4). As mentioned above, $J_{scale}/k_{f_{scale}}$ depends on all days of the season and it might well be that the ratio derived for all days is too small in combination with the decreasing $\mathrm{ClO_x}$ concentrations on 7 and 10 September 2005. Therefore, optimal estimation has to increase $\mathrm{ClO_x}$ to explain the measurements on these days. Within optimal estimation there is no constraint which would stop $\mathrm{ClO_x}$ concentrations exceeding $\mathrm{Cl_y}$. Therefore, the optimal $J_{scale}/k_{f_{scale}}$ ratio for all days of the analysis period requires $\mathrm{ClO_x}$ values larger than $\mathrm{Cl_y}$ to explain the observed ClO mixing ratios on 7 and 10 September 2005. As the average over all retrieved $\mathrm{ClO_x}$ profiles does not exceed $\mathrm{Cl_y}$, these high values are maintained in this study as they can be explained.

The salient features of the findings (retrieved $J_{scale}/k_{f_{scale}}$ ratios) of this study, summarized in Figure 3.6, are the negative slope and the asymptotic behaviour of $J_{scale}/k_{f_{scale}}$ at high $K_{eq_{scale}}$.

Negative slope: An increase in K_{eq} can be obtained either by increasing k_f , decreasing k_r, or both, or decreasing k_f and k_r but decreasing k_r relatively more. The k_r values associated with the prescribed $K_{eq_{scale}}$ shown in Figure 3.6, decrease with increasing $K_{eq_{scale}}$ as does $J_{scale}/k_{f_{scale}}$, while the k_f values increase. The combination of increasing $k_{f\,scale}$ and decreasing k_r shifts the equilibrium towards ClOOCl, reducing the calculated concentration of ClO. To restore the equilibrium such that the measured ClO is obtained, the photolysis of the dimer, J, must increase. The observed decrease in $J_{scale}/k_{f_{scale}}$ can then only be achieved if $k_{f\,scale}$ increases more than J_{scale}. The causes for that behaviour of $J_{scale}/k_{f_{scale}}$, i.e. increasing $K_{eq_{scale}}$ results in decreasing $J_{scale}/k_{f_{scale}}$ ratios, are not yet well understood.

Asymptotic behaviour of $J_{scale}/k_{f_{scale}}$ at high K_{eq_scale}: The results show that the retrieved values of $J_{scale}/k_{f_{scale}}$ do not vary much at high values of $K_{eq_{scale}}$, 1.6 to 2.0, used in the analysis. An increase in $K_{eq_{scale}}$ requires $k_{f\,scale}$ to increase (see above). However, the measured ClO imposes a limit on the amount of ClOOCl that results from the increase in $k_{f\,scale}$. If much of the available ClO is transformed into ClOOCl, a further increase in $k_{f\,scale}$ affects ClOOCl concentrations less than if larger abundances of ClO were available. Once the amount of ClOOCl maximizes, the photolysis rate also encounters a threshold within optimal estimation, such that $J_{scale}/k_{f_{scale}}$ plateaus at high values of $K_{eq_{scale}}$. Additional increases in $K_{eq_{scale}}$ are then achieved within the model by changing k_r. This result suggests a lower limit for $J_{scale}/k_{f_{scale}}$ of $\sim$1.24$\pm$0.12, in combination with high values of $K_{eq_{scale}}$, to explain the Antarctic measurements of ClO.

The $J_{scale}/k_{f_{scale}}$ values obtained from all 19 optimal estimation runs agree with most of the values reported in previous studies (Figure 3.6). Except for $K_{eq_{scale}}$ values smaller than 0.4, the retrieved $J_{scale}/k_{f_{scale}}$ ratios lie within the given uncertainty ranges on K_{eq} and J/k_f reported by the JPL panels. The results indicate that to explain the Antarctic measurements of ClO made in 2005, it is unlikely that the J/k_f ratios are smaller than currently recommended and this would exclude the lower uncertainty range on J/k_f as recommended by the JPL panels. The JPL recommended parameters for J/k_f and K_{eq} can be used within the given uncertainty range as suggested by JPL06 and the more recent JPL09 recommendation to explain the Antarctic ClO measurements made in 2005. However, at the same time, the derived results suggest a greater J/k_f ratio than recommended by JPL. This can be accomplished by either a faster photolysis of ClOOCl, a slower dimer formation rate, or some combination of these two perturbations.

The best fit to the ClO measurements, i.e. the smallest RMS of the difference between modelled and measured ClO, is obtained at $K_{eq_{scale}}$=2.0. In this case $J_{scale}/k_{f_{scale}}$ is 1.23±0.11. In contrast to previous studies, the results presented here suggest that to best represent the ClO measurements, $K_{eq_{scale}}$ must lie towards the upper end of the prescribed range (0.2 to 2.0), in agreement with the recent laboratory study of Ferracci and Rowley (2010). However, the derived K_{eq} values in Ferracci and Rowley were obtained at higher temperatures (256.5<T<312.65 K) than the stratospheric temperatures observed in this study. Calculation of the K_{eq} value derived by Ferracci and Rowley for stratospheric temperatures as shown in Figure 3.6, results in a K_{eq} value of $\sim$1.05$\times K_{eq\,JPL06}$. To explain the ClO measurements, the results presented here do not preclude higher K_{eq} values than currently recommended, even for stratospheric conditions. That said, the decrease in RMS from $K_{eq_{scale}}$=0.2 to 2.0 is small (5%), suggesting that K_{eq} is not well enough constrained by the measurements of ClO to make a robust evaluation of K_{eq}.

Solomon et al. (2000) used measurements from the same ClO microwave radiometer at the same site to derive $J_{scale}/k_{f_{scale}}$ values which best reproduce their measurements. The measurements they used were taken from a different period (1996-2000) when stratospheric temperatures were, on average, 4 K lower than in 2005. The formation rate of the dimer is known to be temperature dependent. Therefore, it is somewhat surprising that the retrieved $J_{scale}/k_{f_{scale}}$ ratio of 1.39 interpolated to the K_{eq} obtained by Solomon et al. (2000) ($K_{eq_{scale}}$=0.86 relative to JPL06), agrees very well with the $J_{scale}/k_{f_{scale}}$ ratio obtained by Solomon et al. (Figure 3.6). A decrease in temperature leads to an increase in the dimer formation rate k_f (Figure 3.1), which in turn leads to a decrease in the J/k_f ratio. However, Solomon et al. used the JPL97 functional form for the temperature dependence of k_f , which is different to the JPL06 expression used here. The difference between JPL97 and JPL06 then partially offsets the effect of the temperature difference between the two studies.

3.7 Kinetic parameters derived from exploring the parameter space

In contrast to the optimal estimation approach, the $k_{f_{scale}}$, J_{scale}, and $K_{eq_{scale}}$ parameter space was explored to derive the optimal ClO-dimer cycle kinetic parameters required to explain the measured ClO. Exploring the parameter space is accomplished by varying the kinetic parameters within a given range that is based on the results presented in previous studies and based on the JPL06 recommendations. Noting, however, that the ClO_x concentrations obtained from SLIMCAT may be uncertain, sensitivity to ClO_x was also explored

by scaling $\mathrm{ClO_x}$ from 0.5 to 1.0. The photochemical box model calculates daily day minus night ClO profiles for every possible combination of those four parameters. From these profiles the RMS values of the difference between measured and modelled ClO concentrations were determined. The results will be presented in this section.

The results from the sampling method would be best represented in a 4D plot. However, a 4D plot is far to complex and impossible to show on 2D paper and for the purpose of this study it is sufficient and necessary to display the results in two dimensions. Therefore, in terms of analyzing the output data, the RMS values calculated for every $K_{eq_{scale}}$ were examined separately. For a given $K_{eq_{scale}}$ value, the minimum RMS value for every combination of $k_{f_{scale}}$ and J_{scale} corresponding to one of the 6 $\mathrm{ClO_x}$ scalings was determined. The minimum RMS values (derived from the 6 possible $\mathrm{ClO_x}$ scalings) are shown for each combination of $k_{f_{scale}}$ and J_{scale} and for $K_{eq_{scale}}$=0.4, 0.8, 1.2, and 1.6 in Figure 3.7. In all cases the lowest RMS values are found for $\mathrm{ClO_{x_{scale}}}$ =1.0 (unshaded regions in Figure 3.7) and the absolute minimum RMS values are obtained for the highest $K_{eq_{scale}}$ value which agrees with the results derived from optimal estimation. While lower RMS values might have been found for $\mathrm{ClO_{x_{scale}}}$ >1.0, this would be physically unrealistic for the reasons detailed above. As shown in Figure 3.7, the optimal combination of the kinetic parameters does not results in just one set of J, k_f, K_{eq}, and $\mathrm{ClO_x}$. Different combinations of $k_{f_{scale}}$ and J_{scale} can reproduce the ClO measurements with a fairly small RMS value. The minimum RMS values define a valley in every J_{scale}–$k_{f_{scale}}$ plane as shown in Figure 3.7, where the magnitude of the RMS values within that valley are not significantly different. The calculated minimum RMS value in the J_{scale}–$k_{f_{scale}}$ plane, for each $K_{eq_{scale}}$, shows little dependence on $K_{eq_{scale}}$, confirming again that the Antarctic ClO measurements do not provide a strong constraint on K_{eq}.

When $K_{eq_{scale}}$ is held constant and if $k_{f_{scale}}$ increases, k_r must also increase (see equation 3.2). However, the resultant increase in k_r is insufficient to produce enough ClO to match the measurements and hence J_{scale} too must increase. This explains the orientation of the valley of minimum RMS values seen in Figure 3.7. The angle that this valley makes with the X-axis decreases slightly with increasing $K_{eq_{scale}}$ indicating a decrease in $J_{scale}/k_{f_{scale}}$ with increasing $K_{eq_{scale}}$, in agreement with the results from the 19 optimal estimation runs described in Section 3.4.1. The ClO measurements only give information on J/k_f , not on these parameters individually. Therefore, the J/k_f ratio that best explains the ClO measurements can be derived from the orientation of the valley with an uncertainty constrained by the width of the valley. For higher $K_{eq_{scale}}$ values (panels b–d in Figure 3.7), the orientation of the valley suggests a $J_{scale}/k_{f_{scale}}$ ratio smaller than 1 which would disagree with the optimal estimation result. However, optimal estimation retrieves the optimal

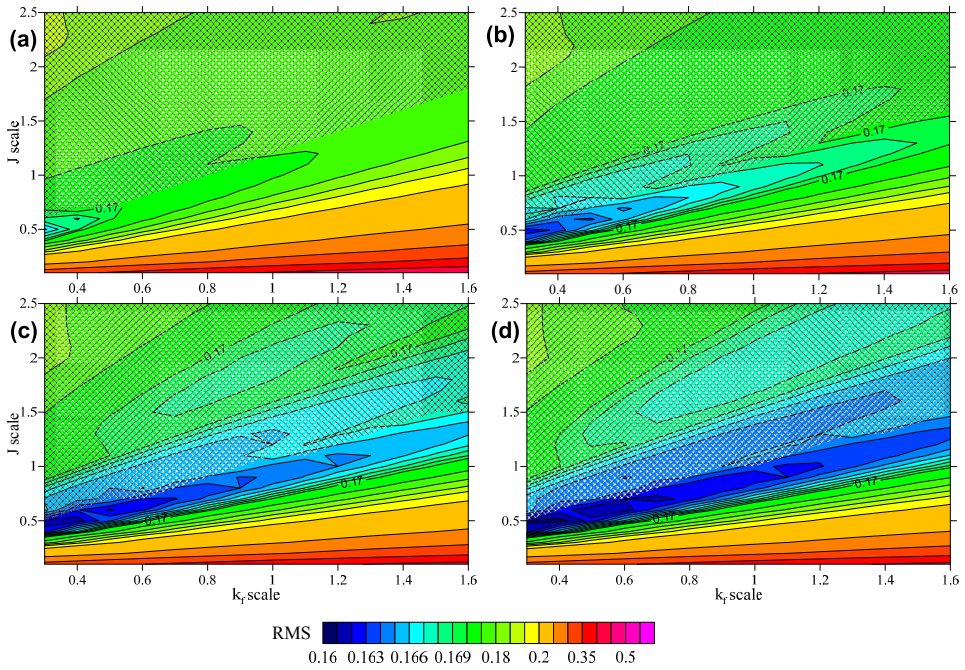

Figure 3.7: Scale factors for J and k_f with the corresponding RMS minimum derived from exploring the whole parameter space by varying $k_{f_{scale}}$, J_{scale}, $K_{eq_{scale}}$, and $\mathrm{ClO_{x_{scale}}}$. The derived RMS minimum values are shown for $K_{eq_{scale}}$ of 0.4 (a), $K_{eq_{scale}}$ of 0.8 (b), $K_{eq_{scale}}$ of 1.2 (c), and $K_{eq_{scale}}$ of 1.6 (d). The hatched area shows the RMS values where the $\mathrm{ClO_x}$ scale factor was not equal to 1 (details see text).

kinetic parameters that correspond to the absolute minimum difference between retrieved and observed ClO profile. Therefore, to compare the results from exploring the parameter space with the results from optimal estimation, the kinetic parameters derived from exploring the parameter space that correspond to the absolute minimum RMS value have to be determined. Therefore, taking the absolute minimum RMS in each panel, the corresponding $J_{scale}/k_{f_{scale}}$ values agree well with the results from the optimal estimation runs. The derived $J_{scale}/k_{f_{scale}}$ values from the sampling method are summarized together with the optimal estimation results in Table 3.1. However, the resulting valley of RMS minima using this $J_{scale}/k_{f_{scale}}$ ratios of 1.66 and 1.25 (Table 3.1) would require $\mathrm{ClO}_{x\,scale}$ values smaller than 1, leading to an increase of the angle that this valley makes with the X-axis.

The range of J_{scale} and $k_{f_{scale}}$ values which correspond to the optimal derived $J_{scale}/k_{f_{scale}}$ ratio retrieved using the optimal estimation approach would form a valley with a greater angle between that valley and the X-axis than that valley formed by the results from exploring the full parameter space. The $\mathrm{ClO_x}$ concentrations are not fixed and can be changed from day to day and from one altitude to another within optimal estimation which contrasts with the treatment of $\mathrm{ClO_x}$ in sampling of the whole parameter space. Due to the high computational demands of the sampling method, $\mathrm{ClO_x}$ was not varied for every day individually

sampling method $\frac{J_{scale}}{k_{f_{scale}}}$	optimal estimation $\frac{J_{scale}}{k_{f_{scale}}}$	$K_{eq_{scale}}$
1.66	1.62±0.24	0.4
1.66	1.40±0.16	0.8
1.66	1.32±0.13	1.2
1.25	1.27±0.28	1.6

Table 3.1: $J_{scale}/k_{f_{scale}}$ corresponding to the absolute RMS minimum as derived from the sampling method compared to the retrieved $J_{scale}/k_{f_{scale}}$ ratios from optimal estimation for a selected number of $K_{eq_{scale}}$ values

i.e. the parameter space exploration scales $\mathrm{ClO_x}$ values on all days and at all levels equally. This can partially explain the differences in the slope of the valley when comparing optimal estimation and the sampling method since the kinetic parameters are not independent of the amount of available $\mathrm{ClO_x}$. Furthermore, the RMS values obtained from exploring the whole parameter space are more than twice as large as those resulting from optimal estimation. Therefore, the results from the optimal estimation approach lead to a better fit to the ClO measurements than the results from exploring the whole parameter space, primarily because $\mathrm{ClO_x}$ cannot change from day to day or from one altitude to another while exploring the whole parameter space. It would require too much computing power to allow $\mathrm{ClO_x}$ values to change from day to day and from one altitude level to another while sampling the parameter space. This shows clearly the limitation of the sampling method.

3.8 Discussion and Conclusions

Two methods, both using ground-based ClO measurements made in Antarctica, to derive the key kinetic parameters that govern the day-time partitioning between ClO and ClOOCl were presented. Due to the data processing of the ClO measurements, where night-time ClO measurements were subtracted from day-time measurements, the day-time ClO profiles only contain information about J/k_f and not for these parameters individually. Therefore, based on the available Antarctic ClO measurements, the best J/k_f ratio was deduced, representing the optimal fit to the measurements. This retrieved J/k_f ratio then provides a range of combinations of J and k_f that are consistent with the ClO measurements. Furthermore, the equilibrium constant K_{eq} was prescribed to values between 0.2 and 2.0$\times K_{eq_{JPL06}}$, to allow a sensitivity study of the derived J/k_f ratios to changes in K_{eq}.

First, the optimal estimation was applied to retrieve the optimal J/k_f ratio that correspond to the minimum of the differences between measured and calculated ClO concentrations by the forward model was presented. To confirm the results from the optimal estimation,

and to test how much more information can be derived when sampling the whole parameter space one run was performed where the kinetic parameters and the $\mathrm{ClO_x}$ profiles were varied within physically plausible ranges to determine the combination of these parameters that minimizes the sum of the square of the differences between the modelled and the measured ClO profiles.

The results retrieved from the 19 optimal estimation runs and from the exploring the whole parameter space agree very well within the given uncertainties of optimal estimation. Comparison of the results from the two methods shows that optimal estimation is a faster way to derive the optimal J/k_f consistent with the measurements. The retrieved J/k_f ratios reflect a range of combinations of J and k_f values which are consistent with the measurements and which are in agreement with the results obtained from sampling the whole parameter space. As optimal estimation is also able to vary the $\mathrm{ClO_x}$ concentrations from day to day and from one altitude level to another, the retrieved values also lead to a better representation of the ClO measurements, i.e. smaller RMS values. Overall the optimal estimation is a reliable method and a much faster approach compared to exploring the parameter space, to derive the kinetic parameters which govern the partitioning of ClO and its dimer.

The derived J/k_f ratios from optimal estimation provide a range of possible combinations for J, k_f and K_{eq} to explain the Antarctic ClO measurements, i.e. there is not only one optimal combination J, k_f and K_{eq}. Using the kinetic parameters derived in pervious laboratory and field studies, and the kinetic parameters currently recommended by JPL06, Table 3.2 summarizes the combination of parameters that correspond to the retrieved J/k_f ratios derived from optimal estimation. The results presented in Table 3.2 are discussed below.

dimer formation rate k_f	photolysis rate J	equilibrium constant K_{eq}
Trolier et al. (1990)	JPL06	Cox and Hayman (1988)
JPL06	$>$ JPL06	Plenge et al. (2005)
$<$ JPL06	JPL06	Plenge et al. (2005)
Nickolaisen et al. (1994)	Burkholder et al. (1990)	Plenge et al. (2005)
$>$ 0.58 $\times$ JPL06	Burkholder et al. (1990)	0.2 $\times$ JPL06
$>$ 1.2 $\times$ JPL06	Burkholder et al. (1990)	2.0 $\times$ JPL06
0.6 to 0.95 $\times$ JPL06	JPL06	JPL06

Table 3.2: Possible combinations of k_f and J values for the derived $J_{scale}/k_{f_{scale}}$ ratios from optimal estimation. These given combinations of J, k_f, and K_{eq} can reproduce the Antarctic ClO measurements.

If the value of k_f recommended by JPL06 is correct and well known, then the findings of this study indicate that the photolysis rate of the ClOOCl dimer is larger than currently recommended by JPL06 and JPL09. However, previous laboratory and field studies showed that there are still discrepancies in the derived temperature dependent k_f values, especially at temperatures encountered in the polar stratosphere. The largest reported value for k_f by Boakes et al. (2005) is about 20% larger than recommended by JPL06 (for temperatures between 190 K and 210 K) and the smallest published value by Trolier et al. (1990) is about 34% smaller than k_f given in JPL06. The k_f value determined by Boakes et al. (2005) can be used to explain the Antarctic ClO measurements of this study, only if a greater photolysis rate of the ClO-dimer than recommended by JPL is used. If the photolysis rate recommended by JPL06 is used then smaller values for k_f, such as k_f reported by Trolier et al. (1990), are needed to explain the Antarctic ClO measurements. This finding is in agreement with the results presented by Stimpfle et al. (2004).

Using a combination of the J value obtained from the Burkholder et al. (1990) absorption cross-sections, which agrees with the value of J found using cross-sections of the more recent study by Papanastasiou et al. (2009), requires a $k_{f\,scale}$ value greater than 0.58 combined with the lowest $K_{eq_{scale}}$ value at 0.2, to be consistent with the ClO measurements. This lower limit for $k_{f_{scale}}$ increases with larger values of $K_{eq_{scale}}$, resulting in $k_f \geq 1.2 \times k_{f_{JPL06}}$ for prescribing $K_{eq_{scale}}$ to 2.0 and assuming that the Burkholder et al. absorptions cross-sections are correct. An increase in both J and k_f relative to the JPL recommendations would lead to an increase in the calculated ozone loss by the ClO dimer cycle, because chlorine is cycled more quickly through the various steps of the cycle. A slower photolysis rate as recommended by JPL06/09 and as derived by Huder and DeMore (1995), would require also a lower k_f value between 0.2 and $1.0 \times k_{f_{JPL06/09}}$, considering the given $K_{eq_{scale}}$ values used in this study.

Prescribing the K_{eq} value derived by Cox and Hayman (1988), results in a $J_{scale}/k_{f_{scale}}$ ratio of 1.54 ± 0.21. This ratio would also include such a combination of J and k_f as mentioned above, i.e. J_{JPL06} and $k_{f_{Trolier}}$, to explain the ClO measurements. This result is in agreement with Stimpfle et al. (2004) who concluded that the laboratory measurement of K_{eq} from Cox and Hayman (1988) agrees best with their ClO and ClOOCl observations ($190 < T < 200$ K). One of the largest J/k_f ratios ($1.75 \pm 0.51 \times (J/k_f)_{JPL06}$) derived in this study requires a prescribed K_{eq} value as reported by Plenge et al. (2005) for stratospheric temperatures. This result suggests that the photolysis rate of the dimer is higher than currently recommended and lies within the range of 1.25 to $2.25 \times J_{JPL06}$ if the k_f recommended by JPL06 is correct. If the photolysis rate determined by JPL06 is used, then k_f has to be smaller than currently recommended (between 45% and 80% of $k_{f_{JPL06}}$). Fur-

thermore, the K_{eq} value obtained by Plenge et al. can be combined with the photolysis rate calculated with the Burkholder et al. (1990) cross-sections and the dimer formation rate as reported by Nickolaisen et al. (1994) to explain the ClO measurements, which is in agreement with WMO (2007).

The suggested uncertainty range on K_{eq} by JPL06 encompasses all results for prescribing K_{eq} to values between 0.5 to 1.9$\times K_{eq_{JPL06}}$ while the uncertainty range on K_{eq} given in the more recent JPL09 recommendation only encompasses the results where K_{eq} was prescribed to values between 0.6 to 1.7$\times K_{eq_{JPL09}}$. Retrieved $J_{scale}/k_{f_{scale}}$ ratios for lower and higher $K_{eq_{scale}}$ values fall outside the uncertainty range given in the JPL panels. This would exclude the K_{eq} derived by von Hobe et al. (2005) and the photolysis rate reported by Pope et al. (2007) from being correct. Most of the previous laboratory and field studies imply a smaller K_{eq} value than recommended by JPL06 (Plenge et al., 2005; Bröske and Zabel, 2006; Avallone and Toohey, 2001). However, this result depends on the temperature that was used to calculate K_{eq} and it is very likely that the given K_{eq} values from these previous studies would be closer to the JPL recommendations for higher temperatures since K_{eq} is known to be temperature dependent (e.g. Santee et al., 2010). A lower K_{eq} value than recommended by the JPL panels implies that the thermal dissociation of the dimer occurs faster than currently thought, resulting in higher ClO concentrations during the night. If K_{eq} is fixed to JPL06, on the other hand, a J/k_f value of 1.35$\pm$0.14$\times(J/k_f)_{JPL06}$ is obtained using the described optimal estimation approach. Applying the J_{JPL06} photolysis rate requires a smaller k_f value than currently recommended and the results show that k_f must lie in the range of 0.6 to 0.95$\times k_{f_{JPL06}}$ to explain the measurements (Table 3.2). This range of the dimer formation rate includes the results determined by Bloss et al. (2001), Trolier et al. (1990) and Nickolaisen et al. (1994) and together with the JPL06 recommendation for J and K_{eq}, these values are consistent with the ClO measurements used in this chapter.

Results from this chapter do not preclude any K_{eq} value between 0.2 and 2.0$\times K_{eq_{JPL06}}$ from being correct. However, the best fit to the measurements is accomplished for greater K_{eq} values than recommended by JPL06. That said, the RMS values from all 19 optimal estimation runs are not significantly different in magnitude, suggesting that K_{eq} is not well constrained by the measurements of ClO as the night-time measurements were subtracted from the day-time measurements.

Day-time and night-time measurements of ClO are required to determine a reliable value of K_{eq}. Although this study does not provide a tight constraint on K_{eq}, the retrieved J/k_f obtained here is robust against the uncertainty in K_{eq}. Furthermore, stratospheric temperatures above Scott Base during the period of ClO measurements, and over the altitude range

where ClO concentrations maximize, varied from 183.7 K to 217.6 K. In contrast, most of the earlier studies took place in conditions with temperatures above 190 K. Schofield et al. (2008), for example, examined Arctic ClO measurements made at temperatures between 200 and 207 K and found a very small K_{eq} value of $0.2\times K_{eq_{JPL06}}$. The differences in the underlying temperature fields could, in part, explain why K_{eq} values higher than currently recommended (JPL06/09) and previously published (Santee et al., 2010) can be used to reproduce the Antarctic ClO measurements used in this chapter. For temperature to be partially responsible for the differences in $K_{eq_{scale}}$ across these studies, the formulation of the temperature dependence (i.e. exp(B/T)) would need to be incorrect. This highlights the need for a greater number of laboratory and field studies at the low temperatures typical of the Antarctic stratosphere. The retrieval of day-time and night-time ClO profiles from Antarctic ground-based measurements separately is currently under investigation. These ground-based ClO measurements could be used in a future study to investigate the kinetic parameters individually and would contribute to the need for field and laboratory studies determining these kinetic parameters, especially k_f and K_{eq}, under stratospheric conditions.

Night-time ClO measurements were used in the past to determine the equilibrium constant (e.g., Stimpfle et al., 2004; Santee et al., 2010). Given these studies and studies performed in the laboratory (e.g., Plenge et al., 2005) it is more likely that $K_{eq_{scale}}$ lies between 0.27 and 0.5 than being far greater than recommended by JPL06. Furthermore, the study by von Hobe et al. (2007) found that their stratospheric ClO observations were described well using a similar K_{eq} as reported in Plenge et al. (2005). The JPL09 recommendation also provides a smaller K_{eq} value ($0.7\times K_{eq_{JPL06}}$) than previously recommended in JPL06. The range of $K_{eq_{scale}}$ between 0.27 and 0.7, together with the results from optimal estimation, suggest that J/k_f values lie between 1.75 ± 0.29 and $1.44\pm0.17\times(J/k_f)_{JPL06}$. The analysis presented in this chapter shows that using these combinations of the kinetic parameters would include J and k_f values which are consistent with the JPL06 recommendations within the given uncertainty ranges. Furthermore, this result would preclude J values smaller than currently recommended (e.g., Pope et al., 2007).

The results from this chapter are in basic agreement with earlier field and laboratory studies. It has been shown that it is crucial to reduce the uncertainty on these kinetic parameters, to investigate these kinetics under stratospheric conditions and therefore to improve understanding of the stratospheric chemical processes.

Chapter 4

Projections of the evolution of Antarctic ozone under different greenhouse gas emissions scenarios

4.1 Introduction

The Montreal Protocol and its amendments and adjustments has significantly reduced emissions of ozone depleting substances (ODSs) to the atmosphere and halogen levels are now decreasing (WMO, 2007; Newman et al., 2006). The ozone layer over polar regions is expected to respond to these changes in stratospheric halogen loading. However, stratospheric ozone is not only affected by changes in ODSs but also by stratospheric changes induced by enhanced greenhouse gases (GHGs). As a result, the future evolution of stratospheric ozone and the timing of ozone, returning to historic levels (e.g. 1960 or 1980) remain uncertain (WMO, 2007). Numerous model studies have been performed to investigate the influence of changing ODSs and changing GHG concentrations on the stratospheric ozone layer through the 21st century.

In 2006, Newman et al. presented an approach to project the date of return of Antarctic ozone to 1980 values, based on estimated future chlorine and bromine abundances. Equivalent effective stratospheric chlorine (EESC) is used today as a measure of ozone depleting chlorine and bromine abundances (WMO, 2007; Newman et al., 2007). EESC is estimated from ground-based halogen observations where transit times into the stratosphere, the greater effectiveness of bromine compared to chlorine, and the destruction rates of halocarbons in the stratosphere are accounted for (Newman et al., 2006, 2007). Newman et al. (2006) calculated an Antarctic EESC that was used together with stratospheric temperatures in a

parametric model to determine the ozone hole area. Using future levels of Antarctic EESC and assuming a constant stratospheric cooling of about 0.25 K decade^{-1}, they concluded that the Antarctic ozone hole will return to 1980 levels by 2068. This date of return is about 16 years later than the multi-model estimate (which is based on coupled chemistry-climate model (CCM) simulations) of the return dates of total column Antarctic ozone reported in SPARC-CCMVal (2010). This difference in the return dates is related to different sources of uncertainties which are discussed in the following.

The projections presented by Newman et al. (2006) are based on a constant stratospheric cooling rate (see above) which is uncertain because of the uncertain magnitude of the cooling related to uncertainties in the future emissions of GHGs. The approach presented by Newman et al. (2006) does not include projections of the date of return of Antarctic ozone using future temperature trends based on different GHG emissions scenarios. Furthermore, the estimates of Antarctic EESC are based on a constant mean age-of-air (i.e. constant transport times). The stratospheric circulation is expected to strengthen in a changing climate (SPARC-CCMVal, 2010), resulting in an increase in transport rates which in turn modifies the fractional release (i.e. the fraction of the chlorine and bromine source gases that are dissociated in the stratosphere). As reported in a subsequent study by Newman et al. (2007) uncertainties in the mean age-of-air result in an uncertainty in the return dates ranging from 2056 to 2077. To account for future temperature changes, which in turn alter the dynamical and chemical processes, numerical models that include the various feedbacks need to be employed.

CCMs are the tools traditionally used to project future changes in ozone and their coupling to climate change (Chapter 1). The latest model studies by Eyring et al. (2010a) and Austin et al. (2010a) investigated the return of ozone to historic levels (1980 and 1960) as a function of latitude, using state-of-the art CCMs from several modelling groups. CCM simulations of Antarctic ozone abundances through the 21$^{\text{st}}$ century show a large inter-model spread in the CCMs used in these studies. The simulations indicate that Antarctic ozone is projected to return to 1980 levels more slowly than in the Arctic. The studies by Eyring et al. (2010a) and Austin et al. (2010a) suggest that the decrease in ODSs is the dominant factor in determining the return of Antarctic ozone to historic levels. As a result, both ODSs and stratospheric ozone return to 1980 levels between 2045 and 2060. In contrast, Arctic total column ozone is projected to return to 1980 levels around 2026, well before the total inorganic stratospheric chlorine abundances ($\mathrm{Cl_y}$) return to 1980 values ($\sim$2046) (SPARC-CCMVal, 2010; Eyring et al., 2010a; Austin et al., 2010a). These results indicate that, climate change will affect Arctic ozone abundances more than Antarctic ozone abundances (Eyring et al., 2010a) due to GHG-induced stratospheric cooling and changes

in transport (SPARC-CCMVal, 2010; Eyring et al., 2010a). Shepherd (2008) found that in a changing climate, the strengthening stratospheric circulation transports more ozone into the Arctic than into the Antarctic. Furthermore, the study by Shepherd (2008) suggest a dynamically-induced warming of the Arctic stratosphere in the future. A return of stratospheric ozone to 1960 values occurs around 2041 in the Arctic stratosphere (Eyring et al., 2010a) while Antarctic ozone returns to 1960 values shortly before the end of this century (SPARC-CCMVal, 2010; Austin et al., 2010a). These simulations, however, are based on only one GHG and one ODSs emissions scenario. Therefore, these simulations cannot account for the full range of uncertainties resulting from the range of possible GHG and ODSs scenarios.

In a second study, Eyring et al. (2010b) analyzed CCM simulations of the 21st century based on different GHG scenarios. Their results indicate that climate change plays a significant role in the evolution of ozone through the 21st century and has to be considered when projecting future stratospheric ozone abundances. They found that the impact of the different GHG scenarios on the ozone return dates is similar for the Antarctic, Arctic and mid latitudes, which vary by $\sim$10 years. This result indicates that the uncertainty in the ozone return dates arising from different GHG scenarios is comparable or smaller than the uncertainty related to the known model differences Eyring et al. (2010b). However, a range of CCM simulations using different GHG scenarios are required to derive a more solid conclusion.

Charlton-Perez et al. (2010) investigated the sources of uncertainty in projections of future stratospheric ozone abundances by separating the contributions from GHGs and the contributions from the differences in the CCMs. They concluded that for the first two thirds of the 21st century (until and after ozone returns to 1980 values) the differences between CCMs are a significant source of uncertainty regarding future ozone levels. Towards the end of this century, the uncertainty resulting from the different GHG scenarios is likely to be the dominant contributor to the uncertainty in the projections. However, the quantification of uncertainty in the ozone projections was not optimal as different models used different GHG scenarios.

The studies summarized above reveal that for an assessment of the uncertainty in ozone projections, more GHG sensitivity simulations need to be performed to untangle the uncertainties resulting from different models and from different GHG scenarios. As stated in Chapter 1, CCMs are computationally very demanding so that sensitivity studies of stratospheric ozone changes to changes in GHGs are limited. Atmosphere-ocean general circulation model (AOGCM) are designed to examine how changes in GHGs affect the global

climate system, thereby taking different GHG emissions scenarios as input. However, depending on the AOGCM, ozone concentrations are either set constant or are calculated off-line and then prescribed in the model simulations. Therefore, ozone concentrations are not affected by GHG-induced temperature changes. Consequently, the use of AOGCMs to investigate the sensitivity of ozone changes to changes in GHGs is precluded. However, temperature trends simulated by AOGCMs could be used to assess the sensitivity of ozone to changes in GHG emissions. As a complement to CCM studies, this chapter aims to test the applicability of semi-empirical models, using temperature trends based on different GHG emissions scenarios as simulated by a state-of-the-art AOGCM (the Hadley Centre coupled Model; HadCM3), to conduct fast and inexpensive projections of the future evolution of Antarctic ozone. Using the presented semi-empirical models to project future ozone abundances provide an approach that accounts for the effect of temperature changes on ozone which is currently missing in AOGCM simulations. The semi-empirical models describe the time rate of change in activated chlorine and its relation to ozone destruction in the Antarctic stratosphere. A first version of the semi-empirical models was developed by Huck (2007). In this chapter these semi-empirical models were modified and then applied to project the future evolution of chlorine and ozone depletion in the Antarctic stratosphere. Huck (2007) used the ozone mass deficit, defined as the mass of ozone destroyed everywhere over Antarctica with respect to 1980 background levels, as a metric to quantify Antarctic ozone depletion. In this chapter a new metric is introduced, $\Delta\overline{O_3}_{>70^\circ}$, which provides a direct measure of the change in ozone averaged over the Antarctic vortex core region, relative to 1960 (see below).

The semi-empirical models require daily values of $\mathrm{Cl_y}$, the amount of activated chlorine ($\mathrm{ClO_x}$), the vortex average extent of polar stratospheric clouds (PSCs) and solar illumination as inputs. To estimate the vortex coverage by PSCs, stratospheric temperatures are required. These were taken from the National Centers for Environmental Prediction and the National Center for Atmospheric Research (NCEP/NCAR) reanalyses for the period 1960 to 2009. Three simulations performed by HadCM3, based on the A1b, A2, and B1 GHG emissions scenarios, provided the stratospheric temperature trends used in this chapter to generate future temperature time series (Section 4.5.2) that were used to project future changes in Antarctic ozone. Besides the temperature trends, no additional meteorological fields from the model simulations of the future climate are required.

In the latest Assessment of ozone depletion (WMO, 2007) the return of ozone to pre-1980 levels was considered as one important milestone in the future development of Antarctic ozone. However, more recent CCM studies suggest than ozone depletion due to man-made ODSs occurred before 1980 (SPARC-CCMVal, 2010). Therefore, in this chapter,

the change in chlorine, and the change in ozone, through the 21st century is investigated with respect to a 1960 reference date. The assumption is made that ozone in 1960 was essentially unaffected by ODSs and the anthropogenic Cl_y concentration was set to zero. To provide a baseline for ozone against which a return to 1960 values can be assessed, a total column ozone background was derived by employing a regression model together with available ground-based and satellite-based ozone observations (Section 4.4.1).

This chapter is organized as follows: Section 4.2 gives a brief overview of the different GHG emissions scenarios, followed by a short description of the AOGCM used in this chapter. The two semi-empirical models employed are described thoroughly, together with the required input parameters in Section 4.3 and Section 4.4. The application of the semi-empirical models to project the future evolution of Antarctic chlorine and ozone is presented in Section 4.5. The derived results are compared with previous studies and discussed in Section 4.6, followed by a conclusion of this chapter in Section 4.7.

4.2 GHG emissions scenarios and AOGCM description

The state of knowledge of the future changes in the climate system due to human-induced perturbations (i.e. climate change) is summarized regularly in assessment reports published by the Intergovernmental Panel on Climate Change (IPCC). For the most recent Assessment Report (AR4 published, in 2007) 23 state-of-the-art AOGCM, produced comprehensive simulations of the past, present and future climate. In addition, different climate change scenarios based on different GHG emissions scenarios as defined by the IPCC Special Report on Emissions Scenarios (SRES) were used by all AOGCMs. The World Climate Research Programme (WCRP) organized a Coupled Model Intercomparison Project (CMIP) with the objective to collect and analyze the results from the simulations performed for the AR4 IPCC report, including the control run, 1% CO_2, and 20th-, 21st-, and 22nd-century. The CMIP multimodel dataset is collected, organized, and archived by the Program for Climate Model Diagnostics and Intercomparison (PCMDI).

In this chapter, simulation of the 21st century climate as performed by HadCM3 taking different emissions scenarios as input were used to investigate the effect of GHGs on the ozone return dates. The model data were downloaded from the WCRP CMIP3 multi-model dataset archived by PCMDI. This chapter concentrates on three GHG emissions scenarios, ranging from low to high GHG concentrations by the end of the 21st century (see below). As the emissions scenarios are described in detail in the IPCC SRES (Nakicènovic̀ and Swart, 2000), only a brief overview is given in the following section.

4.2.1 GHG emissions scenarios

The purpose of the different emissions scenarios is to explore alternative pathways for future changes in climate depending on future human activities, i.e. future GHG emissions. The scenarios are divided into four groups (A1, A2, B1 and B2), where A1 is subdivided into three additional groups, A1b, A1FI, A1T. Of these seven scenarios, three 'marker scenarios' (B2, A1b, and A2) where used in this chapter. The three scenarios were chosen as they provide the lowest, the medium and the highest concentration of GHGs by the end of the 21st. The scenarios are based on different assumptions on population growth, economic structures and technology development, resulting in different future GHG emissions scenarios. The projected future evolution of atmospheric CO_2 concentrations, corresponding to the three scenarios used in this study, are shown in Figure 4.1. The assumption that the CO_2 concentration reaches about 700 ppm by the end of the twenty-first century was made in SRES A1b. The CO_2 concentration is forced to increase to 820 ppm by 2100 in the A2 scenario. The lowest CO_2 concentration is obtained in the more ecologically friendly scenario B1, where concentrations of 550 ppm are reached by 2100. These three scenarios present different path ways for the future evolution of GHG concentrations that can be used to assess the question if the timing of the ozone return to historical levels depends on GHGs, i.e. if the ozone return is delayed, accelerated or not influenced at all by GHG emissions.

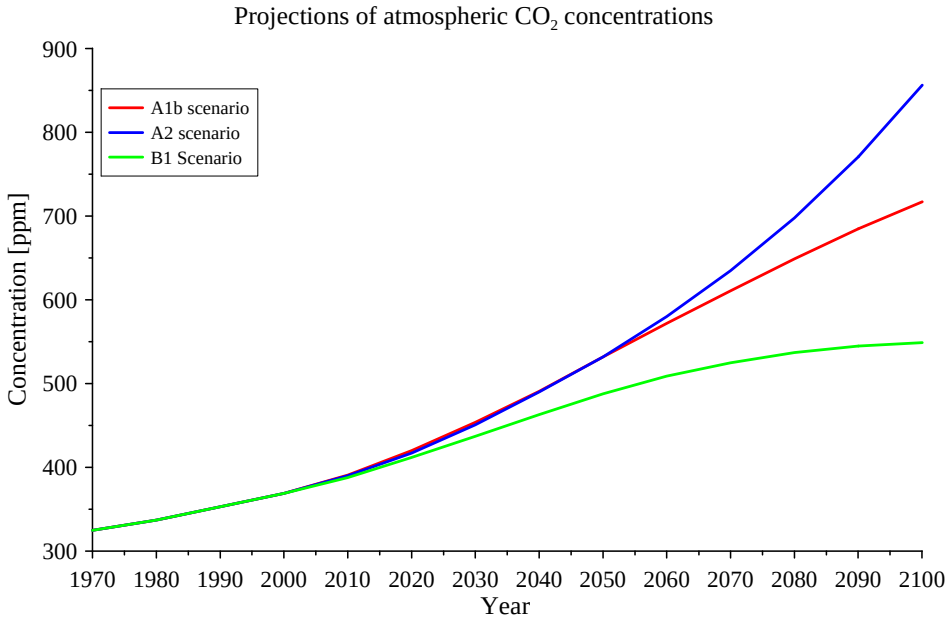

Figure 4.1: Future development of CO_2 concentrations for three GHG emissions scenarios.

4.2.2 Atmosphere-ozone general circulation model - HadCM3

In preparation for the IPCC AR4, the Hadley Centre performed climate change simulations based on different SRES scenarios using the Hadley Centre coupled Model (HadCM3). As the HadCM3 model is described in detail in Gordon et al. (2000), only a brief overview of the model is given in this section.

HadCM3 was modified and improved from the earlier model version HadCM2. The model was developed as a fully coupled ocean-atmosphere system, that does not need adjustments of the fluxes that couple the atmosphere to the oceans to prevent excessive climate drifts (Gordon et al., 2000). The spectral horizontal resolution of the atmospheric model component is T42, comparable to $2.5^\circ \times 3.75^\circ$ on a transformed longitude-latitude grid. In the vertical, the atmospheric component of the model consists of 19 layers, using hybrid vertical coordinates. The model extends in the vertical to approximately 5 hPa (~ 39 km). The radiative effects of minor GHGs, as well as $\mathrm{CO_2}$, water vapour and ozone, are represented by the radiative scheme incorporated in the model (Edwards and Slingo, 1996). The ocean component of HadCM3 has a horizontal resolution of $1.25^\circ \times 1.25^\circ$ on a longitude-latitude grid. The 20 layers in the vertical are distributed such that enhanced resolution close to the surface is obtained. For more information on HadCM3 see also Johns et al. (2003).

The climate change experiments using HadCM3 were made assuming all GHGs (such as $\mathrm{CO_2}$, $\mathrm{CH_4}$, $\mathrm{N_2O}$, and halocarbon species) are well mixed without any spatial variation. Tropospheric and stratospheric ozone trends were calculated off-line and separately on every model level as zonal averages. The stratospheric ozone concentrations, obtained as described below, are independent of the performed climate change experiment with HadCM3. The three-dimensional chemical transport model STOCHEM (Collins et al., 1997) was employed to calculate the tropospheric and stratospheric ozone trends for a selected number of years (1990, 2030, 2060 and 2100). These values were linearly interpolated to obtain the ozone trends for the intermediate years. The calculated ozone trends were then added to a baseline climatology following Li and Shine (1995) but with a number of alterations (Johns et al., 2003). Future stratospheric ozone abundances were estimated by assuming that chlorine and bromine concentrations are decreasing, following the Montreal Protocol. A simple box model is then used to calculate EESC concentrations ($\mathrm{EESC} = \mathrm{Cl} + 40 \times \mathrm{Br}$). Assuming that it takes three years for Cl and Br to get transported from the troposphere into the stratosphere, and assuming that dependence of ozone depletion on EESC is linear, the stratospheric ozone abundances can be calculated as a function of height, longitude and month (Johns et al., 2003). Within HadCM3, stratospheric ozone loss peaks in 2002. From 2060 onwards, stratospheric ozone concentrations should have stabilized to preindustrial

values. However, due to a software error in HadCM3, ozone continues to increase, resulting in a small positive forcing of $+0.17\,\mathrm{W/m^2}$ from stratospheric ozone at the end of the 21^{st} century (Johns et al., 2003).

4.3 Semi-empirical model for chlorine activation

The model approach to project future ozone changes presented in this chapter consists of two semi-empirical models. First a simple equation is needed to describe the vortex averaged time range of change of $\mathrm{ClO_x}$ before the amount $\mathrm{ClO_x}$ can be related to the vortex averaged time rate of change of ozone (Section 4.4). When calculating these vortex average values a constant location of the vortex edge is used as the future development of the Antarctic vortex is unknown and very uncertain. The latitude of 62° S is a valid proxy for the average location of the Antarctic vortex edge (Bodeker et al., 2002) and therefore the vortex averaged $\mathrm{ClO_x}$ abundances, the predictors, are calculated poleward of 62° S geographical latitude. On the other hand, to calculate vortex average ozone abundances, the vortex edge is places at 70° S equivalent latitude (see Appendix A for the definition of equivalent latitude). This equivalent latitude was taken as this chapter aims to project the change of vortex average ozone in the well mixed vortex core region. As a result, the poleward of 62° S true latitude $\mathrm{ClO_x}$ concentrations are used to predict the poleward of 70° S equivalent latitude ozone abundances (Section 4.4). The 70° S equivalent latitude vortex edge location for $\mathrm{ClO_x}$ could not be used in this chapter as the future potential vorticity fields, which are required to determine the equivalent latitudes, were not available. In a vortex average sense the assumption is made that the polar vortex air masses are well mixed and isolated from mid latitude air masses. It has been shown that transport or mixing of mid latitude air across the polar vortex edge is negligible (e.g. Knudsen et al., 1989; Rex et al., 2002; WMO, 2007) and does not affect significantly the chemical compositions when averaged over the polar vortex. As a result, the semi-empirical models do not account for horizontal mixing across the vortex edge.

The semi-empirical model for chlorine activation solves a first order differential equation that describes the time rate of change of activated chlorine, that is collectively described as $\mathrm{ClO_x}$. The change in $\mathrm{ClO_x}$ abundances depends on i) the total amount of available stratospheric chlorine ($\mathrm{Cl_y}$), ii) the extent of PSCs within the polar vortex, iii) solar illumination, and iv) the deactivation of $\mathrm{ClO_x}$ due to chemical reactions forming inert reservoir species. In the sunlit polar stratosphere, active chlorine in the form of Cl reacts rapidly with ozone. As a result, active chlorine compounds are mainly present in the form of chlorine monoxide (ClO) and its dimer, ClOOCl. Therefore, the total amount of activated chlorine can be ap-

proximated by $\mathrm{ClO_x} \simeq \mathrm{ClO} + 2 \times \mathrm{ClOOCl}$.

In the springtime polar stratosphere, activated chlorine is primarily in the form of ClO during the day (e.g. Brasseur and Solomon, 2005) and day-time measurements of ClO can be used as an approximation of day-time $\mathrm{ClO_x}$ abundances. During night-time, when the photolysis is negligible, ClOOCl is the most abundant active chlorine species.

The sinks for stratospheric $\mathrm{ClO_x}$ are reactions of ClO with $\mathrm{NO_2}$ or $\mathrm{HO_2}$, or reactions involving chlorine atoms and methane, forming inactive chlorine reservoir species as described in Chapter 1. During wintertime, $\mathrm{NO_2}$ is tied up as $\mathrm{HNO_3}$ in PSC particles, leading to an enhancement of ClO levels. Therefore, the rate at which the reservoir species $\mathrm{ClONO_2}$ is formed is limited by the chemical loss processes of $\mathrm{HNO_3}$. During the course of the season, as stratospheric temperatures increase, PSCs evaporate and chlorine is no longer re-activated, resulting in a decrease in stratospheric $\mathrm{ClO_x}$ abundances.

The evolution of day-time $\mathrm{ClO_x}$ abundances on a given pressure surface can be described by a first order differential equation in the form of:

$$\frac{d\mathrm{ClO_x}}{dt} = \alpha \cdot \left((\mathrm{Cl_y} - \mathrm{Cl_{y_{1960}}}) - \mathrm{ClO_x}\right) \cdot FAP \cdot FAS - \beta \cdot \mathrm{ClO_x} \cdot (1 - FAP) \quad (4.1)$$

where α and β are fit-coefficients derived by fitting equation 4.1 to observations of ClO (assuming $\mathrm{ClO_x} \approx \mathrm{ClO}$) as described in Section 4.3.3. $\mathrm{Cl_y}$ concentrations were derived as described in Newman et al. (2006) and were provided by P. Newman. The approach by Newman et al. (2006) requires information about the mean age-of-air and the age-of-air spectrum width. For this study, the calculation of $\mathrm{Cl_y}$ is based on the assumption that the mean age-of-air is 5.5 years and the age-of-air spectrum width of 2.75 years is prescribed. $\mathrm{Cl_{y_{1960}}}$ in equation 4.1, refers to the total stratospheric chlorine loading in 1960, which is the reference date for all the calculations performed in this chapter (see Section 4.1). Therefore, the 1960 $\mathrm{Cl_y}$ abundances were subtracted from the $\mathrm{Cl_y}$ time series, assuming that ozone was not affected by anthropogenic chlorine compounds at that time. Hence, the rate of change of $\mathrm{ClO_x}$ is calculated with respect to its 1960 background. FAP in equation 4.1 is the fractional area of the vortex covered with PSCs and is derived from stratospheric temperature fields (see Section 4.3.1). Chlorine activation requires sunlight and therefore the amount of available sunlight is characterized by FAS, the fractional area of the vortex that is exposed to sunlight (details see Section 4.3.2).

The first term on the right hand side of equation 4.1 describes the conversion of $\mathrm{Cl_y}$ to $\mathrm{ClO_x}$ which depends on the total amount of stratospheric chlorine, the occurrence of PSCs

to convert inert reservoir species, and on solar exposure of the polar vortex for photodissociation. The second term describes ClO_x deactivation that accounts for the release of NO_2 as soon as PSCs sublimate and HNO_3 in its gas-form is available for photodissociation. However, sedimentation of HNO_3 containing particles (denitrification) presents a permanent loss of NO_x. Therefore, the chlorine deactivation path via HCl becomes more important then the deactivation via $ClONO_2$ in the Antarctic stratosphere. This might lead to imperfect fitting of the deactivation term (β coefficient) in equation 4.1.

4.3.1 Calculation of FAP

The fractional area of the polar vortex that is covered with PSCs (FAP) was derived from temperature fields that were taken from the NCEP/NCAR reanalyses for the historical period (1980 to 2009). To calculate future FAP time series, future temperature fields were generated that account for the temperature trends from three climate change experiments simulated by HadCM3 (details are given in Section 4.5.2). These stratospheric temperature fields were then used to calculate FAP values on a given pressure surface. First, the PSC area within the polar vortex (referred to as PSC_{area}) was determined by summing the areas of grid boxes between 62°S and 90°S (as mentioned above an average vortex edge location of 62°S was used) where the temperature falls below a threshold of T_{NAT}=195 K. T_{NAT} of 195 K provides an approximate estimate for the threshold that describes type I PSCs occurrence and the onset of heterogeneous processes (Chapter 1). Dividing the derived PSC_{area} by the constant vortex area (area between 62°S and 90°S):

$$FAP = \frac{PSC_{area}}{Vortex_{area}} \tag{4.2}$$

results in the required FAP values at a given pressure surface. FAP values vary between 0 and 1; if the vortex is completely covered with PSCs, FAP is equal 1 and if no PSCs are formed, FAP will be equal to zero.

4.3.2 Calculation of FAS

The available sunlight for photochemical processes is described by FAS which is defined as the fractional area of the polar vortex that is exposed to sunlight. The solar zenith angle (SZA) is used to determine the availability of sunlight for chlorine activation. At Earth's surface, SZA$<$90° indicates that the sun is above the horizon. In the upper atmosphere, however, sunlight is available for SZA greater than 90° due to refraction and scattering of the incident solar radiation. Therefore, to determine the regions of the polar vortex exposed

to sunlight (referred to as $\mathrm{Sun_{area}}$), SZA<95° was used to determine whether an area is exposed to sunlight or not. Similar to FAP, $\mathrm{Sun_{area}}$ is calculated by summing up the areas of grid boxes (0.1×0.1°) between 62°S and 90°S where SZA <95°. The SZA and therefore the $\mathrm{Sun_{area}}$, was determined for every grid box at every minute of the day. $\mathrm{Sun_{area}}$ is then divided by the total vortex area:

$$FAS = \frac{\mathrm{Sun_{area}}}{\mathrm{Vortex_{area}}} \tag{4.3}$$

By averaging the derived FAS values over each 24 hour period, daily FAS values were obtained. Because the vortex area is assumed to not change through the year or from year to year, FAS is the same for every year of the analysis. The calculated daily FAS values are shown in Figure 4.2. Similar to FAP, FAS varies between 0 and 1; if the whole vortex area is exposed to sunlight, FAS will be 1 and if the polar vortex is in complete darkness for 24 hours, FAS will be zero.

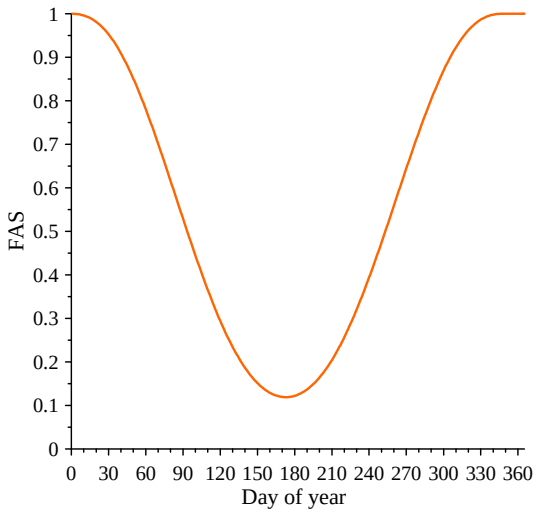

Figure 4.2: Daily values of the fractional area of the polar vortex that is exposed to sunlight (FAS).

4.3.3 Determination of $\mathrm{ClO_x}$ model fit-coefficients

The fit-coefficients α and β were derived by fitting the $\mathrm{ClO_x}$ semi-empirical model (equation 4.1), with the required inputs of FAP, FAS, and $\mathrm{Cl_y}$, to day-time ClO measurements. In this chapter, Antarctic ClO measurements from the Microwave Limb Sounder (MLS) onboard the Upper Atmosphere Research Satellite (UARS, see Chapter 2) were used to train the $\mathrm{ClO_x}$ model. Midday ClO abundances, averaged over the polar vortex, on the 520 K surface, were provided by M. Santee for the period 1992 to 1997. Only measurements made

between 11:00 and 14:00 local solar time with a SZA smaller than 88° were included in the vortex mean amounts. The measurements, used here, are described in detail in Santee et al. (2003). The Antarctic ClO measurements from MLS onboard Aura (Chapter 2) could not be used for this chapter as Antarctic ClO measurements are always made in the late afternoon (17:00 local solar time). Therefore, the assumption that $\mathrm{ClO_x}$ can be approximated by ClO day-time measurements would no longer be valid, as in the afternoon, at higher SZA, $\mathrm{ClO_x}$ is also present in the form of ClOOCl.

The aim of this chapter is to derive vortex average $\mathrm{ClO_x}$ concentrations on 8 pressure levels (200, 150, 100, 70, 50, 30, 20 and 10 hPa) corresponding to altitudes between ∼12 and 30 km. The 12 to 30 km altitude range was chosen to cover the range where most PSCs occur (Brasseur and Solomon, 2005). However, as ClO observations provided on the 520 K potential temperature surface were the only measurements available, the fit-coefficients α and β were derived for one altitude level only. Assuming that the coefficients are altitude independent, these coefficients were then applied to the remaining 7 pressure levels (see below). Tests, where output from a CCM was used to derive these fit-coefficients, showed this assumption is valid as only small differences in the fit-coefficients were derived.

The 50 hPa pressure surface is the closest pressure level to the 520 K potential temperature surface. Therefore, daily FAP values were derived from the daily mean NCEP/NCAR stratospheric temperature fields at 50 hPa by applying equation 4.2. A fourth order Runge-Kutta method (Press et al., 2007) was used to solve the first order differential equation describing the temporal evolution of $\mathrm{ClO_x}$ (equation 4.1). A combination of interval halving and least squares fitting, that minimizes the sum of the square of the residuals, was used to find the best set of parameters that optimally fits the ClO measurements. The aim of the fitting procedure is to derive the α and β fit-coefficients so that the solution of equation 4.1, best describes the ClO measurements (assuming $\mathrm{ClO_x} \simeq \mathrm{ClO}$). To determine these coefficients, a mapping procedure is applied (interval halving), where a reasonable estimate of starting values α_i and β_j and a step size $\Delta\alpha_i$ and $\Delta\beta_j$ are made. In this study, the coefficients are incremented by $\pm 2\Delta\alpha_i$, and $\pm\Delta\alpha_i$ and by $\pm 2\Delta\beta_j$, and $\pm\Delta\beta_j$, respectively. This results in ten different starting values for α and β (e.g. [α_i,β_j], [$\alpha_i + \Delta\alpha_i$,$\beta_j$], [$\alpha_i$,$\beta_j + \Delta\beta_j$], [$\alpha_i + \Delta\alpha_i$], [$\beta_j - \Delta\beta_j$]...). For each of the 25 combinations of [α_i, β_j] equation 4.1 is solved using the Runge-Kutta method and χ^2 is calculated as:

$$\chi^2 = \sum [\mathrm{ClO_{meas}} - \mathrm{ClO_{xmodel}}(\alpha_i, \beta_j)]^2 \tag{4.4}$$

The combination of α_i and β_j which results in the smallest χ^2 value is then used in the next iteration as new starting parameters, where the step sizes $\Delta\alpha_i$ and $\Delta\beta_j$ are reduced by 20%. This procedure is iterated up to 100 times, until the minimum of χ^2 is found with the

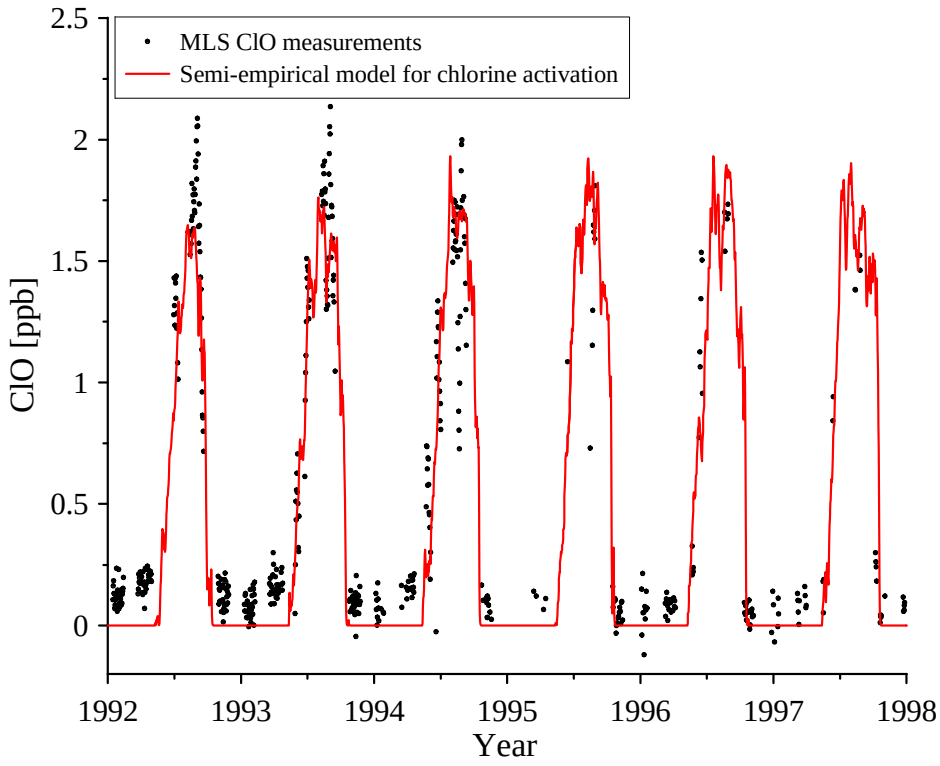

Figure 4.3: ClO measurements and the best semi-empirical model fit.

corresponding parameters α_i and β_j. The derived fit-coefficients α_i and β_j then represent the best set of parameters that reproduce the measurements.

The values for α and β derived in this way are 3.3767 and 1.2461, respectively. The ClO measurements together with the $\mathrm{ClO_x}$ abundances modelled by the first semi-empirical model using the derived fit-coefficients, are shown in Figure 4.3 for the period 1992-1997. The model reproduces the ClO measurements fairly well with a root mean square (RMS) of the differences between the ClO measurements and modelled $\mathrm{ClO_x}$ abundances of 0.2466 ppb. Therefore, the activation and deactivation of chlorine is captured well by the model and the derived fit-coefficients can be used to calculate $\mathrm{ClO_x}$ abundances for the observation period 1960 to 2009 and to project future chlorine levels for the period 2010 to 2100 (Section 4.5).

4.4 Semi-empirical model for the change in ozone

The total amount of activated chlorine within a partial column extending from 200 hPa to 10 hPa was derived from modelled vortex mean $\mathrm{ClO_x}$ time series (see below) calculated for every pressure level (200, 150, 100, 70, 50, 30, 20 and 10 hPa) by applying equation

4.1 and then related to the time rate of change of ozone by a second semi-empirical model. As stated above, the vortex averaged ozone is calculated within the area poleward of 70° S equivalent latitude (referred to as $\overline{O_3}_{>70^\circ}$) and the change in the vortex averaged ozone is hereafter denoted as $\Delta\overline{O_3}_{>70^\circ}$. The semi-empirical model consists of two terms, one describing ozone destruction due to catalytic cycles involving active chlorine compounds and the other describing in-situ production through the Chapman chemistry:

$$\frac{d\Delta\overline{O_3}_{>70^\circ}}{dt} = \underbrace{[A \cdot MAC^2 + B \cdot MAC] \times (1 - R)}_{\text{ozone destruction}} - \underbrace{C \cdot \Delta\overline{O_3}_{>70^\circ} \cdot F_{act}}_{\text{ozone production}} \tag{4.5}$$

where A, B, and C are the fit-coefficients that are derived by fitting the equation to observations of $\Delta\overline{O_3}_{>70^\circ}$. $\Delta\overline{O_3}_{>70^\circ}$ in DU is the ozone change with respect to 1960 ozone abundances ($\Delta\overline{O_3}_{>70^\circ} = \overline{O_3}^{1960}_{>70^\circ} - \overline{O_3}^{year}_{>70^\circ}$; see Section 4.4.1).

MAC in equation 4.5 is the total mass of activated chlorine in kg. To calculate MAC, first, the mass of chlorine ($\mathrm{mass_{Cl}}$) is calculated for every layer between the given pressure levels:

$$\mathrm{mass_{Cl}} = \mathrm{ClO_x} \cdot \frac{M_{Cl}}{M_{air}} \cdot A \cdot [p_2 - p_1] \cdot \frac{1}{g} \tag{4.6}$$

where $\mathrm{ClO_x}$ is the modelled $\mathrm{ClO_x}$ mixing ratio between pressure level p_1 and p_2 given in pascals, M_{Cl} is the molecular mass of chlorine (35.45 g mol^{-1}), M_{air} is the molecular mass of dry air (around 29 g mol^{-1}), A is the area of the polar vortex in m^2 and g is the gravitational acceleration of the Earth (9.81 m s^{-2}). Summing the mass of chlorine over all 7 layers, results in the total mass of chlorine (referred to as $\mathrm{TotalMass_{Cl}}$) within the partial column extending from 200 hPa to 10 hPa. In making this calculation the assumption was made that $\mathrm{ClO_x}$ is equally distributed over the whole polar vortex. However, since sunlight is essential to activate chlorine the total mass of activated chlorine is calculated by multiplying the total mass of chlorine by FAS. MAC is then given by:

$$MAC = \mathrm{TotalMass_{Cl}} \cdot FAS \tag{4.7}$$

The term $(1 - R)$ in equation 4.5, with $R = \frac{\Delta\overline{O_3}_{>70^\circ}}{\overline{O_3}^{1960}_{>70^\circ} - 150}$, accounts for saturation effects. This term will be zero if ozone is destroyed completely within the partial column where activated chlorine is found. Below and above this partial column ozone is not depleted and therefore, the total column ozone abundance averaged over the polar vortex cannot get smaller than 150 DU, which is the lowest estimated vortex average ozone determined by Bodeker et al. (2002). Therefore, $\Delta\overline{O_3}_{>70^\circ}$ is limited to values smaller than or equal to ($\overline{O_3}^{1960}_{>70^\circ} - 150$). Furthermore, the saturation term $(1 - R)$ restrains the ozone depletion. Despite the fact that ozone is destroyed immediately within each grid box when chlorine is available, ozone is

destroyed more slowly if the vortex average amount of ozone is considered, as there are grid cells within the vortex where no chlorine is present and therefore, no ozone destruction takes place within that grid cell. Both grid cells with and without chlorine have to be accounted for when considering vortex average ozone loss.

F_{act} in equation 4.5 is an approximation for the time rate of change of ozone resulting from the in-situ production via the Chapman chemistry (Chapter 1). The actinic flux is the quantity of light available to molecules at a particular location for absorption and photodissociation. To calculate the actinic flux, first the area of the polar vortex exposed to sunlight (SZA<=90°) was determined and is denoted as $\mathrm{Sun}_{\mathrm{area}}$. The actinic flux of the direct solar irradiance can then be approximated by:

$$F_{act} = \cos(SZA) \times e^{(\frac{-1}{\cos(SZA)})} \times \mathrm{Sun}_{\mathrm{area}} \tag{4.8}$$

where the solar irradiance incident at the top of the atmosphere scales as $\cos(SZA)$ and the air mass, that describes the optical path length through Earth's atmosphere, is approximated by $1/\cos(SZA)$ for small SZA. In this chapter, equation 4.8 is applied to larger SZA so that the approximation for the optical path length introduces some uncertainties. However, these uncertainties are minimal. Furthermore, for the use of F_{act} in equation 4.5 it is assumed that F_{act} is unitless as the fit-coefficients are accounting for any type scalings. As the polar vortex area is a constant, the actinic flux is the same for every year of the analysis period. The daily F_{act} values as derived in this chapter are shown in Figure 4.4.

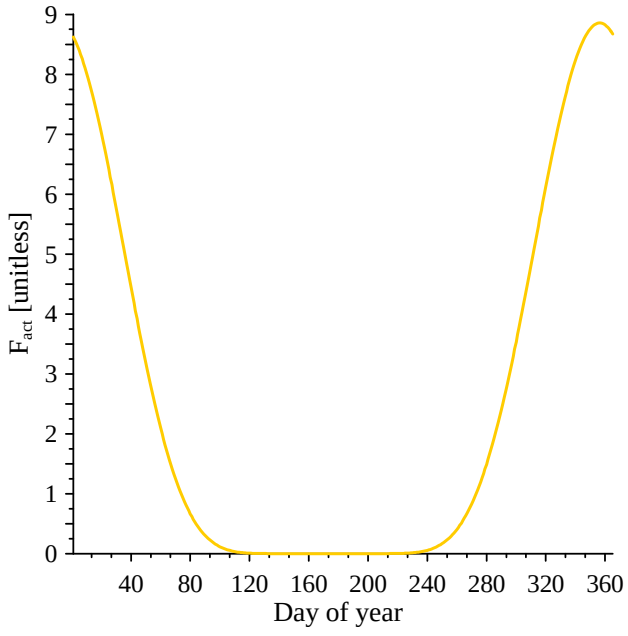

Figure 4.4: Daily F_{act} values used as an approximation for in-situ ozone production.

The time rate of change of ozone is equal to the rate limiting time steps of the catalytic destruction cycles (Anderson et al., 1991). The ClO-dimer cycle (Chapter 1 and 3) is the dominant contributor to the overall ozone loss, followed by the ClO-BrO catalytic cycle (Chapter 1). The catalytic cycle involving ClO and $\mathrm{HO_2}$ and the cycle involving ClO and O represent a minor loss of ozone in the Antarctic lower stratosphere as each of those cycle contributes less than 5% to the total loss of ozone (Anderson et al., 1991; Salawitch et al., 1993). Barrett et al. (1988) and Salawitch et al. (1993) show that the rate limiting time step of the ClO-dimer cycle is the dimer formation rate, and that the rate of ozone destruction is therefore given by:

$$\frac{d[O_3]}{dt} = -2k[ClO]^2[M] \tag{4.9}$$

where the terms in brackets denote concentrations, $[M]$ is the air density and k is the dimer formation rate. Therefore, the effect of the ClO-dimer cycle on ozone is quadratic in ClO. However, more recent study by Harris et al. (2010) state that a nearly linear relationship between ozone loss and $\mathrm{ClO_x}$ exist. Therefore, to account for both, the linear and quadratic dependence are included in the semi-empirical model (equation 4.5) and the fit-coefficients A and B provide the information of the degree of the linear or quadratic dependence of ozone on activated chlorine.

The semi-empirical model for the change in ozone was fitted to observations of $\Delta\overline{O_3}_{>70^\circ}$ for the period 1980 to 2009 to derive the fit-coefficients A, B, and C (see Section 4.4.1). To derive $\Delta\overline{O_3}_{>70^\circ}$ values, the 1960 ozone background has to be determined and this is described in the following section, before the fitting method and the derived fit-coefficients are presented.

4.4.1 Calculation of 1960 ozone baseline

In this analysis we require a measure of Antarctic ozone depletion that is referenced to a time when ozone was not significantly affected by anthropogenic enhancement of stratospheric halogens. Specifically we want to quantify the degree to which ozone has changed from levels typically of 1960, i.e. this 1960 baseline needs to be representative of the ozone climatology around 1960. This is functionally equivalent to determining 1960 Antarctic vortex average ozone abundances when the temperature is neither anomalously warm nor anomalously cold. To quantify this baseline a regression model was employed to untangle the contribution of chlorine-induced ozone changes and of temperature-induced ozone changes to the overall change in ozone. The regression model is regressed against vortex averaged ground-based and satellite-based total column ozone abundances for the period 1960 to 2009. The calculation of the vortex average total column ozone from the

observations is described in the following before the regression model is introduced.

The first long-term comprehensive observations of Antarctic total column ozone abundances became available from satellite-based measurements in late 1978. Before that, only sporadic ground-based measurements of ozone were made at different locations in the Antarctic using Dobson and Brewer spectrophotometers. These sparse ozone measurements cannot be used on their own as an estimate of total column ozone abundances within the polar vortex in the period before satellite-based measurements were available (1960 to 1978). If the available Antarctic ground-based measurements would be used as representative vortex averaged ozone abundances from 1960 to 1978 a large sampling bias would be introduced. Therefore, an approach was developed to derive an estimate for the vortex averaged ozone abundances from 1960 and 1978, using the ground-based measurements but also the satellite-based measurements from 1978 onwards (more details are given below). The calculation of the vortex averaged ozone abundances derived from satellite-based measurements is described in the following before the approach which was used derived an estimate for vortex averaged ozone values from 1960 to 1978 is presented as the satellite-based measurements are required to derive this estimate.

As stated in Section 4.3, the area poleward of 70° equivalent latitude was taken to represent the well mixed stratospheric air of the inner vortex that is subject to the severe Antarctic ozone depletion. Therefore, for the area poleward of 70° S equivalent latitude, the total column ozone area weighted mean was calculated from daily satellite-based total column ozone measurements from 1979 to 2009. The vortex average total column ozone abundance is hereafter denoted by $\overline{O_{3>70^\circ}}$. The total column ozone measurements were taken from a combined total column ozone data-base, which is described in detail in Bodeker et al. (2005). Briefly, the data-base combines measurements from a number of different satellite-based instruments such as the Total Ozone Mapping Spectrometer (TOMS) instruments, retrievals from the Global Ozone Monitoring Experiment (GOME) instruments, Solar Backscatter Ultra Violet (SBUV) instruments and data from the Ozone Monitoring Instrument (OMI). Offset and drifts between the different datasets have been removed through comparisons with the global ground-based World Ozone and Ultraviolet Data Center (WOUDC) Dobson and Brewer spectrophotometer network. This results in a global homogeneous total column ozone data set that combines the advantages of good spatial coverage from satellite measurements with the long-term stability of ground-based measurements Struthers et al. (2009).

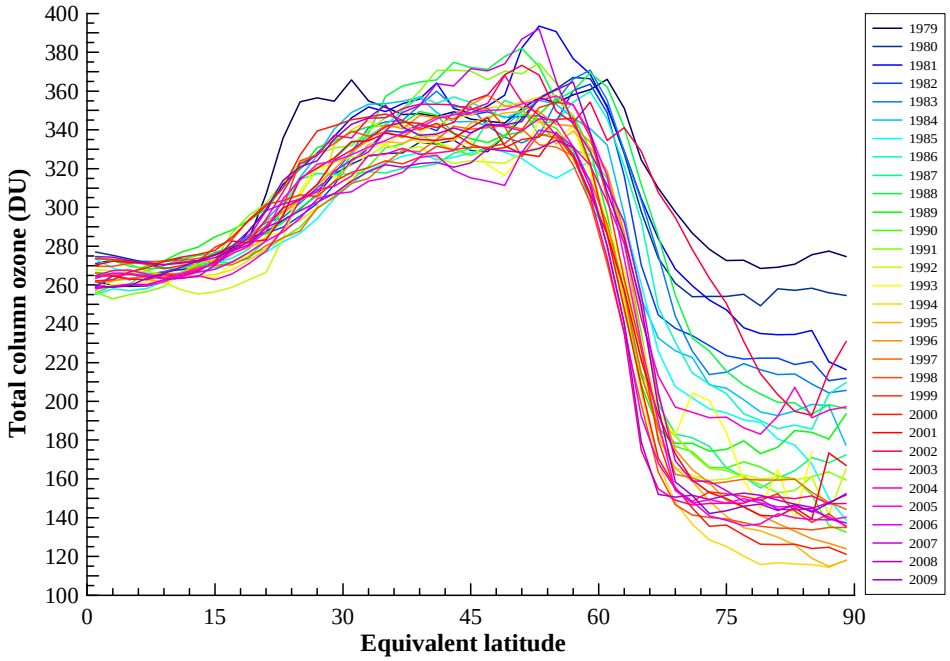

Figure 4.5: Zonal mean total column ozone as a function of equivalent latitude for 1 October of the years 1979 to 2009 derived from a combined total column ozone data-base Bodeker et al. (2005).

To calculate the daily $\overline{O_{3>70^\circ}}$ values, equivalent latitude is used to determine if the measurements were made inside or outside of the polar vortex. The equivalent latitude coordinates were derived from the potential vorticity (PV) fields on the 550 K potential temperature surface as described in detail in Appendix A, resulting in a PV versus equivalent latitude relationship. The required PV fields were taken from the NCEP/NCAR reanalyses. Before the area weighted total column ozone mean is calculated, the ozone measurements extracted from the total column ozone data-base were remapped from a longitude/latitude coordinate system into an equivalent latitude coordinate system. The PV value at 550 K potential temperature surface is extracted using bilinear interpolation from the NCEP/NCAR fields at the location of the ozone measurement. Given the PV value, the associated equivalent latitude can be determined from the PV versus equivalent latitude relationship. Applying this method, the equivalent latitude corresponding to the daily total column ozone measurements can be determined. Then, the total column ozone measurements were averaged along each equivalent latitude. As an example, total column ozone zonal mean by equivalent latitude are shown in Figure 4.5 for each 1 October of the years 1979 to 2009.

Using the described method, daily $\overline{O_{3>70^\circ}}$ were calculated for the period 1979 to 2009. Unfortunately, there are missing total column ozone measurements poleward of 70° S equivalent latitude on some days. Especially during polar night and if the polar vortex is centered around the pole, no satellite-based or ground-based spectroscopic measurements can

be made at the higher equivalent latitudes due to the lack of sunlight. If the area weighted mean was calculated using only the available ozone measurements poleward of 70° S equivalent latitude, for example, if only two measurements out of 10 are available, a sampling bias would likely be introduced. Therefore, in case of missing measurements poleward of 70° S equivalent latitude a bias correction was applied. First, the monthly mean meridional profile of ozone by equivalent latitude was calculated. However, monthly mean values also suffer from spatial sampling bias. To correct for this, it is assumed that if the monthly mean ozone values have an anomaly of some DU with respect to the climatological mean for the period 1979 to 2009 at equivalent latitude i, then this monthly mean anomaly holds at all equivalent latitudes poleward of i. Therefore, the climatological mean for every month for every equivalent latitude was calculated. If the monthly mean total column ozone is not available at a given equivalent latitude i, the ozone anomaly (i.e. deviation from the climatological mean) is calculated for the monthly mean at equivalent latitude $i-1$. The calculated anomaly is then added to the climatological mean at equivalent latitude i and to all equivalent latitudes poleward of i. This procedure is applied to every missing monthly mean value within the analysis period, resulting in a complete data set of monthly mean total column ozone values. This complete monthly mean data set can then be used for the spatial sampling bias correction of the daily data. A correction factor (F_c), using the filled monthly mean total column ozone data set was calculated:

$$F_c = \frac{\overline{M}^{mo}_{y,incomplete}}{\overline{M}^{mo}_{y,complete}} \tag{4.10}$$

where $\overline{M}^{mo}_{y,incomplete}$ refers to the area weighted mean calculated by sampling the monthly mean meridional profile only at those equivalent latitudes where daily data are available. The term $\overline{M}^{mo}_{y,complete}$ refers to the area weighted mean calculated using the complete monthly mean total column ozone data set. This correction factor is then applied to the area weighted total column ozone mean on days where data gaps poleward of 70° S equivalent latitude exist. Applying this correction results in a filled daily data set of $\overline{O_3}_{>70^\circ}$.

Antarctic ground-based measurements

As stated above, to generate $\overline{O_3}_{>70^\circ}$ values for the period 1960-1978 only sporadic ground-based total column ozone measurements made in the Antarctic are available. These measurements cannot be used on their own to represent $\overline{O_3}_{>70^\circ}$ as there are only a few measurements per day from available, sometimes even none and therefore an large sampling bias would be introduced when averaging measured ozone abundances over the vortex area. However, they can be used, as described below, to estimate of how much more or less ozone was observed before comprehensive satellite measurements were available. In this chapter,

Brewer and Dobson measurements from 8 Antarctic stations (see Table 4.1) which were provided by WOUDC, were used to derive an estimate of $\overline{O_3}_{>70^\circ}$ for the period before satellite measurements were available. The method of how the estimate was obtained is illustrated in Figure 4.6 and is described below.

Antarctic station	Latitude	Longitude
Admundsen Scott (South Pole)	90° S	0° W
Byrd	80° S	120° W
Halley	75.4° S	26.3° W
Hallet	72.2° S	170.1° E
Base King Baudouin	70.5° S	24.3° E
Syowa	69° S	39.4° E
Faraday/Vernadsy	65.2° S	64.2° W
King George Island	62° S	58.2° W

Table 4.1: Antarctic stations from which ground-based total column ozone measurements were used in this chapter.

First, the equivalent latitude of each total column ozone measurement at each of the 8 Antarctic stations was calculated in the same manner as for the satellite-based measurements. To estimate the ozone amount inside the vortex, only Antarctic measurements made poleward of 65° S equivalent latitude were used. Furthermore, if more than one ozone measurement per station and day was available, the daily total column ozone mean was calculated.

To generate $\overline{O_3}_{>70^\circ}$ for e.g. 1 October 1960, the Antarctic measurements on that day made at equivalent latitudes poleward of 65° S were used to estimate of how much more or less ozone was observed than in a chosen 'target year'. The target year was picked from the 1979 to 2009 period where satellite-based measurements exist, under two conditions. The first condition is that the calculated $\overline{O_3}_{>70^\circ}$ derived from satellite measurements on e.g. 1 October must exist and secondly, the total column ozone satellite-based measurements at the same equivalent latitude of total column ozone measurement from the Antarctic station must be available. For example, if there are three Antarctic measurements available on 1 October 1960 (black crossed in Figure 4.6) and the picked target year is 1980 (solid line in Figure 4.6) then the deviation between the Antarctic ground-based measurements and the satellite-based measurements at the same equivalent latitude made in 1980 (orange dots in Figure 4.6) is calculated. The mean deviation of these three measurements is then added to $\overline{O_3}_{>70^\circ}$ of the target year 1980, resulting in an estimate of the $\overline{O_3}_{>70^\circ}$ for the 1$^{\mathrm{st}}$ October 1960. This method was applied to estimate $\overline{O_3}_{>70^\circ}$ for every day from 1960 to 1978.

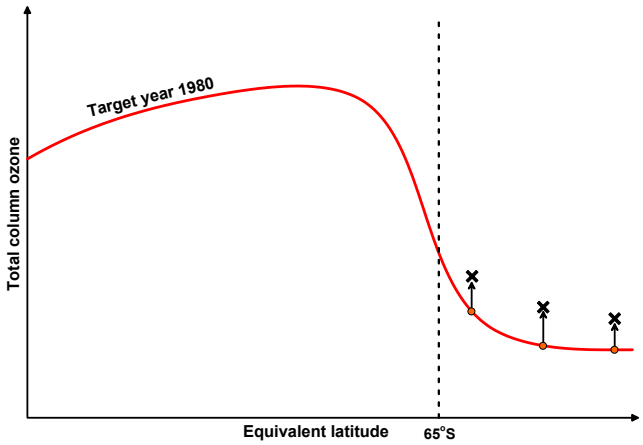

Figure 4.6: Schematic to illustrate how the Antarctic ground-based measurements (black crosses) were used to estimate $\overline{O_{3>70^\circ}}$ before 1979 (for details see text).

Regression model

This filled time series of daily $\overline{O_{3>70^\circ}}$ for the period 1960 to 2009 is then used to estimate the ozone abundances that represent 1960 ozone values by employing a regression model. Similar to the ozone loss semi-empirical model (equation 4.5) a quadratic and linear dependence of ozone depletion on chlorine, here represented by $\mathrm{Cl_y}$, is included in the regression model. Furthermore, the model accounts for temperature-induced changes in ozone. Using the regression model allows the separation of the contribution of chemistry-induced changes from contribution of temperature-induced changes to the overall evolution of ozone and therefore, the 1960 $\overline{O_{3>70^\circ}}$ baseline representing ozone values irrespective of wether 1960 was anomalously warm or cold. The regression model is formulated as:

$$O_3 = A \times Cl_y^2 + B \times Cl_y + C \times T' + D \tag{4.11}$$

where the fit-coefficients (A, B, C, and D) were determined independently for every day of the year. These fit-coefficients, the total amount of chlorine ($\mathrm{Cl_y}$) and the temperature anomaly (T'), calculated by subtracting the annual mean temperature (1960-2009) from the area mean temperature for a given day of a given year, are assumed to describe the evolution $\overline{O_{3>70^\circ}}$ from 1960 to 2009. It might be noted, that when applying the regression model fit to the observations, the estimated $\overline{O_{3>70^\circ}}$ between 1960 and 1978 are assigned lower weights than the $\overline{O_{3>70^\circ}}$ values derived from satellite measurements (from 1979 onwards).

The fit-coefficients derived for every day of the year are shown in Figure 4.7. The non-zero value of A indicates a non-linear dependence of ozone on $\mathrm{Cl_y}$. The primarily positive A coefficient counteracts the ozone depletion induced by chlorine compounds suggesting that the dependence of ozone on $\mathrm{Cl_y}$ is less than linear. Especially during winter, where the

severe ozone depletion occurs (between day ∼240 and ∼280), the A coefficient reaches its maximum. A test where the $\mathrm{Cl_y}$ concentrations between 1990 and 2010 were reduced showed that the dependence of ozone on $\mathrm{Cl_y}$ gets less than linear due to the saturation effect, i.e. ozone is destroyed almost completely. Therefore, no matter how much chlorine gets activated, no additional ozone will be depleted. The period 1990 to 2010 was chosen as this is where $\mathrm{Cl_y}$ maximized. The B coefficient is primarily negative, indicating the linear dependence of ozone on the chlorine compounds.

The temperature-induced change in ozone is represented by the fit-coefficient C. Dynamical-induces ozone changes (transport) and natural-induced changes in ozone (e.g. solar cycle, and volcanic eruptions) are accounted for in the fit-coefficient C as long as these disturbances are reflected in the temperature, i.e. volcanic eruptions lead to a stratospheric cooling and therefore enhanced ozone depletion. Therefore, the third term on the right hand side of equation 4.11 represents a proxy for dynamical and natural processes. The C coefficients are mainly positive until day 346 (around 12 December), i.e. ozone responds to temperature as expected, i.e. lower temperatures result in less ozone.

The D fit-coefficient represents the 1960 ozone that would have been available if $\mathrm{Cl_y}$ concentrations were zero in that year.

The regression model fit to the measured $\overline{O_3}_{>70^\circ}$ time series for 1 October is shown as an example in Figure 4.8. $\overline{O_3}_{>70^\circ}$ decreased by ∼160 DU over a ∼50 year period. The regression model tracks the changes in ozone fairly well for the period 1979-2009. Because less confidence lies in estimated $\overline{O_3}_{>70^\circ}$ abundances from 1960 to 1978, these values act only as a guide for the regression model and the model does not aim to track the variability in these $\overline{O_3}_{>70^\circ}$ exactly.

The question stated above of how much ozone would have existed in 1960, irrespective of wether it was a warm or cold year (C=0), can now be answered by calculating the 1960 ozone values using the derived fit-coefficients A, B, and D, together with the given amount of $\mathrm{Cl_y}$ in 1960. These daily total column ozone values are representative for the vortex average ozone abundances in 1960 ($\overline{O_3}^{1960}_{>70^\circ}$) and are referred to as the 1960 ozone baseline (black line in Figure 4.9). The $\overline{O_3}^{1960}_{>70^\circ}$ show a clear annual cycle but with short-term variability. Towards the end of the year ozone increases from around 340 DU to about 400 DU which is unrealistic and cannot be explained with any chemical process. To reduce the physically unrealistic intra-annual variability, a 2^{nd} order Fourier expansion to the daily values was used to create the smoothed time series shown as a red trace in Figure 4.9. Ozone departures from the 1960 baseline are then calculated independently for each

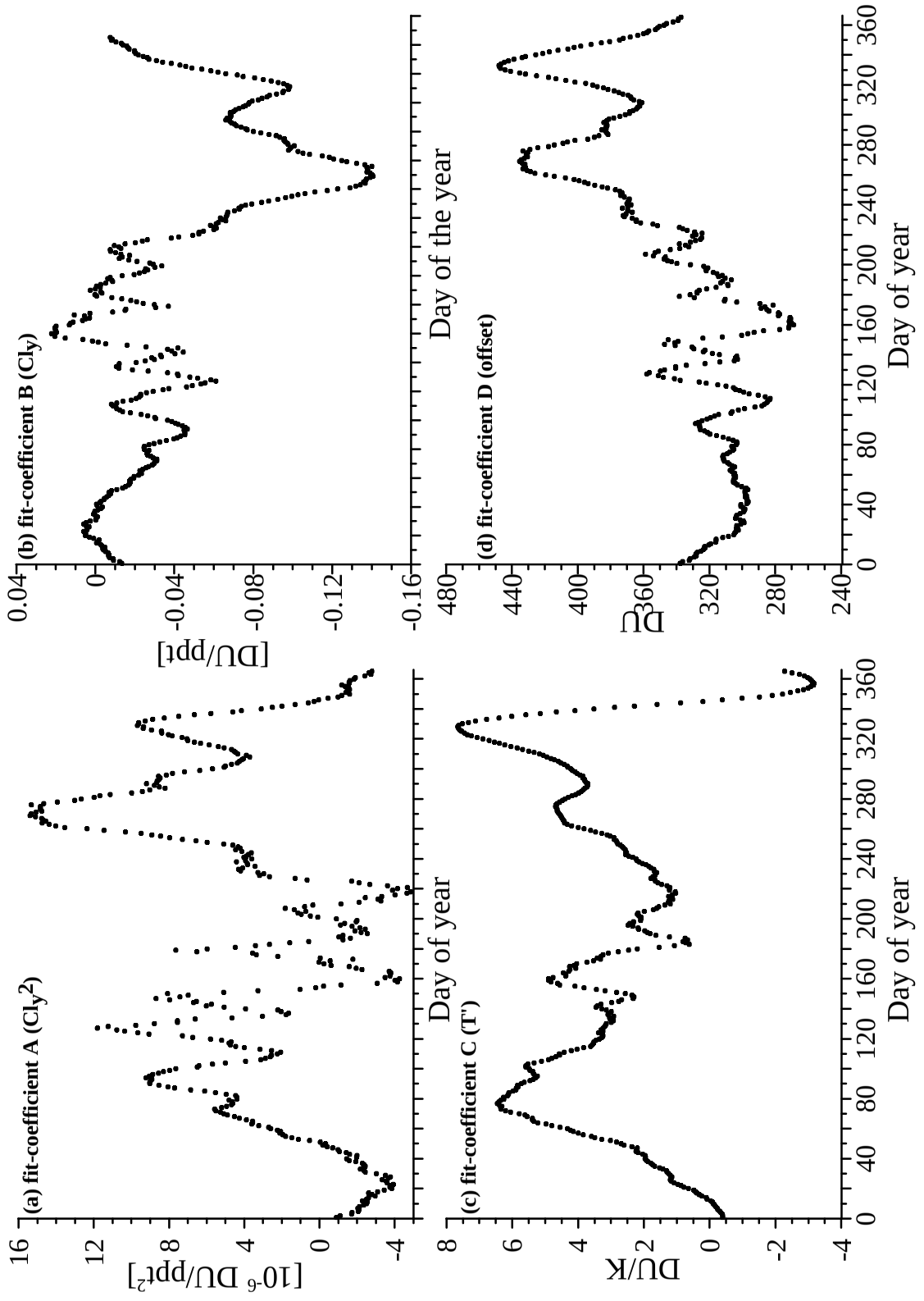

Figure 4.7: Derived daily fit-coefficients from the regression model fit to $\overline{O_{3>70^\circ}}$ values for the period 1960 to 2009.

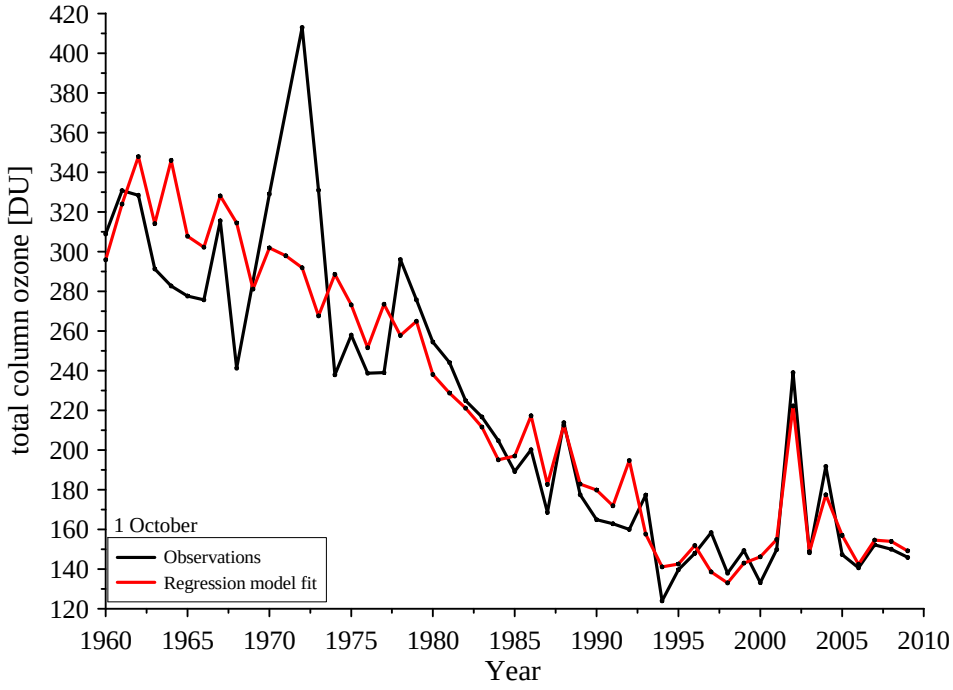

Figure 4.8: Measured $\overline{O_{3>70^\circ}}$ for the period 1960 to 2009 (black line) and regression model fit (red line).

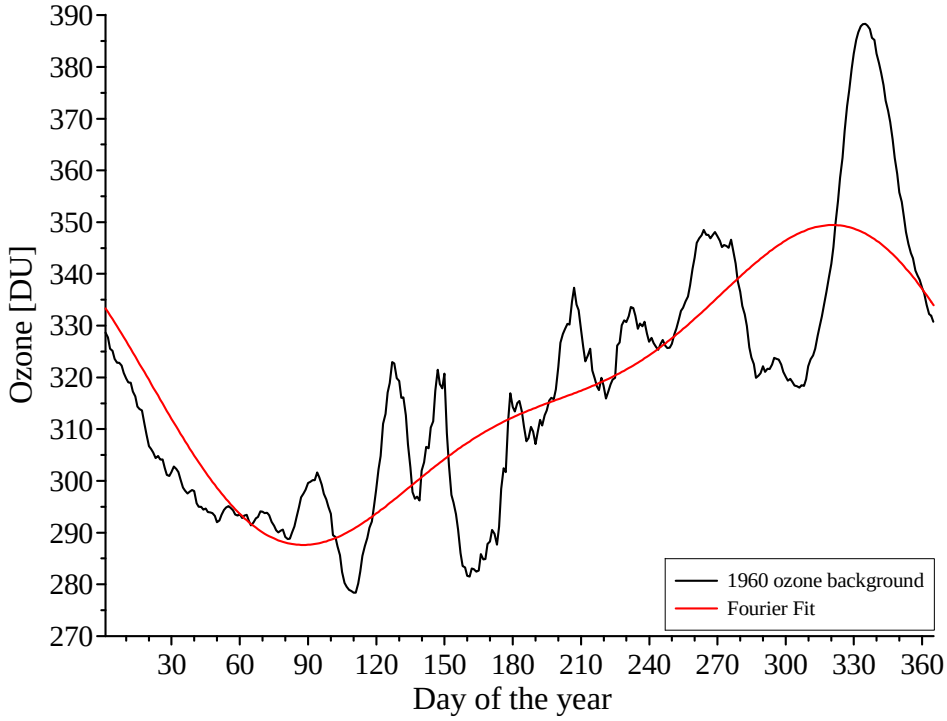

Figure 4.9: Calculated $\overline{O}^{1960}_{3>70^\circ}$ baseline (black) and the fit to the baseline using a Fourier expansion (red).

day for the period 1980 to 2009 (hereafter referred to as ozone anomalies $\Delta\overline{O_{3>70^\circ}}$) (Figure 4.10). This period was chosen as the $\overline{O_{3>70^\circ}}$ values before 1980 are only estimates (see above) and not very reliable and therefore $\overline{O_{3>70^\circ}}$ values from 1960 to 1979 were not used to train the semi-empirical model for the change in ozone. Negative ozone anomalies $\Delta\overline{O_{3>70^\circ}}$ in Figure 4.10 indicate that there was more ozone available than in 1960 due to natural variability or due to transport processes that are not reflected in stratospheric temperatures. Furthermore, the $\Delta\overline{O_{3>70^\circ}}$ values appear to have an offset of about 20 DU, i.e. 1960 ozone levels are not reached during anytime of the year. This offset most likely results from gas phase chemistry involving chlorine compounds (Chapter 1) that does not require PSCs. With an increase in ozone depleting substances, more chlorine is available to destroy ozone via the catalytic $\mathrm{ClO_x}$ cycle and therefore the offset increases. To estimate the offset, the $\Delta\overline{O_{3>70^\circ}}$ which are nonzero at the beginning of each year where no heterogeneous chemistry occurs were extracted from the $\Delta\overline{O_{3>70^\circ}}$. Then the regression model (equation 4.11) was employed to model these offset $\Delta\overline{O_{3>70^\circ}}$ values (indicated by the red line in Figure 4.10). As the semi-empirical model, applied in this chapter, only accounts for ozone destruction via heterogeneous chemistry, this offset was subtracted from the $\Delta\overline{O_{3>70^\circ}}$ time series. This time series of the change in ozone with respect to 1960 is used as the input to the fitting of equation 4.5.

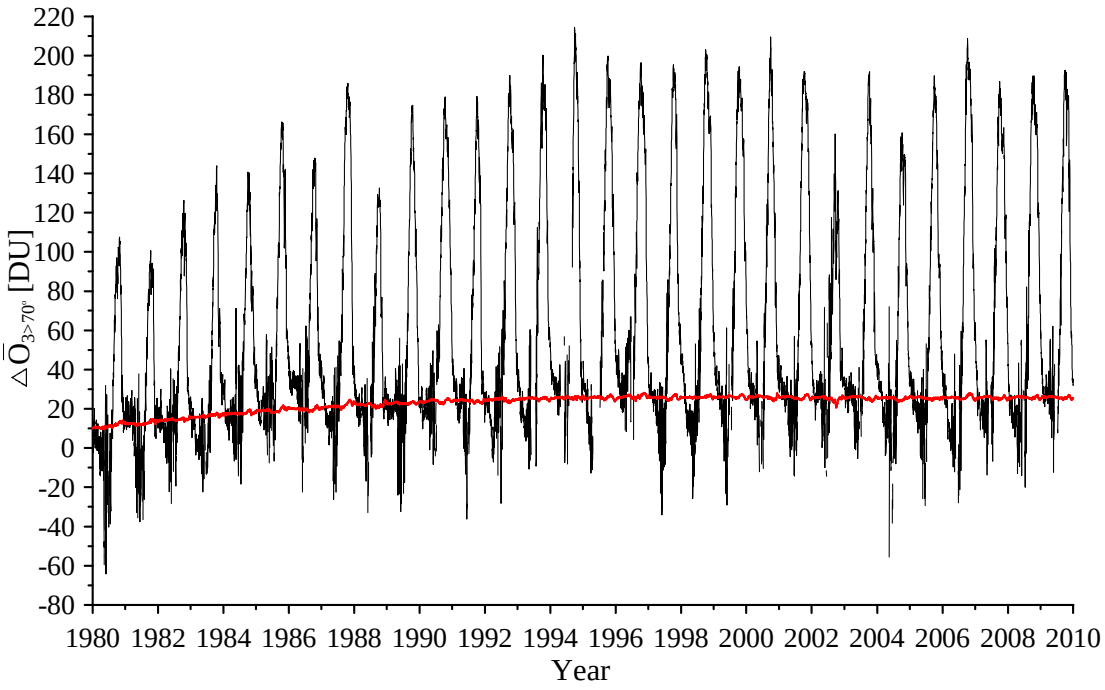

Figure 4.10: Derived ozone anomalies ($\Delta\overline{O_{3>70^\circ}}$) in DU with respect to 1960 levels based on satellite and ground-based observations (black). The red line indicates the offset (the deviation from $\Delta\overline{O_{3>70^\circ}}$=0), resulting most likely from gas phase chemistry.

4.4.2 Determining the fit-coefficients for the semi-empirical model describing the change in ozone

In addition to the time series of the change in ozone, the inputs required to fit equation 4.5 are MAC and the actinic flux (F_{act}) which were calculated as described above. Because the semi-empirical model only accounts for ozone depletion induced by chlorine compounds activated on the surface of PSCs, the fit of $\Delta\overline{O_3}_{>70^\circ}$ is started on the day where MAC first becomes non zero. This first order differential equation is solved by applying the Runge-Kutta method and the same fitting method as for the chlorine activation model (Section 4.3.3) is applied. The algorithm determines an optimal set of parameters that results in the smallest difference between the modelled and observed $\Delta\overline{O_3}_{>70^\circ}$ values. The fit-coefficients A, B, and C derived by the fitting algorithm, are 61.12, 4.93, and 0.0032, respectively. The calculating $A \times MAC^2$ (first term right hand side of equation 4.5) and comparing this term to $B \times MAC$, indicates that the quadratic dependence of ozone depletion on chlorine is the dominant effect of chlorine chemistry on changes in ozone. The in-situ production (represented by coefficient $C \times \Delta\overline{O_3}_{>70^\circ} \times Fact$) plays a minor role in describing the variability of $\Delta\overline{O_3}_{>70^\circ}$ through the year and from year to year.

The measured $\Delta\overline{O_3}_{>70^\circ}$ time series and the semi-empirical model output are shown in Figure 4.11. The model tracks the changes in total column ozone anomalies very well, especially towards the end of the analysis period, including the anomalous years e.g. 2002 (which was included in the fitting). The correlation coefficient (R^2 value) between the measured and semi-empirical modelled $\Delta\overline{O_3}_{>70^\circ}$ values was found to be 0.909 and the slope of the linear fit 0.95. This shows that the model fits the measurements very well, describing 90.9% of the variance. In the first decade (1980 to 1990) the model underestimates $\Delta\overline{O_3}_{>70^\circ}$ in the polar stratosphere. This result suggests that the calculated total mass of activated chlorine underestimates the ozone depletion in that period. However, the generally good agreement of the semi-empirical modelled and observed $\Delta\overline{O_3}_{>70^\circ}$ values allows this model to be applied to project future changes in stratospheric ozone and to estimate the timing of the return of Antarctic ozone to historic values.

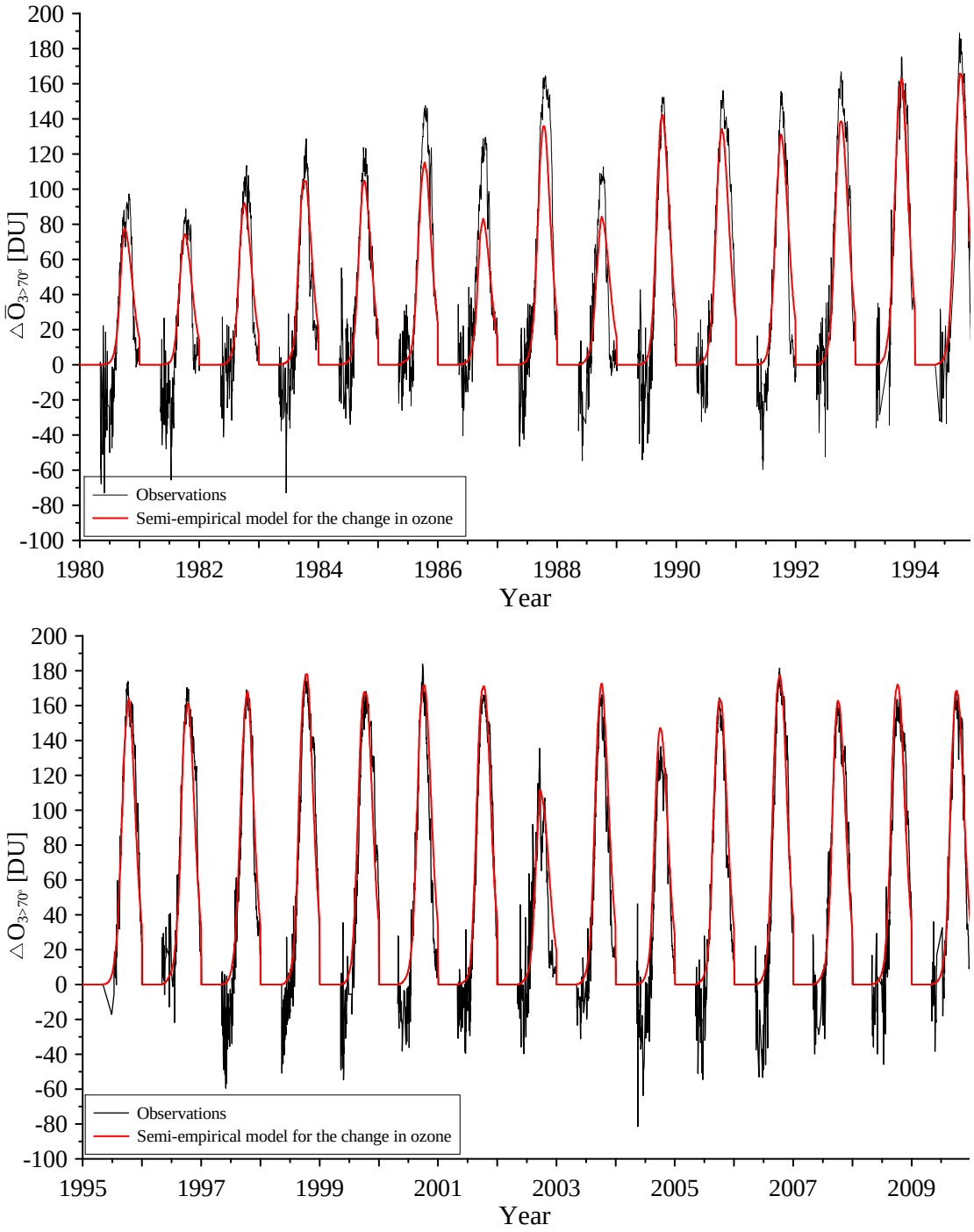

Figure 4.11: Vortex averaged total column ozone loss (ΔO_3) in DU as derived from observations (black line) compared to the semi-empirical model output (red line) for the period 1980 to 2009.

4.5 Evolution of Antarctic chlorine and ozone anomalies

4.5.1 Evolution of Antarctic chlorine

The semi-empirical model for chlorine activation was employed to calculate the vortex mean $\mathrm{ClO_x}$ concentration from 1960 to 2100 using the α and β fit-coefficients obtained by fitting equation 4.1 to observations. The $\mathrm{ClO_x}$ time series were calculated at eight pressure surfaces to encompass the whole altitude range where PSCs activate chlorine. An estimate of $\mathrm{Cl_y}$ from 1960 to 2100, together with daily FAS values, were derived as described in Section 4.3. Besides these input quantities, the semi-empirical model also requires daily FAP values at every pressure level to calculate daily $\mathrm{ClO_x}$ abundances. To calculate these daily FAP values (equation 4.2), daily stratospheric temperature fields at every pressure level of interest are required. For the historic period 1960 to 2009, daily mean NCEP/NCAR temperature fields were calculated and used to derive daily FAP values at all eight pressure levels by applying equation 4.2. For the future period 2010 to 2100, daily mean temperature fields, that account for the future temperature trend as simulated by HadCM3, were generated as described in Section 4.5.2. The future temperature trends were extracted from the monthly mean temperature fields modelled by HadCM3 for the period 2000 to 2100, at eight pressure levels, based on three SRES scenarios. The vortex average (using the same location of the vortex edge as for the observations, i.e. 62° S) annual mean HadCM3 temperatures on eight pressure levels for three SRES scenarios, respectively, are shown in Figure 4.12. The HadCM3 model simulates stratospheric warming throughout the 21$^{\mathrm{st}}$ century at all pressures below 20 hPa. CCM simulations of the future evolution of stratospheric temperatures also simulate a positive temperature trend below 20 hPa. However, a difference of up to 0.8 K decade^{-1} between the modelled HadCM3 and the modelled temperature trends from CCMs exists which is further discussed in Section 4.6. The evolution of the HadCM3 temperature time series is driven by changes in ozone abundances, changes in GHGs, and changes in dynamics. The strong warming simulated by HadCM3 at pressure levels below 20 hPa is likely to be associated with the prescribed ozone increase in the three SRES simulations. This temperature increase seems to overwhelm the stratospheric cooling from enhanced GHGs. After the prescribed ozone stabilizes in 2060 (Johns et al., 2003) the GHG-induced changes in temperature become more apparent. From 2060 to 2100, stratospheric temperatures increase further, however, the temperature trends are far smaller than simulated for the 2000 to 2060 period. This further increase results in part from a software error in HadCM3 where ozone continues to increase slightly, resulting in a small positive feedback on stratospheric temperatures Johns et al. (2003).

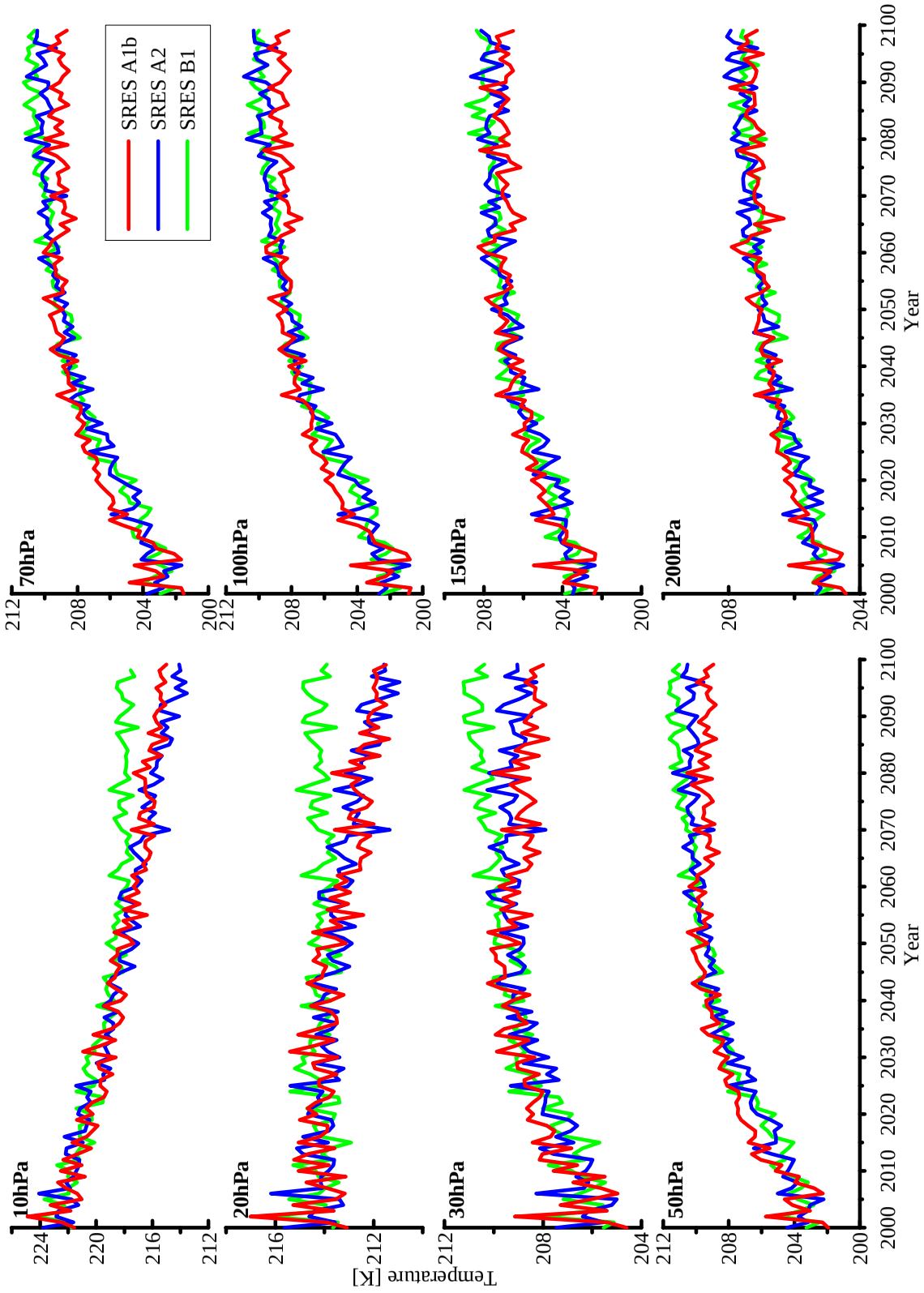

Figure 4.12: Vortex averaged annual mean temperature simulated by HadCM3 on eight pressure levels for three SRES scenarios, namely B1 (green), A1B (red) and A2 (blue).

Changes in stratospheric temperatures due to enhanced GHG concentrations induce changes of the stratospheric circulation. Model simulation suggests a strengthening stratospheric circulation in a changing climate related to enhanced GHGs (SPARC-CCMVal, 2010). The CO_2 concentrations in the A2 scenario are about 120 ppm higher than in A1b, such that the stratospheric circulation is expected to be stronger in the simulations based on the A2 scenario. This could in part explain why the stratospheric temperatures are higher towards the end of this century at pressure levels below 20 hPa in simulations based on the A2 scenario than those based on the A1b scenario, as a stronger stratospheric circulation is related to higher temperatures over the polar regions (Chapter 1). However, to what extent increased ozone, enhanced GHGs and changes in dynamics contribute to the temperature increase/decrease cannot be analysed in this study, as the ozone fields used within HadCM3 were not available. Otherwise, a regression model could have been used to determine the contributions of ozone, GHGs and dynamics, respectively, to the simulated temperature trend.

4.5.2 Generating future temperature time series

To generate future temperature in this chapter, daily mean temperature fields calculated from NCEP/NACR reanalyses for the period 1960 to 2009 and monthly mean temperature fields from HadCM3 from 2000 to 2100 are available. The overlap period where both observations and HadCM3 temperature fields are available (2000 to 2009) is referred to as the 'observation period' in the following. The sub-period 'future' extends from 2010 to 2100. Rather than using the monthly mean HadCM3 temperature fields to calculate future FAP time series, the temperature trends from HadCM3 are used. Using the temperature trends instead of the modelled temperature fields has the advantage that the results do not depend on one fixed temperature scenario. As a result, daily future temperature fields are generated by using NCEP/NCAR temperature fields from 2000 to 2009 that are evolved into the future by adding the simulated temperature trends from HadCM3 for the period 2010 to 2100 to these NCEP/NCAR fields. Furthermore, the Monte Carlo method is employed to account for future temperature variability. How the future daily temperature fields at eight pressure levels were generated, which were then used to calculate daily FAP time series for the period 2010 to 2100, is described below.

First, to extract the temperature trends for the 21st century from the monthly mean temperature fields modelled by HadCM3, a Fourier expansion was fitted to the simulated temperature fields, separately for every GHG emissions scenario.

The Fourier expansion in the form:

$$\begin{aligned} T(t) &= A_0 + \sum_{i=1}^{3} A_i \cdot \sin(2\,i\pi\,t) + B_i \cdot \cos(2\,i\pi\,t) \\ &+ C_0 \cdot t + \sum_{j=1}^{2} C_j \cdot t \cdot \sin(2\,j\pi\,t) + D_j \cdot t \cdot \cos(2\,j\pi\,t) \\ &+ E_0 \cdot t^2 + E_1 \cdot t^2 \cdot \sin(2\,\pi\,t) + F_1 \cdot t^2 \cdot \cos(2\,\pi\,t) \end{aligned} \tag{4.12}$$

was applied separately to each grid box (2.5°×3.75°) between 62° S and 90° S and at every pressure level, resulting in 15 fit-coefficients. The parameter t is the time in decimal years. The first terms on the right hand side (A and B coefficients) model the mean annual cycle in the temperature time series, while the second (C and D coefficients) and third (E and F coefficients) terms model the linear and non-linear trend in the annual cycle, respectively. The derived fit-coefficients are now used to derive daily future temperature fields that account for the temperature trend modelled by HadCM3.

Equation 4.12 was employed in a second step to derive temperature anomalies (ΔT) by subtracting the calculated daily temperature ($T(t)$) at a given grid point (longitude/latitude) of every year during the observation period (y_{obs}=2000, 2001, ..., 2009) from the calculated daily temperature at the same grid point of every year in the future (y_{target} =2010, 2011, ..., 2100):

$$\Delta T_{y_{target}}^{y_{obs}} = T_{y_{target}}^{Eq.4.12} - T_{y_{obs}}^{Eq.4.12} \tag{4.13}$$

Then, to generate the future daily temperature ($T_{y_{target}}^{future}$) at that given grid point, the temperature anomalies are added to the daily mean NCEP/NCAR temperature at that location from the observation period:

$$T_{y_{target}}^{future} = T_{y_{obs}}^{NCEP/NCAR} + \Delta T_{y_{target}}^{y_{obs}} \tag{4.14}$$

Equation 4.13 and 4.14 are applied to every grid point between 62° S and 90° S for all days of the years 2010 to 2100, resulting in nine possible temperature fields per day for each year. To generate the temperature field for a given target year in the future, there are 9 possible temperature fields to chose from. Using a Monte Carlo method, 1000 different temperature time series for the period 2010 to 2100 were obtained and used for further analysis. For any target year in the future (e.g. 2020), a year between 2000 and 2009 was randomly picked (e.g. 2005) and the temperature field calculated via:

$$T_{2020}^{future} = T_{2005}^{NCEP/NCAR} + \Delta T_{2020}^{2005} \tag{4.15}$$

was chosen to be part of the new generated temperature time series. For every month of the target year a new year from the observation period is randomly picked. This is done for every year between 2010 and 2100, resulting in 1000 statistically equivalent temperature times series. Overall there are 9^{90} possible combinations of temperature fields which can be used to generate future time series. The 1000 time series of daily temperature fields for each of the three GHG emissions scenarios were then used to derive FAP time series on each of the 8 pressure levels using equation 4.2. The August to November mean FAP values at 70 hPa for the observation period together with the generated FAP values averaged over all 1000 Monte Carlo runs for each SRES scenario are shown in Figure 4.13.

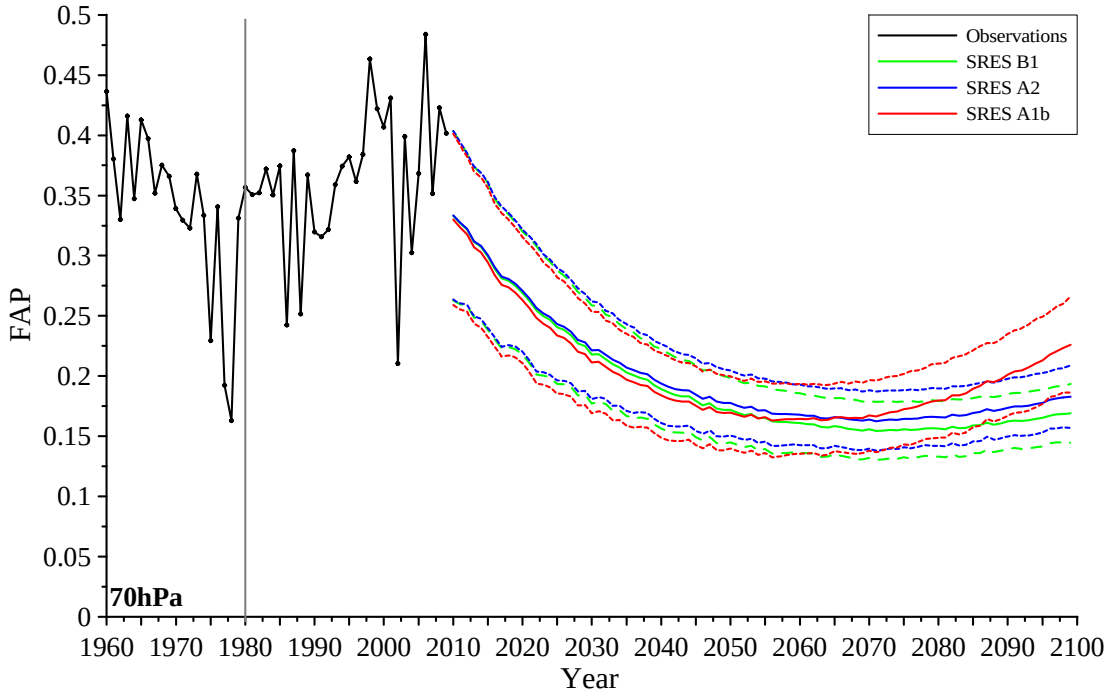

Figure 4.13: Calculated August to November mean FAP time series based on NCEP/NCAR temperature fields (black) for the period 1960 to 2009. For the period 2010 to 2100 the generated FAP values were averaged over all Monte Carlo simulations and are shown for three SRES scenarios; A1b (red), A2 (blue) and B1 (green). The dotted lines represent the 1σ uncertainty range derived from the Monte Carlo simulations. The vertical grey line indicates the FAP value in 1980. 1980 has been used as the benchmark for return dates of Antarctic ozone (WMO, 2007).

The annual mean FAP values through the observation period (1960-2009) indicate that stratospheric temperatures at 70 hPa increased from 1960 to the 1980, resulting in fewer PSCs. A long-term warming trend in the Antarctic lower stratosphere from 1960 to 1980 was also reported in Chapter 4 of the 2006 Ozone Assessment (WMO, 2007). In this period of stratospheric warming less chemical ozone loss can occur as less chlorine is activated

due to heterogeneous chemistry. This temperature influence can obscure ozone depletion due to halogen chemistry prior to 1980. From 1980 onwards, stratospheric cooling leads to an increase in the area of the vortex covered by PSCs. Dynamical variability of the Antarctic vortex led to higher temperatures and therefore lower FAP values in some of the years during the observation period (e.g. 2002, 2004) (WMO, 2007).

The big gap between the observations (2009) and the beginning of the future FAP values (2010) as shown in Figure 4.13 results from the continuous positive temperature trend within all three SRES simulations of HadCM3 from 2000 onwards (Figure 4.12). In 2010, adding e.g. the positive temperature trend from 2000 to 2010 to the NCEP/NCAR temperature field of 2000, results in higher temperatures and therefore lower FAP values. The decrease in FAP values from 2010 to 2060 is also related to the positive temperature trend modelled in HadCM3 (5 K at 70 hPa). Once the prescribed ozone in HadCM3 stabilized (Section 4.5.1) FAP increases for the A1b scenario corresponding to the simulated cooling trend on HadCM3 (Figure 4.12). FAP values at 70 hPa for the A2 scenario, which is the scenario with the highest CO_2 concentration, do not increase much from 2060 onwards which corresponds to the simulated stratospheric warming (1.3 K from 2060 to 2100 at 70 hPa). The fact that the scenario with the highest CO_2 concentration does not lead to the strongest cooling effect of the stratosphere can, in part, be explained with a strengthening stratospheric circulation with enhances GHGs (Section 4.5.1 and Chapter 1). The FAP values for the B1 scenario continue to decrease after 2060 and by the end of this century, the lowest FAP values, associated with the highest stratospheric temperatures, are obtained this scenario.

The variability in the FAP values (indicated by the magnitude of 1σ uncertainty range in Figure 4.12) is a result of the variability in the NCEP/NCAR temperature fields from 2000 to 2009. And as these NCEP/NCAR temperature fields were used for every SRES scenario, the magnitude of 1σ is expected to the similar for every SRES scenario.

The calculated FAP time series from 1960 to 2100 at eight pressure levels can now be used as a input to the chlorine activation semi-empirical model (equation 4.1). Given the amount of Cl_y and the amount of available sunlight, FAS, the semi-empirical model is used to calculate ClO_x times series for the observations period (1960-2009) on eight pressure levels. The model then is used to project the future evolution of ClO_x (2010-2100) based on three SRES scenarios. As indicated above, the Cl_y concentrations are with respect to 1960 levels.

The Antarctic vortex mean (62°S to 90°S) modelled ClO_x time series were used to calculate the total mass of activated chlorine (MAC) within a partial column from 200 to 10 hPa. Equation 4.7 was applied to derive MAC time series from 1960 to 2009, where MAC is zero in 1960 per construction and to derive 1000 MAC times series for each of the three SRES scenarios from 2010 to 2100. The results indicate that activated chlorine levels were already elevated with respect to 1960 values by 1980 (MAC=0.025×10^8 kg).

The contribution to the total amount of MAC from each of the 7 layers are shown in Figure 4.14 for a selected number of years (2000, 2020, 2050 and 2099). MAC values for 2000 are based on observations, while the MAC values for the future period were averaged over all Monte Carlo simulations based on one SRES scenario (B1). The atmospheric layers between 150 and 70 hPa contribute the largest amount to the total mass of activated chlorine, a result which is independent of the year and SRES scenario. The MAC values peaked in 1998 (not shown) and are now decreasing in response to the reduction in ozone depleting substances. By the end of this century, maximum values of MAC less than 0.05×10^8 kg will be reached under the B1 scenario. The results show that independent of the SRES scenario, MAC does not return to 1960 levels by the end of this century.

4.5.3 Future evolution of Antarctic ozone depletion

The derived MAC abundances were then used as input to the ozone anomaly ($\Delta\overline{O_3}_{>70^\circ}$) semi-empirical model (equation 4.5). Using the fit-coefficients derived by fitting to observations, together with MAC and F_{act}, the evolution of Antarctic ozone can be estimated for the full period from 1960 to 2100. As MAC was derived for three GHG emissions scenarios, the semi-empirical model can be applied to conduct projections of Antarctic ozone for these scenarios, through the 21st century. These ozone anomaly projections can be used to provide estimates of the return of Antarctic ozone loss to historic levels e.g. 1960 or 1980 levels. Uncertainties of the ozone anomaly projections are captured through the 1000 MAC Monte Carlo generated time series. As the Monte Carlo method creates the same uncertainties for each SRES scenario by construction as the uncertainty is coming from randomly 'picking' a NCAEP/NCAR temperature field from the 2000 to 2009 observation period. These underlying temperature fields are the same for every scenario. Therefore it is expected that the uncertainty in the ozone anomaly projection is similar for every SRES scenario.

The August to November $\Delta\overline{O_3}_{>70^\circ}$ mean from 1960 to 2100, evaluated using equation 4.5 based on real-world MAC to 2009, and thereafter the MAC time series for three SRES scenarios and averaged over the 1000 Monte carlo simulations are shown in Figure 4.16.

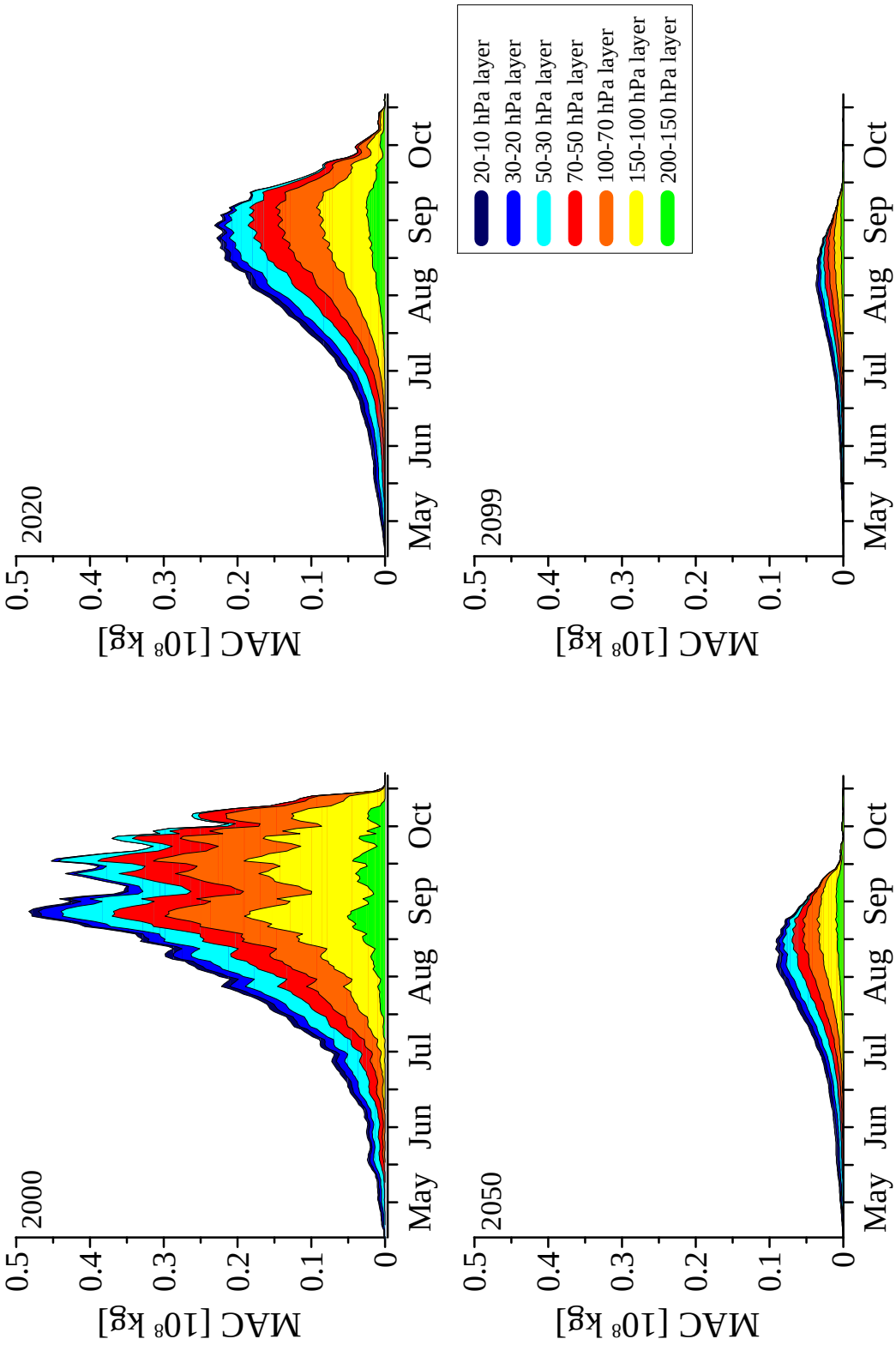

Figure 4.14: Contribution of every layer between 200 and 10 hPa to the total MAC for the 2000, 2020, 2050, and 2099. MAC values for 2000 are based on observations, while MAC abundances for the future years were obtained by averaging the 1000 Monte Carlo simulations based on SRES B1. The interannual variability in the future years is smoothed due to the calculated of the average.

Histograms of the probability density function (PDF) of the return dates to 1980 levels from the 1000 Monte Carlo simulation are also shown in Figure 4.14, separately for each SRES scenario. The salient features of Figure 4.16 are:

(i) The $\Delta\overline{O_3}_{>70^\circ}$ in the Antarctic stratosphere maximizes in the late 1990s and thereafter slowly decreases.

(ii) Antarctic $\Delta\overline{O_3}_{>70^\circ}$ returns to 1980 levels between 2030 and 2040 depending on the SRES scenario.

(iii) Enhanced GHGs delay the return of $\Delta\overline{O_3}_{>70^\circ}$ to 1980 values by about 2 years.

(iv) Antarctic $\Delta\overline{O_3}_{>70^\circ}$ does not return to 1960 levels in the 21$^{\text{st}}$ century.

The sharp increase in ozone depletion from 1960 to its maximum in 1998 as shown in Figure 4.16 coincides with the period of increasing stratospheric chlorine. In 1998 about 49% from the 1960 ozone values was destroyed via catalytic cycles involving chlorine compounds. Traditionally, 1980 ozone abundances were used as the benchmark for return dates for Antarctic ozone and the ozone hole area was the primary metric to estimate the severity of the Antarctic ozone depletion (e.g WMO, 2007). The ozone hole area is calculated from the area where total column ozone values are less than 220 DU. The 220 DU was chosen because it is lower than the pre-1980 observed total column ozone abundances. Therefore, the ozone hole area is by construction zero in 1980. The size of the ozone hole is mainly controlled by catalytic ozone deleting cycles involving chlorine and bromine compounds (Newman and Nash, 2004). However, as the results of this chapter show, chlorine compounds were present before 1980 and therefore Antarctic ozone was affected by the catalytic cycles prior to 1980. About 15% from the 1960 ozone values was destroyed before 1980 (Figure 4.16). Using the ozone hole area as a metric underestimates the severity of Antarctic ozone depletion due to catalytic cycles. More recent model simulations also suggest that ozone was affected by ozone depleting substances prior to 1980 (SPARC-CCMVal, 2010). After stratospheric chlorine levels peak, a general moderate downward trend in ozone depletion is observed from the maximum depletion to the end of the observation period (2009). The deviations from this overall decrease in ozone loss in some years such as 2002, 2004, and 2006 is a result of dynamical variability (WMO, 2007). The 2002 and 2004 Antarctic winters were unusual warm due to higher wave activity, resulting in an early break up of the vortex (WMO, 2007). On the other hand, in 2006, the polar vortex was unusually cold as a result of lower wave activity (Yang et al., 2008). The strong polar vortex lasted longer than usual, resulting in more ozone depletion (Yang et al., 2008).

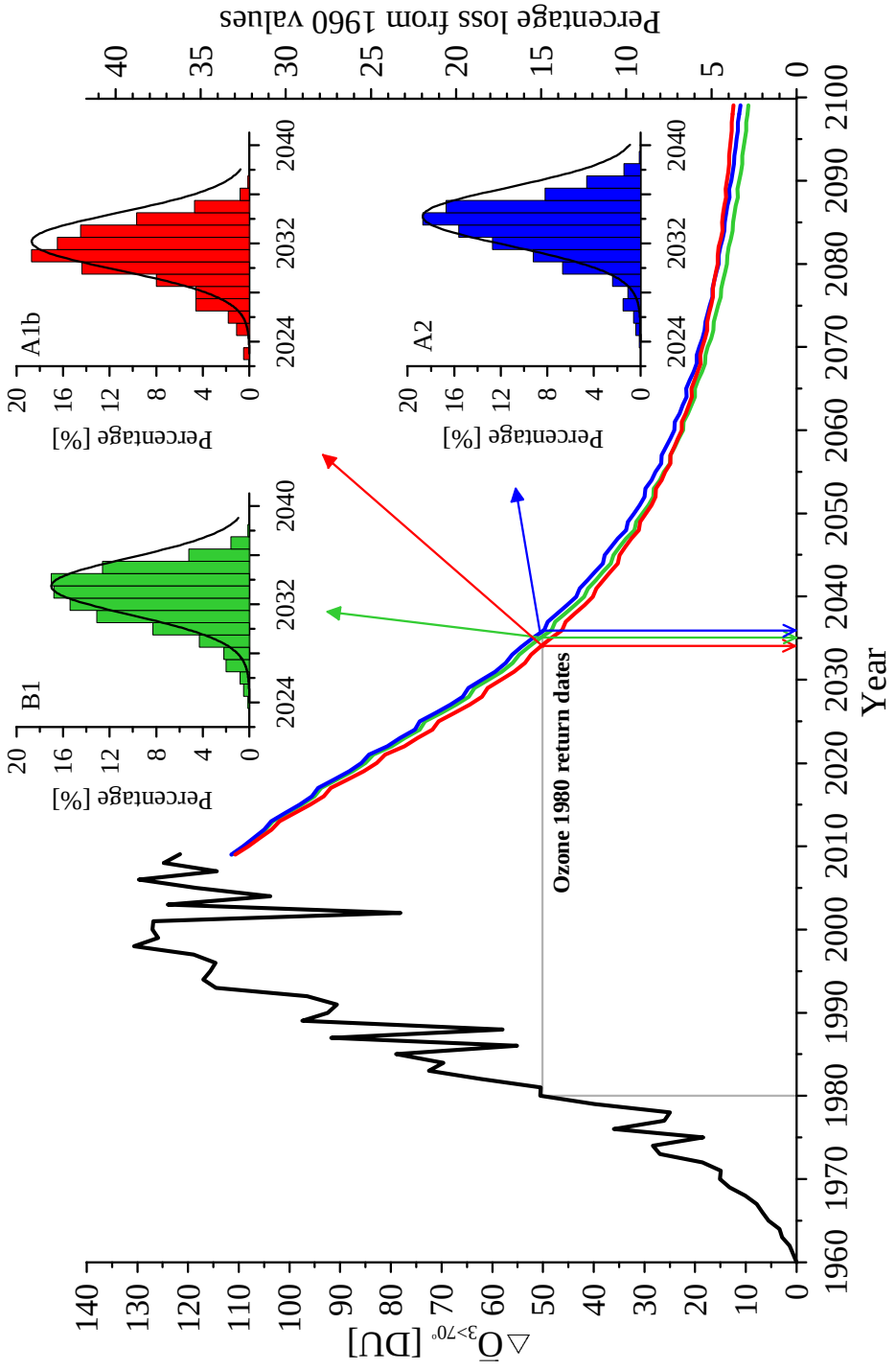

Figure 4.15: August to November averaged $\Delta\overline{O_3}_{>70^\circ}$ from 1960 to 2100, where the August to November mean $\Delta\overline{O_3}_{>70^\circ}$ values from 2010 onwards are averaged over the 1000 Monte Carlo runs for each SRES scenario. The green line represent the SRES B1 scenario, red represents the results from the A1b scenario and the blue line corresponds to the derived results based on A2 scenario. The three histograms display the PDF of the $\Delta\overline{O_3}_{>70^\circ}$ return dates to 1980 levels for the three SRES scenarios. The total column ozone loss from 1960 values in percent is also indicated (y-axes on the right hand side).

As discussed in Section 4.5.2, the gap between the observed $\Delta\overline{O_3}_{>70^\circ}$ and the modelled $\Delta\overline{O_3}_{>70^\circ}$ values based on NCEP/NCAR temperature fields and HadCM3 temperature trends (Figure 4.16), results from the continued positive temperature trend simulated by HadCM3 from 2000 onwards. As the positive temperature trend is added to the NCEP/NCAR temperature fields, less ozone is depleted in 2010 and thereafter than during the observation period (2000 to 2009). The overall downward trend in ozone depletion continues through the 21$^{\mathrm{st}}$ century, independent of the SRES scenario (Figure 4.16).

The Monte Carlo simulations performed for all three SRES scenarios indicate that $\Delta\overline{O_3}_{>70^\circ}$ returns to 1980 values between 2030 and 2040 (Figure 4.16). Based on the SRES A1b scenario $\Delta\overline{O_3}_{>70^\circ}$ returns to 1980 values in 2032$\pm$2.3. This return date is the earliest among the three SRES scenarios and corresponds to the largest temperature trend simulated by HadCM3 to 2060 (Figure 4.12). The majority of the 1000 Monte Carlo simulations project a return date of 2031 and 2032 as shown is the PDF in Figure 4.16. The range of return dates derived from the A1b scenario overlaps with the return dates projected from the calculations based on the B1 and A2 scenarios. The simulations based on the B1 scenario indicate that $\Delta\overline{O_3}_{>70^\circ}$ returns to 1980 levels in 2033$\pm$2.3 (Monte Carlo mean), where the majority of the Monte Carlo simulations suggest a return date of 2033 and 2034 (Figure 4.16). The latest return date is obtained from the Monte Carlo simulations based on the A2 scenario (2034$\pm$2.4). From 2000 to 2050, HadCM3 simulates a positive temperature trend of 0.57 to 0.81 K decade^{-1} at 100 and 70 hPa, respectively. However, for the A1b and B2 scenarios, HadCM3 simulates larger trends (details see Section 4.6). As the 100 to 70 hPa region most contribute to MAC abundances (Figure 4.14) more ozone is destroyed which keeps the $\Delta\overline{O_3}_{>70^\circ}$ longer at higher levels. However, $\Delta\overline{O_3}_{>70^\circ}$ returns to 1980 levels only 1 and 2 years later than under the B1 and A1b scenario, respectively. The majority of the Monte Carlo simulations based on A2 scenario suggest that $\Delta\overline{O_3}_{>70^\circ}$ returns in 2034 and 2035. The general result that can be drawn from this analysis is that the timing of the return of Antarctic ozone to 1980 values is largely insensitive to GHG emissions. Furthermore, $\mathrm{Cl_y}$ used in this chapter does not return to 1960 levels by the end of the 21$^{\mathrm{st}}$ century. As a result ozone is affected by ozone depleting substances beyond the end of the 21$^{\mathrm{st}}$ century and therefore Antarctic $\Delta\overline{O_3}_{>70^\circ}$ is projected not to return to 1960 levels by the end of the 21$^{\mathrm{st}}$ century.

4.6 Discussion

The derived return dates of $\Delta\overline{O_3}_{>70^\circ}$ to 1980 levels from this study for the three SRES scenarios compared to return dates determined in earlier studies, are summarized in Figure 4.16. The return date of $\mathrm{Cl_y}$ to 1980 levels, as derived from the $\mathrm{Cl_y}$ time series used in this study, is also included in Figure 4.16. It should be noted that the metrics used to derive the dates of return of Antarctic ozone are different. Austin et al. (2010a) and Eyring et al. (2010a) used October means of the vortex averaged total column ozone (62° to 90° S), while Newman et al. (2006) used the ozone hole area as the metric to derive return dates.

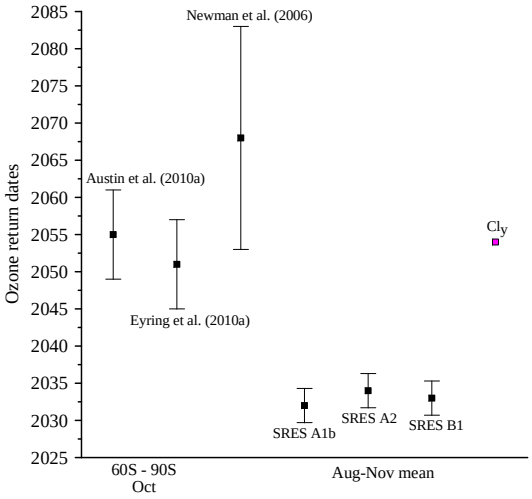

Figure 4.16: Dates of return of $\Delta\overline{O_3}_{>70^\circ}$ to 1980 levels as derived from previous studies compared to the results of this study. The error bars on the return dates from Austin et al. (2010a) and Eyring et al. (2010a) show the uncertainties from climate noise and from internal model variability while the error bars on the return dates from this chapter show the uncertainties from climate noise only. The error bars on the return dates derived by Newman et al. (2006) include the uncertainty arising from the uncertainties in the mean age-of-air. The date of return to 1980 levels of $\mathrm{Cl_y}$ (as used in this study) is indicated by the magenta square.

Previous studies by Austin et al. (2010a) and Eyring et al. (2010b) suggested that Antarctic total column ozone abundances return to 1980 values between 2045 and 2060 (Figure 4.16). This return date is up to $\sim$ 25 years later than the results presented in this chapter. This difference in the projections can be explained with (i) the positive temperature trend modelled by HadCM3 and (ii) with the missing feedback of temperature on ozone and ozone on temperature in AOGCMs (hereafter denoted as temperature$\leftrightarrow$ozone feedback). The temperature tends from 2000 to 2049 and from 2050 to 2099 (at pressure levels where the contribution to MAC maximizes (Figure 4.14)) simulated by HadCM3 for all three SRES scenarios are summarized in Table 4.2. For the pressure levels that contribute

the most to MAC, the temperature trend is positive, irrespective of which SRES scenario is used. CCM simulations of the future evolution of stratospheric temperatures, based on the A1b scenario, also simulate a positive temperature trend below 30 hPa (multi model mean) (SPARC-CCMVal, 2010). The results from the CCM studies indicate that the temperature trend at the pressure levels 150, 100, 70 hPa is smaller than 0.4 K decade^{-1} (2000 to 2049), and smaller than 0.2 K decade^{-1} (2050 to 2099). The temperature trends simulated by HadCM3 are overestimated compared to the results derived from CCM simulations. As less ozone is destroyed at higher temperatures, this overestimation, especially from 2000 to 2049 is most likely the reason why the results presented in this chapter suggest a much earlier ozone return date for the Antarctic than projected by various CCM studies.

SRES scenario	pressure level [hPa]	2000 to 2049	2050 to 2099
B1	150	0.30 K/decade	0.10 K/decade
	100	0.66 K/decade	0.22 K/decade
	70	1.02 K/decade	0.25 K/decade
A1b	150	0.42 K/decade	0.09 K/decade
	100	0.84 K/decade	0.13 K/decade
	70	1.22 K/decade	0.11 K/decade
A2	150	0.28 K/decade	0.18 K/decade
	100	0.57 K/decade	0.30 K/decade
	70	0.81 K/decade	0.36 K/decade
CCM	150	$\leq$0.4 K/decade	$\leq$0.2 K/decade
A1b	100	$\leq$0.4 K/decade	$\leq$0.2 K/decade
	70	$\leq$0.4 K/decade	$\leq$0.2 K/decade

Table 4.2: Temperature trends from 2000 to 2049 and from 2050 to 2099 averaged over September-October-November for all SRES scenarios considered in this chapter and from the CCM simulations (SPARC-CCMVal, 2010).

The positive temperature trend simulated by HadCM3 results partly from the increase in ozone abundances, a effect that is also present in CCMs, as more ozone results in more absorption of UV radiation and therefore, leading to a warmer stratosphere. However, the difference between HadCM3 and CCMs is that in HadCM3 the temperature$\leftrightarrow$ozone feedback is missing. Changes in stratospheric temperatures induce changes in stratospheric ozone chemistry leading to more or less ozone depletion in a changing climate. This effect of temperature-induced changes on ozone are not considered in HadCM3, which explains the overestimation of the temperature trends. HadCM3 does not include any chemistry and ozone was calculated off-line. It might also be that the ozone time series, prescribed in HadCM3, was overestimated. But more likely is that the missing temperature$\leftrightarrow$ozone feedback results in the ozone and temperature trends in HadCM3 being elevated above what would have been the case with the feedback included. The temperature$\leftrightarrow$ozone feedback is included in CCMs. This most likely explains why the results from this chapter are different

to those obtained from CCM studies. This result indicates that considering the coupling of temperature and ozone depletion delays the return of Antarctic ozone to 1980 levels by $\geq$2 decades.

$\mathrm{Cl_y}$ returns to 1980 levels in 2054 which is more 20 years later than $\Delta\overline{O_3}_{>70^\circ}$ returns to 1980 values, independent of the GHG emissions scenarios (Figure 4.16). It should be noted that the derived results show a similar behaviour than ozone returning to 1980 levels in the southern mid latitudes. The $\Delta\overline{O_3}_{>70^\circ}$ return dates derived in this chapter are comparable with the return dates in the southern mid latitudes (Eyring et al., 2010a). In the southern mid latitudes ozone returns faster than $\mathrm{Cl_y}$ by about 15 years.

$\Delta\overline{O_3}_{>70^\circ}$ is projected not to return to 1960 levels within the 21$^{\mathrm{st}}$ century, independent of the SRES scenario. By the end of the 21$^{\mathrm{st}}$ century, ozone depletion induced by catalytic cycles involving chlorine compounds persists as a result of the long atmospheric life-time of the chlorine source gases such as CFCs.

The results presented above indicate that the evolution of $\Delta\overline{O_3}_{>70^\circ}$ throughout the 21$^{\mathrm{st}}$ century shows a small sensitivity to changes in GHG concentrations. Contrary, the CCM study by Eyring et al. (2010a) suggested that the ozone return dates in the Antarctic stratosphere vary by $\sim$10 years, depending on the GHG emissions. This result cannot be confirmed by the results of this chapter. The return dates in this work only vary by up to 2 years. The insensitivity of the ozone return dates on GHGs emissions can be explained with the missing temperature$\leftrightarrow$ozone feedback in HadCM3. Due to the missing feedback the stratospheric warming induced by increased ozone concentrations offsets the stratospheric cooling due to enhanced GHG concentrations. As the temperature$\leftrightarrow$ozone feedback in HadCM3 is missing, irrespective of how cold the stratosphere due to enhances GHG would get, ozone increases further as it is unaffected by stratospheric temperature changes. In CCMs, however, the temperature$\leftrightarrow$ozone feedback is included and therefore GHG-induces temperature changes affect ozone. This results suggest that if the temperature$\leftrightarrow$ozone feedback is considered in numerical models than, ozone is longer kept at lower values resulting in a delay of a return to historic levels.

Newman et al. (2006) estimated that the ozone hole area returns to 1980 levels in 2068, which is the latest return date reported in previous studies. However, this result assumes that the Antarctic lower stratosphere cools by about 0.25 K decade^{-1} through the 21$^{\mathrm{st}}$ century. In contrast, both CCM and HadCM3 simulated increases in Antarctic stratospheric temperatures (between 150 and 30 hPa) through the 21$^{\mathrm{st}}$ century. The return date derived by Newman et al. (2006) is insensitive to temperature changes induced by changes in ozone

and changes in GHGs and therefore, the method presented by Newman et al. might not be the most reliable approach to estimate the Antarctic ozone recovery.

In this chapter, the uncertainties in the return dates of $\Delta\overline{O_3}_{>70^\circ}$ consists of uncertainties in the modelled temperatures and uncertainties in the evolution of future ozone depleting substances, as well as uncertainties arising from the semi-empirical model approach. The evolution of future stratospheric temperatures depends on ozone, GHGs, and stratospheric dynamics. The uncertainties on the HadCM3 simulated temperature trends used in this chapter were already discussed above. Furthermore, this chapter is based on $\mathrm{Cl_y}$ estimated by the approach presented in Newman et al. (2006), using a mean age-of-air of 5.5 years and a constant fractional release value. However, future changes in climate are expected to change the stratospheric circulation which is turn changes the mean age of air and fractional release values. Therefore, changes in both mean age-of-air and fractional release contribute to the uncertainties in Antarctic ozone return dates derived in this chapter.

4.7 Conclusions

A semi-empirical model approach to project the time rate of change of $\Delta\overline{O_3}_{>70^\circ}$ with respect to 1960 levels has been implemented. The semi-empirical models were trained on satellite observations of ClO and on observed $\Delta\overline{O_3}_{>70^\circ}$ with respect to 1960 levels, based on satellite and ground-based measurements. The model results agree well with the observations which confirms the applicability of semi-empirical models. Therefore, the semi-empirical models were used to project future changes in activated chlorine and $\Delta\overline{O_3}_{>70^\circ}$ in the Antarctic stratosphere. The evolution of activated chlorine depends strongly on the availability of PSCs, and hence on temperature. The temperature trends, as simulated by HadCM3, were used to approximate future formation of PSCs in the Antarctic stratosphere.

The ozone tendency follows the change in MAC by construction of the semi-empirical models. Therefore, MAC and $\Delta\overline{O_3}_{>70^\circ}$ maximized in 1998 and are now moderately decreasing. The projections of the return dates of Antarctic $\Delta\overline{O_3}_{>70^\circ}$ using different GHG emissions scenarios suggest that $\Delta\overline{O_3}_{>70^\circ}$ values return to 1980 levels ahead of $\mathrm{Cl_y}$ by up to $\sim$20 years. The results presented above indicate, that the decrease in $\Delta\overline{O_3}_{>70^\circ}$ is dominated by $\mathrm{Cl_y}$, however, the differences in the $\mathrm{Cl_y}$ return date and the return date of $\Delta\overline{O_3}_{>70^\circ}$ is modulated by temperature.

The results presented above suggest that ozone returns to 1980 values about 5 to 28 years earlier than previously reported. This difference in the ozone loss projections most likely results from the prescribed temperature trend used in this chapter. The HadCM3 model simulated a higher positive temperature trend through the 21^{st} century compared to CCM simulations. Less chlorine is activated in a warmer stratosphere and as a result, ozone projected in this chapter returns earlier to 1980 levels than would otherwise be the case. This result suggests that the missing temperature↔ozone feedback in HadCM3 accelerates the return of ozone in the Antarctic stratosphere. The temperature↔ozone feedback is included and considered in CCMs. Therefore, CCM simulations are the most appropriate way to assess the question of ozone recovery dates and a continuous improvement of CCMs is needed to reduce uncertainties in projections of future ozone. The results presented above indicate that to reliably project future ozone levels the temperature↔ozone feedback has to be included in numerical models.

To derive a more robust conclusion about the sensitivity of the return dates on $\Delta\overline{O_3}_{>70^\circ}$ to changes in GHG emissions this analysis can be applied to different AOGCM model outputs. Furthermore, the knowledge about the ozone time series that is prescribed in AOGCMs would allow a more detailed study of the individual contributions of changes in ozone, GHGs, and dynamics to the future evolution of stratospheric temperatures. Besides the uncertainty in GHG emissions, there are also uncertainties in the future evolution of ozone depleting substances (WMO, 2007). The question of how the uncertainties in the future emissions of ODSs affects the timing of the ozone return dates was not assessed in this chapter and remains an open question for future work. The semi-empirical model approach can easily be used to conduct projections under several ozone depleting substance emissions scenarios to account for the full range of uncertainties.

The aim of this chapter was to test the applicability of using AOGCM temperature trends, that include the effects of climate change, to project future ozone levels in the Antarctic stratosphere and to estimate the sensitivity of the date of return for Antarctic ozone to historic levels, on GHG emissions. It was found that it is not very reliable to use AOGCMs temperature trends together with a semi-empirical model approach to conduct projections of the future ozone levels. The temperature↔ozone feedback is not included in the AOGCM and it is not included in the semi-empirical models either. Therefore, both tools separately cannot be used to reliably conduct projections. However, coupling the AOGCM to the semi-empirical models would provide a powerful tool to conduct fast and inexpensive projections of the future evolution of Antarctic ozone and the sensitivity of the return dates on GHG emissions could be reliably assessed.

Chapter 5

A semi-empirical diagnosis of polar chemistry in a chemistry-climate model

5.1 Introduction

The previous chapter presented an application of semi-empirical models to simulate reactive chlorine abundances and Antarctic ozone anomalies. In this chapter semi-empirical models are employed for a different purpose i.e. as a means of diagnosing, assessing and validating the polar heterogenous chemistry schemes employed in chemistry-climate models (CCMs) in the Antarctic as well as in the Arctic. The chemistry-climate model validation activity of SPARC (CCMVal; Eyring et al. (2008)) has highlighted the importance of process orientated validation of CCMs. While the CCMVal report of 2010 (SPARC-CCMVal, 2010) presented an analysis of polar ozone chemistry, this was primarily a comparison of HCl, $\mathrm{HNO_3}$ and $\mathrm{H_2O}$ concentrations with climatologies of those quantities derived from observations. As such, it was not a process oriented validation. This chapter outlines how such a process oriented validation might be undertaken using a semi-empirical model as a diagnostic tool.

The semi-empirical models used in Chapter 4 are not suitable for assessing individual key chemical processes that govern the activation and deactivation of chlorine and therefore to determine the extent of polar ozone depletion. Only one of the two main pathways for chlorine deactivation, i.e. formation of $\mathrm{ClONO_2}$, was considered in the semi-empirical model of chlorine activation and deactivation. In addition, the deactivation path is independent of $\mathrm{HNO_3}$ concentrations. As a result, the semi-empirical models used in Chapter 4 cannot capture the interhemispheric differences in chlorine deactivation. The effectiveness of individual chemical reactions for chlorine activation and deactivation also depends on the

availability/concentration of individual chemical species such as NO_x, Cl, and ozone. To include these processes, additional terms are required. To that end, the semi-empirical models used in Chapter 4 are significantly expanded to describe e.g. the tendencies in HNO_3, HCl, $ClONO_2$ and ozone.

This new semi-empirical model, referred to as SWIFT (Semi-empirical Weighted Iterative Fit Technique), describes the time rate of change of key quantities driving chlorine activation and deactivation. The basic equations for SWIFT were obtained from M. Rex (personal communication) and were then adapted for this chapter by (i) training SWIFT on ozone observations instead of ozone loss rates, (ii) including diabatic descent rates when calculating the chemical ozone depleting and (iii) applying SWIFT to the Arctic and Antarctic separately. As for the semi-empirical model employed in Chapter 4, SWIFT accounts for heterogeneous polar chemistry only. The correct representation of the chlorine partitioning, i.e. how much chlorine is present in its reactive forms (Cl, ClO, $ClOOCl$) compared to the abundances of chlorine present in the reservoir species (HCl and $ClONO_2$) is essential in accurately simulating ozone loss in the polar stratosphere.

Section 5.2 describes the set of first order differential equations that comprise SWIFT. The training of SWIFT on observations is described in Section 5.3 followed by a discussion of the fit-coefficients and their interpretation. When it came to applying SWIFT to a state-of-the-art chemistry climate model, in this case the EMAC-FUB (MA-ECHAM5/MESSy model system with the FUBRad radiation parameterizations), a number of issues were revealed that complicated the use of SWIFT as a diagnostic tool. Some of these issues are common across all CCMs e.g. SWIFT makes the assumption that little or no exchange of air occurs across the vortex boundary whereas, as shown by Struthers et al. (2009), CCMs tend to have more permeable vortex boundaries than is found in reality. Other issues were specific to the EMAC-FUB simulation when used as an example of SWIFT diagnosis. It was found that in many winters the formation of PSCs in EMAC-FUB was underestimated. This was traced to a bug in the PSC subroutine in EMAC-FUB which has subsequently been fixed. The fact that SWIFT could not be easily applied to EMAC-FUB output shows that this semi-empirical approach to CCM validation is likely to provide a very robust means of revealing deficiencies in CCMs. Therefore, this chapter focusses on fitting SWIFT to observed time series of the key trace gases in the polar stratosphere to provide the set of SWIFT fit-coefficients which can then act as the standard against which future application of SWIFT to CCMs can be compared. While a first look at the fitting of SWIFT to EMAC-FUB is presented in Section 5.4, this is only a preliminary study of the use of SWIFT in assessing EMAC-FUB. The chapter concludes with Section 5.5 which provides an outlook for further development and in particular how SWIFT might be applied to CCM validation

in the future. The EMAC-FUB data interpolated onto isentropic levels which were used in this chapter were provided by M. Kunze.

5.2 The semi-empirical model - SWIFT

SWIFT simulates the vortex average evolution of ozone, HCl, $ClONO_2$, gaseous HNO_3, HNO_3 (liquid/solid phase), and ClO_x on a chosen isentropic surface. Similar to the semi-empirical models described in Chapter 4, SWIFT is driven by daily values of the fractional area of the vortex covered by PSCs (FAP) and daily values of the 24 hour average fractional area of the vortex exposed to sunlight (FAS). Likewise, SWIFT makes the same assumptions about vortex isolation as were made for the semi-empirical models used in Chapter 4. However, unlike Chapter 4, all quantities in SWIFT are vortex averages calculated within the dynamical boundary demarcating the vortex edge. Therefore, in addition to temperature fields, wind and potential vorticity (PV, definition is given in Appendix A) fields on the chosen potential temperature surface are also required. Using daily wind and potential vorticity fields, the vortex edge can be determined by employing the method described in Nash et al. (1996). First the meridional impermeability (see Appendix A) at each equivalent latitude (κ) is calculated by multiplying the meridional gradient in potential vorticity with the horizonal wind speed. The vortex edge is then located at the meridional maximum in κ. The detailed calculation of equivalent latitude and κ, as well as the definition of vortex existence, is described in detail in Appendix A.

As stated above, SWIFT describes the tendency (time rate of change) of key chemical compounds in the polar stratosphere. The first order differential equations that comprise SWIFT assume that these tendencies result from the effects of heterogeneous chemistry only. Homogeneous chemical ozone depletion is assumed to be negligible as is mixing across the vortex edge (Schoeberl et al., 1992). Because Chapter 4 dealt with vertically integrated quantities, no consideration of the contribution of diabatic descent (see Chapter 1) to the trace gas tendencies was required. SWIFT, however, is applied on isentropic surfaces and as such, the effects of diabatic descent need to be corrected for. The tendency of some species X at a given isentropic surface should therefore be considered as:

$$\frac{d[X]}{dt} = \underbrace{\frac{\partial[X]}{\partial t}}_{\text{chemical change}} + \underbrace{\frac{\partial[X]}{\partial \theta} \cdot \frac{\partial \theta}{\partial t}}_{\text{diabatic descent}} \tag{5.1}$$

The chemical change, described by $\partial[X]/\partial t$, is what SWIFT focusses on. The second term on the right hand side of equation 5.1 describes the contribution of vertical diabatic trans-

port of X to the time rate of change in X, where $\partial[X]/\partial\theta$ is the vertical gradient of species X with respect to potential temperature and $\partial\theta/\partial t$ is the change in potential temperature with time.

It is usually only ozone which is sufficiently long-lived and which has a large enough vertical gradient that a correction for the contribution from diabatic descent (equation 5.1) needs to be applied. The lifetimes for reservoir species such as HCl, $\mathrm{ClONO_2}$, $\mathrm{HNO_3}$ are much shorter than for ozone and the tendency in these species is dominated by chemical effects such that

$$\frac{\partial[X]}{\partial t} \gg \frac{\partial[X]}{\partial\theta} \cdot \frac{\partial\theta}{\partial t} \tag{5.2}$$

and so equation 5.1 reduces to just the first term on the right hand side.

The chemically induced changes in ozone and related species, which are described by the first term on the right hand side of equation 5.1 ($\partial[X]/\partial t$), are not independent of each other. Therefore, SWIFT consists of a set of coupled differential equations which must be fitted simultaneously to derive the fit-coefficients.

5.2.1 The ozone tendency equation

SWIFT is primarily designed to describe the tendency in ozone concentrations. Given the concentration of activated chlorine in the polar stratosphere, the expectation might be that $\partial[O_3]/\partial t$ would depend on the square of the active chlorine concentration (see equation 4.9). Harris et al. (2010) showed that V_{PSC}, the volume of polar air cold enough for possible PSC existence, is a good proxy for chlorine activation and a number of other studies (Rex et al., 2004; Tilmes et al., 2004; Harris et al., 2010) found a nearly linear relationship between ozone loss and V_{PSC}. Harris et al. (2010) also showed that the relationship between ozone loss and the amount of activated chlorine ($\mathrm{ClO_x}$) is close to linear. Finally, the study by Tilmes et al. (2004) showed that the vortex average ozone loss is also an almost a linear function of the fraction of the time the air mass is exposed to sunlight. Therefore, the overall time rate of change in ozone can be formulated as:

$$\frac{d[O_3]}{dt} = -D \cdot [\mathrm{ClO_x}] \cdot FAS + \frac{\partial[O_3]}{\partial\theta} \cdot \frac{\partial\theta}{\partial t} \tag{5.3}$$

where D represents the empirical fit-coefficient, $\mathrm{ClO_x}$ is the vortex average concentration of activated chlorine described further below, and FAS represents the fractional area of the vortex that is exposed to sunlight. As in Chapter 4, FAS was calculated by applying equation 4.3, although it is now calculated as the fractional area with the dynamical vortex boundary, and not the area poleward of 62^oS as was done in Chapter 4, that is exposed to

sunlight. The change in ozone due to diabatic transport is represented by the second term on the right hand side of equation 5.3.

To apply equation 5.3, the evolution of ClO_x ($ClO_x = Cl + ClO + 2\times ClOOCl$) through the winter/spring has to be determined. The amount of ClO_x available to destroy ozone depends on partitioning of the total inorganic stratospheric chlorine loading (Cl_y = ClO_x + HCl + $ClONO_2$), i.e. the portion of Cl_y in the form of ClO_x compared to the portion of Cl_y in the form of non-ozone destroying reservoir species such as $ClONO_2$ and HCl, where most of the inorganic chlorine resides (Santee et al., 1996). The minor reservoir species $HOCl$ is not considered in SWIFT as the catalytic cycle involving ClO and HO_2 contributes less than 5% to the total loss of ozone (Salawitch et al., 1993). For an accurate representation of chlorine activation within the vortex, SWIFT needs to represent the key processes that convert the reservoir species into reactive chlorine and vice versa. Once the reservoir species have been calculated by SWIFT, the amount of reactive chlorine is calculated by:

$$[ClO_x] = [Cl_y] - [HCl] - [ClONO_2] \tag{5.4}$$

where Cl_y is the total concentration of all inorganic chlorine species and where HCl and $ClONO_2$ time series are generated by first order differential equations described in sections 5.2.2 and 5.2.3 below. Cl_y is assumed to be constant inside the vortex during winter/spring.

SWIFT accounts for several key mechanisms that control the balance between ClO_x and the reservoir species, $ClONO_2$ and HCl, which can be broadly divided into chlorine activation and deactivation. The chemical reactions involved in these processes, and their implementation in SWIFT, are described below. The equations that are implemented in SWIFT are colored in the following sections so that they can be attributed to the terms given in Figure 5.1, which summarizes all equations incorporated in SWIFT.

5.2.2 Chlorine activation

A detailed discussion of the heterogeneous chemistry underlying ozone depletion was presented in Chapter 1. A brief precise of that material, relevant to the specific formulation of the SWIFT equations, is provided here. Heterogeneous reactions on the surface of solid and liquid particles that involve $ClONO_2$, H_2O, and HCl provide two effective mechanisms to activate chlorine. The hydrolysis of $ClONO_2$ results in the formation of $HOCl$ and HNO_3:

$$ClONO_2(g) + H_2O(s,l) \rightarrow HOCl(g) + HNO_3(s,l) \tag{R1}$$

where (g) refers to the gas phase and (s,l) to the solid or liquid phase, respectively. $HOCl$ is quickly photolyzed, releasing chlorine and hydroxyl radicals. The effectiveness of reaction R1 depends strongly on the composition of the particles involved in the heterogeneous reactions. As described in Chapter 1, these particles include (depending on the particle type), HNO_3, sulfuric acid and/or water. At higher sulfuric acid concentrations, or at lower temperatures, more of the H_2O is taken up onto the particles to be used in reaction R1. Accordingly, reaction R1 becomes more important at very low temperatures. The hydrolysis of $ClONO_2$ is implemented in the model by:

$$\mathrm{ClONO2_{hydro}} = -\mathrm{H} \cdot [\mathrm{ClONO_2}] \cdot FAP' \tag{5.5}$$

where H is the fit-coefficient. The $ClONO_2$ hydrolysis (reaction R1) is only triggered when reaction R2 (see below) becomes sufficiently slow i.e. when the coverage of the vortex by PSCs exceeds some threshold. The FAP' term in equation 5.5 accounts for this threshold sensitivity of $ClONO_2$ hydrolysis by being defined as $FAP - yy$, where yy is also a model fit coefficient. FAP' is set to have a minimum value of zero. As in Chapter 4, FAP was calculated by applying equation 4.2, although it is now calculated as the fractional area with the dynamical vortex boundary, and not the area poleward of 62° S as was done in Chapter 4.

The uptake of HCl onto liquid PSC particles increases the reactivity of $ClONO_2$. As stratospheric temperatures decrease, the solubility of HCl increases and the reaction:

$$\mathrm{ClONO_2(g) + HCl(s,l) \rightarrow Cl_2(g) + HNO_3(s,l)} \tag{R2}$$

becomes faster than the hydrolysis of $ClONO_2$ (reaction R1). Cl_2 is rapidly photolyzed in the sunlit atmosphere, releasing two chlorine atoms. As a result, Cl_2 cannot build up in significant quantities. Accordingly, in SWIFT, the photolysis of Cl_2 is ignored and reaction R2 together with the photolysis of Cl_2 is equivalent to a system that directly produces ClO_x. When HCl concentrations are low, reaction R2 is limited by the uptake of HCl onto the PSC particles and the effectiveness depends not only on the concentration of $ClONO_2$ but also on the HCl concentrations. Furthermore, for low HCl concentrations, reaction R1 dominates the chlorine activation, representing a sink for $ClONO_2$. The efficiency of chlorine activation via reaction R2 (i.e. the reaction of $ClONO_2$ with HCl, hereafter referred to as $ClONO2wHCl$) is implemented in the SWIFT model by:

$$\mathrm{ClONO2wHCl} = -A \cdot [\mathrm{ClONO_2}] \cdot [\mathrm{HNO_3}] \cdot FAP \tag{5.6}$$

and for very low HCl concentrations ($\mathrm{HCl} \leq$10 ppt)

$$\mathrm{ClONO2wHCl_{low}} = -A \cdot [\mathrm{ClONO_2}] \cdot [\mathrm{HCl}] \cdot [\mathrm{HNO_3}] \cdot FAP \tag{5.7}$$

where A is the fit-coefficient and the term $[\mathrm{HNO_3}] \cdot FAP$ acts as a proxy for the availability of reactive surfaces. Reactions 5.6 and 5.7 drive changes in both the $\mathrm{ClONO_2}$ and HCl.

The photodissociation of $\mathrm{ClONO_2}$ is also a source of reactive chlorine because the primary end products are Cl and $\mathrm{NO_3}$. The photodissociation is represented in SWIFT by:

$$\mathrm{ClONO2_{photo}} = -G \cdot [\mathrm{ClONO_2}] \cdot FAS \tag{5.8}$$

where the fit-coefficient G describes the efficiency of the photodissociation.

5.2.3 Chlorine deactivation

$\mathrm{ClONO_2}$ is one of the most important chlorine reservoir species in the polar stratosphere and is formed by the three body process:

$$\mathrm{ClO} + \mathrm{NO_2} + \mathrm{M} \rightarrow \mathrm{ClONO_2} + \mathrm{M} \tag{R3}$$

where the third body M is a collision partner needed for conservation of momentum. This reaction provides an effective mechanism to convert reactive chlorine into the chemically inert reservoir species $\mathrm{ClONO_2}$. However, reaction R3 is limited by the amount of available $\mathrm{NO_2}$. As the winter polar lower stratosphere is heavily denoxified (Chipperfield et al., 1997), i.e. removal of gaseous nitrogen oxide ($\mathrm{NO_x}$) by converting $\mathrm{NO_x}$ species into $\mathrm{HNO_3}$ (Chapter 1), the recovery of $\mathrm{ClONO_2}$ is driven by the release of $\mathrm{NO_2}$ from the photolysis of $\mathrm{HNO_3}$.

$$\mathrm{HNO_3} + h\nu \rightarrow \mathrm{OH} + \mathrm{NO_2} \tag{R4}$$

However, the amount of gaseous $\mathrm{HNO_{3_g}}$ is suppressed by the uptake of $\mathrm{HNO_{3_g}}$ onto PSCs particles which inhibits the reformation of $\mathrm{ClONO_2}$. When temperatures rise and PSCs evaporate, gaseous $\mathrm{HNO_{3_g}}$ is released and reaction R4 produces $\mathrm{NO_2}$. This is followed by the fast reaction with ClO which deactivates reactive chlorine.

When ClO concentrations are high, reaction R3 is fast and it can be assumed made that $\mathrm{ClONO_2}$ is directly produced from reaction R4. The photolysis of $\mathrm{HNO_3}$ as a source of $\mathrm{ClONO_2}$ is presented in SWIFT as:

$$\mathrm{HNO3_{photo}} = B \cdot [\mathrm{HNO_3}](g) \cdot FAS \tag{5.9}$$

where B is the fit-coefficient and HNO_{3_g} is provided by a separate first order differential equation described further below. For very low ClO_x concentrations ($ClO_x \leq 0.2\,ppb$) and therefore low ClO concentrations, the production of $ClONO_2$ via reaction R3 is limited and depends on the amount of available reactive chlorine:

$$HNO3_{photo\_low} = B \cdot [ClO_x] \cdot [HNO_3](g) \cdot FAS \tag{5.10}$$

An alternative pathway for the deactivation of chlorine is provided by the production of HCl, with the most important source reactions being:

$$ClO + OH \rightarrow HCl + O_2 \tag{R5}$$

$$Cl + CH_4 \rightarrow HCl + CH_3 \tag{R6}$$

Unless ozone concentrations are very low, the formation of the relatively inert reservoir species HCl plays a secondary role in deactivating chlorine as the timescale of reforming HCl is about the same as the timescale for HNO_3 photolysis (Santee et al., 1996, and references therein). As a result, reactions R5 and R6 are much slower than the deactivation of chlorine compounds via the formation of $ClONO_2$ (reaction R3) and both reactions R5 and R6 can be ignored when calculating vortex average ozone. When ozone decreases to very low values, e.g. during the formation of the Antarctic ozone hole, the main loss process for chlorine:

$$Cl + O_3 \rightarrow ClO + O_2 \tag{R7}$$

cannot occur and the Cl concentration increases. As a result, reaction R6 becomes very fast, and chlorine is primarily deactivated by forming the reservoir species HCl. The chlorine deactivation by HCl production is implemented in SWIFT by:

$$Chorine_{prod} = C \cdot [ClO_x] \cdot FAS \cdot \frac{1}{O_3} + F \cdot ClO_x \cdot FAS^2 \tag{5.11}$$

where C and F are the fit-coefficients and the term $[ClO_x] \cdot FAS$ describes the photolysis of ClO and $ClOOCl$, both of which release chlorine atoms that can react with methane CH_4 (reaction R6) contributing to the HCl recovery.

The chemical reactions described above drive chlorine deactivation and activation, and thereby control the balance between ClO_x and the reservoir species $ClONO_2$ and HCl. For reactions R2 and R4, HNO_{3_g} is required. As the denoxification of the lower stratosphere is completed within the first few weeks during winter, the assumption is made that total HNO_3 has no source. Therefore, all nitrogen containing species, except $ClONO_2$, (NO_y = NO_x + HNO_3) are present in the form of HNO_3, i.e. NO_y = HNO_3. The production of HNO_3

via reaction R2 can be neglected as the $\mathrm{ClONO_2}$ abundances are relatively small (about 2 ppb) compared to the $\mathrm{NO_y}$ concentrations (between 8 and 18 ppb). Based on this assumption, the change in the vortex average total $\mathrm{HNO_3}$ concentration is primarily determined by photolysis and denitrification. However, the photolysis of $\mathrm{HNO_3}$ is slow during winter and can be neglected in SWIFT. The microphysical processes that describe the formation, growth, and sedimentation of PSC particles are very complex and cannot be captured in any detail in this simple semi-empirical model approach. To describe the details of nucleation, growth and sedimentation a Lagrangian microphysical model that calculates the temporal changes in $\mathrm{HNO_3}$ along trajectories, accounting for growth, evaporation and transport, is needed. However, although $\mathrm{HNO_3}$ concentrations are needed for the chemistry in activating and deactivating chlorine, it is not a key species and a rather simple description of denitrification is sufficient to describe the chemical processes. Therefore, denitrification as implemented in SWIFT only depends on the size of the PSC area, i.e. FAP. Gravitational sedimentation of $\mathrm{HNO_3}$ containing PSC particles provides an efficient process to denitrify the stratosphere, however, particles sizes of many micrometers (10 to 20 μm) are required before denitrification sets in. PSC particles grow rapidly if the temperature falls below the ice frost point, since water ice can then accumulate on these particles. Depending on the lifetime of PSC particles, they can also grow if their trajectories stay within the area of the vortex where the temperature is below T_{NAT}. A prerequisite for these two processes are large values for FAP. Therefore, in the model, denitrification is triggered if FAP exceeds a threshold value yy and then the fraction greater than the threshold is scaled with the amount of available total $\mathrm{HNO_3}$. In SWIFT, the effectiveness of denitrification is represented by:

$$\mathrm{HNO3_{denit}} = -E \cdot [\mathrm{HNO_3}] \cdot FAP' \tag{5.12}$$

where E is a fit-coefficient. FAP' is zero if FAP is smaller than the threshold yy and otherwise FAP'=$FAP - yy$ as was the case for the hydrolysis of $\mathrm{ClONO_2}$.

From the total amount of $\mathrm{HNO_3}$ calculated by SWIFT, the gaseous $\mathrm{HNO_3}$ is computed by:

$$[\mathrm{HNO_3}](g) = [\mathrm{HNO_3}](t) \cdot (1 - FAP) + zz \cdot [\mathrm{HNO_3}](t) \cdot FAP$$

where zz is a fit-coefficient. Other than when PSCs exist, i.e. FAP=0, $\mathrm{HNO_3}$ total is equal to gas phase $\mathrm{HNO_3}$ ($\mathrm{HNO_3(g)}$) while when PSCs exist, $\mathrm{HNO_{3_g}}$ is a scaling of $\mathrm{HNO_3}$(t).

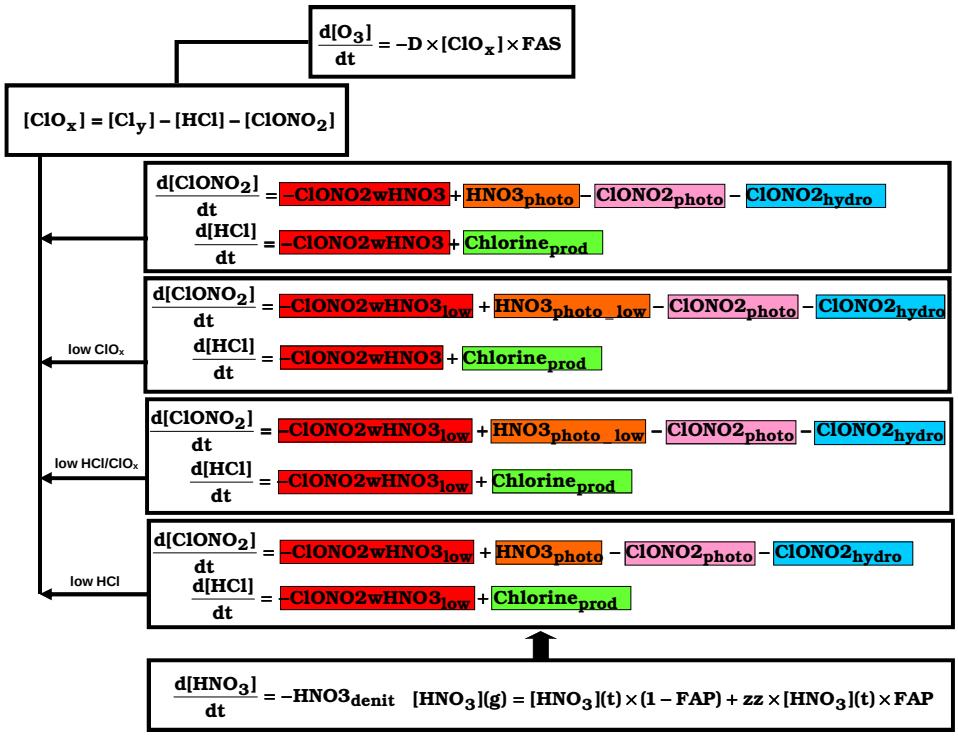

Figure 5.1: SWIFT model equations where the individual terms are color coded corresponding to the equations given in Sections 5.2.2 and 5.2.3. (individual processes are described in text).

5.3 Empirical determination of the fit-coefficients

The first step towards using SWIFT as a means of validating the polar heterogeneous chemistry in CCMs, is to fit SWIFT to real world observations to obtain the set of fit-coefficients against which coefficients derived from fitting to the CCM can be compared. Here, the SWIFT equations are fitted to satellite observations of ozone, HCl, and gaseous $\mathrm{HNO_3}$ (all obtained from the AURA-MLS instrument) and to $\mathrm{ClONO_2}$ (obtained from the ACE-FTS instrument). The satellite instruments are described in Chapter 2. Vortex average concentrations of these trace gases were provide on the 460 K ($\sim$20 km) surface by M. Santee. This surface was chosen as this is where polar ozone loss maximizes (e.g. Konopka et al., 2004). When calculating those vortex mean values, rather than using the PV value demarcating the vortex edge on each day, the median value derived separately for each winter was used. To remain consistent with the calculation of the observed trace gas time series, the FAP and FAS values required were also calculated over the dynamical vortex area demarcated by seasonally constant PV values. For the Arctic, the 35.6 PVU (potential vorticity unit) contour is used while for the Antarctic the 31.2 PVU contour is used to mark the vortex edge. As described in Appendix A, the existence of the vortex is based on the seasonal behaviour of κ which requires PV and wind fields as input. These fields, together

with temperature fields, were obtained from the latest reanalyses of the European Center for Medium-Range Weather Forecasts (ECMWF), ERA-interim.

Before being used to establish the fit-coefficients, the contribution of diabatic descent to the ozone tendency must be determined (right hand term in equation 5.1). Diabatic descent rates for the 460 K surface, representative of the Arctic and Antarctic stratosphere, were extracted from Rosenfield et al. (1994) who also show that the interannual differences in the diabatic descent rates in the Arctic and Antarctic vortex are relatively small. While the values taken from Rosenfield et al. (1994) were for years different from those used here, the small interannual variability, and the fact that SWIFT tracks the increase in ozone early in the season (see below), suggests that using these values to correct for the effects of diabatic descent is valid. The assumption of insignificant interannual variability may introduce uncertainties, especially in the dynamically more active Arctic vortex. The vertical gradient in ozone ($\partial[O_3]/\partial\theta$) was derived from a seven year climatology of HALOE (Halogen Limb Occultation Experiment) and UARS-MLS vortex average ozone observations. This ozone gradient, together with the diabatic descent, is used to estimate the vortex average vertical ozone transport.

Fitting the SWIFT equations to observations during one Arctic winter (2004/2005) and one Antarctic winter (2006) results in two sets of 10 fit-coefficients derived separately for the Arctic and Antarctic. The differential equations (Figure 5.1) are solved by employing a fourth order Runge-Kutta method (Press et al., 2007). As was done with the semi-empirical models used in Chapter 4, a combination of the interval halving method and the non-linear least squares fitting method, that minimizes the sum of the squares of the residuals, is used to find the best set of parameters that optimally fits the measurements (for details see Chapter 4). The sum of the squares of the residuals is calculated individually for all species and is then accumulated into a total sum. The optimization procedure described in Chapter 4 minimizes the total sum to derive the fit-coefficients. Because the ACE-FTS measurements of $\mathrm{ClONO_2}$ are less reliable (see Chapter 2), the sum of the squares of the residuals from the $\mathrm{ClONO_2}$ fitting is weighted by 0.3 compared to those from the other fits. On the other hand, because the fit to ozone is deemed to be the primary output from SWIFT, the sum of the squares of the residuals from the ozone fit is weighted by 3.

To simplify the fitting procedure, to allow the seasonal evolution of the different trace gases to be displayed in the same figure, and to allow the fit-coefficients to be directly compared, all measurement time series to which SWIFT was fitted were normalized by dividing each time series by the value on the first day of the season (see Table 5.1). SWIFT is initialized on the first day when FAP becomes non-zero, e.g. PSC formation starts, and ozone, $\mathrm{Cl_y}$,

Species	Arctic	Antarctic
HNO_{3_g}	11.8 ppb	10.6 ppb
$ClONO_2$	1.8 ppb	2.4 ppb
HCl	1.8 ppb	2.4 ppb
O_3	2.9 ppb	2.6 ppb

Table 5.1: Scaling factors as used to compare the normalized model concentrations with satellite observation.

and HNO_3 are set to unity. Further, it is assumed that Cl_y is only present in the form of HCl, $ClONO_2$ and ClO_x. Since within the model no chlorine activation can occur without the presence of PSCs, the initial value for ClO_x is set to zero and, as a result, the ratio of HCl to Cl_y and the ratio of $ClONO_2$ to Cl_y can be derived from the observations at the beginning of the simulation. Therefore, according to the satellite measurements, the initial value for $ClONO_2$ is set to $\sim$30% of Cl_y and to $\sim$70% of Cl_y for HCl.

As the time rate of change in total HNO_3 depends only on FAP and is therefore independent of the concentration of the other key species controlling chlorine activation and deactivation, the fit-coefficients E, yy, and zz can be derived independently of the other SWIFT equations. The fitting of the HNO_3 tendency equation is described in Section 5.3.1 below. Once this fit has been completed, the remaining 7 fit parameters are derived as described in Section 5.3.2.

5.3.1 Fitting the HNO_3 equation

To determine the fit-coefficients E, zz, and yy, SWIFT calculates the evolution of total HNO_3 from which HNO_{3_g} is derived. The sum of the squares of the differences between the SWIFT modelled HNO_{3_g} and the Aura-MLS HNO_{3_g} observations is minimized, resulting in two optimal sets of parameters for the Arctic and Antarctic. The derived fit-coefficients are summarized in Table 5.2. The modelled total HNO_3 and HNO_{3_g} using the derived fit-coefficients, together with the MLS HNO_{3_g} observations are shown in Figure 5.2.

Fit-coefficient	Arctic	Antarctic
E	0.26	0.02
zz	0.81	0.48
yy	0.58	0.35

Table 5.2: Derived fit-coefficients for the Arctic and Antarctic by applying SWIFT to gas phase HNO_3 Aura-MLS observations.

As shown in Figure 5.2, the model simulates higher rates of denitrification for the Antarctic than for the Arctic as expected due to the larger PSC extent (greater FAP values) in the Antarctic. The uptake of HNO_{3_g} onto PSC particles occurs rapidly, as soon as PSCs form, resulting is a relatively steep decrease in HNO_{3_g} at the beginning of the Antarctic winter. The HNO_{3_g} concentration minimizes with the maximum in FAP. As temperature and solar radiation increases, PSCs evaporate as represented by decreasing FAP values, and HNO_{3_g} is released. As soon as FAP falls below the threshold for denitrification (represented by yy), total HNO_3 concentrations stay constant. With the completed disappearance of PSCs, HNO_{3_g} equals HNO_3 total.

As Arctic temperatures are not as low as in the Antarctic, fewer PSCs are formed resulting in a smaller rate of denitrification than in the Antarctic. This interhemispheric difference is reproduced by SWIFT, where the concentration of HNO_3 total is reduced by 60% during the Antarctic winter while the denitrification in the Arctic results in a reduction of about 50% in these particular winters. The uptake of HNO_{3_g} at the beginning of the winter occurs about as rapidly as in the Antarctic as soon as PSCs are formed, resulting in about the same slope of the HNO_{3_g} decrease as in the Antarctic. The ratio of HNO_3 total to HNO_{3_g} is smaller in the Arctic than in the Antarctic and therefore less HNO_{3_g} is tied up in PSC particles in the Arctic winter. As in the Antarctic, as soon as FAP values fall below the threshold for denitrification, HNO_3 total remains constant and with the disappearance of PSCs, HNO_{3_g} concentrations increase.

An initial examination of the HNO_3 fit-coefficients in both hemispheres might lead one to conclude that the efficiency of the denitrification process is higher in the Arctic than in the Antarctic. It should be noted however that the denitrification process in the Arctic is triggered at higher FAP values than in the Antarctic. The difficulty here is that the seasonal evolution of HNO_3 and HNO_{3_g} results from the combined effects of multiple terms whose fit-coefficients are correlated. Rather than comparing the individual fit-coefficients, a better test of the complementarity of the coefficients is to use the coefficients derived for one hemisphere in the equations for the other hemisphere. When the Antarctic coefficients are used in the Arctic, a reasonable fit to the observations is obtained (red dashed line right hand panel of Figure 5.2). This suggests that when comparing results from SWIFT fitted to observations with SWIFT fitted to CCMs, rather than comparing the fit-coefficients, it is more meaningful to use the coefficients from one system in the equations for the other and then compare the quality of the fits. Because of the interdependence of the fit-coefficients, a similar evolution in HNO_3 can be modelled for quite dissimilar fit-coefficients. Alternatively, if fit-coefficients are derived simultaneously for two systems (e.g. Arctic and Antarctic, or reality and a CCM) and are found to provide equally acceptable quality of fits in both

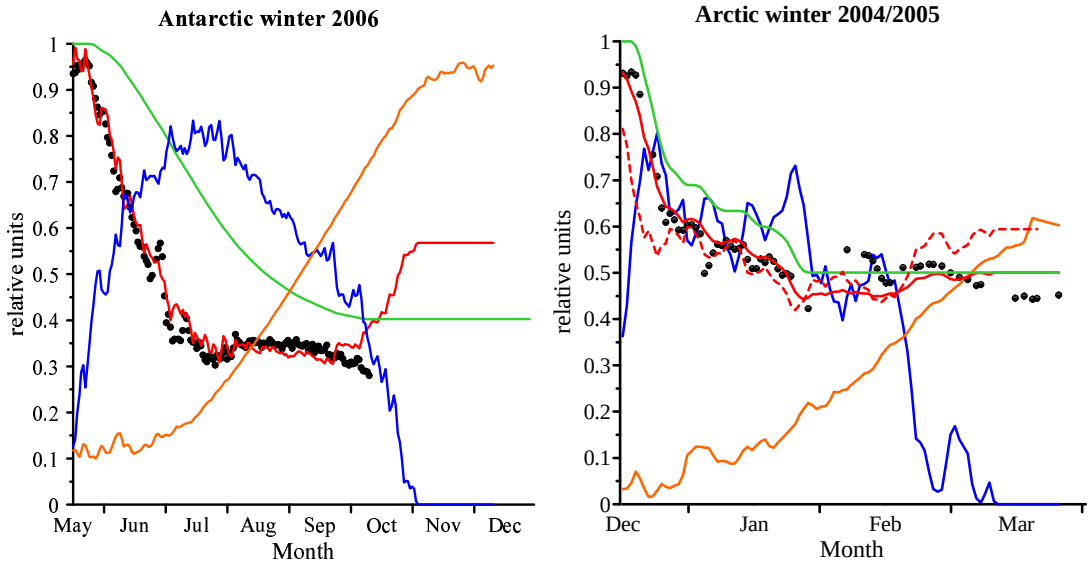

Figure 5.2: Modelled HNO_3 total (green line) and HNO_3 gas phase (red line) compared to MLS observations of gaseous HNO_3 (black symbols) for one Antarctic and one Arctic winter. The dashed red line in the right panel represent the SWIFT modelled HNO_3 gas phase using the derived fit-coefficients from the Antarctic observations. The calculated FAP (blue line) and FAS (orange line) are also included in this figure.

systems, the behaviour of the two systems can be taken to be comparable. The strategy then is to fit SWIFT to both systems separately (obtaining two sets of fit-coefficients) and then simultaneously (obtaining a single set of fit-coefficients). If the sum of the squares of the differences between the fits and the data being fitted changes substantially between these two approaches, the systems are fundamentally different.

It should also be noted that the fits derived above are for a single Antarctic winter and a single Arctic winter. Anomalous behaviour is one of these cases might produce fit-coefficients that are not generally representative of that hemisphere. Future analysis will extend this work to multiple years. In spite of these caveats, the results presented above indicate that the denitrification process is captured fairly well by SWIFT so that the derived evolution of HNO_3 total and HNO_{3_g} can be used to model the vortex average evolution of the remaining species.

5.3.2 Simulating chlorine activation and deactivation

The SWIFT equations were fitted to observations of vortex averaged ozone, $ClONO_2$ and HCl to derive the remaining fit-coefficients. The resulting fits, together with the HNO_{3_g} fit, are shown, together with the observed vortex averaged trace gas concentrations, for the Antarctic vortex in Figure 5.3 and for the Arctic vortex in Figure 5.4. The corresponding

fit-coefficients, that provide a measure of the importance of the individual chemical reactions driving chlorine activation and deactivation, are summarized in Table 5.3.

Fit-coefficient	Arctic	Antarctic	see equations
A	0.31	0.25	5.6, 5.7
B	0.35	0.21	5.9, 5.10
C	0.00	0.0061	5.11
D	0.063	0.032	5.3
F	0.39	0.45	5.11
G	0.11	0.38	5.8
H	0.60	0.00	5.5

Table 5.3: Derived fit-coefficients by applying SWIFT to Aura-MLS and ACE-FTS measurements.

In 2006, the Southern Hemisphere lower stratosphere was cold enough so that 50% and more of the polar vortex was covered by PSCs from mid-June to the end of September. With the formation of PSCs, particles take up $\mathrm{HNO_{3_g}}$, and HCl and heterogenous processes convert the reservoir species into reactive chlorine. As a result HCl concentrations decrease and together with $\mathrm{ClONO_2}$, reactive chlorine is formed leading to an increase in $\mathrm{ClO_x}$ concentrations (Figure 5.3). The observed strong decline in HCl at the beginning of the winter is well reproduced by SWIFT. The minimum in HCl coincides with the maximum FAP values at the beginning of August. In contrast to the measurements, modelled HCl concentrations drop almost to zero by the end of July/beginning of August. During that period, $\mathrm{ClONO_2}$ concentrations increase slightly and do not drop below $\sim$0.16 ppb. Furthermore, the reactive chlorine concentrations peak by the end of July and decrease thereafter. As soon as FAP values no longer increase, HCl and $\mathrm{ClO_x}$ concentrations reverse their previous trends.

With the onset of PSC evaporation, and therefore decreasing FAP values, the HCl concentrations start to increase. This increase results from the release of HCl due to the evaporation of PSC particles but also from the reaction of chlorine with methane (reaction R6), where the latter contribution to the HCl recovery becomes more important with lower ozone abundances towards the end of the winter. With the increase in HCl, reactive chlorine is deactivated, as seen in the decline in $\mathrm{ClO_x}$. The decline in $\mathrm{HNO_{3_g}}$ slows once FAP maximizes and less $\mathrm{HNO_3}$ is taken up onto PSC particles. As a result, more $\mathrm{HNO_{3_g}}$ is available for photodissociation (reaction R4) which, however, is slow. The small rise in $\mathrm{ClONO_2}$ concentrations is a result of the photolysis of $\mathrm{HNO_{3_g}}$. The photodissociation of $\mathrm{HNO_{3_g}}$ does not produce enough $\mathrm{NO_x}$ that can combine with ClO to deactivate chlorine via reaction R3. As a result, chlorine is kept active longer and ozone concentrations decrease further, even though the activation of chlorine on PSC particles is reduced. With the decline

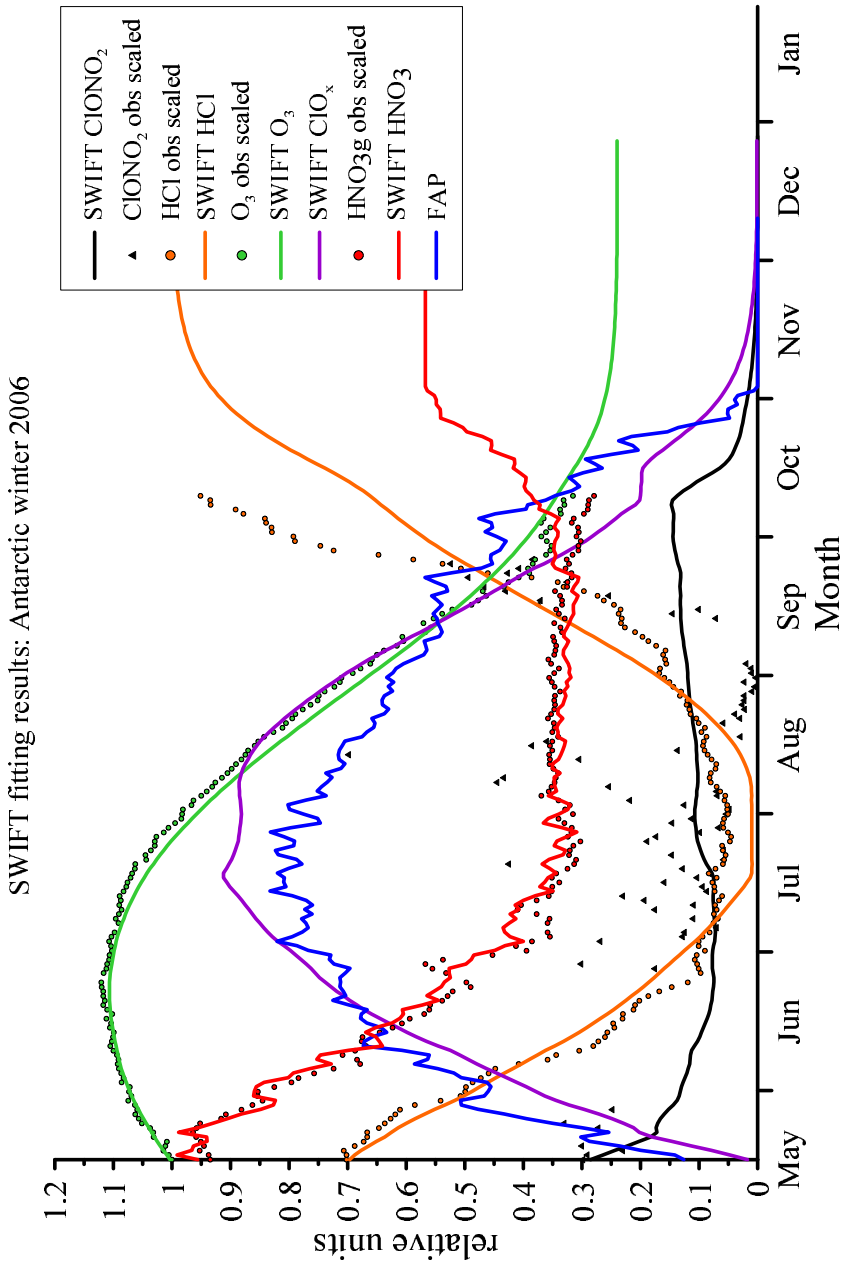

Figure 5.3: Evolution of vortex average $ClONO_2$ (black line), HCl (orange line), HNO_{3_g} (red line), ozone (green line) and ClO_x (purple line) concentrations together with calculated FAP values (blue line) as simulated by SWIFT and as observed by Aura-MLS (ozone, HCl, HNO_{3_g}) and ACE-FTS ($ClONO_2$) for the Antarctic winter 2006. The vortex average concentrations are calculated within a constant potential vorticity contour of 31.2 PVU.

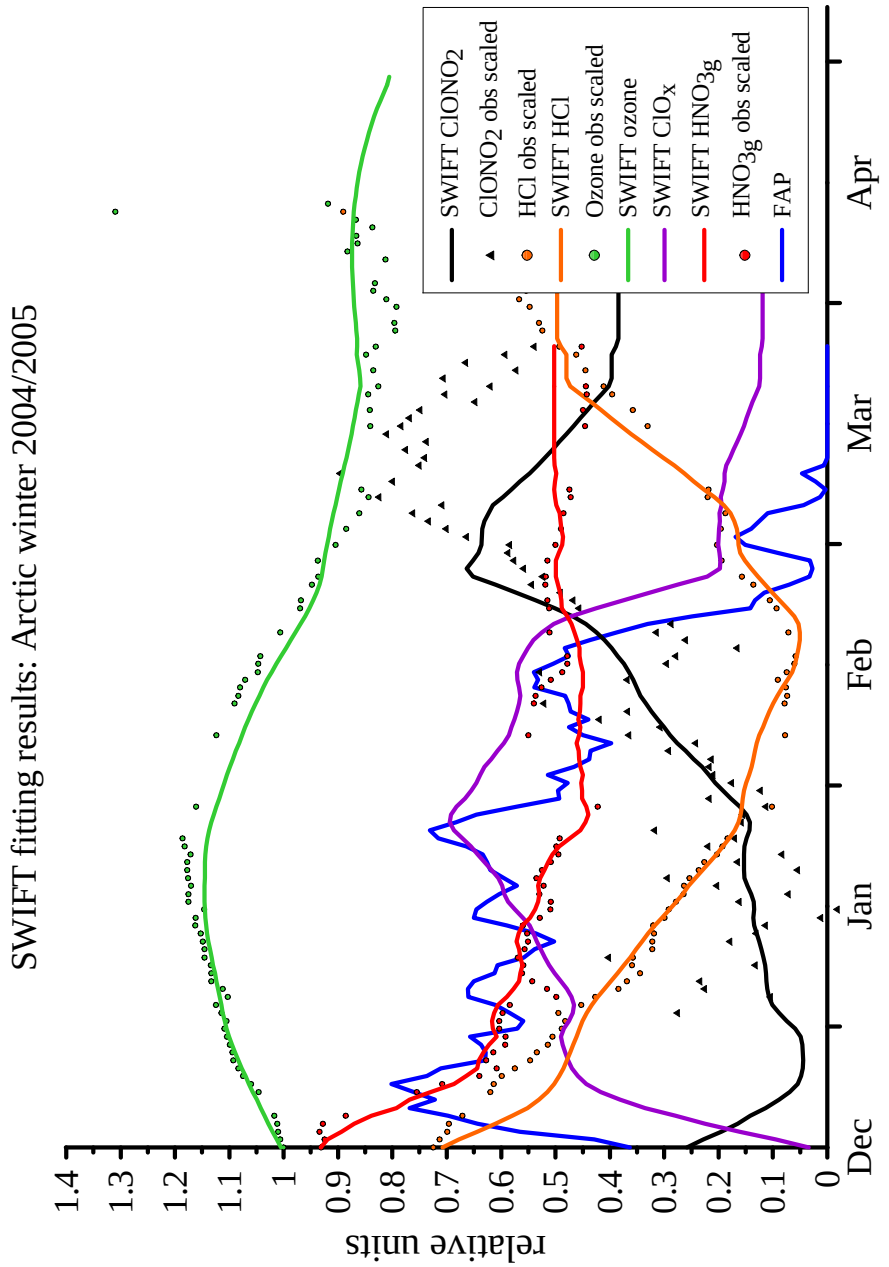

Figure 5.4: Evolution of vortex average $ClONO_2$ (black line), HCl (orange line), HNO_{3_g} (red line), ozone (green line) and ClO_x (purple line) concentrations together with calculated FAP values (blue line) as simulated by SWIFT and as observed by Aura-MLS (ozone, HCl, HNO_{3_g}) and ACE-FTS ($ClONO_2$) for the Arctic winter 2004/2005. The vortex average concentrations are calculated within a constant potential vorticity contour of 35.6 PVU.

in ozone, more chlorine atoms can build up and the reaction R6 becomes an effective deactivation mechanism for chlorine. This explains the rapid reformation of HCl at the end of the winter. The preferential reformation of HCl in the Antarctic is also represented in the coefficients B and F (Table 5.3). As represented by the fit-coefficient F, the photodissociation of ClO_x that releases chlorine atoms, plays the dominant role in deactivating chlorine by reforming HCl while the smaller coefficient B indicates that the reformation of $ClONO_2$ via reaction R3 plays a minor role in chlorine deactivation. The observed steep rate of increase in $ClONO_2$ at the end of the winter is not reproduced by SWIFT. However, this increase most likely results from an ACE-FTS sampling artifact (Santee et al., 2008b) (see Chapter 2) rather than from chemistry. Furthermore, the photolysis of $ClONO_2$ dominates the overall tendency in $ClONO_2$ (represented in fit-coefficient G). This photodissociation causes the steep decline in $ClONO_2$ in October which is related to the stagnant ClO_x decline during that time. The hydrolysis of $ClONO_2$ does not contribute to chlorine activation at all as the H coefficient is zero. This indicates that the HCl concentration does not go low enough so that reaction R1 becomes important. By the end of the analysis period, all inorganic chlorine is in the form of HCl and therefore the dominant chlorine reservoir species at the beginning and at the end of Antarctic winter is HCl.

The overall vortex average evolution of ozone is well captured by SWIFT. At the beginning of the winter, ozone concentrations increase due to downward vertical transport across potential temperature surfaces. This ozone supply partially masks the ozone depletion due to catalytic cycles as shown in Figure 5.5. In the Antarctic winter, diabatic descent ceases by the end of July (Rosenfield et al., 1994). As a result, no vertical transport of ozone occurs and only chemical processes contribute to the ozone tendency (Figure 5.5). At 460 K, the ozone concentration decreases by about 70% from its initial value. However, without any vertical transport of ozone, almost all ozone would have been depleted at that potential temperature as shown in Figure 5.5.

In the dynamically more disturbed Arctic vortex, temperatures in the lower stratosphere are higher than in its southern counterpart and the vortex is covered by PSCs for a shorter time period. Furthermore, PSCs cover less of the vortex compared to the Antarctic such that FAP values exceeding 0.5 occur over a time period of only 1.5 months (mid December to the end of January) compared to 3-4 months in the Antarctic. Because ACE-FTS samples outside or near the vortex edge in December 2004 (Santee et al., 2008b), no ACE-FTS $ClONO_2$ measurements inside the vortex are available before the beginning of 2005. However, the onset of chemical processes that activate chlorine starts with the formation of PSCs, and therefore the model is initialized from the first day of PSC occurrence, regardless of whether measurements exists or not.

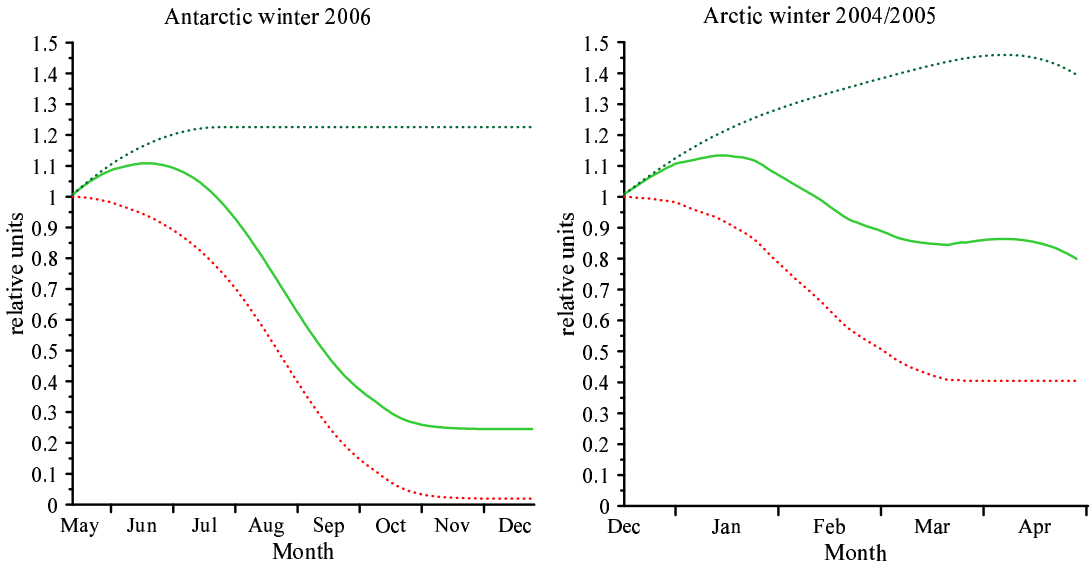

Figure 5.5: SWIFT modelled vortex average ozone concentrations (green) for the Antarctic winter 2006 and the Arctic winter 2004/2005. The dark green line indicates vortex average ozone concentrations if no chemical destruction would occur and the red line indicates vortex average ozone concentrations if there was no diabatic descent inside the vortex.

SWIFT reproduces the vortex averaged evolution of HCl very well in the Arctic winter. The measurements and the model show a continuous decrease in HCl as soon as PSCs are formed and until PSCs evaporate, starting in mid February. Even when stratospheric temperatures increase, HCl remains suppressed, whereas $ClONO_2$ increases rapidly (Figure 5.4). $ClONO_2$ hydrolysis, whose effectiveness is represented by H, is the most effective reaction for chlorine activation in the first few weeks at the beginning of the winter, resulting in the strong decrease in $ClONO_2$. However, this decrease does not last long, as with the uptake of HCl onto PSCs particles, reaction R2 is favored for chlorine activation. The steep increase in ClO_x changes to a more moderate increase due to reaction R2. The uptake of HNO_{3_g} onto PSCs particles is less than observed in the Antarctic. Therefore, more HNO_{3_g} is available, and as soon as enough sunlight is available (beginning of January) small amounts of NO_x are released leading to the formation of $ClONO_2$, even though chlorine activation via reaction R2 still takes place.

Once heterogeneous processes slow, a strong increase in $ClONO_2$ is observed, which is well reproduced by SWIFT. This early deactivation of chlorine, by the end of January, prevents severe ozone depletion in the Arctic. From the end of January onwards to the beginning of March, $ClONO_2$ is the dominant reservoir species and the equilibrium between $ClONO_2$ and HCl slowly recovers at the end of the winter. Contrary to the Antarctic winter, where FAP values well above 0.5 were present, and HCl concentrations were increasing, HCl concentrations do not increase until PSCs evaporate at the end of February. This result,

together with the more moderate increase in HCl at the end of the winter, indicates that the formation of HCl via reaction R6 is suppressed due to the lack of chlorine atoms. This inter-hemispheric difference in chlorine deactivation is represented in the fit-coefficients (Table 5.3).

In the Arctic winter, the evolution of vortex averaged ozone is also well represented by SWIFT. The amount of ozone reduces by about 20% during the winter (light green trace in right-hand panel of Figure 5.5). Without vertical transport of ozone, chemical ozone destruction would have caused a reduction in ozone of about 60% (red trace in right-hand panel of Figure Figure 5.5). This difference is larger than was observed for the Antarctic because of the stronger diabatic transport in the Arctic vortex than in the Antarctic vortex. This large influence in the Arctic highlights the importance of considering diabatic descent when determining the chemical ozone loss within the Arctic vortex. It also highlights the need for diabatic descent rates to be produced as an output from CCMs if SWIFT is to be used as a diagnostic for those CCMs.

The results presented above show that SWIFT reproduces the observed vortex average evolution of the key species for polar ozone loss well. This demonstrates that SWIFT is able to capture the key sensitivities of ozone loss to chlorine activation and deactivation.

5.4 Application of SWIFT to EMAC-FUB

To test SWIFT as a diagnostic tool for assessing the heterogeneous chemistry in CCMs, output from the EMAC-FUB CCM was used to derive the SWIFT fit-coefficients. The EMAC-FUB model is described in Section 5.4.1. Because a number of issues were revealed when applying SWIFT to EMAC-FUB, only preliminary results (i.e. only the HNO_3 fits) are presented in Section 5.4.2. In Section 5.5 a brief overview is given on the issues in EMAC-FUB, and in CCMs in general, that prevent direct application of SWIFT. This is followed by an outlook on how SWIFT might be adapted to better deal with known deficiencies in CCMs.

5.4.1 Model description - EMAC-FUB

EMAC-FUB is based on the 5^{th} generation European Centre Hamburg GCM, ECHAM5 (Roeckner et al., 2003) that is coupled to the Modular Earth Submodel System (MESSy) (Jöckel et al., 2005). The EMAC-FUB model includes a spectrally resolved short-wave radiation routine (Nissen et al., 2007) as well as the atmospheric chemistry module MECCA1

(Sander et al., 2005) that can be used for tropospheric and stratospheric chemistry calculations. The chemistry module includes stratospheric homogeneous and heterogeneous ozone chemistry involving the basic ozone, CH_4, HO_x, and NO_x chemistry and the main chlorine and bromine reactions in the stratosphere. The module also accounts for the ozone related chemistry of the troposphere, including non-methane hydrocarbon chemistry. The kinetic reaction rates, as recommended by Sander et al. (2003), are used in the chemistry scheme.

In the vertical, the model consists of 39 levels on a hybrid-pressure grid, extending from the surface to the uppermost layer centered at 0.01 hPa ($\sim$80 km). Therefore, the model not only includes the troposphere but also the stratosphere and mesosphere. The enhanced vertical resolution near the tropopause is 500 m. The spectral horizonal resolution of T42 was chosen for the model, i.e. 42 wave numbers are used to describe all of the fields in the model. The corresponding quadratic Gaussian grid has a resolution of approximately $2.8^\circ \times 2.8^\circ$ in latitude and longitude. Gravity wave drag, which, in part, drives the meridional circulation in the middle atmosphere, is parameterized following Miller et al. (1989).

For this chapter, EMAC-FUB data were extracted from the CCMVal-SCN2d sensitivity simulation covering the period from 1960 to 2100. This simulation includes anthropogenic and natural forcings. Greenhouse gas (GHG) concentrations are taken from the SRES A1b scenario IPCC (2001) and ozone depleting substances (ODSs) are based in the adjusted A1 scenario from WMO (2007). Natural variability due to solar variability, the quasi biennial oscillation (QBO) and volcanic activity is considered in the simulation. The lower boundary conditions such as sea surface temperatures (SSTs) and sea ice were simulated externally by an AOGCM based on the SRES A1b GHG scenario and then prescribed in the SCN2d simulation.

5.4.2 Preparation of EMAC-FUB input

Output from EMAC-FUB from four Arctic winters (1960/1961, 1999/2000, 2049/2050, 2099/2100) and four Antarctic winters (1961, 2000, 2050, and 2100) were used in this study. Because the SWIFT model is designed to capture key processes in the polar stratosphere, the model fit-coefficients are not expected to be time dependent; all time dependence is captured through the year-to-year changes in Cl_y, FAS and FAP. Theoretically, the SWIFT fit-coefficients should be traceable to fundamentals of the chemistry such as reaction rate coefficients and/or photolysis coefficients.

To calculate the vortex averages of the key chemical species obtained from EMAC-FUB, first the location of the vortex edge must be determined. For this purpose, wind fields were extracted from EMAC-FUB simulations and potential vorticity (PV) fields were calculated from the required EMAC-FUB output and provided by M. Kunze. Both wind and PV fields were used to calculate the location of the vortex edge by applying the method described in Nash et al. (1996) and Appendix A. On days when the vortex exists, PV values demarcating the vortex edge are determined. These daily values were used to calculate the yearly median PV value demarcating the vortex edge for each winter. The derived median PV values for the Arctic and Antarctic winters are summarized in Table 5.4. These values are not dissimilar to those calculated from for the observations, indicating that EMAC-FUB generates a dynamical vortex of realistic area. To quantify the seasonal evolution of all trace gases, the area weighted mean within the given median PV contour demarcating the vortex edge is calculated for each species. Furthermore, similar to the observations, FAS and FAP values were also derived based on the location of the vortex edge. The temperature fields required for the calculation of FAP were also extracted from EMAC-FUB and provided by M. Kunze.

Fit-coefficient	Year	median PV [PVU]
Arctic	1960/1961	29.3
	1999/2000	35.4
	2049/2050	33.2
	2099/2100	29.7
Antarctic	1961	-32.1
	2000	-33.5
	2050	-32.4
	2100	-30.4

Table 5.4: Calculated median vortex edge potential vorticity (in PV units) as derived from EMAC-FUB model output.

5.4.3 Fitting the $\mathrm{HNO_3}$ equation

When applying SWIFT to the EMAC-FUB output, the same assumptions are made as for the observations. As shown below, known model deficiencies may at times lead to a breakdown in these assumptions which complicates the fitting of SWIFT to the model output. As was done with the observations, the fit-coefficients describing the efficiency of the denitrification within EMAC-FUB are first derived by applying SWIFT to the vortex averaged concentrations of $\mathrm{HNO_{3_g}}$. As in the case of the observations, the EMAC-FUB vortex average trace gases are divided by the values given in Table 5.5 to produce time series that have a normalized initial value. The SWIFT model is initialized on the first day when PSCs are

formed, i.e. when FAP is greater than zero. The resultant SWIFT fits for the four Antarctic and Arctic winters are shown in Figure 5.6 and Figure 5.7, respectively. The corresponding fit-coefficients are summarized in Table 5.6.

	Year	scale factor $\mathrm{HNO_{3g}}$
Arctic	1960/1961	9.88
	1999/2000	9.72
	2049/2050	10.25
	2099/2100	9.77
Antarctic	1961	8.67
	2000	8.87
	2050	8.95
	2100	7.60

Table 5.5: Scale factors applied to EMAC-FUB modelled $\mathrm{HNO_{3_g}}$ concentrations.

	Year	E	yy	zz
Arctic	1960/1961	0.037	0.18	1.0
	1999/2000	0.014	0.00	1.0
	2049/2050	0.088	0.26	0.98
	2099/2100	0.011	0.00	1.0
Antarctic	1961	0.037	0.38	0.92
	2000	0.063	0.50	0.84
	2050	0.014	0.006	0.65
	2100	0.012	0.00	0.57

Table 5.6: Scale factors as applied to EMAC-FUB modelled $\mathrm{HNO_{3_g}}$ concentrations to be comparable to SWIFT model output.

The fit-coefficients show clear interannual variability. However, as cautioned above, a more meaningful assessment of the degree of agreement between SWIFT fits to two different systems is whether the fit-coefficients derived from one system can provide an adequate fit when applied in the second system. To this end, the fit-coefficients derived from reality (see Table 5.2) for the Antarctic and Arctic were used in the EMAC-FUB $\mathrm{HNO_3}$ tendency equations to generate the time series shown with red dashed lines in Figure 5.6 and Figure 5.7, respectively. The quality of the Arctic fits is compromised by the fact that this version of the EMAC-FUB simulation contained a bug in the PSC code (which has subsequently been fixed) which resulted in no PSCs forming in the Arctic stratosphere (see further discussion below). The Arctic fits are therefore excluded from this discussion. In spite of the fact that the same bug was present in the code used to simulate PSCs in the Antarctic, using the $\mathrm{HNO_3}$ fit-coefficients derived from reality for EMAC-FUB in the Antarctic results in broadly similar behaviour in 1961 and 2000, and very similar behaviour in 2050 and 2100. This suggests that EMAC-FUB shows a seasonal evolution in gas phase $\mathrm{HNO_3}$ that is quite

consistent with that found in reality. A test with output from the revised version of EMAC-FUB is expected to lead to even better agreement between the fits.

The Antarctic lower stratospheric temperatures modelled by EMAC-FUB are sufficiently low that more than half of the polar vortex is covered by PSCs for about 4 months in every winter of the analysis period. The EMAC-FUB $\mathrm{HNO_{3_g}}$ concentrations show a steep increase in the first weeks of the winter. This increase is present in all four winters and indicates that the denoxification is not completed by the beginning of the winter and/or vertical transport within the polar vortex provides a source for $\mathrm{HNO_{3_g}}$. Therefore, the production of $\mathrm{HNO_{3_g}}$ is greater than the uptake of $\mathrm{HNO_{3_g}}$ onto PSC particles. When the polar vortex is denoxified, PSC particles take up $\mathrm{HNO_{3_g}}$ and its concentration rapidly decreases. Once the FAP values maximize, the steep decline changes to a more moderate decrease in $\mathrm{HNO_{3_g}}$. Even when temperatures increase and PSCs evaporate, $\mathrm{HNO_{3_g}}$ does not increase but rather levels off at a constant value. Due to the large PSC extent resulting from the EMAC-FUB temperatures, and the high uptake rate of $\mathrm{HNO_{3_g}}$, a high rate of denitrification (between 60% and 80%) is simulated by SWIFT. Furthermore, for the first two winters (1961 and 2000) $\mathrm{HNO_{3_g}}$ and total $\mathrm{HNO_3}$ simulated by SWIFT are nearly the same which is also represented in the empirical fit-parameter zz.

It is not expected that SWIFT should perfectly fit the $\mathrm{HNO_{3_g}}$ concentrations modelled by EMAC-FUB as the microphysical processes are so complex and are not included in SWIFT (see above). However, the steep increase at the beginning of the winter needs further investigation. The next step would be to extract the $\mathrm{NO_x}$ data from the CCM simulation. The $\mathrm{NO_x}$ data from EMAC-FUB are readily available and so extending the analysis in this way can be done in a future study. If the vortex average concentration of $\mathrm{NO_x}$ is greater than zero, the polar vortex is not completely denoxified. During polar night, the production of $\mathrm{HNO_{3_g}}$ primarily occurs via the heterogeneous reaction on aerosol droplets ($\mathrm{H_2SO_4/H_2O}$ solutions):

$$\mathrm{N_2O_5}(g) + \mathrm{H_2O}(s,l) \rightarrow 2 \times \mathrm{HNO_3}(g) \qquad \text{(R8)}$$

Reaction R8 is very fast and has no strong temperature dependence (Peter, 1997). Therefore, this reaction provides a very effective way to produce $\mathrm{HNO_3}$ as the gas-phase conversion of $\mathrm{NO_2}$ to $\mathrm{HNO_{3_g}}$ is very slow (Brasseur and Solomon, 2005). Therefore, if for example, aerosol surfaces within EMAC-FUB are too small, an incomplete denoxification at the beginning of the winter can result. Another reason for incomplete conversion of nitrogen species into $\mathrm{HNO_{3_g}}$ could be that the reaction rates for the heterogeneous chemistry are too slow or the modelled temperatures are too high, so that the uptake of $\mathrm{H_2O}$ onto sulfate aerosols ($\mathrm{H_2SO_4}$) and therefore reaction R8 are delayed. If EMAC-FUB shows that the vortex average concentrations of $\mathrm{NO_x}$ are not zero at the beginning of the winter, this

would indicate that one of the processes discussed above is not well represented in EMAC-FUB.

One solution to this problem would be to use $\mathrm{NO_y} = \mathrm{NO_x} + \mathrm{HNO_3}$ instead of $\mathrm{HNO_{3_g}}$ to fit the equation in SWIFT. As one assumption in SWIFT is that all $\mathrm{NO_y}$ is in $\mathrm{HNO_3}$ the fit-coefficients derived from the observations would be still comparable with the coefficients derived from EMAC-FUB data. This correction should eliminate the steep increase in $\mathrm{HNO_{3_g}}$ at the beginning of the winter (Figure 5.6). If, however, the vortex is completely denoxified at 460 K, this would suggest that vertical transport provides a source for $\mathrm{HNO_{3_g}}$ and, depending on the diabatic descent rate in the model, this source can cause the steep increase in $\mathrm{HNO_{3_g}}$ as shown in Figure 5.6. If the latter is the case, an additional term accounting for diabatic descent needs to be included in SWIFT so that this source of $\mathrm{HNO_{3_g}}$ is considered. Without any further investigation it is not possible to judge which process within EMAC-FUB is causing the increase in $\mathrm{HNO_{3_g}}$. As a result, the denitrification process is difficult to quantify and it is very difficult to interpret the derived fit-coefficients and to compare these coefficient to the observations.
EMAC-FUB simulates much higher temperatures in the lower stratospheric in the Northern Hemisphere compared to the Southern Hemisphere, so that fewer PSCs are formed in the Arctic winters. For all four Arctic winters, FAP values stay below 0.5 and the variation in these FAP values is higher than in the Antarctic as a result of the more dynamically variable Arctic vortex. The smaller extent of PSCs affects the denitrification in the Arctic as less $\mathrm{HNO_{3_g}}$ is taken up by PSCs particles. The overall rate of denitrification is reduced compared to the Antarctic and SWIFT models a reduction of $\mathrm{HNO_3}$ total between 15 and 30%. The further decrease in $\mathrm{HNO_{3_g}}$ after PSCs evaporate indicates the loss of $\mathrm{HNO_{3_g}}$ due to photolysis (reaction R4) or due to vertical transport inside the polar vortex. For all Arctic winters, the concentration of $\mathrm{HNO_{3_g}}$ simulated by SWIFT is identical to that for total $\mathrm{HNO_3}$. This result is somewhat surprising and is investigated further below.

As in the Antarctic, $\mathrm{HNO_{3_g}}$ concentrations increase at the beginning of each winter. The increase is not as steep as in the Antarctic but the increase takes place over a longer period. The differences in the slope of the $\mathrm{HNO_{3_g}}$ increase indicates that the denoxification process is not completed in the Arctic and Antarctic at the beginning of the winter. If vertical transport would cause that increase, it would be expected that the gradient is greater in the dynamically more disturbed Arctic vortex, as the diabatic descent rates are greater there than in the Antarctic (Rosenfield et al., 1994).

As indicated from the results presented above, one possible cause for the increase in $\mathrm{HNO_{3_g}}$ is the incorrect representation of lower stratospheric temperature fields in EMAC-FUB. Ho-

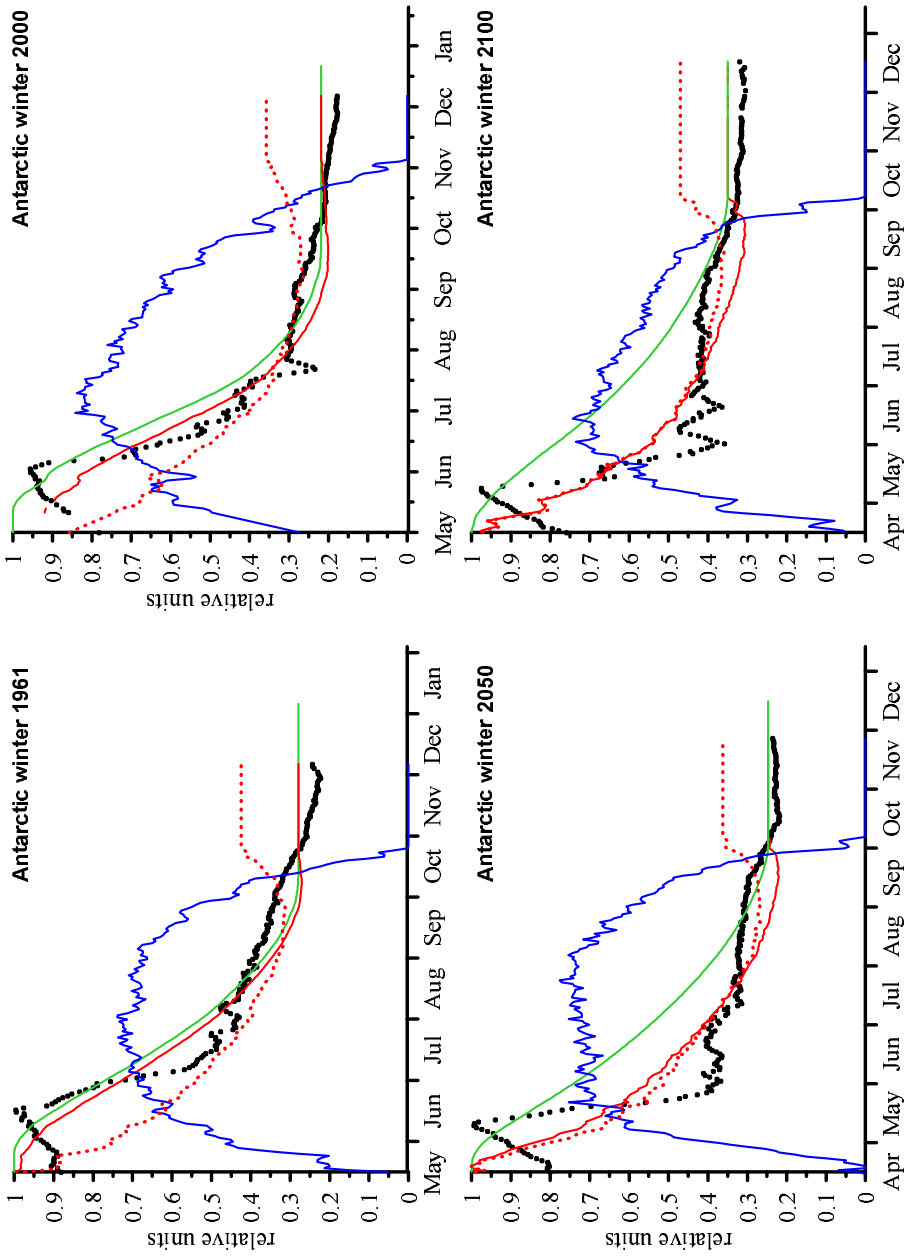

Figure 5.6: Modelled vortex average HNO_{3_g} concentrations from EMAC-FUB (black symbols) compared to SWIFT modelled concentrations of HNO_{3_g} (red solid line) and HNO_3(t) (green line) for the Antarctic winters 1961, 2000, 2050 and 2100. The dashed red line presents the SWIFT modelled HNO_{3_g} using the fit-coefficients derived from the observations. The blue line indicates FAP values calculated from EMAC-FUB temperature fields.

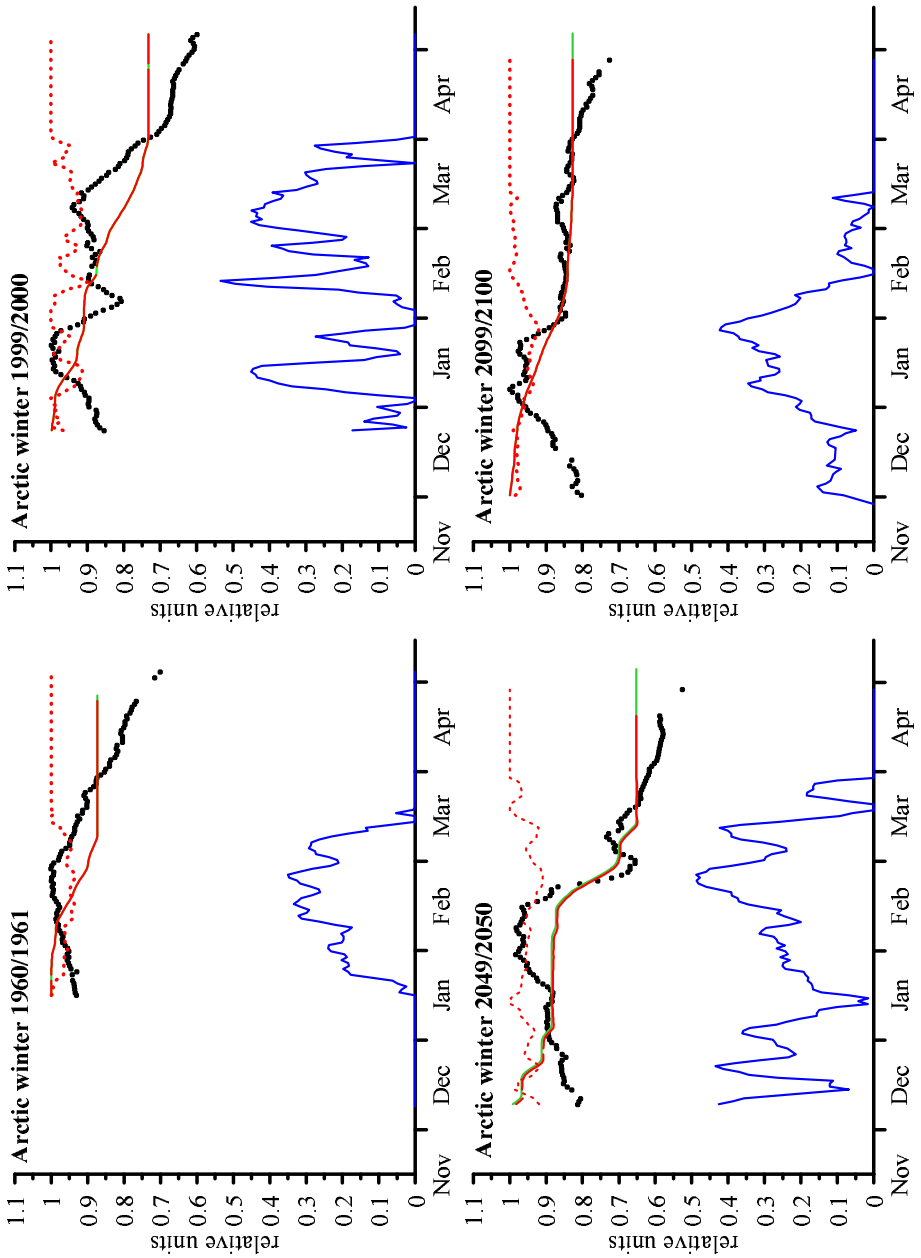

Figure 5.7: Modelled vortex average HNO_{3_g} concentrations from EMAC-FUB (black symbols) compared to simulated concentrations of HNO_{3_g} (red solid line) and HNO_3(t) (green line) from SWIFT for the Arctic winters 1960/1961, 1999/2000, 2049/2050 and 2099/2100. It should be noted that SWIFT modelled HNO_{3_g} is identical to SWIFT modelled HNO_3 total and therefore the red and green lines overlap. The dashed red line presents the SWIFT modelled HNO_{3_g} using the fit-coefficients derived from the observations. The blue line indicates FAP values calculated from EMAC-FUB temperature fields.

wever, this possibility seems to be very unlikely as the FAP values used here were derived from the EMAC-FUB temperature fields. A rather more likely possibility is that the PSC formation temperature in EMAC-FUB is different from the formation temperature used here. If, for example, a lower PSC formation temperature is used in EMAC-FUB than in SWIFT, the heterogenous chemistry would start earlier in SWIFT than it does in the EMAC-FUB model as SWIFT produces FAP earlier than EMAC-FUB. As a result, the simulated evolution of the trace gas species would not agree with the evolution simulated by EMAC-FUB. Even more so, the derived fit-coefficients would be reduced solely because of the lower PSC formation temperature in EMAC-FUB and this could lead to a incorrect interpretation of the key processes in the CCM. As a different PSC formation temperature is not uncommon in CCMs because of known temperature biases and different microphysical schemes, this possible cause of uncertainties has to be considered when applying SWIFT to CCMs.

Besides $\mathrm{HNO_{3_g}}$, EMAC-FUB also provides $\mathrm{HNO_3}$(nat) data which represents the amount of the total $\mathrm{HNO_3}$ taken up into PSC particles. It transpired that EMAC-FUB did not produce any, or only very little, $\mathrm{HNO_3}$(nat) in the Arctic winter 1960/1961 and 1999/2000, and even in the Antarctic, the $\mathrm{HNO_3}$(nat) concentrations were very low. This result strongly indicates that the PSC formation temperature in EMAC-FUB is lower than the temperature threshold used to calculate FAP here. It was later found that an error in the PSC subroutine in EMAC-FUB caused deficiencies in the simulation of PSC formation, because even if the simulated temperatures were very low, no PSCs were formed. This could be one explanation for why EMAC-FUB $\mathrm{HNO_{3_g}}$ increases at the beginning of the winter, as shown in Figure 5.6 and Figure 5.7.

The results presented above show that SWIFT is not directly applicable to EMAC-FUB output. Some behaviour issues such as the steep $\mathrm{HNO_3}$ increase at the beginning of the Antarctic and Arctic winter need further detailed investigation and additional model output to find the actual causes for that increase. Furthermore, using the example of differences in the PSC formation temperature between EMAC-FUB and SWIFT it was shown that it is very likely that model deficiencies will affect the SWIFT calculations. SWIFT does not account for any model deficiencies and therefore further development is required to apply SWIFT to CCM output. The issues mentioned above need to be resolved first, before the rest of the parameters can be determined because otherwise a correct assessment of the results is not possible. As a result, EMAC-FUB output was not used to derive the remaining 7 parameters. Instead, an outlook for future work is presented in the following section.

5.5 Conclusion and Outlook

The main differences between CCM simulations of the atmosphere and the real atmosphere result from internal model deficiencies. The CCMVal initiative focusses on process-oriented validation of CCMs to assess their performance and reliability. A comparison of CCM model output with observations and other models allows identification of model deficiencies. Therefore, while model deficiencies are often known, they are also often difficult to quantify. SWIFT, as it stands, does not accommodate any model deficiencies. Therefore, if SWIFT applied to CCM output produces different results to SWIFT applied to observations, it is difficult to identify if the differences result from a dynamical deficiency, which may then violate some of the assumptions in SWIFT, or from an inability of the CCM to accurately simulate the chemical process under consideration. This section will provide a general discussion of where CCMs, in general, currently have short-comings and how these might be problematic for the application of SWIFT.

As reported in SPARC-CCMVal (2010), large differences among CCMs exist regarding PSC formation, PSC types, and PSC particle sizes. Traditionally, the PSC formation temperature, T_{NAT}, is calculated according to Hanson and Mauersberger (1988) and depends on $\mathrm{HNO_3}$ mixing ratios, $\mathrm{H_2O}$ mixing ratios and pressure, while T_{ICE} is calculated according to Marti and Mauersberger (1993). However, due to known polar temperature biases (SPARC-CCMVal, 2010) it is not uncommon that PSC formation temperatures deviate from the formation temperature calculated by applying the expressions given in Hanson and Mauersberger (1988) and Marti and Mauersberger (1993) in CCMs. The PSC formation temperature used to calculate FAP in SWIFT was calculated based on Hanson and Mauersberger (1988) using a prescribed $\mathrm{H_2O}$ and $\mathrm{HNO_3}$ profile. Using a PSC formation temperature in SWIFT that is different to that used in CCMs leads to an incorrect representation of the chemical processes as the timing of chlorine activation and deactivation depends on the occurrence of PSCs. Therefore, before applying SWIFT to CCM output, the PSC formation temperature used in the CCM needs to be known to reliably assess the processes in CCMs.

SWIFT, as is stands, does not account for any production of $\mathrm{HNO_3}$ as it is assumed that the polar vortex is denoxified at the beginning of the SWIFT integration. Only denitrification can change $\mathrm{HNO_3}$ concentrations in SWIFT. However, it is known that $\mathrm{HNO_3}$ is transported downward by diabatic descent in the polar vortex (Arnold et al., 1998). Diabatic heating rates and therefore the vertical velocity in the polar vortex varies among the CCMs. As a result, the degree to which $\mathrm{HNO_3}$ is transported vertically depends on the CCM. To account for $\mathrm{HNO_3}$ production in SWIFT, the CCM modelled diabatic descent rates should

be included in the HNO_3 equation as it was done for ozone in this chapter. Another advantage of implementing the diabatic descent is that it allows for the investigation of the processes leading to an HNO_3 increase at the beginning of the winter, i.e. it could be investigated if the HNO_3 increase results from an incomplete denoxification at the beginning of the winter or if the HNO_3 increase is caused by vertical transport across isentropic surfaces.

In applying SWIFT to observations, it is assumed that the air masses inside the vortex are well isolated from mid latitude air masses and horizonal mixing is negligible. However, as shown in the study by Austin et al. (2010b), in some CCMs mixing across the vortex edge occurs and is usually too high. Therefore, applying SWIFT to CCM output without accounting for horizontal mixing processes can result in an underestimation of catalytic ozone depletion as mixing across the vortex edge provides a source/sink for trace gases. Without accounting for mixing, one could conclude that the key processes leading to chlorine activation and deactivation are not well represented in the CCM. To prevent such an incorrect conclusion, horizontal mixing needs to be included in SWIFT before it can be applied to CCMs. One possible solution could be to determine the concentration of the trace gas outside of the polar vortex. Knowing the trace gas concentration inside the vortex and outside, an additional 'mixing parameter' M could be introduced in SWIFT:

$$(\mathrm{TraceGas}_{\mathrm{inside}} - \mathrm{TraceGas}_{\mathrm{outside}}) * M \tag{5.13}$$

SWIFT would model the trace gas concentration inside the vortex and the concentration outside the vortex is assumed to be constant. M is a empirical fit-coefficient accounting for meridional mixing. Including this term (equation 5.13) into the SWIFT equations would provide a measure of how much mixing across the vortex edge occurs in CCMs and to what extent mixing affects the chemical processes could be estimated. Future tests are required to investigate the applicability of such an additional term in SWIFT.

The ability of SWIFT to simulate the key chemical processes leading to chlorine activation and deactivation was demonstrated in this chapter. As these processes are well represented, SWIFT simulated the Antarctic and Arctic evolution of ozone very well. To investigate the applicability of SWIFT as a diagnostic tool to evaluate chemical processes in CCMs, further development of the SWIFT equations, and an assessment of possible model deficiencies that affect the polar ozone chemistry in CCMs, is required. Accounting for model deficiencies in SWIFT and then applying SWIFT to CCM output would not only provide a tool to assess the representation of key chemical processes driving ozone depletion but it would also provide a tool to quantify the effect of model deficiencies on chemical processes driving ozone depletion. Therefore, possible causes for the inaccurate representation of polar ozone loss in CCMs can be assessed by applying SWIFT to CCM output. Knowing

which process is poorly represented in CCMs or knowing the effect of model deficiencies on polar ozone chemistry, is a first step to improve the CCMs.

Chapter 6

Conclusion and Outlook

The aim of this thesis was to assess sources of uncertainties in model simulations of polar stratospheric ozone levels and model projections of the future of the Antarctic ozone hole. This thesis focussed on three sources of uncertainty arising from: (i) uncertainties in key kinetic reaction rates used by CCMs to calculate ozone depletion, (ii) uncertainties in future emissions of GHGs and (iii) uncertainties in the representation of key processes, such as chlorine activation and deactivation, driving polar ozone depletion in CCMs. Ground-based and satellite-based measurements of key trace gases involved in polar ozone destruction were used to investigate these uncertainties.

To reliably model stratospheric ozone loss it is essential to reduce the uncertainties on the key kinetic parameters governing the effectiveness of the ClO-dimer cycle (Kawa et al., 2009) which is the most important contributor to overall polar ozone loss (SPARC, 2009). Using Antarctic day-time ClO profile measurements, this thesis presented two approaches to derive the key kinetic parameters which control the day-time partitioning of ClO and its dimer and therefore polar ozone depletion. It was found that the derived J/k_f ratios are in overall agreement with previous studies and the results indicate that the lower uncertainty range on this ratio recommended by JPL06 and JPL09 could be excluded. Furthermore, the results suggest that if K_{eq} lies in the range of the derived values from previous studies (e.g. Plenge et al., 2005; Stimpfle et al., 2004; Santee et al., 2010), then the retrieved J/k_f ratio would lie in the upper half of the given uncertainty range reported by JPL06 and JPL09. As the study was limited by the information content provided by the ClO measurements, since only day-time measurements were available, is was not possible to individually quantify J and k_f.

To explore the full set of parameters (J, k_f, and K_{eq}) individually, additional information is required such as day-time and night-time measurements as well as hourly measu-

rements describing the diurnal evolution of ClO during the day and night. This highlights the importance of developing an approach to separately extract the day-time and night-time information from measured ClO spectra. Such an approach requires finding a way to remove baseline artefacts, and most importantly, to remove the interference of the ozone and nitrogen dioxide lines in the measured ClO spectrum. Such an approach is currently under investigation (Brian Connor, personal communication) and therefore, if successful, day-time and night-time ClO measurements can be used in a future study to investigate the drivers of day-time and night-time partitioning of ClO and ClOOCl individually.

Day-time and night-time ClO measurements from the Arctic and Antarctic would allow an investigation of interhemispheric differences in the effectiveness of the ClO-dimer cycle for depleting ozone. The Arctic vortex is dynamically more disturbed than its southern counterpart resulting, on average, in about 10 K higher stratospheric temperatures than in the Antarctic. The kinetic reaction rates k_f and K_{eq} are known to be temperature dependent; an increase in temperature results in a decrease in k_f, i.e. a slowing of the dimer formation, and therefore a decrease in K_{eq}, i.e. ClOOCl decomposes and ClO is favored during night-time. Therefore, using Arctic and Antarctic night-time measurements of ClO to derive estimates of K_{eq} could reveal information about the temperature dependence of the equilibrium constant and could reduce the current uncertainty range on K_{eq}. Furthermore, the analysis of day-time Arctic and Antarctic measurements of ClO tests the J/k_f ratio temperature dependence (assuming J is well know) and its implication for the effectiveness of the ClO dimer cycle. Using ClO measurements from both the Arctic and Antarctic can therefore be used to derive estimates of the relationship between temperature and the effectiveness of the ClO-dimer cycle in both hemispheres.

Most of the field studies recently performed to investigate the kinetics of the ClO-dimer cycle focussed on ClO and/or ClOOCl measurements made in the Arctic. The study presented here highlights the need for more studies examining the key kinetic parameters under stratospheric conditions observed in the Antarctic. It was shown previously that ClOOCl measurements can be made in the Arctic stratosphere (Stimpfle et al., 2004; Wetzel et al., 2010) and that these measurements provide a useful addition to ClO measurement to test the reliability of the J/k_f ratio and K_{eq} derived in the laboratory. Therefore, in addition to Antarctic ClO measurements, Antarctic measurements of ClOOCl would provide useful means of investigating interhemispheric differences, and to reduce the uncertainties on the kinetics, and to improve our understanding of the ClO-dimer cycle and its effectiveness.

ClO and its dimer are in thermal equilibrium during most of the day-time and night-time and the day-time partitioning between ClO and ClOOCl is then driven by the J/k_f ratio.

Only for a few hours after sunrise and a few hours after sunset, are ClO and ClOOCl in non-equilibrium conditions and it is during this time of the day when information about J and k_f individually can be obtained. This highlights the need for in-situ and/or ground-based measurements during this non-equilibrium period to test the fidelity of the kinetics separately. The ability to extract hourly ClO profiles without subtracting the night-time measurement is a prerequisite for investigating J and k_f during this non-equilibrium condition between ClO and its dimer. The use of satellite measurements (e.g. from UARS-MLS, AURA-MLS) is precluded for such a study as the overpass of the satellite is limited to two times a day which does not necessarily coincide with dusk and dawn.

Another technique to assess our understanding of polar chemical processes and their role in ozone depletion is to formulate a semi-empirical model that describes these processes. This thesis presented such a semi-empirical model, SWIFT, that describes the key processes of chlorine activation and deactivation in the polar stratosphere. Instead of using kinetic reactions rates, empirical fit-coefficients were used that describe the effectiveness of the chemical reactions driving ozone destruction in the Arctic and Antarctic. This model was trained on satellite measurements of key trace gases involved in chlorine activation and deactivation. It was shown that SWIFT describes the these key processes and the resultant ozone loss well, including the interhemispheric differences of chlorine deactivation at the end of the winter.

Knowing that SWIFT correctly describes the atmospheric processes driving polar ozone chemistry, this thesis aimed to test the applicability of SWIFT as a diagnostic tool for investigating the representation of these key processes in coupled chemistry-climate models (CCMs). However, when applying SWIFT to CCM output, a number of issues were revealed which complicated the application of SWIFT. CCMs are known to have deficiencies such as excessive mixing across the vortex edge. The formulation of SWIFT does not easily accommodate such model deficiencies. Dynamical deficiencies in the CCM, which may then violate some of the fundamental assumptions in SWIFT (such as large mixing across the vortex edge), may prevent the use of SWIFT to identify chemical deficiencies. This thesis showed that to use SWIFT as a diagnostic tool, additional terms have to be incorporated in the SWIFT equations which account for CCM deficiencies. SWIFT could then provide a powerful tool not only to assess the chemical processes represented in CCMs but also to quantify the contribution of model deficiencies to the overall performance of the key processes controlling ozone depletion in CCMs. The preliminary results presented here suggest that with further development SWIFT can provide a powerful diagnostic tool for assessing and validating CCMs.

Another source of uncertainty in projections of ozone through the 21st century is that that arises from GHG and ozone depleting substance emissions scenarios. As the atmosphere-ocean general circulation models (AOGCMs) currently used to project future changes in the global climate system are not suitable for assessing the future evolution of stratospheric ozone and an alternative approach, complementary to CCMs, was presented in this thesis. This approach consists of semi-empirical models that describe the evolution of vortex average activated chlorine concentrations that can be related to the vortex average evolution of total column ozone loss, with respect to 1960 levels, in the Antarctic stratosphere. The models are driven by vortex averaged PSC coverage, that can be calculated from any temperature field, and by solar illumination. Using NCEP/NCAR temperature fields, these models were trained on satellite measurements. It was shown that the semi-empirical models reproduce the observations of activated chlorine and ozone loss well including the interannual variability.

Future ozone projections were conducted for three different GHG emissions scenarios where the corresponding temperature trends were extracted from the output of a state-of-the-art AOGCM, HadCM3. The semi-empirical models together with a temperature time series that includes the simulated temperature trends obtained from HadCM3, were then employed to simulate the future evolution of activated chlorine and ozone loss averaged over a constant vortex area for the period 2010 to 2100. 1000 Monte Carlo simulations were performed for each GHG emissions scenario to account for variability in the future temperature fields. It was found that using the modelled temperature trend from HadCM3, Antarctic ozone returns to 1980 levels about 20 years earlier than $\mathrm{Cl_y}$ returns to 1980 levels. Furthermore, ozone return dates derived here were about 25 years earlier than previously suggested by various CCM studies (Austin et al., 2010a; Eyring et al., 2010a). It was shown that the primary cause for the early return can be traced back to the missing temperature$\leftrightarrow$ozone feedback in HadCM3. The results presented here show that if the temperature$\leftrightarrow$ozone feedback is broken, the return dates of Antarctic ozone to historic levels (i.e. 1980 and 1960) are largely independent of GHG emissions. Independent of the GHG emissions scenario, the increase in stratospheric temperatures due to increasing ozone overwhelms the cooling effect of enhanced GHGs within HadCM3. However, as the temperature$\leftrightarrow$ozone feedback is not accounted for in HadCM3, the GHG-induced stratospheric cooling cannot affect ozone, i.e. no matter how cold the stratosphere will get due to enhanced GHGs, ozone increases further as it was calculated off-line and in HadCM3 ozone changes are unaffected by changes in temperature. In CCMs, on the other hand, the temperature$\leftrightarrow$ozone feedback is included. Therefore, GHG-induced cooling affects ozone via temperature, as lower temperatures results in more PSCs and therefore more chlorine activation. In CCM simulations the ozone is kept longer at lower values due to that temperature$\leftrightarrow$ozone feedback and the-

refore ozone returns to historic levels 25 years. Based on these results, it can be concluded that to reliably project the future of the stratospheric ozone layer and to assess the changes in stratospheric ozone due to changes in GHGs, the temperature↔ozone feedback has to be included in model simulations.

The results of this thesis emphasis the importance of the temperature↔ozone feedback when projecting the future evolution of stratospheric ozone. If the feedback is broken then reliable ozone projections cannot be conducted and the return of ozone to historical levels cannot be precisely estimated. AGCMs do not include the temperature↔ozone feedback and neither does the semi-empirical model presented here. Based on the study presented here, extending the functionality of an AOGCM to have some representation of polar stratospheric chemistry, through the use of a semi-empirical model that takes the AOGCM temperature fields as input does not solve the temperature↔ozone feedback problem. However, coupling the semi-empirical model to an AOGCM in such a way that both models run parallel so that the temperature fields from the AOGCM drive the polar ozone chemistry, and then in turn the derived ozone radiatively forces changes in temperature, would provide a powerful tool to conduct accurate simulations of the future evolution of stratospheric ozone. The AOGCM generates temperature fields based on dynamical and radiative processes as well as trace gas concentrations which provide input to the semi-empirical models. The semi-empirical model then generates ozone fields and feeds them back into the AOGCM. The AOGCM used these ozone fields in the next time step to generate new temperature fields. This semi-empirical model and AOGCM coupling would provide a tool to assess the uncertainties in ozone projections due to uncertainties in future GHG emissions. Furthermore, this coupling could also be used to investigate the contribution of existing uncertainties in the emissions of ozone depleting substances to the overall uncertainty in ozone projections.

Projections of future ozone changes by employing the semi-empirical model presented in this thesis is only applicable in the Antarctic stratosphere. To apply the model in the dynamically more disturbed Arctic stratosphere, additional terms would have to be included. Expanding the applicability of the semi-empirical models to the Arctic would provide a tool to examine the interhemispheric differences in the ozone return dates. Furthermore, it would allow an assessment of interhemispheric differences in the sensitivity of the ozone return dates to enhanced GHGs, i.e. the question ‘Do GHGs have a greater influence on the evolution of stratospheric ozone in the dynamically disturbed Arctic than in the Antarctic?’ could be addressed.

This thesis, further, emphasizes the importance of atmospheric measurements of trace gases. Atmospheric measurements are essential and useful to test our current understanding of chemical key reactions driving polar ozone loss but also to evaluate the performance of numerical models. Especially long-term measurements are indispensable for addressing key questions in stratospheric ozone behaviour over the last decades.

Appendix A

A.1 Potential temperature

The potential temperature of an air parcel is defined as the temperature that a parcel of dry air at pressure p and temperature T would have if it were adiabatically compressed or expanded to a standard pressure p_0 (1013 hPa). Potential temperature can be calculated using:

$$\theta = T \cdot (\frac{p_0}{p})^{\frac{R}{c_p}} \tag{A.1}$$

where R is the gas constant for dry air and c_p is the specific heat at constant pressure. For dry air R/c_p is 0.286. Surfaces of constant potential temperature are referred to as isentropic surfaces. The potential temperature is a conserved quantity for adiabatic motions and air parcels following the motion move along an isentropic surface (surface of constant θ).

A.2 Potential vorticity and calculation of equivalent latitude

Potential vorticity (PV) is an important diagnostic tool for stratospheric dynamical processes. One use is used to describe the location of the polar vortex edge (see below). Potential vorticity is the sum of the curl of the wind field (vorticity) and the planetary vorticity (also known as the Coriolis parameter) due to Earths's rotation multiplied by vertical 'stretching' or horizonal compression ('shrinking') of an air column and is written as:

$$PV = -g \cdot (f + \zeta_\theta) \cdot \frac{\partial \theta}{\partial p} \tag{A.2}$$

where g is the acceleration due to gravity and $f = 2\Omega sin\phi$ is the Coriolis parameter where Ω is the angular velocity of the Earth and ϕ is the latitude. $\zeta_\theta = \frac{\partial v}{\partial x} - \frac{\partial u}{\partial y}$ is the vertical

component of the curl of the wind field (relative vorticity) on a given isentropic surface where u and v are the zonal- and meridional wind components, respectively. Further, $\frac{\partial\theta}{\partial p}$ is change potential temperature (θ) with respect to pressure p.

In the absence of friction in an adiabatic flow potential vorticity is a conserved quantity. Because the Coriolis parameter increases with latitude, PV on an isentropic surface in the stratosphere generally increases from the equator to the pole. The PV value is normally negative in the south and positive in the north.

Potential vorticity is usually quoted in potential vorticity units (PVU), where

$$1PVU = 10^{-6}\frac{K \cdot m^2}{s \cdot kg} \tag{A.3}$$

Because PV is a dynamically quasi-conserved property of the atmosphere, lines of constant PV tend to follow dynamical structures in the atmosphere. Therefore, a PV can be used to define a new dynamically sensitive coordinate viz; equivalent latitude (see below). Using the equivalent latitude as meridional coordinate gives the polar vortex-centered view (Nash et al., 1996; Butchart and Remsberg, 1986), i.e. equivalent latitudes are zonally symmetric arranged around the pole. As equivalent latitude is a useful quantity in describing vortex behaviour, the calculation of equivalent latitude is described in the following.

A.3 Equivalent latitude

Equivalent latitude (ϕ_e) is defined as the geographic latitude that encloses the same area as a PV contour. The equivalent latitude is derived from an isentropic potential vorticity PV field. The calculation of ϕ_e is performed separately for the northern and southern hemisphere.

To derive the ϕ_e for the northern or southern hemisphere, the maximum and minimum PV values for the chosen hemisphere are first determined. The range between the maximum and minimum value is divided into 100 PV values, equally spaced, so that the first PV value corresponds to the minimum and the hundredth PV value corresponds to the maximum. For every PV contour of those 100 PV values, the geographical area enclosed by each contour is calculated (hereafter referred to as A_{PV_i}, for $1 \leq i \leq 100$). Starting, for example, at the equator, for every grid box (latitude/longitude) with a corresponding PV value, the area of

this box is calculated.

$$A_{gridbox} = \frac{2\pi \times E_R^2 \times [sin(\mathrm{SLat}) - sin(\mathrm{NLat})]}{\mathrm{NumLong}} \tag{A.4}$$

where E_R is the radius of the earth (6371000 m), SLat is the latitude of the southerly boundary and NLat is the latitude of the northerly boundary in radians. $\mathrm{NumLong}$ is the total number of longitudes of the underlaying PV field which depends on the horizontal resolution of the PV field.

The PV value of the grid box is attributed to one of the 100 PV values (referred to as i). For example, if the PV value of that grid box corresponds to the 10th value of the 100 PV values, i.e. i=10, then the calculated area of that grid box is added to the area enclosed by the 10th PV contour, i.e. the area is added to $A_{PV_{10}}$ and to all lower order (the cell area is added to A_{PV_1} to $A_{PV_{10}}$. This is done for every grid box between in the hemisphere, resulting in PV contours with a corresponding area. The area corresponding to the first PV value (minimum) should be the area of the whole hemisphere and the area corresponding to the last PV value (maximum) should be zero. The equivalent latitude can be calculated from these calculated areas by applying:

$$\phi_e(i) = \arcsin(1 - \frac{A_{PV_i}}{2\pi \times E_R^2}); \tag{A.5}$$

where A_{PV_i} is the calculated area enclosed by the ith PV value of the total 100 PV values. This process results in 100 equivalent latitudes (from 0 to 90^o) corresponding to 100 PV values. The potential vorticity versus equivalent latitude is shown in Figure A.1. The location of the highest horizontal gradient of PV can be used as an indicator for the location of the vortex edge (see below). The transformation from the two dimensional geographical grid (longitude/latitude) to one dimension equivalent latitude has the advantage that the area enclosed by the equivalent latitude is conserved, following dynamical structures. As a result, for a fixed geographical location, the equivalent latitude changes with time.

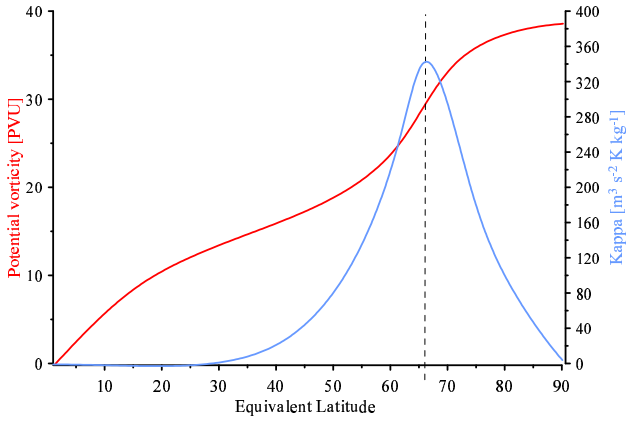

Figure A.1: Schematic of potential vorticity versus equivalent latitude (red line) together with the meridional impermeability κ (blue line). The location of the polar vortex edge is located at the maximum of κ.

A.4 Using equivalent latitude to define the vortex edge

The boundary of the polar vortex and mid-latitude air is indicated by the position of the strong horizontal gradient of PV on an isentropic surface. The vortex edge can be calculated by employing the method described in Nash et al. (1996). First, the meridional impermeability (κ) is calculated:

$$\kappa = \frac{dPV}{d\phi_e} \times |v| \tag{A.6}$$

where $\frac{dPV}{d\phi_e}$ is the potential vorticity gradient with respect to equivalent latitude and v is the horizontal wind speed on a given potential temperature surface. The wind speed is averaged along each PV contour.

The value of κ is a measure of the strength of the barrier to horizontal mixing. Low values of κ indicate regions of high meridional mixing, while high values of κ indicate regions of high impermeability and low meridional mixing. The location of the dynamical vortex edge can then be determined by finding the maximum of κ (Figure A.1)

Calculating κ for every day of the Antarctic or Arctic winter period and determining the daily maximum κ can also be used to estimate the longevity of the vortex. In the Antarctic winter, if the daily maximum κ is greater than 10% of the winter's maximum κ, then the polar vortex is assumed to exists (Bodeker et al., 2005). As the Arctic vortex is dynamically more variable than the Antarctic vortex, the threshold criterion for vortex existence was increased to 20% of the winter maximum κ.

Abbreviations

ACE-FTS	Atmospheric Chemistry Experiment - Fourier Transform Spectrometer
AGCM	Atmospheric general circulation model
AOGCM	Atmosphere-ocean general circulation model
BDC	Brewer Dobson Circulation
CCM	Coupled chemistry-climate model
CCMVal	Chemistry-climate model validation activity
CFCs	Chlorofluorocarbons
CGCM	Coupled general circulation model
CMIP	Coupled Model Intercomparison Project
DU	Dobson unit
ECMWF	European Centre for Medium-Range Weather Forecasts
EESC	Equivalent effective stratospheric chlorine
FAP	Fractional area of the vortex covered by polar stratospheric clouds
FAS	Fractional area of the polar vortex that is exposed to sunlight
GHG	Greenhouse gas
HALOE	Halogen Limb Occultation Experiment
IUPAC	International Union of Pure Applied Chemistry
IPCC	Intergovernmental Panel on Climate Change
JPL	Jet Propulsion Laboratory
MLS	Microwave Limb Sounder
NCAR	National Center for Atmospheric Research
NCEP	National Centers for Environmental Prediction
NDACC	Network for the Detection of Atmospheric Composition Change
NIWA	National Institute of Water and Atmospheric Research
ODS	Ozone-depleting substance
PCMDI	Program for Climate Model Diagnostics and Intercomparison
ppb	part per billion = 10^{-9}
ppm	part per million = 10^{-6}
ppt	part per trillion = 10^{-12}
PSC	Polar stratospheric cloud
PV	Potential vorticity

SST	sea surface temperature
SRES	Special Report on Emissions Scenarios
SWIFT	Semi-empirical Weighted Iterative Fit Technique
SZA	Solar zenith angle
UARS	Upper Atmosphere Research Satellite
UV	Ultraviolet
WCPR	World Climate Research Programme
WMO	World Meteorological Organization
WOUDC	World Ozone and Ultraviolet Data Center

Bibliography

Anderson, J. G., Brune, W. H., and Proffitt, M. H.: Ozone Destruction by Chlorine Radicals Within the Antarctic Vortex: The Spatial and Temporal Evolution of ClO-O_3 Anticorrelation Based on in Situ ER-2 Data, J. Geophys. Res., 94, 11,465–11,479, 1989.

Anderson, J. G., Toohey, D. W., and Brune, W. H.: Free radicals within the Antarctic vortex: The role of CFCs in Antarctic ozone loss, Science, 251, 39–46, 1991.

Arnold, F., Burger, V., Gollinger, K., Roncossek, M., Schneider, J., and Spreng, S.: Observations of nitric acid perturbations in the winter Arctic stratosphere: Evidence for PSC sedimentation, J. Atmos. Chem., 30, 49–59, 1998.

Atkinson, R., Baulch, D. L., Cox, R. A., Crowley, J. N., Hampson, R. F., Hynes, R. G., Jenkin, M. E., Rossi, M. J., and Troe, J.: Evaluated kinetic and photochemical data for atmospheric chemistry: Volume III - gas phase reactions of inorganic halogens, Atmos. Chem. Phys., 7, 981–1191, 2007.

Austin, J., Scinocca, J., Plummer, D., Oman, L. D., Waugh, D. W., Akiyoshi, H., Bekki, S., Braesicke, P., Butchart, N., Chipperfield, M. P., Cugnet, D., Dameris, M., Dhomse, S., Eyring, V., Frith, S. M., Garcia, R. R., Garny, H., Gettelman, A., Hardiman, S. C., Kinnison, D. E., Lamarque, J. F., Mancini, E., Marchand, M., Michou, M., Morgenstern, O., Nakamura, T., Pawson, S., Pitari, G., Pyle, J., Rozanov, E., Shepherd, T. G., Shibata, K., Teyssedre, H., Wilson, R. J., and Yamashita, Y.: The decline and recovery of total column ozone using a multi-model time series analysis, J. Geophys. Res., 2010a.

Austin, J., Struthers, H., Scinocca, J., Plummer, D. A., Akiyoshi, H., Baumgaertner, A. J. G., Bekki, S., Bodeker, G. E., Braesicke, P., Brühl, C., Butchard, N., Chipperfield, M. P., Cugnet, D., Dameris, M., Dhomse, S., Frith, S. M., Garny, H., Gettelman, A., Hardiman, S. C., Joëckel, P., Kinnison, D. E., Kubin, A., Lamarque, J. F., Langematz, U., Mancini, E., Marchand, M., Michou, M., Morgenstern, O., Nakamura, T., Nielsen, J. E., Pitari, G., Pyle, J., Rozanov, E., Shepherd, T. G., Shibata, K., Smale, D., Teyssedre, H., and Yamashita, Y.: Chemistry-climate model simulations of spring Antarctic ozone, J. Geophys. Res., 2010b.

Avallone, L. M. and Toohey, D. W.: Tests of halogen photochemistry using in situ measurements of ClO and BrO in the lower polar stratosphere, J. Geophys. Res., 106, 10 411–10 421, 2001.

Barath, F. T., Chavez, M. C., Cofield, R. E., Flower, D. A., Frerking, M. A., Gram, M. B., Harris, W. M., Holden, J. R., Jarnot, R. F., Kloezeman, W. G., Klose, G. J., Lau, G. K., Loo, M. S., Maddison, B. J., Mattauch, R. J., McKinney, R. P., Peckham, G. E., Pickett, H. M., Siebes, G., Soltis, F. S., Suttie, R. A., Tarsala, J. A., Waters, J. W., and Wilson, W. J.: The Upper Atmosphere Research Satellite Microwave Limb Sounder Instrument, J. Geophys. Res., 98, 10,751–10,762, 1993.

Barrett, J. W., Solomon, P. M., de Zafra, R. L., Jaramillo, M., Emmons, L., and Parrish, A.: Formation of the Antarctic ozone hole by the ClO dimer mechanism, Nature, 336, 455–458, 1988.

Bates, D. R. and Nicolet, M.: The photochemistry of atmospheric water vapour, J. Geophys. Res., 55, 301, 1950.

Bernath, P. F., McElroy, C. T., Abrams, M. C., Boone, C. D., Butler, M., Camy-Peyret, C., Carleer, M., Clerbaux, C., Coheur, P. F., Colin, R., DeCola, P., DeMaziere, M., Drummond, J. R., Dufour, D., Evans, W. F. J., Fast, H., Fussen, D., Gilbert, K., Jennings, D. E., Llewellyn, E. J., Lowe, R. P., Mahieu, E., McConnell, J. C., McHugh, M., McLeod, S. D., Michaud, R., Midwinter, C., Nassar, R., Nichitiu, F., Nowlan, C., Rinsland, C. P., Rochon, Y. J., Rowlands, N., Semeniuk, K., Simon, P., Skelton, R., Sloan, J. J., Soucy, M. A., Strong, K., Tremblay, P., Turnbull, D., Walker, K. A., Walkty, I., Wardle, D. A., Wehrle, V., Zander, R., and Zou, J.: Atmospheric Chemistry Experiment (ACE): Mission overview, Geophys. Res. Lett., 32, 2005.

Beyer, K. D., Seago, S. W., Chang, H. Y., and Molina, M. J.: Composition and freezing of aqueous H_2SO_4/HNO_3 solutions under polar stratospheric conditions, Geophys. Res. Lett., 21, 871–874, 1994.

Bloss, J. W., Nickolaisen, S. L., Salawitch, R. J., Friedl, R. R., and Sander, S. P.: Kinetics of the ClO self-reaction and 210 nm absorption cross section of the ClO dimer, J. Phys. Chem. A, 105, 11 226–11 239, 2001.

Boakes, G., Hindy Mok, W. H., and Rowley, D. M.: Kinetic studies of the ClO + ClO association reaction as a function of temperature and pressure, Phys. Chem. Chem. Phys., 7, 4102–4113, 2005.

Bodeker, G. E., Struthers, H., and Connor, B. J.: Dynamical containment of Antarctic ozone depletion, Geophys. Res. Lett., 29, 10.1029/2001GL014 206, 2002.

Bodeker, G. E., Shiona, H., and Eskes, H.: Indicators of Antarctic ozone depletion, Atmos. Chem. Phys., 5, 2603–2615, 2005.

Boone, C. D., Nassar, R., Walker, K. A., Rochon, Y., McLeod, S. D., Rinsland, C. P., and Bernath, P. F.: Retrievals for the atmospheric chemistry experiment Fourier-transform spectrometer, Applied Optics, 44, 7218–7231, 2005.

Brasseur, G. P. and Solomon, S.: Aeronomy of the middle atmosphere: chemistry and physics of the stratosphere and mesosphere, Springer, 32, 643, 2005.

Brewer, A. W.: Evidence for a world circulation provided by the measurements of helium and water vapour distribution in the stratosphere, Q. J. Roy. Meteor. Soc., 75, 351–363, 1949.

Bröske, R. and Zabel, F.: Thermal decomposition of ClOOCl, J. Phys. Chem. A, 110, 3280–3288, 2006.

Burkholder, J. B., Orlando, J. J., and Howard, C. J.: Ultraviolet absorption cross sections of Cl_2O_2 between 210 and 410 nm, J. Phys. Chem., 94, 687–695, 1990.

Butchart, N. and Remsberg, E. E.: The area of the stratospheric polar vortex as a diagnostic for tracer transport on an isentropic surface, Journal of Atmospheric Science, 43, 1319–1339, 1986.

Butz, A., Bosch, H., Camy-Peyret, C., Chipperfield, M. P., Dorf, M., Kreycy, S., Kritten, L., Prados-Roman, C., Schwarzle, J., and Pfeilsticker, K.: Constraints on inorganic gaseous iodine in the tropical upper troposphere and stratosphere inferred from balloon-borne solar occultation observations, Atmos. Chem. Phys., 9, 7229–7242, 2009.

Charlton-Perez, A. J., Hawkins, E., Eyring, V., Cionni, I., Bodeker, G. E., Kinnison, D. E., Akiyoshi, H., Frith, S. M., Garcia, R. R., Gettelman, A., Lamarque, J. F., Nakamura, T., Pawson, S., Yamashita, Y., Bekki, S., Braesicke, P., Chipperfield, M. P., Dhomse, S., Marchand, M., Mancini, E., Morgenstern, O., Pitari, G., Plummer, D., Pyle, J. A., Rozanov, E., Scinocca, J., Shibata, K., Shepherd, T. G., Tian, W., and Waugh, D. W.: The potential to narrow uncertainty in projections of stratospheric ozone over the 21st century, Atmos. Chem. Phys., 10, 9473–9486, 2010.

Chen, H. Y., Lien, C.-Y., Lin, W.-Y., Lee, Y. T., and Lin, J. J.: UV Absorption Cross Section of ClOOCl Are Consistent With Ozone Degradation Models, Science, 324, 781–784, 2009.

Chipperfield, M. P.: Multiannual simulations with a three-dimensional chemical transport model, J. Geophys. Res., 104, 1781–1805, 1999.

Chipperfield, M. P.: New version of the TOMCAT/SLIMCAT off-line chemical transport model: Intercomparison of stratospheric tracer experiments, Q. J. Roy. Meteor. Soc., 132, 1179–1203, 2006.

Chipperfield, M. P., Lutman, E. R., Kettleborough, J. A., Pyle, J. A., and Roche, A. E.: Model studies of chlorine deactivation and formationof $CIONO_2$ collar in the Arctic polar vortex, J. Geophys. Res., 102, 1467–1478, 1997.

Cicerone, R. J., Stolarski, R. S., and Walters, S.: Stratospheric ozone destruction by man-made chlorofluoromethanes, Science, 185, 1165–1167, 1974.

Collins, W. J., Stevenson, D. S., Johnson, C. E., and Derwent, R. G.: Tropospheric ozone in a global-scale three-dimensional Lagrangian model and its response to NO_X emission controls, J. Atmos. Chem., 26, 223–274, 1997.

Connor, B. J., Parrish, A., Tsou, J.-J., and McCormick, M. P.: Error analysis for the ground-based microwave ozone measurements during STOIC, J. Geophys. Res., 100, 9283–9291, 1995.

Cox, R. A. and Hayman, G. D.: The stability and photochemistry of dimers of the ClO radical and implications for Antarctic ozone depletion, Nature, 332, 796–800, 1988.

Crutzen, P. J.: The influence of nitrogen oxides on the atmospheric ozone content, Q. J. Roy. Meteor. Soc., 96, 320–325, 1970.

Crutzen, P. J.: Ozone production rates in an oxygen-hydrogen-nitrogen oxide atmosphere, J. Geophys. Res., 76, 7311–7327, 1971.

Crutzen, P. J. and Arnold, F.: Nitric acid cloud formation in the cold Antarctic stratosphere: A major cause for the springtime ‘ozone hole’, Nature, 342, 651–655, 1986.

De Zafra, R. L., Jaramillo, M., Parrish, A., Solomon, P., Connor, B., and Barret, J.: High concentrations of chlorine monoxide at low altitudes in the Antarctic spring stratosphere, Nature, 328, 408–411, 1987.

De Zafra, R. L., Jaramillo, M., Barrett, J. W., Emmons, L. K., Solomon, P. M., and Parrish, A.: New observations of a large concentration of ClO in the springtime lower stratosphere over Antarctica and its implications for ozone-depleting chemistry, J. Geophys. Res., 94, 11 423–11 428, 1989.

Dobson, G. M. B.: A photoelectric spectrophotometer for measuring the amount of atmospheric ozone, Proc. Roy. Soc., 43, 324, 1931.

Drdla, K. and Müller, R.: Temperature thresholds for polar stratopsheric ozone loss, Atmos. Chem. Phys. Discuss., 10, 28 687–28 720, 2010.

Edwards, J. M. and Slingo, A.: Studies with a flexible new radiation code .1. Choosing a configuration for a large-scale model, Q. J. R. Meteorol. Soc., 122, 689–719, 1996.

Eyring, V., Harris, N. R. P., Rex, M., Shepherd, T. G., Fahey, D. W., Amanatidis, G. T., Austin, J., Chipperfield, M. P., Dameris, M., Forster, P. M. F., Gettelman, A., Graf, H. F., Nagashima, T., Newman, P. A., Pawson, S., Prather, M. J., Pyle, J. A., Salawitch, R. J., Santer, B. D., and Waugh, D. W.: A strategy for process-oriented validation of coupled chemistry-climate models, Bull. Amer. Met. Soc., 86, 1117, 2005.

Eyring, V., Chipperfield, M., Giorgetta, M. A., Kinnison, D. E., Mancini, E., Matthes, K., Newman, P. A., Pawson, S., Shepherd, T. G., and Waugh, D. W.: Overview of the New CCMVal Reference and Sensitivity Simulations in Support of Upcoming Ozone and Climate Assessments and Planned SPARC CCMVal, SPARC Newsletter, 30, 20–26, 2008.

Eyring, V., Cionni, I., Bodeker, G. E., Charlton-Perez, A. J., Kinnison, D. E., Scinocca, J. F., Waugh, D. W., Akiyoshi, H., Bekki, S., Chipperfield, M. P., Dameris, M., Dhomse, S., Frith, S. M., Garny, H., Gettelman, A., Kubin, A., Langematz, U., Mancini, E., Marchand, M., Nakamura, T., Oman, L. D., Pawson, S., Pitari, G., Plummer, D. A., Rozanov, E., Shepherd, T. G., Shibata, K., Tian, W., Braesicke, P., Hardiman, S. C., Lamarque, J. F., Morgenstern, O., Pyle, J. A., Smale, D., and Yamashita, Y.: Multi-model assessment of stratospheric ozone return dates and ozone recovery in CCMVal-2 models, Atmos. Chem. Phys., 10, 9451–9472, 2010a.

Eyring, V., Cionni, I., Lamarque, J. F., Akiyoshi, H., Bodeker, G. E., Charlton-Perez, A. J., Frith, S. M., Gettelman, A., Kinnison, D. E., Nakamura, T., Oman, L. D., Pawson, S., and Yamashita, Y.: Sensitivity of 21^{st} century stratospheric ozone to greenhouse gas scenarios, Geophys. Res. Lett., 37, 2010b.

Fabry, C. and Buisson, H.: Etude de l'extremite ultra-violette du spectre solaire, J. Phys. Rad., 6, 197–226, 1921.

Farman, J. C., Gardiner, B. G., and Shanklin, J. D.: Large losses of total ozone in Antarctica reveals seasonal ClO_x/NO_x interactions, Nature, 315, 207–210, 1985.

Farmer, C. B., Toon, G. C., Schaper, P. W., Blavier, J. F., and Lowes, L. L.: Stratospheric trace gases in the spring 1986 Antarctic atmosphere, Nature, 329, 126–130, 1987.

Feng, W., Chipperfield, M. P., Dorf, M., Pfeilsticker, K., and Ricaud, P.: Mid-latitude ozone changes: studies with a 3-D CTM forced by ERA-40 analyses, Atmos. Chem. Phys., 7, 2357–2369, 2007.

Ferracci, V. and Rowley, D. M.: Kinetic and thermochemical studies of the ClO + ClO + M $\leftrightarrows$ Cl_2O_2 + M reaction, Phys. Chem. Chem. Phys., 12, 11 596–11 608, 2010.

Finlayson-Pitts, B. J. and Pitts, J. N.: Chemistry of the Upper and Lower Atmosphere, Academic Press, 1999.

Frieler, K., Rex, M., Salawitch, R. J., Canty, T., Streibel, M., Stimpfle, R. M., Pfeilsticker, K., Dorf, M., Weisenstein, D. K., and Godin-Beekmann, S.: Toward a better quantitative understanding of polar stratospheric ozone loss, Geophys. Res. Lett., 33, L10 812, doi:10.1029/2005GL025 466, 2006.

Gordon, C., Cooper, C., Senior, C. A., Banks, H., Gregory, J. M., Johns, T. C., Mitchell, J. F. B., and Wood, R. A.: The simulation of SST, sea ice extents and ocean heat transports in a version of the Hadley Centre coupled model without flux adjustments, Climate Dynamics, 16, 147–168, 2000.

Hanson, D. and Mauersberger, K.: Laboratory studies of the nitric acid trihydrate: Implications for the South Polar Stratosphere, Geophys. Res. Lett., 15, 855–858, 1988.

Harris, N. R. P., Lehmann, R., Rex, M., and von der Gathen, P.: A closer look at Arctic ozone loss and polar stratospheric clouds, Atmos. Chem. Phys., 10, 8499–8510, 2010.

Hassler, B., Bodeker, G. E., and Dameris, M.: Technical Note: A new global database of trace gases and aerosols from multiple sources of high vertical resolution measurements, Atmos. Chem. Phys., 8, 5403–5421, 2008.

Huck, P. E.: The Coupling of Dynamics and Chemistry in the Antarctic Stratosphere, Doctor of philosophy in physics, University of Canterbury, 2007.

Huder, K. J. and DeMore, W. B.: Absorption Cross Sections of the ClO Dimer, J. Phys. Chem., 99, 3905–3908, 1995.

IPCC: (Intergovernmental Panel on Climate Change), Climate Change 2001: The Scientific Basis: Contribution of Working Group I to the Third Assessment Report of the Intergovernmental Panel on Climate Change, edited by J. T. Houghton et al., 881 pp., Cambridge Univ. Press., New York., 2001.

IPCC: Intergovernmental Panel on Climate Change (IPCC), Climate Change 2007: Synthesis Report. Contribution of Working Groups I, II and III to the Fourth Assessment Report

of the Intergovernmental Panel on Climate Change [Core Writing Team, Pachauri, R.K and Reisinger, A. (eds.)]. IPCC, Geneva, Switzerland, 104 pp., 2007.

Jöckel, P., Sander, R., Kerkweg, A., Tost, H., and Lelieveld, J.: Technical Note: The Modular Earth Submodel System (MESSy) - a new approach towards Earth System Modeling, Atmos. Chem. Phys., 5, 433–444, 2005.

Johns, T. C., Gregory, J. M., Ingram, W. J., Johnson, C. E., Jones, A., Lowe, J. A., Mitchell, J. F. B., Roberts, D. L., Sexton, D. M. H., Stevenson, D. S., Tett, S. F. B., and Woodage, M. J.: Anthropogenic climate change for 1860 to 2100 simulated with the HadCM3 model under updated emissions scenarios, Climate Dynamics, 20, 583–612, 2003.

Kalnay, E., Kanamitsu, M., Kistler, R., Collins, W., Deaven, D., Gandin, L., Iredell, M., Saha, S., White, G., Woollen, J., Zhu, Y., Chelliah, M., Ebisuzaki, W., Higgins, W., Janowiak, J., Mo, K. C., Ropelewski, C., Wang, J., Leetmaa, A., Reynolds, R., Jenne, R., and Joseph, D.: The NCEP/NCAR 40-year reanalysis project, Bulletin of the American Meteor. Soc., 77, 437–471, 1996.

Kawa, S. R., Stolarski, R. S., Newman, P. A., Douglass, A. R., Rex, M., Hofmann, D. J., Santee, M. L., and Frieler, K.: Sensitivity of polar stratospheric ozone loss to uncertainties in chemical reaction kinetics, Atmos. Chem. Phys., 9, 8651–8660, 2009.

Keith, D. W., Parson, E., and Morgan, M. G.: Research on global sun block needed now, Nature, 463, 426–427, 2010.

Knudsen, B. M., Larsen, N., Mikkelsen, I. S., Morcrette, J. J., Braathen, G. O., Kyrö, E., Fast, H., Gernandt, H., Kanzawa, H., Nakane, H., Dorokhov, V., Yushkov, V., Hansen, G., Gil, M., and Shearman, R. J.: Ozone depletion in and below the Arctic vortex for 1997, Geophys. Res. Lett., 25, 627–630, 1989.

Konopka, P., Steinhorst, H. M., Grooss, J. U., Gunther, G., Muller, R., Elkins, J. W., Jost, H. J., Richard, E., Schmidt, U., Toon, G., and McKenna, D. S.: Mixing and ozone loss in the 1999-2000 Arctic vortex: Simulations with the three-dimensional Chemical Lagrangian Model of the Stratosphere (CLaMS), J. Geophys. Res., 109, 2004.

Lary, D. J.: Gas phase atmospheric bromine photochemistry, J. Geophys. Res., 101, 1505–1516, 1996.

Lary, D. J.: Catalytic destruction of stratospheric ozone, J. Geophys. Res., 102, 21,515–21,526, 1997.

Lary, D. J. and Pyle, J. A.: Diffuse radiation, twilight and photochemistry, J. Atmos. Chem., 13, 373–392, 1991.

Li, D. and Shine, K. P.: A 4-dimensional ozone climatology for UGAMP models, UGAMP Internal Report 35, 1995.

Liou, K. N.: An Introduction to Atmospheric Radiation, Academic Press, 84, 2002.

Livesey, N. J. and Wu, W. G.: EOS MLS retrieval processes algorithm theoretical basis., Techn. Report, Jet Propulsion Laboratory, 1999.

Livesey, N. J., Read, W. G., Froidevaux, L., Waters, J. W., Santee, M. L., Pumphrey, H. C., Wu, D. L., Shippony, Z., and Jarnot, R. F.: The UARS microwave limb sounder version 5 data set: Theory, characterization, and validation, J. Geophys. Res., 108, 2003.

Livesey, N. J., Van Snyder, W., Read, W. G., and Wagner, P. A.: Retrieval algorithms for the EOS Microwave Limb Sounder (MLS), Ieee Transactions on Geoscience and Remote Sensing, 44, 1144–1155, 2006.

Manney, G. L., Daffer, W. H., Zawodny, J. M., Bernath, P. F., Hoppel, K. W., Walker, K. A., Knosp, B. W., Boone, C., Remsberg, E. E., Santee, M. L., Harvey, V. L., Pawson, S., Jackson, D. R., Deaver, L., McElroy, C. T., McLinden, C. A., Drummond, J. R., Pumphrey, H. C., Lambert, A., Schwartz, M. J., Froidevaux, L., McLeod, S., Takacs, L. L., Suarez, M. J., Trepte, C. R., Cuddy, D. C., Livesey, N. J., Harwood, R. S., and Waters, J. W.: Solar occultation satellite data and derived meteorological products: Sampling issues and comparisons with Aura Microwave Limb Sounder, J. Geophys. Res., 112, 2007.

Marti, J. and Mauersberger, K.: A survey and new measurement of ice vapor pressure at temperatures between 170 and 250K, Geophys. Res. Lett., 20, 363–366, 1993.

McCartney, E. J.: Absorption and emission by atmospheric gases , John Wiley and Sons, Inc., p. 320, 1983.

McElroy, C. T., Salawitch, R. J., Wofsky, S. C., and Logan, J. A.: Antarctic ozone: Reductions due to synergistic interactions of chlorine and bromine, Nature, 321, 759–762, 1986.

Miller, M. J., Palmer, T. N., and Swinbank, R.: Parameterization and influence of subgrid scale orography in general circulation and numerical weather prediction models, Meteorol. Atmos. Phys., 40, 84–109, 1989.

Molina, L. T. and Molina, M. J.: Production of the Cl_2O_2 from the Self-Reaction of the ClO Radical, J. Phys. Chem., 91, 433–436, 1987.

Molina, M. J. and Rowland, F. S.: Stratospheric sink for chlorofluoromethanes: chhlorine atomc-atalysed destruction of ozone, Nature, 249, 810–812, 1974.

Morgenstern, O., Giorgetta, M. A., Shibata, K., Eyring, V., Waugh, D. W., Shepherd, T. G., Akiyoshi, H., Austin, J., Baumgaertner, A. J. G., Bekki, S., Braesicke, P., Bruhl, C., Chipperfield, M. P., Cugnet, D., Dameris, M., Dhomse, S., Frith, S. M., Garny, H., Gettelman, A., Hardiman, S. C., Hegglin, M. I., Jockel, P., Kinnison, D. E., Lamarque, J. F., Mancini, E., Manzini, E., Marchand, M., Michou, M., Nakamura, T., Nielsen, J. E., Olivie, D., Pitari, G., Plummer, D. A., Rozanov, E., Scinocca, J. F., Smale, D., Teyssedre, H., Toohey, M., Tian, W., and Yamashita, Y.: Review of the formulation of present-generation stratospheric chemistry-climate models and associated external forcings, J. Geophys. Res., 115, 2010.

Nakiċenovič, N. and Swart, R.: Special Report on Emissions Scenarios. A Special Report of Working Group III of the Intergovernmental Panel on Climate Change. , Cambridge University Press, Cambridge, United Kingdom and New York, NY, USA., p. 599 pp, 2000.

Nash, E. R., Newman, P. A., Rosenfield, J. E., and Schoeberl, M. R.: An objective determination of the polar vortex using Ertel's potential vorticity, J. Geophys. Res., 101, 9471–9478, 1996.

Newman, P. A. and Nash, E. R.: On the size of the Antarctic ozone hole, Geophys. Res. Lett., 31, doi:10.1029/2004GL020596, 2004.

Newman, P. A., Nash, E. R., Kawa, S. R., Montzka, S. A., and Schauffler, S. M.: When will the Antarctic ozone hole recover?, Geophys. Res. Lett., 33, doi:10.1029/2005GL025232, 2006.

Newman, P. A., Daniel, J. S., Waugh, D. W., and Nash, E. R.: A new formulation of equivalent effective stratospheric chlorine (EESC), Atmos. Chem. Phys., 7, 4537–4552, 2007.

Nickolaisen, S. L., Friedl, R. R., and Sander, S. P.: Kinetics and mechanism of the ClO-ClO reaction - pressure and temperature dependence of the bimolecular and termolecular channels and thermal-decomposition of chlorine peroxide, J. Phys. Chem., 98, 155–169, 1994.

Nissen, K. M., Matthes, K., Langematz, U., and Mayer, B.: Towards a better representation of the solar cycle in general circulation models, Atmos. Chem. Phys., 7, 5391–5400, 2007.

Oman, L., Waugh, D. W., Pawson, S., Stolarski, R. S., and Newman, P. A.: On the influence of anthropogenic forcings on changes in the stratospheric mean age, J. Geophys. Res., 114, 2009.

Oman, L. D., Waugh, D. W., Kawa, S. R., Stolarski, R. S., Douglass, A. R., and Newman, P. A.: Mechanism and feedback causing changes in upper stratospheric ozone in the 21st century, J. Geophys. Res., 115, 2010.

Osterman, G. B., Salawitch, R. J., Sen, B., Toon, G. C., Stachnik, R. A., Pickett, H. M., Margitan, J. J., Blavier, J.-F., and Peterson, D. B.: Balloon-borne measurements of stratospheric radicals and their precursors: implications for the production and loss of ozone, Geophys. Res. Lett., 24, 1107–1110, 1997.

Papanastasiou, D. K., Papadimitriou, V. C., Fahey, D. W., and Burkholder, J. B.: UV Absorption Spectrum of the ClO Dimer (Cl_2O_2) between 200 and 420 nm, J. Phys. Chem. A, 113, 13 711–13 726, 2009.

Parrish, A.: Millimeter-wave remote-sensinf of ozone and trace constituents in the stratosphere, Proceedings of the Ieee, 82, 1915–1929, 1994.

Parrish, A., deZafra, R. L., Solomon, P. M., and Barrett, J. W.: A ground-based technique for millimeter wave spectroscopic observations of stratospheric trace constituents, Radio Science, 23, 106–118, 1988.

Parrish, A., Connor, B. J., Tsou, J. J., McDermid, I. S., and Chu, W. P.: Ground-based microwave monitoring of stratospheric ozone, J. Geophys. Res., 97, 2541–2546, 1992.

Parrondo, M. C., Yela, M., Gil, M., von der Gathen, P., and Ochoa, H.: Mid-winter lower stratosphere temperatures in the Antarctic vortex: comparison between observations and ECMWF and NCEP operational models, Atmos. Chem. Phys., 7, 435–441, 2007.

Peter, T.: Microphysics and Heterogeneous Chemistry of Polar Stratospheric Clouds, Annu. Rev. Phys. Chem., 48, 785–822, 1997.

Petty, G. W.: A first course in atmospheric radiation, Sundog Publishing, p. 444, 2004.

Plenge, J., Kuehl, S., Vogel, B., Mueller, R., Stroh, F., von Hobe, M., Flesch, R., and Ruehl, E.: Bond Strength of Chlorine Peroxide, J. Phys. Chem. A, 109, 6730–6734, 2005.

Pope, F. D., Hansen, J. C., Bayes, K. D., Friedl, R. R., and Sander, S. P.: Ultraviolet absorption spectrum of chlorine peroxide, ClOOCl, J. Phys. Chem. A, 111, 4322–4332, 2007.

Press, W. H., Teukolsky, S. A., Vetterling, W. T., and Flannery, B. P.: Numerical Recipes: the art of scientific computing , Cambridge University Press, 2007.

Pundt, I., Pommereau, J. P., Phillips, C., and Lateltin, E.: Upper limit of iodine oxide in the lower stratosphere, J. Atmos. Chem., 30, 173–185, 1998.

Rex, M., Salawitch, R. J., Harris, N. R. P., von der Gathen, P., Braathen, G. O., Schulz, A., Deckelmann, H., Chipperfield, M. P., Sinnhuber, B.-M., Reimer, E., Alfier, R., Bevilacqua, R., Hoppel, K. W., Fromm, M. D., Lumpe, J., Küllmann, H., Kleinböhl, A., Bremer, H., von König, M., Künzi, K., Toohey, D. W., Vömel, H., Richard, E. C., Aikin, K., Jost, H.-J., Greenblatt, J. B., Loewenstein, M., Podolske, J. R., Webster, C. R., Flesch, G. J., Scott, D. C., Herman, R. L., Elkins, J. W., Ray, E. A., Moore, F. L., Hurst, D. F., Romashkin, P. A., Toon, G. C., Sen, B., Margitan, J. J., Wennberg, P., Neuber, R., Allart, M., Bojkov, B. R., Claude, H., Davies, J., Davies, W., De Backer, H., Dier, H., Dorokhov, V., Fast, H., Kondo, Y., Kyrö, E., Litynska, Z., Mikkelsen, I. S., Molyneux, M. J., Moran, E., Nagai, T., Nakane, H., Parrondo, C., Ravegnani, F., Skrivankova, P., Viatte, P., and Yushkov, V.: Chemical depletion of Arctic ozone in winter 1999/2000, J. Geophys. Res., 107, 8276, doi:10.1029/2001JD000533, 2002.

Rex, M., Salawitch, R. J., von der Gathen, P., Harris, N. R. P., Chipperfield, M. P., and Naujokat, B.: Arctic ozone loss and climate change, Geophys. Res. Lett., 31, L04116, doi:10.1029/2003GL018844, 2004.

Rodgers, C. D.: Retrieval of atmospheric temperature and composition from remote measurements of thermal radiation, Rev. Geophys. Space Sci, 14, 609–624, 1976.

Rodgers, C. D.: Characterization and error analysis of the profiles retrieved from remote sounding measurements, J. Geophys. Res., 95, 5587–5595, 1990.

Rodgers, C. D.: Inverse Methods For Atmospheric Sounding: Theory and Practice, World Scientific Publishing Co. Pte. Ltd., 2, 240, 2000.

Roeckner, E., Baeuml, G., Bonventura, L., Brokopf, R., Esch, M., Giorgetta, M. A., Hagemann, S., Kirchner, I., Kornblueh, L., Manzini, E., Rhodin, A., Schlese, U., Schulzweida, U., and Tompkins, A.: The atmospheric general circulation model ECHAM5. Part I: Model description, MPI Report 349, p. 121 pp, 2003.

Rosenfield, J. E., Newman, P. A., and Schoeberl, M. R.: Computation of diabatic descent in the stratospheric polar vortex, J. Geophys. Res., 99, 16677–16689, 1994.

Salawitch, R. J., Wofsy, S. C., Gottlieb, E. W., Lait, L. R., Newman, P. A., Schoeberl, M. R., Loewenstein, M., Podolske, J. R., Strahan, S. E., Proffitt, M. H., Webster, C. R., May, R. D., Fahey, D. W., Baumgardner, D., Dye, J. E., Wilson, J. C., Kelly, K. K., Elkins, J. W., and Chan, K. R.: Chemical loss of ozone in the Arctic polar vortex in the winter of 1991-1992, Science, 261, 1146–1149, 1993.

Sander, R., Kerkweg, A., Jockel, P., and Lelieveld, J.: Technical note: The new comprehensive atmospheric chemistry module MECCA, Atmos. Chem. Phys., 5, 445–450, 2005.

Sander, S. P., Friedl, R. R., Golden, D. M., Kurylo, M. J., Huie, R. E., Orkin, V. L., Moortgat, G. K., Ravishankara, A. R., Kolb, C. E., Molina, M. J., and Finlayson-Pitts, B. J.: Chemical Kinetics and Photochemical Data for Use in Atmospheric Studies, Evaluation Number 14, JPL Publication 02–25,, Jet Propulsion Laboratory, Pasadena, CA, USA, 2003.

Sander, S. P., Friedl, R. R., Golden, D. M., Kurylo, M. J., Moortgat, G. K., Keller-Rudek, H., Wine, P. H., Ravishankara, A. R., Kolb, C. E., Molina, M. J., Finlayson-Pitts, B. J., Huie, R. E., and Orkin, V. L.: Chemical Kinetics and Photochemical Data for Use in Atmospheric Studies, Evaluation Number 15, JPL Publication 06-02, Jet Propulsion Laboratory, 2006.

Sander, S. P., Finlayson-Pitts, B. J., Friedl, R. R., Golden, D. M., Huie, R. E., Keller-Rudek, H., Kolb, C. E., Kurylo, M. J., Molina, M. J., Moortgat, G. K., Orkin, V. L., Ravishankara, A. R., and Wine, P. H.: Chemical Kinetics and Photochemical Data for Use in Atmospheric Studies, JPL Publication 09-31, Jet Propulsion Laboratory (Interim update to JPL06), 2009.

Santee, M. L., Froidevaux, L., Manney, G. L., Read, W. G., Waters, J. W., Chipperfield, M. P., Roche, A. E., Kumer, J. B., Mergenthaler, J. L., and Russell, J. M.: Chlorine deactivation in the lower stratospheric polar regions during late winter' Results from UARS, J. Geophys. Res., 101, 18,835–18,859, 1996.

Santee, M. L., Manney, G. L., Waters, J. W., and Livesey, N. J.: Variations and climatology of ClO in the polar lower stratosphere from UARS Microwave Limb Sounder measurements, J. Geophys. Res., 108, 2003.

Santee, M. L., Lambert, A., Read, W. G., Livesey, N. J., Manney, G. L., Cofield, R. E., Cuddy, D. T., Daffer, W. H., Drouin, B. J., Froidevaux, L., Fuller, R. A., Jarnot, R. F., Knosp, B. W., Perun, V. S., Snyder, W. V., Stek, P. C., Thurstans, R. P., Wagner, P. A., Waters, J. W., Connor, B. J., Urban, J., Murtagh, D., Ricaud, P., Barret, B., Kleinbohl, A., Kuttippurath, J., Kullmann, H., von Hobe, M., Toon, G. C., and Stachnik, R. A.: Validation of the Aura Microwave Limb Sounder ClO measurements, J. Geophys. Res., 113, doi:10.1029/2007JD008 762, 2008a.

Santee, M. L., MacKenzie, I. A., Manney, G. L., Chipperfield, M. P., Bernath, P. F., Walker, K. A., Boone, C. D., Froidevaux, L., Livesey, N. J., and Waters, J. W.: A study of stratospheric chlorine partitioning based on new satellite measurements and modeling, J. Geophys. Res., 113, 2008b.

Santee, M. L., Sander, S. P., Livesey, N. J., and Froidevaux, L.: Constraining the chlorine monoxide (ClO)/chlorine peroxide (ClOOCl) equilibrium constant from Aura Micro-

wave Limb Sounder measurements of nighttime ClO, Proc Natl Acad Sci U S A, 107, 6588–6593, 2010.

Schoeberl, M. R., Lait, L. R., Newman, P. A., and Rosenfield, J. E.: The Structure of the Polar Vortex, J. Geophys. Res., 97, 7859–7882, 1992.

Schofield, R., Connor, B. J., Kreher, K., Johnston, P. V., and Rodgers, C. D.: The retrieval of profile and chemical information from ground-based UV-visible spectroscopic measurements, JQSRT, 86, 115–131, 2004.

Schofield, R., Frieler, K., Wohltmann, I., Rex, M., von Hobe, M., Stroh, F., Koch, G., Peter, T., Canty, T., Salawitch, R., and Volk, C. M.: Polar Stratospheric Chlorine Kinetics from a Self-Match Flight during SOLVE-II/EUPLEX, Geophys. Res. Lett., 35, L01 807, doi:10.1029/2007GL031 740, 2008.

Shepherd, T. G.: Dynamics, stratospheric ozone, and climate change, Atmos. Ocean, 46, 117–138, 2008.

Shindell, D. T. and de Zafra, R. L.: Chlorine monoxide in the Antarctic spring vortex 2. A comparison of measured and modeled diurnal cycling over McMurdo Station, 1993, J. Geophys. Res., 101, 1475–1487, 1996.

Solomon, P. M., De Zafra, R. L., Parrish, A., and Barrett, J. W.: Diurnal variation of stratospheric chlorine monoxide: A critical test of chlorine chemistry in the ozone layer, Science, 224, 1210–1214, 1984.

Solomon, P. M., Connor, B. J., DeZafra, R. L., Parrish, A., Barrett, J. W., and Jaramillo, M.: High concentrations of chlorine monoxide at low altitudes in the Antarctic spring stratosphere: secular variation, Nature, 328, 411–413, 1987.

Solomon, P. M., Barrett, J. W., Connor, B. J., Zoonematkermani, S., Parrish, A., Lee, A., Pyle, J., and Chipperfield, M.: Seasonal observations of chlorine monoxide in the stratosphere over Antarctica during the 1996-1998 ozone holes and comparison with SLIMCAT three-dimensional model, J. Geophys. Res., 105, 28,979–29,001, 2000.

Solomon, P. M., Connor, B. J., Barrett, J. W., Mooney, T., Lee, A., and Parrish, A.: Measurements of stratospheric ClO over Antarctica in 1996-2000 and implications for ClO dimer chemistry, Geophys. Res. Lett., 29(15), 1708, 2002.

Solomon, P. M., Barrett, J. W., Mooney, T., Connor, B. J., Parrish, A., and Siskind, D. E.: Rise and decline of active chlorine in the stratosphere, Geophys. Res. Lett., 33, L18 807, 2006.

Solomon, S.: The hole truth - What's news (and what's not) about the ozone hole, Nature, 427, 289–291, 2004.

Solomon, S., Garcia, R. R., Rowland, F. S., and Wuebbles, D. J.: On the depletion of Antarctic ozone, Nature, 321, 755–758, 1986.

Solomon, S., Garcia, R. R., and Ravishankara, A. R.: On the role of iodine in ozone depletion, J. Geophys. Res., 99, 20 491–20 499, 1994.

SPARC: The Role of Halogen Chemistry in Polar Stratospheric Ozone Depletion: Report from the June 2008 Cambridge, UK Workshop for an Initiative under the Stratospheric Processes and Their Role in Climate (SPARC) Project of the World Climate Research Programme, Tech. rep., printed No. 33, 2009.

SPARC-CCMVal: SPARC Report on the Evaluation of Chemistry-Climate Models, V. Eyring, T. G. Shepherd, D. W. Waugh (eds.), Tech. Rep. SPARC Report No. 5, WCRP-132, WMO/TD-No. 1526, http://www.atmosp.physics.utoronto.ca/SPARC, 2010.

Stimpfle, R. M., Wilmouth, D. M., Salawitch, R. J., and Anderson, J. G.: First measurements of ClOOCl in the stratosphere: The coupling of ClOOCl and ClO in the Arctic polar vortex, J. Geophys. Res., 109, D03 301, doi:10.1029/2003JD003 811, 2004.

Stolarski, R. S. and Cicerone, R. J.: Stratospheric chlorine: A possible sink for ozone, Can. J. Chem., 52, 1610–1614, 1974.

Struthers, H., Bodeker, G. E., Austin, J., Bekki, S., Cionni, I., Dameris, M., Giorgetta, M. A., Grewe, V., Lefevre, F., Lott, F., Manzini, E., Peter, T., Rozanov, E., and Schraner, M.: The simulation of the Antarctic ozone hole by chemistry-climate models, Atmos. Chem. Phys., 9, 6363–6376, 2009.

Tilmes, S., Muller, R., Grooss, J. U., and Russell, J. M.: Ozone loss and chlorine activation in the Arctic winters 1991-2003 derived with the tracer-tracer correlations, Atmos. Chem. Phys., 4, 2181–2213, 2004.

Toon, O. B., Hamill, P., Turco, R. P., and Pinto, J.: Condensation of HNO_3 and HCl in winter polar stratosphere, Geophys. Res. Lett., 13, 1284–1287, 1986.

Trolier, M., Mauldin III, R. L., and Ravishankara, A. R.: Rate coefficient for the termolecular channel of the self-reaction of ClO, J. Phys. Chem., 94, 4896–4907, 1990.

Uppala, S. M., Kallberg, P. W., Simmons, A. J., Andrae, U., Bechtold, V. D., Fiorino, M., Gibson, J. K., Haseler, J., Hernandez, A., Kelly, G. A., Li, X., Onogi, K., Saarinen, S., Sokka, N., Allan, R. P., Andersson, E., Arpe, K., Balmaseda, M. A., Beljaars, A.

C. M., Van De Berg, L., Bidlot, J., Bormann, N., Caires, S., Chevallier, F., Dethof, A., Dragosavac, M., Fisher, M., Fuentes, M., Hagemann, S., Holm, E., Hoskins, B. J., Isaksen, L., Janssen, P., Jenne, R., McNally, A. P., Mahfouf, J. F., Morcrette, J. J., Rayner, N. A., Saunders, R. W., Simon, P., Sterl, A., Trenberth, K. E., Untch, A., Vasiljevic, D., Viterbo, P., and Woollen, J.: The ERA-40 re-analysis, Q. J. R. Meteorol. Soc., 131, 2961–3012, 2005.

von Hobe, M., Grooß, J.-U., Múller, R., Hrechanyy, S., Winkler, U., and Stroh, F.: A re-evaluation of the ClO/Cl_2O_2 equilibrium constant based on stratospheric in-situ observations, Atmos. Chem. Phys., 5, 693–702, 2005.

von Hobe, M., Salawitch, R. J., Canty, T., Keller-Rudek, H., Moortgat, G. K., Grooss, J.-U., Mueller, R., and Stroh, F.: Understanding the kinetics of the ClO dimer cycle, Atmos. Chem. Phys., 7, 3055–3069, 2007.

von Hobe, M., Stroh, F., Beckers, H., Benter, T., and Willner, H.: The UV/Vis absorption spectrum of matrix-isolated dichlorine peroxide, ClOOCl, Phys. Chem. Chem. Phys., 11, 1571–1580, 2009.

Waters, J. W., Froidevaux, L., Harwood, R. S., Jarnot, R. F., Pickett, H. M., Read, W. G., Siegel, P. H., Cofield, R. E., Filipiak, M. J., Flower, D. A., Holden, J. R., Lau, G. K. K., Livesey, N. J., Manney, G. L., Pumphrey, H. C., Santee, M. L., Wu, D. L., Cuddy, D. T., Lay, R. R., Loo, M. S., Perun, V. S., Schwartz, M. J., Stek, P. C., Thurstans, R. P., Boyles, M. A., Chandra, K. M., Chavez, M. C., Chen, G. S., Chudasama, B. V., Dodge, R., Fuller, R. A., Girard, M. A., Jiang, J. H., Jiang, Y. B., Knosp, B. W., LaBelle, R. C., Lam, J. C., Lee, K. A., Miller, D., Oswald, J. E., Patel, N. C., Pukala, D. M., Quintero, O., Scaff, D. M., Van Snyder, W., Tope, M. C., Wagner, P. A., and Walch, M. J.: The Earth Observing System Microwave Limb Sounder (EOS MLS) on the Aura satellite, Ieee Transactions on Geoscience and Remote Sensing, 44, 1075–1092, 2006.

Wennberg, P. O., Brault, J. W., Hanisco, T. F., Salawitch, R. J., and Mount, G. H.: The atmospheric column abundance of IO: Implications for stratospheric ozone, J. Geophys. Res., 102, 8887–8898, 1997.

Wetzel, G., Oelhaf, H., Kirner, O., Ruhnke, R., Friedl-Vallon, F., Kleinert, A., Maucher, G., Fischer, H., Birk, M., Wagner, G., and Engel, A.: First remote sensing measurements of ClOOCl along with ClO and ClONO2 in activated and deactivated Arctic vortex conditions using new ClOOCl IR absorption cross sections, Atmos. Chem. Phys., 10, 931–945, 2010.

Wilmouth, D. M., Hanisco, T. F., Stimpfle, R. M., and Anderson, J. G.: Chlorine-Catalyzed Ozone Destruction: Cl Atom Production from ClOOCl Photolysis, J. Phys. Chem. A, 113, 14 099–14 108, 2009.

WMO: Scientific Assessment of Ozone Depletion: 2006, World Meteorological Organisation, Global Ozone Research and Monitoring Project - Report No. 50, 2007.

Yang, E.-S., Cunnold, D. M., Newchurch, M. J., Salawitch, R. J., McCormick, M. P., Russell, J. M., Zawodny, J. M., and Oltmans, S. J.: First stage of Antarctic ozone recovery, J. Geophys. Res., 113, doi:10.1029/2007JD009 675, 2008.